Evolution of gas and dust in circumstellar environments: from protoplanetary discs to the formation of planets

Pablo Rivière Marichalar

UAM
UNIVERSIDAD AUTONOMA
DE MADRID

Madrid 2013

Universidad Autónoma de Madrid

Departamento de Física Teórica

Evolución de gas y polvo en entornos circumestelares: desde los discos protoplanetarios a la formación de planetas

Memoria presentada por el licenciado

Pablo Rivière Marichalar

para optar al título de Doctor en Ciencias Físicas

Madrid 2013

David Barrado y Navasués, Doctor en Ciencias Físicas y
Director del Centro Astronómico Hispano-Alemán

y

Carlos Eiroa de San Francisco, Doctor en Ciencias Físicas y
Profesor Titular de la Universidad Autónoma de Madrid,

CERTIFICAN que la presente memoria

Evolution of gas and dust in circumstellar environments: from protoplanetary discs to the formation of planets

ha sido realizada por **Pablo Rivière Marichalar** bajo nuestra dirección y tutela respectivamente. Consideramos que esta memoria contiene aportaciones suficientes para constituir la Tesis Doctoral del interesado.

En Madrid, a 12 de Octubre de 2012

David Barrado y Navasués Carlos Eiroa de San Francisco

Quiero dedicar este trabajo de tesis a la memoria de mi Padre, a mi madre, que tanto me ha apoyado siempre, a Laura por apoyarme y aguantarme y a la gente de CAB-Villafranca por el maravilloso tiempo compartido.

Resumen de la tesis en castellano

Comprender la evolución del gas y el polvo en discos circumestelares es uno de los temas más importantes de la astronomía moderna, conectado con uno de sus mayores desafíos: comprender la formación de sistemas planetarios. Los discos circumestelares se pueden encontrar en alrededor de estrellas de práctivamente todas las edades, y la propia materia circumestelar sigue un camino evolutivo que conecta los diferentes tipos de discos conocidos. Las estrellas más jóvenes poseen a su alrededor discos protoplanetarios ricos en gas y polvo, con un ratio típico de gas a polvo de en torno a 100. Los diversos procesos de limpieza del polvo y el gas producen rápidamente huecos interiores en la estructura del disco, dando lugar a sistemas más evolucionados, conocidos como de transición. Finalmente, los discos de *debris* son discos ricos en polvo pero pobres en gas, en los cuales el polvo procede de la destrucción por colisiones de cuerpos de mayor tamaño, precursores de los planetas, denominados planetesimales.

Las propiedades de los discos circumestelares han sido extensamente estudiadas durante los últimos 30 años. Gracias a observaciones en el infrarrojo cercano, medio y lejano, tanto desde tierra como desde el espacio, así como a observaciones desde tierra en el submilimétrico, se pueden estimar las propiedades del polvo. Comparando las distribuciones espectrales de energía (SED, por sus siglas en inglés) con modelos de disco se puede profundizar en el conocimiento de los parámetros físicos del disco, especialmente de la masa de polvo y radio interior. A su vez, el uso de imágenes resueltas a distintas longitudes de onda nos permite estudiar mejor su extensión y otros parámetros que no pueden ser delimitados mediante el simple uso de modelos de SED. En el sigo XXI, el instrumento *Multiband Imaging Photometer for Spitzer* (MIPS), a bordo del telescopio espacial *Spizter* ha sido extensamente usado para estudiar las propiedades del polvo frío en discos circumestelares. Así mismo, el *Spitzer Infrared Spectrograph* (IRS) fue extensamente empleado para caracterizar la composición mineralógica de los granos de polvo, tanto en sistemas protoplanetarios como en los más evolucionados discos de *debris*, en aquellos casos en los que una población de granos calientes había sobrevivido a los mecanismos de limpieza, permitiendo la aparición de líneas de emisión de diversos silicatos.

Aunque el gas domina la masa del disco en los sistemas protoplanetarios, es más difícil de estudiar que el polvo, dado que la molécula de H_2 (que es la especie gasesosa más abundante) carece de momento dipolar eléctrico, provocando que las líneas de transición rotacionales sean especialmente débiles. De este modo, la observación de emisión de gas en discos circumestelares se ha visto en cierto modo impedida por la carencia de una instrumentación adecuada para observar espectroscópicamente en el infrarrojo lejano, donde se produce la mayoría de la emisión. El telescopio espacial *Herschel Space Observatory* (de ahora en adelante HSO) ha abierto por fin esta ventana observacional con gran sensibilidad. El instrumento *Photodetector Array Camera & Spectrometer* (PACS), con su sensibilidad y resolución angular sin precedentes en el infrarrojo lejano, permite la detección de gas y polvo en discos poco intensos. Además, su menor tamaño de haz resulta en un menor índice de contaminación por fuentes de fondo. El programa GASPS es un *Open Time Key Program* del telescopio HSO que ha observado fotométrica y espectroscópicamente más de 250 estrellas, con el objetivo de hacer un seguimiento de la evolución del polvo y el gas en sistemas circumestelares. La muestra incluye estrellas en diversas asociaciones estelares jóvenes ($<$ 30 Myr) y cercanas al sol (20–140 pc). Las observaciones espectroscópicas se centraron en la detección de la línea de [OI] en 63.18 μm, que es la línea de emisión más intensa en el infrarrojo lejano en discos circumestelares. Las observaciones fotométricas se obtuvieron en las longitudes de onda propias de PACS, 70, 100 y 160 μm, donde se produce el pico de emisión del polvo frío.

En la presente Tesis se exponen algunos de los resultados más destacados del programa GASPS en las regiones de Taurus, *TW Hydrae Association* (TWA) y *β Pictoris Moving Group* (BPMG), tres asociaciones estelares en distintos estados evolutivos: Taurus, que con una edad de 1–3 Myr y a tan solo 140 pc es una de las localizaciones más observadas para el estudio de discos protoplanetarios; TWA, que con una edad de 7-10 Myr posee tanto discos de transición o incluso protoplanetarios, como discos de debris; y BPMG, que con una edad de 12-20 Myr tan solo posee ya discos de debris, pero con gran diversidad de características.

0.1 Objetivos de la investigación

Los principales objetivos de la investigación son:

1. Estudiar la evolución del gas en sistemas circumestelares, en concreto en las asociaciones jóvenes de Taurus, TWA y BPMG. Determinar la presencia de gas en discos con distintas edades, así como las estadísticas de discos con detecciones de gas frente al total de discos, nos permitirá mejorar nuestro conocimiento sobre las escalas de tiempos implicadas en los procesos de limpieza del gas primigenio. Así mismo, estudiaremos la presencia de gas en algunos sistemas peculiares, como HD 172555, donde el gas no puede tener un origen primigenio. Por otro lado, la detección de diversas especies atómicas y moleculares, como [OI] y H_2O, y el estudio comparativo de la frecuencia de detección de las distintas especies nos permitirá mejorar nuestro conocimiento de la química de estos sistemas; química que a su vez se encuentra íntimamente ligada a los procesos de formación planetaria.

2. Estudiar la evolución del polvo en sistemas circumestelares. Si bien el polvo circumestelar ha sido más ampliamente estudiado hasta el presente, nunca se ha hecho con la sensibilidad que nos brinda el *Telescopio Espacial Herschel* en el infrarrojo lejano. Mediante el modelado de las poblaciones de polvo en asociaciones a distintas edades podremos mejorar nuestra comprensión de la física implicada. Por otro lado, los tiempos medios de vida derivados hasta el presente para discos protoplanterios se han basado fundamentalmente en el infrarrojo medio y cercano. Sin embargo, el infrarrojo lejano traza el polvo frío en el disco, por lo que es de esperar que las escalas de tiempo sean distintas en diferentes regiones del espectro.

0.2 Planteamiento y metodología

Para abordar nuestros objetivos de investigación, se redujeron y analizaron diversas observaciones del HSO en las mencionadas asociaciones. Tras compilar fotometría en otras longitudes de onda, se construyeron SED's para las diversas fuentes, con el objetivo de comparar dichas SED's con espectros sintéticos producidos con diversas aproximaciones y profundizar en el conocimiento de las propiedades del polvo. Los espectros sintéticos se generarán empleando diversos códigos. La fase polvo se puede modelar usando MCFOST o GRaTeR; el grueso de objetos en BPMG se modelaron empleando este códio, si bien en el caso de HD 181327 se empleó un modelo más detallado hecho con GRaTeR, por las complicaciones asociadas a una mineralogía peculiar. Por otro lado, en los casos en los que se pudo también realizar un modelado del gas, se empleó el códio ProDiMo. Por otro lado, en el caso de TWA se emplearon tan solo modelos sencillos de cuerpo negro modificado dada la gran diversidad de propiedades en los discos de la muestra.

Así mismo, las observaciones espetroscópicas se emplearon para estimar las masas de gas, así como para comparar los flujos derivados con las predicciones de diversos modelos, permitiendo así establecer las regiones y mecanismos de emisión de las especies gaseosas en distintos casos evolutivos.

La comparación de las tendencias entre las diversas asociaciones permite comprender mejor la evolución de las distintas fases que conforman la materia circumestelar.

0.3 Aportaciones originales

A continuación se exponen los principales resultados de la investigación desarrollada en las distintas asociaciones estelares estudiadas.

En la región de Taurus:

- Detección de vapor de agua caliente por primera vez en sistemas protoplanetarios, demostrando que aproximadamente el 24 % de los discos ricos en gas poseen además una importante reserva de agua. Hemos mostrado que la emisión procede de una región a aproximadamente 1 unidad astronómica (UA) de la estrella central, región que contiene en su interior la conocida como "línea de nieve", distancia a partir de la cual el agua pasa de encontrarse en estado vapor a encontrarse en estado hielo, con las consiguientes implicaciones para las modernas teorías de formación de planetas telúricos.

En el grupo de movimiento de TW Hydrae:

- Detección por primera vez del flujo a 100 y 160 μm de TWA 07 y a 100 μm de TWA 03A. Empleando modelos de cuerpo negro modificado, hemos estimado la presencia de dos poblaciones de polvo distintas en torno a TWA 07, y derivamos una temperatura de 20 K para la más lejana, entre las más frías detectadas hasta la fecha.

- Detección por primera vez de emisión de oxígeno atómico en el disco de TWA 04B (HD 98800 B), un sistema cuadruple que no presenta signos de acreción magnetosférica. Usando modelos de emisión simples, estimamos una masa de gas en el rango $9.5 \times 10^{-3} - 6.0 \times 10^{-2}$ $M_{\oplus}$. Esta es la primera detección de gas en torno a TWA 04B.

- Detección por primera emisión de oxígeno atómico en TWA 01. Un modelado detallado, empleando otras líneas de emisión detectadas previamente, permite estimar una masa de gas de entre 160 y 1600 $M_{\oplus}$.

En el grupo de movimiento de β Pictoris:

- Detección por primera vez del flujo fotosférico a 70 μm en AT Mic y HD 146624. Detección por primera vez del flujo a 70 μm en HD 29391, con un valor tan sólo 22 mJy, pero en exceso sobre el valor fotosférico, resultando en una de las luminosidades fraccionales infrarrojas más pequeñas detectadas hasta la fecha: $\mathrm{LIR}/\mathrm{L}_{*} = 4.6 \times 10^{-6}$

- Detección por primera vez del flujo a 100 μm en HD 203, HD 164249, HD 172555, HD 181296, HD 35850, HIP 10679 y HIP 11437.

- Detección por primera vez del flujo a 160 μm en HD 172555, HD 35850, HIP 10679 y HIP 11437.

- Hemos modelado en detalle las SEDs de las estrellas con disco de *debris* de estos objetos usando el código MCFOST y realizando un análisis bayesiano de los resultados para estudiar la distribución estadística de los distintos parámetros físicos.

- Detección por primera vez de emisión de oxígeno atómico en HD 172555. Se trata de una detección especialmente importante por tratarse HD 172555 de un disco de debris, donde no se espera, en condiciones normales, detectar líneas de emisión de gas, dada su escasa cantidad. En consonancia con el trabajo previo de Lisse et al. (2009) relativo al espectro IRS del objeto, donde se encontraba emisión por silicatos en torno a 10 μm y una detección tentativa de SiO, consideramos que el origen más probable para el gas es un evento estocástico, parecido a la colisión violenta que originó la Luna.

0.4 Conclusiones

A continuación se resumen las principales conclusiones del presente trabajo de tesis.

1. Las estrellas T Tauri en la región de formación estelar de Taurus con discos ricos en gas poseen todavía a la edad de 1–3 Myr una considerable reserva de vapor de agua en torno a 1 AU. La desaparición de dicha reserva de agua puede estar ligada a la formación de planetas telúricos.
2. Los discos presentes en TWA muestran una gran variedad de propiedades, tanto en su contenido de polvo como en su contenido de gas y geometría. Esto demuestra que debe haber muchos y variados factores, y no solo la edad, influyendo en la evolución de los discos circumestelares.
3. La temperatura calculada para el anillo exterior en el disco de TWA 07 (20 K) indica cómo es posible la existencia de anillos considerablemente más fríos que nuestro Cinturón de Kuiper. Comprender la física asociada a este tipo de discos tan fríos es un importante desafío para futuras líneas de investigación.
4. Si bien hemos detectado [OI] en dos discos en TWA, en ningún caso detectamos agua. Esto parece indicar que la reserva de agua caliente, que puede ser considerada como un fenómeno común a la edad de Taurus, desaparece antes de $\sim$ 7 Myr.
5. La emisión del gas en discos particularmente planos puede ser difícil de detectar, pese a poder poseer cantidades importantes de gas.
6. A la edad de 12–20 Myr hemos detectado emisión de oxígeno atómico en HD 172555, demostrando que los eventos estocásticos pueden jugar un importante papel en la evolución del gas en los discos de debris desde edades muy tempranas.

0.5 Futuras líneas de investigación

El programa GASPS ha producido un conjunto de observaciones de gran interés para el estudio de discos circumestelares. Una tarea de gran importancia es por tanto la elaboración de un catálogo final que pueda ser empleado por la comunidad astronómica. Para ello, emplearemos la última versión disponible del software de reducción de datos (HIPE), así como de los archivos de calibración. Dicho catálogo final constará no sólo de los productos finales de la reducción (imágenes fotométricas a 70/100/160 μm y espectros finales de los 5×5 spaxels), sino que se proveerá al usuario con los correspondientes flujos fotométricos y espectrosópicos, resultando en el más extenso catálogo de flujos espectroscópicos en discos circumestelares hasta la fecha.

Si bien el consorcio de investigadores de GASPS ha producido una considerable cantidad de artículos hasta la fecha, estos se han dedicado al análisis de los resultados para las distintas asociaciones de forma individual o al modelado detallado de fuentes concretas. Una tarea pendiente de gran importancia es el estudio estadístico comparativo de las detecciones de gas y polvo en las distintas asociaciones, como medio de estudiar la evolución de ambos componentes con la edad.

A un nivel más concreto, el origen de la emisión del agua a 63 μm, y por extensión de otras líneas de emisión, sigue siendo incierto. El uso de observaciones complementaria a las realizadas con PACS es fundamental para este cometido. Concretamente, hemos solicitado tiempo de telescopio con el Espectrógrafo Criogénico Echelle de Alta Resolución (CRIRES, por sus siglas en inglés), con el objetivo de observar líneas de emisión de agua en infrarrojo cercano (alrededor de 3 μm). Dichas líneas de agua se originarían en una reserva similar (si no la misma) a la que origina la emisión detectada con PACS. La elevada resolución espacial de CRIRES (0.2 arcsec) así como espectral (3 km/s) nos permitirá distinguir si la emisión se origina en el disco o en el outflow. Si se origina en el disco, esperamos detectar la línea centrada en la longitud de onda de reposo y con un perfil de doble pico debido a la rotación kepleriana. Si se origina en el outflow, esperamos detectar un fuerte desplazamiento hacia el rojo o el azul producido por el movimiento de caída del gas.

El uso del *Atacama Large Millimeter/submillimeter Array* (ALMA) será de vital importancia en los próximos años para el estudio de los discos circumestelares y la formación planetaria. Gracias a su gran resolución espacial, podremos obtener información detallada de la distribución del polvo y el gas y su geometría, lo que permitirá, por ejemplo, detectar de forma sistemática estructuras resultantes de la interacción entre el disco y posibles planetas o planetesimales ya existentes, como torsiones, grumos, asimetrías y brazos de espiral. Además, su gran sensibilidad permitirá la detección de gas (mediante, p. ej., observaciones de CO) en sistemas pobres donde la emisión haya escapado los límites de detección existentes hasta el presente. En ese sentido, la participación en diversas campañas de observación con

ALMA de objetos previamente observados con Herschel es el complemento perfecto para la investigación desarrollada hasta el presente. Beneficiarse de los resultados de ALMA no requiere tan sólo la implicación en proyectos científicos afines, sino que es fundamental adquirir la destreza necesario en el tratamiento de los datos. La participación en diversos *workshops* y congresos permitirá la adquisición de dichas habilidades.

Finalmente, el modelado del gas en los discos de debris requiere de un código capaz de tratar las dinámicas del gas y el polvo de forma separada, que no asuma una misma distribución espacial para ambas fases, que sea capaz de trabajar en ambientes a muy baja densidad, con composiciones distintas de la solar y con una dependencia temporal para la química del sistema. El programa GASPS hace uso de los códigos MCFOST/GRATER para modelar la fase polvo y de PRoDiMo para modelar la fase gas, si bien PRoDiMo también es capaz de modelar la fase polvo. En los próximos meses, trabajaremos en la adaptación del último a las necesidades descritas.

Universidad Complutense de Madrid

Departamento de Astrofísica

Evolution of gas and dust in circumstellar environments: from protoplanetary discs to the formation of planets

A dissertation submitted by

Pablo Rivière Marichalar

in partial fulfillment of the requirements for the degree of

Doctor in Physics

Madrid 2013

In the original unity
of the first thing lies
the secondary cause of all things,
with the germ of their inevitable
annihilation.

En la unidad original
de la primera cosa
se halla la causa secundaria
de todas las cosas,
junto con el germen
de un inevitable aniquilación.

Edgar Alla Poe, "Eureka"

Abstract

Understanding the evolution of gas and dust in circumstellar discs is a major topic in present day astronomy, linked to one of the most interesting challenges: understanding the formation of planets. Circumstellar discs can be found around stars at different ages, and circumstellar matter follows an evolutionary path that links the different kinds of discs known. The youngest stars harbour protoplanetary discs that are gas and dust rich, with typical gas-to-dust ratios around 100. Very soon, clearing processes inner gaps in these discs, resulting in more evolved transitional discs. Finally, debris discs are dusty, gas poor discs where the dust comes from the collisional grinding of planetesimals.

The properties of circumstellar discs have been extensively studied over the last 30 years or so. Thanks to ground and space based observations in the near, mid and far-IR, and also ground based observations in the sub-milimetric, the properties of dust can be estimated. Spectral Energy Distribution (SED) models can be used to compute some disc parameters like the dust mass and minimum inner radius of the disc. Also, resolved imaging can help to better constrain disc properties, and get insight in some parameters that do not impact the SED shape. In the 21th century, the Multiband Imaging Photometer for Spitzer (MIPS) and the InfraRed Array Camera (IRS) *Spitzer* instruments were widely used to study the properties of dusty discs in evolved systems. The Spitzer Infrared Spectrograph (IRS) was also used to characterize dust grains composition and sizes in circumstellar environments.

Even though the gas dominates the mass in a protoplanetary disc, it is more difficult to study than dust, because H_2 lacks a permanent electric dipole moment, causing the IR pure rotational transitions to be very weak. The study of gas emission in circumstellar environments thus have suffered from the lack of sensitive instrumentation to spectroscopically observe gas in the far-IR, where most of the line emission from the disc is present. The *Herschel Space Observatory* has opened this window with great success. The *Photodetector Array Camera & Spectrometer* (PACS) (Poglitsch et al., 2010) unprecedented sensitivity and angular resolution in

the far-IR enables the detection of gas and dust in faint, dusty debris discs in the wavelength range where the cold Kuiper-Belt like dust emission peaks (70-200 μm). Its smaller beam size compared with previous instrumentation results in a lower rate of confusion with background sources. PACS spectroscopy covers the strong cooling lines of [OI] at 63 μm and [CII] at 158 μm, providing a powerful probe of the gas content. The Gas Around Protoplanetary Systems (GASPS) programme is a *Herschel Open Time Key Programme* that has spectroscopically and photometrically observed more than 250 stars within more than 400 hours, aiming to follow the evolution of gas and dust in circumstellar environments. The sample includes stars in several young ($<$ 30 Myr) stellar associations near the sun (20–140 pc). Spectroscopic line observations were focused on the [OI] line at 63.18 μm, which is the strongest disc emission line in the far-IR, while photometric observations were taken at 70, 100 and 160 μm.

In the present Thesis manuscript, results of the GASPS programme for discs in Taurus, TW Hydra Association (TWA) and β Pictoris Moving Group (BPMG) are presented. SEDs are modeled with different approaches to get insight on the dust properties, and line fluxes are compared with predictions from models to constrain the masses implied and understand the origin of the gas. The main results are the detection of a reservoir of warm water vapour in protoplanetary systems in Taurus, as well as the detection of [OI] emission toward one debris disc (namely HD 172555) and one transitional/debris disc (TWA 04B, or HD 98800 B).

Contents

List of Figures

List of Tables

Chapter 1

Introduction

According to the ‘inward-out’ paradigm for the collapse of a molecular cloud (Shu et al., 1987), protoplanetary discs are a natural by-product of star formation processes: the gravitational collapse of the gas cloud produces the disc as a result of angular momentum conservation. Following this paradigm, the first steps in the collapse of a molecular cloud result in the formation of a protostar at the centre due to the infall of low angular momentum material. As the system evolves, high angular momentum matter form an accretion disc from where material falls into the star due to gravitational and viscous evolution. The disc extends to the centrifugal radius, which is expected to grow with time as $R_{cent} \propto \Omega^2 t^3$, where Ω is angular velocity of the core (Terebey et al., 1984). Numerical models of collapsing molecular cores show that discs are formed within 10^4 years (Yorke et al., 1993). The formation of the disc leads to the opening of a cavity in the envelope surrounding the forming star, making the central source visible for the first time in the process. The gravitational infall of circumstellar material heats the disc; while the material is accreted on the star, the disc cools down and decreases its mass.

Most protoplanetary discs have been detected through its infrared excess: the dust surrounding the system absorbs light from the central star and re-emits in the IR, resulting in fluxes higher than the expected from photospheric emission. By modeling the Spectral Energy Distributions (SEDs) of these systems, information about the dust geometry and mass can be obtained. Lada & Wilking (1984), after studying protoplanetary systems in Ophiuchus, proposed three different classes of objects with protoplanetary discs, based in the shape of the SED. Objects with the excess rising in the near and mid-IR (Class I), objects with a declining but prominent excess in the mid and near-IR (Class II), and objects with negligible excess (Class

III). Later on Lada (1987) refined the classification by including criteria based on the slope of the SED from 2 to about 25 μm, defined as:

$$\alpha_{IR} = \frac{d\log(\lambda F_\lambda)}{d\log(F_\lambda)} \tag{1.1}$$

Class I objects have $\alpha_{\rm IR} > 0.3$; Class II objects have $-1.6 < \alpha_{\rm IR} < -0.3$; Class III objects have $\alpha_{\rm IR} < -1.6$. The more embedded objects were then included in the classification as Class 0 objects (Andre et al., 1993), characterized by a lack of optical and near-IR emission due to strong extinction by the envelope. This classification can somehow be linked to the previous taxonomy of T Tauri stars. Classical T Tauri stars, with strong H_α emission and UV excess due to gas accretion processes, can be identified with Class II objects; weak lined T Tauri stars, with signs of no accretion or very small accretion, can be identified with Class III objects.

Strom et al. (1989) drove the first survey to estimate the occurrence of protoplanetary discs. After studying a sample of 83 pre-main sequence (PMS) stars, they deduced that disc lifetimes are in the range 3×10^6 to 10^7 yr. The survey was based in near-IR data, and therefore, their results mainly affect the inner regions of the disc: only dust very close to the star (R $\lesssim$ 1.0 AU) becomes hot enough to produce detectable emission in the near-IR. Later on, Haisch et al. (2001) surveyed the clusters NGC 2264, NGC 2362 and NGC 1960 to study the evolution of the fraction of discs with age using JHKL photometry, and concluded that by 3 Myr, 50% of stars in a cluster have lost their inner disc, and by 6 Myr almost the whole population show no near-IR excess, signpost of inner disc clearing. To probe more distant regions of the disc, one has to move to mid and far-IR, and sub-millimeter wavelengths. The *Spitzer Space Telescope* systematically proved the planet forming regions ($\lesssim$ 5 AU) with a big dynamic range thanks to the IRAC unprecedented sensitivity in the mid-IR ($3.6 - 8.0$ μm). For clusters $\leq$ 1Myr, disc fractions are of the order of 70-80% (Winston et al., 2007; Gutermuth et al., 2008). For 2–3 Myr old clusters, the fraction of stars with disc is 40-50 % (Lada et al., 2006). At 8-10 Myr, protoplanetary discs showing an IRAC excess are $\leq$ 5% (Sicilia-Aguilar et al., 2006; Hernández et al., 2007). Therefore, the dissipation timescales for the planet forming regions of protoplanetary discs are very similar to those found for the inner disc. Finally, results from the Star Formation: From Cores to Disks (c2d, Evans & c2d Team, 2005) and Formation and Evolution of Planetary Systems (FEPS, Meyer et al., 2004) *Spitzer* programmes showed that an upper limit for outer disc lifetime is $\sim$ 10 Myr. Finally, Mamajek (2009) made the most extensive study to date, summarizing the results from previous surveys, and concluded that the typical protoplanetary disc lifetime is $\sim$ 2.5 Myr, the e-folding time from the exponential law used to fit the data, but a large scatter was present; the author pointed that any statement regarding primordial discs ages has to be considered in a statistical way. All together, these facts show how once the inner disc is dissipated and accretion stops, the whole disc dissipates very fast. Therefore, primordial circumstellar material can last for several Myr at all radii, but the dissipation of the entire disc proceed very fast once the inner disc is cleaned. This fact is known as the “two-timescale problem”.

The main factor affecting the primordial disc gas evolution/dissipation is viscous transport. The accretion itself is driven by the disc viscosity. To conserve angular momentum, material from the disc is lost through accretion channels. In a typical disc, the rate at which material is removed equals the accretion rate, and is proportional to the viscosity of the disc (Hartmann et al., 1998). As a result of accretion into the central star, the disk expands outwards to account for the angular momentum lost. But pure viscous evolution predicts an smooth evolution of the disc properties, in contradiction with the very rapid disc dissipation observed.

Another important factor affecting the evolution of protoplanetary gas is photo-evaporation by far-UV and extreme-UV photons and X-rays from the central star and nearby massive stars. The relative importance of each of these energetic components remains to be understood. The so-called UV-switch models combine the effects of viscous accretion and photo-evaporation to explain the evolution of protoplanetary discs. In these models, the regions of the disc beyond $\sim$ 10 AU are heated by EUV photons that trigger a photo-evaporative wind. According to these models, the first stages in the evolution of the disc are dominated by viscous accretion: material from the inner disc is accreted onto the star while the outer disc acts as a reservoir of material for the inner disc. But once the accretion rates are similar to photo-evaporation rates the outer disc can not resupply any more the inner disc due to the photo-evaporative wind, and the inner disc dissipates in a timescale of $\sim 10^5$ yr.

Finally, grain growth and dust settling are the main factors affecting the evolution of dust in protoplanetary systems. Grain growth is also of major importance as it leads to the formation of planetesimals, and therefore is linked with planet formation. Small dust grains (r $\sim 0.1\mu$m) are coupled to the gas, suffering gas drag as a consequence. But as grains collide with each other, they grow in size as they stick together, and finally they become decoupled from the gas. Once they are over a certain size, they suffer a drag toward the mid-plane of the disc and start to settle, increasing the density of grains in the most interior regions of the disc. The rise in density in the mid-plane increases the number of collisions, resulting in the further formation of planetesimals. Therefore, the evolution of the protoplanetary disc ends with a disc devoid of gas and small dust particles, but with a large population of big grains and planetesimals. Later on, these planetesimals start to collide among them, replenishing the disc with dust grains as a result of destructive collisions, and producing a second generation of dusty discs. We will focus on debris discs characteristics forward in this section.

One of the most important questions in present day astronomy is how planets form. According to the core accretion model for planet formation, planets form in protoplanetary systems through the aggregation of dust particles into planetesimals, and of planetesimals into planets. Laboratory experiments (Blum et al., 2000) show that dust grains growth must take place in protoplanetary discs. Through observations of the silicate feature at 10 μm, Bouwman et al. (2001) concluded that the shifts observed for the centre of the feature could be due to grain growth. The growth from small dust grains to planets involves ~13 orders of magnitude in size and ~ 40 orders of magnitude in mass (Birnstiel et al., 2010), and some caveats remain to be solved in our understanding of the mechanism, like the so-called meter size barrier: particles around one meter in size achieve velocities large enough for mutual collisions to be destructive, and also to drift radially into the star very fast (Weidenschilling, 1977; Nakagawa et al., 1986). Given that planets are formed in protoplanetary discs, the timescale given by Strom et al. (1989) for disc dissipation was also the first observational timescale for planet formation.

Transition discs (Strom et al., 1989; Najita et al., 2007) were first identified by Strom et al. (1989) as objects with no excess at $\lambda < 10\mu$m, but significant excess at $\lambda \geq 10\mu$m. The lack of near-IR excess is interpreted as the result of inner disc clearing processes. At this stage, the star may be still accreting, but accretion rates are 10–100 times lower than in the protoplanetary phase. The radius of the gap is typically in the range 1–20 AU, and may be the result of interactions between the disc and a planetary body (Lin & Papaloizou, 1993), or the result of photo-evaporation of the inner disc in UV-switch models. Therefore, transition discs seem to represent the last stages in the evolution of protoplanetary discs. Different authors use different definitions for transition discs, making the comparison of frequencies of transition discs between different studies a hard task. Nevertheless, there is a bunch of astronomical objects whose SED can mimic that of a transition disc with a given geometry, like asymptotic giant branch stars. According to Lada et al. (2006), ~8–20 % of stars (depending on spectral type) with discs in at 2–3 Myr show weak IRAC excess, in agreement with a transition disc. Other authors computed similar transition disc fractions, in the range 10–20% (Hernández et al., 2007; Currie et al., 2009; Dahm & Carpenter, 2009). If the inner hole is produced by photo-evaporation, then the transition stage should be very short ($\leq$ 0.5Myr). But if the inner holes is due to grain growth or giant planet formation, then the transition stage can last for much more time. The small number of transition discs detected suggests that the lifetime for these discs is very short. Is has been suggested that it is a common but short phase in the life of a circumstellar disc, and represents the last phase in the evolution of the primordial disc before dissipation. If they really represent the last stages in the evolution of a protoplanetary discs, then the small frequency of transition discs again suggests a very fast clearing mechanism. Different authors have arrived to different conclusions at different ages and for different associations about the origin of the gap; some argue that the gap is produced by giant planet formation (see e.g. Najita et al., 2007), while others studies in different regions agree with a photo-evaporation scenario (see e.g. Cieza et al., 2008). Overall, the mechanism responsible for gap opening depends on individual disc properties together with environmental characteristics.

We have shown that by 10^7 yr most protoplanetary discs have dissipated. However, a considerable amount of main sequence stars already show evidence of dust at ages > 10^7 yr. There are at least three mechanisms that can deplete the dust content in a circumstellar disc in very short timescales. The first is radiation pressure, that remove dust grains in timescales much shorter than the orbital period. The second mechanism is Poynting-Robertson drag (Wyatt, 2005b): a process by which stellar radiation pressure causes a dust grains to spiral into the star due a component of radiation pressure tangential to the grain's motion. The timescale for Poynting-Robertson drag is much shorter than the age of the disc. The last mechanism is mutual collisions between dust grains, also with a timescale shorter than the age of the disc. Given the short timescales (compared to the age of the disc) for dust grains removal, it soon became clear that this dust must be of second generation when compared with primordial dust present in protoplanetary discs. It is thought that this second generation dust could have its origin in mutual collisions between an unseen population of planetesimals. For that reason, these discs are known as debris discs. Debris discs are then the last stage in the evolution of circumstellar environments. The regions surrounding the star are replenished with dust through collisional cascades triggered by large bodies inside rings of circumstellar mater that resemble our own Asteroid and Kuiper belts. Therefore, debris discs can be considered signposts for the existence of planets, or at least of comets. The first observations of debris discs surrounding young stars were made in the mid-1980s, when an abnormal, overabundant infrared flux was observed in Vega (Aumann et al.,

1984) and β Pictoris (Smith & Terrile, 1984), where the disc was also imaged. Since the discovery of IR excess emission around the main sequence star Vega, hundreds of stars with debris discs have been detected, mainly thanks to IRAS, ISO and *Spitzer Space Telescope* observations. To date, more than 20 of the brightest debris discs have been imaged (Krivov, 2010), revealing the presence of different structures like clumps, spirals, warps, and wing asymmetries, that have been linked to the presence of a perturbing planetary mass object. Studies made with *Spitzer* data revealed a fraction of debris discs around A to K stars of $\sim 15\%$ (Su et al., 2006; Siegler et al., 2007; Trilling et al., 2007; Hillenbrand et al., 2008).

If debris dust is produced by collisions between planetesimals in a ring like our own Kuiper Belt, then particles need certain velocities for mutual collisions to become destructive. In protoplanetary systems, the dust movement is effectively braked by the gas drag, making relative velocities small. But in debris discs there is no gas left to brake the gas. The lack of gas is not enough for debris disc particles to have large velocities: as a result of protoplanetary disc evolution they are expected to have a low velocity dispersion. Therefore, the planetesimals must be stirred by some mechanism. There are two different models to explain the stirring mechanisms: self-stirring (Kenyon & Bromley, 2004) and pre-stirring by planets in the inner gap (Wyatt, 2005a; Mustill & Wyatt, 2009). Future observations will help us to understand what is the main mechanism responsible of the stirring of the disc.

Overall, circumstellar discs can be used as snapshots of the history of our own Solar System, allowing astronomers to better understand the evolution of our planetary system. In the other hand, comparison of spectroscopic results in other debris discs with Solar System experiments can help us to better understand the chemistry and physics of circumstellar matter far from the Sun.

1.1 Young stellar associations

Because the timescales implied in disc evolution are long, the study of the evolution of circumstellar environments requires an alternative tool, other than direct observation. By observing stars at different ages, we get snapshots of the evolution of the system that help us to build the full history. But the ages of isolated systems are hard to constrain. On the other hand, the ages of stellar associations are well known, and their members are coeval. An alternative approach is then to observe stars belonging to young stellar associations and moving groups at different ages.

The discovery of several, nearby ($\lesssim$ 100 pc), young ($\lesssim$ 50 Myr) sparse stellar associations or moving groups provided the best framework to study the evolution of dust in circumstellar discs. The main moving groups in the Sun vicinity are the β Pictoris Moving Group, the TW Hydrae Association, the AB Doradus Moving Group, the Tucana/Horologium association, and the η Chamaeleontis Cluster.

Details on each individual association or moving group are given in the corresponding chapters.

1.2 The Herschel Space Observatory and GASPS

The properties of circumstellar discs have been extensively studied over the last 30 years or so (see recent reviews by e.g. Krivov, 2010; Williams & Cieza, 2011, and references therein). The Multiband Imaging Photometer for Spitzer (MIPS) was widely used to study the properties of dusty discs in evolved systems (e.g. Bryden et al., 2006; Rebull et al., 2008). The *Spitzer* Infrared Spectrograph (IRS) was also used to characterise dust grains in circumstellar environments (e.g. Chen et al., 2006; Morales et al., 2009; Oliveira et al., 2011). By fitting models to the spectral energy distribution (SED) of a disc, the amount of dust, the geometry of the disc, the dust composition, and the grain size distribution can be estimated. Also, the study of direct images (thermal emission or scattered light images) can help us to constrain some properties of the disc that do not impact the SED, like the geometry for optically thin discs. Even though the gas dominates the mass in a protoplanetary disc, it is more difficult to study than dust, because H_2 lacks a permanent electric dipole moment, causing the IR pure rotational transitions to be very weak. A further difficulty is that emission from important molecules, like CO (the most widely used molecule to probe the gas content in protoplanetary discs to date), is often optically thick; also CO frozens out in the cold mid-plane of the disc, making them poor tracers of the overall gas content.

The *Herschel Space Observatory* (Pilbratt et al., 2010) was launched on 14 May 2009 as the fourth ‘cornerstone’ mission in the ESA science programme. The optical design is that of a Cassegrain telescope with a primary mirror of 3.5 m passively cooled, divided into 12 segments brazed together. The undersized secondary (30.8 cm) is a single peace that yields an effective primary size of 3.28 m. It is the largest space telescope ever launched. The main scientific objectives of the mission are linked to the physics of the inter-stellar medium (ISM), from observations of solar system objects and relics of the formation of the solar system, to the star formation history of the universe and cosmology, through protoplanetary disc observations. It is performing photometry and spectroscopy in the 55-671 μm range, filling an important gap in wavelength between earlier infrared science from space and ground based facilities.

The scientific payload consist of:

- The Photodetector Array Camera and Spectrometer (PACS, Poglitsch et al., 2010), that performs integral-field spectroscopy and imaging photometry in the 60-210 μm wavelength range using two Ge:Ga photoconductor arrays (stressed and unstressed) with 16×25 pixels and two filled silicon bolometer arrays with 16×32 and 32×64 pixels. In photometric mode it simultaneously observes in two bands: one at 60-85 μm or 85-125 μm, and another one at 125-210 μm. In spectroscopic mode it can image a field of 47×47 arcsecs resolved into 5×5 spaxels (spatial pixels) with spectral resolution $\sim$ 175 km/s in two different modes: a narrow mode called line spectroscopy, centred on any of the lines present in the range, and a range spectroscopy mode, with a larger wavelength coverage.

- The Spectral and Photometric Imaging REceiver (SPIRE, Griffin et al., 2010) a sub-millimetre camera and spectrometer that contains a three-band imaging photometer working at 250, 350 and 500 μm, and an imaging Fourier-transform spectrometer (FTS) that covers the 194-671 μm range.

- The Heterodyne Instrument for the Far Infrared (HIFI) (HIFI, de Graauw et al., 2010), that consists on seven heterodyne receivers that cover the 480?1250 GHz range with SIS mixers and the 1410-1910 GHz range with hot electron bolometer (HEB) mixers, with resolutions that are better than 0.1 km/s.

Herschel is producing a valuable dataset for the study of circumstellar environments, allowing to observe both the dust in the continuum and the gas emission in the far-IR. The PACS instrument is a useful tool for the study of protoplanetary and debris discs, covering with great sensitivity the wavelength range (55-220 μm) where cold dust emission peaks (100-200 μm). Its smaller beam size compared with previous far-IR instruments results in a smaller background confusion. PACS spectroscopy allows for the detection of a few molecular species like CO, H_2O and OH and the strong cooling lines of [OI] and [CII] at 63 and 158 μm respectively.

1.3 The GASPS survey

The *Herschel* Open Key Time Programme *"Gas in Protoplanetary Systems"* (GASPS; Dent et al. 2013, submitted) is a far-IR spectroscopic and photometric survey that aims to study the presence and distribution of gas and dust in circumstellar disc systems around young low- and intermediate-mass stars. GASPS has observed ~ 250 stars within 400 allocated hours, covering both photometry and spectroscopy. Observations were made between Dec 2010 and July 2012. The programme targeted the [OI] fine structure line at 63.18 μm using a narrow wavelength window (PACS line spectroscopy). [OI] is an important coolant in molecular clouds, photodissociation regions and circumstellar discs. Models also show that it is the brightest far-IR emission line for circumstellar systems. Using a two-phase strategy, a sub-sample of the most brightest objects at [OI] in 63 μm was also observed in [OI] at 145 μm and [CII] at 158 μm, together with several H_2O and CO transitions in the 78–180 μm range. An overview of the species present is shown in Table 1.1. The main objective of the survey was to allow the detection of gas in systems with a disc mass similar to existing sub-millimeter dust surveys. Additionally, stars were observed at 70, 100 and 160 μm with the PACS photometer.

The targets range from HAeBe stars to T Tauri stars, with spectral types from A0 to M6. The sample includes stars with total disc masses in the range 10^{-1} to 10^{-3} $M_\oplus$, to avoid a mass bias in the study. In the sample, there is also a number of Class III objects in young associations, together with a number of young debris discs, with masses as low as 10^{-9} $M_\oplus$. To allow age estimations, stars in the sample belong to several associations at different ages, from Taurus at 1–3 Myr to Tucana-Horologium at ~ 30 Myr. The more embedded objects where not included to avoid confusion from the surrounding material.

1.4 Overview of the thesis

The present work focuses on the analysis of *Herschel* observations of circumstellar discs in young stellar associations, with special emphasis on the gas phase. In Chapter 2 we describe spectroscopic observations of [OI] toward Taurus stars, together with the discovery of o-H_2O emission at 63.32 μm in eight members of the association, and propose a model to describe the origin of the water emission. In Chapter 3 we describe photometric and spectroscopic observations of dust and gas in TWA; simple blackbody models are used to derive the main properties of discs in the association. The first detections of [OI] emission toward TWA 01 and TWA 04B are reported, and the origin of the gas emission is discussed. In Chapter 4 we describe photometric and spectroscopic observations of discs in the BPMG, and simple blackbody models, together with more sophisticated MCFOST models are used to derive dust properties. We also report the first detection of atomic oxygen emission toward a debris disc in HD 172555. In Chapter 5 we describe in detail the detection of [OI] emission toward HD 172555, derive an atomic oxygen gas mass using simplistic assumptions, and propose a possible origin for the atomic gas. Finally, in Chapter 6 we discuss the main conclusions of this work and propose future lines of investigation to exploit the GASPS dataset and the results from this Thesis.

Table 1.1: Atomic and molecular transitions in PACS spectra.

Species	Transition	λ_0 (μm)
[OI]	$^3P_1 \rightarrow\ ^3P_2$	63.184
o-H_2O	$8_{18} \rightarrow 7_{07}$	63.324
DCO^+	J = 22-21	189.570
o-H_2O	$7_{07} \rightarrow 6_{16}$	71.946
CH^+	J = 5-4	72.14
CO	J = 36-35	72.843
p-H_2O	$4_{13} \rightarrow 3_{22}$	144.518
CO	J = 18-17	144.784
[OI]	$^3P_0 \rightarrow\ ^3P_1$	145.525
o-H_2O	$4_{23} \rightarrow 3_{12}$	78.741
OH	1/2 – 3/2	79.11
OH	1/2 – 3/2	79.18
CO	J = 33-32	79.360
[CII]	$^2P_{3/2} \rightarrow\ ^2P_{1/2}$	157.741
p-H_2O	$3_{31} \rightarrow 4_{04}$	158.309
p-H_2O	$3_{22} \rightarrow 2_{11}$	89.988
CH+	J = 4-3	90.02
CO	J = 29-28	90.163
o-H_2O	$2_{12} \rightarrow 1_{01}$	179.527
CH^+	J = 2-1	179.610
o-H_2O	$2_{21} \rightarrow 2_{12}$	180.488

Chapter 2

Warm water vapour in circumstellar discs around stellar members of Taurus

A version of this chapter has been published as a letter to the editor in Astronomy and Astrophysics, Riviere-Marichalar et al. (2012b)

2.1 Introduction and short summary of the Taurus Star Forming Region.

Discs are natural by-products of star formation and the birthplaces of planets. One of the key questions intimately linked with planet formation and the concept of planet habitability is how much vapour and icy water is present in discs and how it is radially distributed. However, it is only recently that observations of water vapour in discs have become possible.

Carr & Najita (2008), using the *Spitzer* InfraRed Spectrograph (IRS), reported a rich molecular emission-line spectrum dominated by rotational transitions of hot water from the disc of AA Tau. They concluded that the molecular emission seen in the mid-IR has a most likely origin within the 2-3 AU inner regions of the disc. Salyk et al. (2008) detected water emission in the 10-20 μm region with Spitzer-IRS, as well as water and hydroxyl emission around 3 μm with *NIRSPEC* on *Keck II*, for both DR Tau and AS 205A. The emission comes from the disc atmospheres of

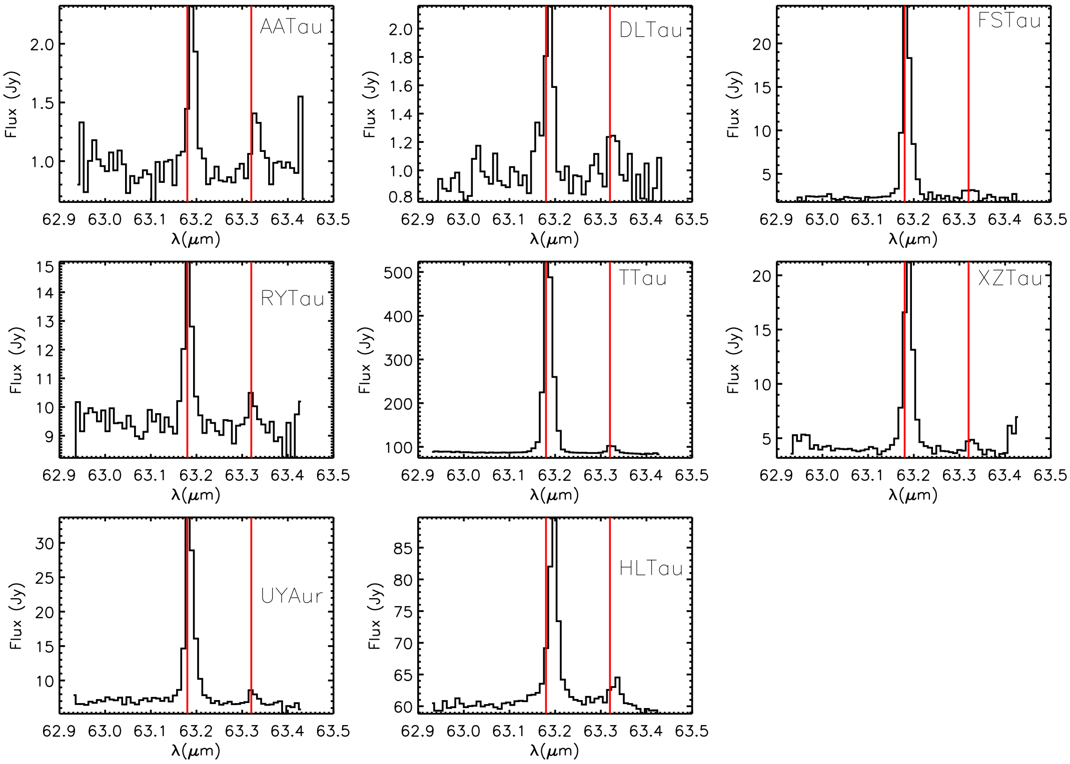

Figure 2.1: Spectra for the objects with a 63.32 μm feature detection ($> 3\sigma$). The red lines indicate the rest wavelength of the [OI] and o-H_2O emission.

the objects and the excitation temperatures[1] were found to be ~ 1000 K, which is typical of terrestrial planet formation regions. Pontoppidan et al. (2010b) performed a survey for more protoplanetary discs in Ophiuchus, Lupus, and Chamaeleon, again with *Spitzer-IRS*, and concluded that the presence of mid-IR molecular emission lines, including those of water, is a common phenomenon in discs around Sun-like stars. Also, Pontoppidan et al. (2010a) presented a sample of ground-based observations of pure rotational lines of water vapour in the protoplanetary discs of AS 205A and RNO 90 that was analysed to measure line widths of 30–60 km s^{-1}, which is consistent with an origin in a disc in Keplerian rotation at a radius of ~1 AU, and gas temperatures in the range 500–600 K.

The *Herschel Space Observatory* (Pilbratt et al., 2010) has opened the far-IR window with unprecedented sensitivity, allowing astronomers to survey the atomic and molecular gas content of disc regions that are cooler than those probed by *Spitzer* and ground-based instruments. Predictions of the water lines detectable

---

[1] Remember: $\frac{n_u}{n_l} = exp - \left(\frac{\Delta E}{kT_{ex}}\right)$, where T_{ex} is the excitation temperature, n_u and n_l the number of particles in the upper and lower level respectively, and g_u, g_l their statistical weights

by Herschel can be found in Cernicharo et al. (2009) and Woitke et al. (2009b). Hogerheijde et al. (2011) presented the first detection of cold water in the disc of the ~10 Myr old TW Hya, using *Herschel-HIFI*.

In this chapter, we report the first detection of the o-H_2O line at 63.32 μm in a subsample of protoplanetary discs around T Tauri stars in the 1-3 Myr old Taurus star forming region. The Taurus association is among the closest active star forming regions (140 pc, Bertout et al., 1999; Torres et al., 2009), with more than 250 members known, mainly low mass T Tauri, extending in a region of 10 deg. According to Torres et al. (2009), the depth of the complex is ~ 20 pc. The most complete census of Taurus Young Stellar Objects (YSOs) by Rebull et al. (2010) added a total of 148 new candidate members to the previously known list of 215 members, and 33 of them have already been confirmed as members, most of them Class II M stars. The final sample of confirmed Taurus members contain a 10% of Class I objects, a 8 % of Flat Class II objects, a 51 % of Class II objects and a 31 % of Class III objects. Class I and II stars are mainly found in the surrounding of dark clouds, while Class III objects are found everywhere within the cloud. There are also many jets within the star forming region, mainly associated with the most embedded objects.

In Sec. 2.2 we describe the sample, observations and the methodology for data reduction. In Sec. 2.3 we show our main results and discuss the origin of the line, together with some correlations between the line luminosity and some stellar and disc/jet parameters. Finally, in Sec. 2.4 we overview our main conclusions about the water content in Taurus protoplanetary discs.

2.2 Spectroscopic observations and data reduction

This study is based on a sample of 68 classical and weak-line T Tauri stars from the Taurus star forming region with spectral measurements from *Herschel*-PACS centred at the wavelength of the [OI] $^3P_1 \rightarrow {}^3P_2$ 63.184 μm line. The Taurus star-forming region is one of the main targets for the study of protoplanetary systems, because it is among the nearest star-forming regions (d = 140 pc) with a well-known population of more than 300 young stars and brown dwarfs according to Kenyon et al. (2008), Luhman et al. (2010), and Rebull et al. (2010).

The observations described in this chapter are part of the *Herschel* Open Time Key Programme *GASPS* [P.I. W. Dent], (Mathews et al., 2010, see). For this study, we analyzed the line scan spectra of 68 stars with spectral types ranging from late F-early G to mid M. The PACS spectral observations were made in chop/nod pointed line mode. The observing times ranged from 1215 to 6628 seconds, depending on the number of nod cycles. The data were reduced using the Herschel Interactive Processing Environment (HIPE) version 7, the dedicated tool for the reduction and analysis of *Herschel* data. A modified version of the PACS pipeline was used, which included: saturated and bad pixel removal, chop subtraction, relative spectral response-function correction, and flat fielding. Many observations suffer from systematic pointing errors, in some cases as large as 8 arcsec, and are always shifted to the East. This is due to a plate scale error in the star tracker, which is normally negligible except in areas where the tracked stars are asymmetrically distributed within the field, as in Taurus. The mis-pointing translates into systematic small shifts in the line centre position. When the star was well centred within a single spaxel, we extracted the flux from that spaxel and applied the proper aperture correction. When the flux was spread over more than one spaxel, we co-added the spaxels.

Table 2.1: Line positions and fluxes from PACS spectra.

Name	Sp. type	$\lambda_{H_2O} - \lambda_{[OI]}$	[OI] flux	$o - H_2O$ flux
–	–	(μm)	(10^{-17} W/ m^2)	(10^{-17} W/m^2)
AA Tau	K7	0.140	2.2 ± 0.13	0.80 ± 0.13
DL Tau	K7	0.141	2.4 ± 0.15	0.65 ± 0.14
FS Tau	M0	0.139	37 ± 0.26	2.00 ± 0.33
RY Tau	K1	0.139	10 ± 0.42	1.95 ± 0.38
T Tau	K0	0.138	830 ± 0.75	27.8 ± 0.7
XZ Tau	M2	0.139	32.2 ± 0.48	2.11 ± 0.48
HL Tau	K7	0.142	54.3 ± 0.71	8.14 ± 0.80
UY Aur	M0	0.139	33.6 ± 0.37	1.90 ± 0.32

Notes. All spectral types from the compilation of Luhman et al. (2010).

Table 2.2: Source list, spectral types, and 63 μm line fluxes for sources with no o-H_2O emission at 63.32 μm

Name	SP. Type	$o - H_2O$ flux	[OI] flux
–	–	(10^{-17} W/m^2)	(10^{-17} W/m^2)
Anon 1	M0	<1.17	<1.17
BP Tau	K7	<0.94	0.95 ± 0.27
CIDA2	M5.5	<0.89	<0.89

Table 2.2: continued.

Name	SP. Type	o − H_2O flux	[OI] flux
–	–	(10^{-17} W/m^2)	(10^{-17} W/m^2)
CI Tau	K7	<0.92	3.26 ± 0.45
CoKu Tau/4	K3	<1.37	2.15 ± 0.15
CW Tau	K3	<1.26	7.12 ± 0.41
CX Tau	M2.5	<0.94	< 0.8
CY Tau	M1.5	<1.41	1.15 ± 0.44
DE Tau	M1	<1.23	< 0.10
DF Tau	M2	<1.28	6.11 ± 0.58
DG Tau	K6?	<1.32	134 ± 1.7
DG Tau B	< K6	<1.25	42.6 ± 1.2
DH Tau	M1	<1.07	< 0.7
DK Tau	K6	<0.53	1.6 ± 0.3
DL Tau	K7	<1.14	2.2 ± 0.2
DM Tau	M1	<0.89	0.7 ± 0.2
DN Tau	M0	<0.77	0.6 ± 0.2
DO Tau	M0	<1.21	0.7 ± 0.1
DP Tau	M0.5	<0.92	14.8 ± 3.0
DQ Tau	M0	<0.98	2.1 ± 0.4
DS Tau	K5	<0.58	0.9 ± 0.2
FF Tau	K7	<1.11	< 10
FM Tau	M0	<1.24	< 1.3
FO Tau	M3.5	<0.96	< 1.2
FQ Tau	M3	<0.91	< 0.9
FT Tau	–	<1.25	1.7 ± 0.5
FW Tau	M5.5	<1.08	< 0.8
FX Tau	M1	<1.82	1.4
GG Tau	M5.5	<1.24	5.1 ± 0.4
GH Tau	M2	<0.84	< 16
GIK Tau	K7	<0.74	3.1 ± 1.4
GM Aur	K7	<1.21	2.4 ± 0.5
GO Tau	M0	<1.23	< 0.6
Haro 6-13	M0	<1.43	7.0 ± 0.5
Haro6-37	M1	<1.84	1.0 ± 0.2
HBC 347	K1[1]	<1.69	< 1.2
HBC 356	K2[1]	<0.94	< 0.8

Table 2.2: continued.

Name	SP. Type	$o-H_2O$ flux	[OI] flux
–	–	(10^{-17} W/m^2)	(10^{-17} W/m^2)
HBC 358	M3.5	<1.29	< 1.4
HK Tau	M0.5	<0.90	3.4 ± 0.2
HN Tau	K5	<0.64	4.1 ± 0.2
HO Tau	M0.5	<1.46	< 10
HV Tau	M1	<0.72	5.2 ± 0.8
IP Tau	M0	<0.83	< 0.7
IQ Tau	M0.5	<1.38	1.5 ± 0.3
04158+2805	M5.25	<1.06	5.7 ± 0.4
LkCa 1	M4	<1.06	< 0.8
LkCa 3	M1	<0.94	< 1.0
LkCa 4	K7	<0.98	< 1.0
LkCa 5	M2	<1.16	< 1.0
LkCa 7	M0	<0.88	< 0.9
LkCa 15	K5	<0.52	1.0 ± 0.2
SAO 76428	F8?	<1.58	3.1 ± 0.4
SU Aur	G2	<0.72	8.6 ± 0.3
UX Tau	K5	<0.99	3.4 ± 0.2
UZ Tau	M2	<0.60	4.5 ± 1.4
V710 Tau	M0.5	<1.17	< 12
V773 Tau	K3	<0.77	6.5 ± 0.3
V819 Tau	K7	<1.21	< 0.9
V927 Tau	M4.75	<0.88	< 0.8
VY Tau	M0	<1.30	< 1.1

2.3 Results and discussion: detection of water at 63 μm.

Among the sample of 68 Taurus targets studied in this chapter, 33 have discs that are rich in gas. These 33 all show the [OI] $^3P_1 \rightarrow ^3P_2$ line in emission at 63.18 μm (signal-to-noise ratio > 3, with values ranging from 3 to 375). In 8 of these 33 targets (~ 24%), an additional fainter emission-line at 63.32 μm is detected (Fig.1). We computed 63.32 μm line fluxes by fitting a Gaussian plus continuum curve to the spectrum using DIPSO [2]. To improve the line fitting, the noisier edges of the spectral range were removed (i.e., $\lambda < 63.0$ and $\lambda > 63.4$). The results are listed in Table 2.1, where we report the peak position of the feature with respect to the observed wavelength of the [OI] 63.18 μm line. According to these fits, the peak of the feature is at $\lambda_0 = 63.32\,\mu$m. The FWHM is 0.020 μm, i. e., the instrumental FWHM for an unresolved line. We identify the feature as the ortho-H_2O $8_{18} \rightarrow 7_{07}$ transition at 63.324 μm ($E_{\mathrm{Upper\ Level}}$=1070.7 K, Einstein A=1.751 s^{-1}) since no other abundant species emit strongly at or close to the observed wavelength of the feature. This water feature was observed by Herczeg et al. (2011) in the outflow of NGC 1333 IRAS 4B.

The o-H_2O emission is only present in spectra with [OI] detections. The targets FS Tau, HL Tau, and T Tau display extended emission in the [OI] 63.18 μm line, but only T Tau show hints of extended emission in the 63.32 μm o-H_2O line. T Tau is an exceptional object. It is a triple star system that drives at least two jets. It was the most line rich PMS star observed by ISO (Lorenzetti, 2005) and resembles more a hot core than a PMS star, since the continuum emission is quite extended (~ 3.5 arcsec at 70 μm). It is impossible to tell how much of the line emission comes from the discs, from the outflows, or even from the surrounding envelope.

Table 2.3: Star and disc (jet) parameters for T Tauri stars in Taurus observed with PACS.

Name –	L_*[1] ($L_\oplus$)	$F_{850\mu m}$[2] (mJy)	L_X[1] (10^{30}erg/s)	$\alpha(2-8\mu m)$[3] –	$L_{OI6300Å}$[4] (10^{30}erg/s)
AA Tau	0.8	144 ± 5	1.241	-1.10	0.41
DL Tau	0.9	440 ± 40	–	-0.77	0.15
FS Tau	0.32	49 ± 6	3.224	-0.84	–
RY Tau	7.6	560 ± 30	5.520	–	2.32
T Tau	8.048	628 ± 17	8.048	–	–
XZ Tau	0.48	–	0.96	-0.28	–
HL Tau	1.53	2360 ± 90	3.84	0.10	–
UY Aur	0.86	202 ± 6	–	-0.58	3.23
Anon 1	2.6	< 8	4.139	-2.65	–
BP Tau	0.95	130 ± 7	1.365	-1.36	–
CIDA 2	0.32	< 14	–	-2.56	–
CI Tau	0.87	324 ± 6	0.195	-1.03	0.16
CoKu Tau/4	0.15	9 ± 3	–	-2.58	–
CW Tau	1.1	66 ± 6	2.844	-1.01	15.69

---

[2] http://star-www.rl.ac.uk/docs/sun50.htx/sun50.html

Table 2.3: Continued

Name –	$L_*{}^1$ ($L_\oplus$)	$F_{850\mu m}{}^2$ (mJy)	$L_X{}^1$ (10^{30}erg/s)	$\alpha(2-8\mu m)^3$ –	$L_{OI6300Å}{}^4$ (10^{30}erg/s)
CX Tau	0.28	25 ± 6	–	-1.26	–
CY Tau	0.50	140 ± 5	0.133	-1.46	0.016
DE Tau	1.33	90 ± 7	–	-1.33	0.16
DF Tau	1.46	8.8 ± 1.9	–	-1.28	1.58
DG Tau	1.7	1100 ± 100	–	-0.49	55.55
DG Tau B	5.5	–	–	–	–
DH Tau	0.56	57 ± 9	8.458	-1.89	–
DK Tau	1.3	80 ± 10	0.916	-0.90	0.63
DL Tau	0.9	440 ± 40	–	-0.77	–
DM Tau	0.3	237 ± 12	–	-2.23	–
DN Tau	0.69	201 ± 7	1.155	-1.39	0.12
DO Tau	1.01	258 ± 42	–	-0.86	3.38
DP Tau	0.2	< 10	–	-0.55	–
DQ Tau	0.52	208 ± 8	–	-0.90	0.39
DS Tau	0.56	39 ± 4	–	-1.38	0.12
FF Tau	0.69	< 4	0.796	-2.69	–
FM Tau	0.46	32 ± 8	–	-1.13	0.011
FO Tau	0.77	13 ± 3	0.065	-1.31	–
FQ Tau	0.28	28 ± 7	0.120	-1.47	–
FT Tau	–	121 ± 5	–	-1.16	–
FW Tau	0.68	4.5 ± 1.1	–	-2.46	–
FX Tau	1.02	17 ± 3	0.502	-1.45	–
GG Tau	0.9	1255 ± 57	–	-1.13	0.15
GH Tau	0.81	15 ± 3	0.109	-1.53	–
GIK Tau	1.03	33 ± 7	0.833	-0.66	0.13
GM Aur	1.1	–	–	-1.94	0.053
GO Tau	0.37	173 ± 7	0.249	-1.49	–
Haro 6-13	2.11	395 ± 56	0.799	-0.76	–
Haro 6-37	1.05	245 ± 7	–	-1.35	–
HBC 347	0.43	< 9	–	–	–
HBC 356	0.27	< 9	–	–	–
HBC 358	0.28	< 9	0.383	-2.49	–
HK Tau	0.56	–	0.079	-1.54	0.20
HN Tau	0.25	29 ± 3	–	-0.41	0.33

Table 2.3: Continued

Name	L_*[1]	$F_{850\mu m}$[2]	L_X[1]	$\alpha(2-8\mu m)$[3]	$L_{OI6300Å}$[4]
–	($L_\oplus$)	(mJy)	(10^{30}erg/s)	–	(10^{30}erg/s)
HO Tau	0.17	44 ± 6	0.047	-1.45	–
HV Tau	0.54	47 ± 4	–	-2.56	–
IP Tau	0.43	34 ± 5	–	-1.61	–
IQ Tau	0.88	178 ± 3	0.416	-1.29	–
04158+2805	–	–	0.882	-0.03	–
LkCa 1	0.38	< 8	0.232	-2.31	–
LkCa 3	1.91	< 9	–	-2.68	–
LkCa 4	0.75	< 4	–	-2.59	0.011
LkCa 5	0.37	< 4	0.432	-2.59	–
LkCa 7	0.92	< 9	–	-2.59	0.010
LkCa 15	0.75	428 ± 11	–	-1.68	–
SAO 76428	–	< 12	–	–	–
SU Aur	9.9	74 ± 3	9.464	-1.33	–
UX Tau	2.02	173 ± 3	–	-2.64	–
UZ Tau	0.89	560 ± 7	0.890	-0.80	3.04
V710 Tau	1.1	152 ± 6	1.378	-1.07	–
V773 Tau	5.6	9.2 ± 2.9	9.488	-1.62	–
V819 Tau	0.91	< 9	2.445	-2.59	0.0075
V927 Tau	0.8	< 10	–	-2.55	–
VY Tau	0.41	< 10	–	-1.71	–

(1): stellar luminosities and X ray luminosities from Güdel et al. (2007)

(2): fluxes at 850 μm from Andrews & Williams (2005)

(3): 2 to 8 μm near-IR slope from Luhman et al. (2010)

(4): [OI] line luminosities at 6300 Å from Hartigan et al. (1995)

To help us understand the origin of the o-H_2O emission, we compared the line intensity with several star and disc (jet) parameters. We computed survival analysis ranked statistics using the ASURV code (Feigelson & Nelson, 1985; Isobe et al., 1986). We also created random populations to test the validity of the correlations. The result of this analysis is summarised in Table 2.4, where the probability that there is no correlation according to Spearman's and Kendall's tests are given. The same probabilities for random populations with the same dynamic range and distribution of upper limits as the studied parameter are given in brackets. The star and disc parameters used in the analysis are listed in Table 2.3.

Table 2.4: Probabilities for correlations between o-H_2O line intensity and stellar/disc parameters.

Observable	Points n	Spearman's prob.	Kendall's prob.
$L_{[OI]}$	68	0.0009 (0.4090)	0.0000 (0.196)
63 μm flux	64	0.0147 (0.2635)	0.0002 (0.4567)
850 μm flux $^{(2)}$	57	0.0145 (0.2596)	0.0131 (0.8496)
L_{star} $^{(3)}$	65	0.2608 (0.1130)	0.2267 (0.5535)
L_X $^{(3)}$	65	0.0225 (0.9912)	0.0087 (0.6012)
$\alpha(2\mu m - 8\mu m)$ $^{(4)}$	62	0.026 (0.1547)	0.0023 (0.3850)
$L_{[OI]6300Å}$ $^{(5)}$	27	0.1291 (0.3255)	0.1008 (0.3450)

Notes. The values obtained for random populations are shown in brackets. Accurate only if N > 30. (2): 850 μm continuum fluxes from Andrews & Williams (2005). (3): Values from Güdel et al. (2007). (4): SED slope from Luhman et al. (2010). (5): OI luminosities at 6300 Å from Hartigan et al. (1995).

The survival analysis shows a correlation between the o-H_2O line fluxes and the [OI] line fluxes at a significance level of 0.99 (see Fig. 2.2, top left). This relationship suggests that both lines have a similar origin. The H_2O emission is correlated with the continuum emission at 63 μm, but at a significance level of 0.95 in the Spearman statistics (Fig. 2.2, top right). The 850 μm continuum flux can be used as a proxy for the amount of dust present in the disc. A survival analysis shows a possible correlation with the 850 μm continuum flux, at a significance level of 0.95 in both Spearman and Kendall statistics, although a large scatter is present (Fig. 2.2, bottom left, fluxes from Andrews & Williams, 2005). A correlation with neither the stellar luminosity (Fig. 2.2, middle right, stellar luminosities from Güdel et al., 2007) nor the spectral type is found. There seems to be a weak correlation with the slope of the SED measured between 2 μm and 8 μm, used as a proxy for the presence of hot dust (Fig. 2.2, bottom right, slopes from Luhman et al., 2010). The significance of this correlation is dominated by T Tau, which has the highest o-H_2O flux in the sample. There is likely no link between mass loss rate and L_{H_2O}. The [OI] luminosity at 6300 Å is proportional to the mass loss rate (Hartigan et al., 1995). Although the sample is too small to test this relationship conclusively, we note that while $L_{[OI]6300Å}$ spans four orders of magnitude, the H_2O luminosity spans only one order of magnitude (see Fig. 2.3). Finally, the survival analysis statistics points to a possible relationship with the X-ray luminosity L_x (X-ray luminosities from Güdel et al., 2007). While the Spearman probability for the real sample is only

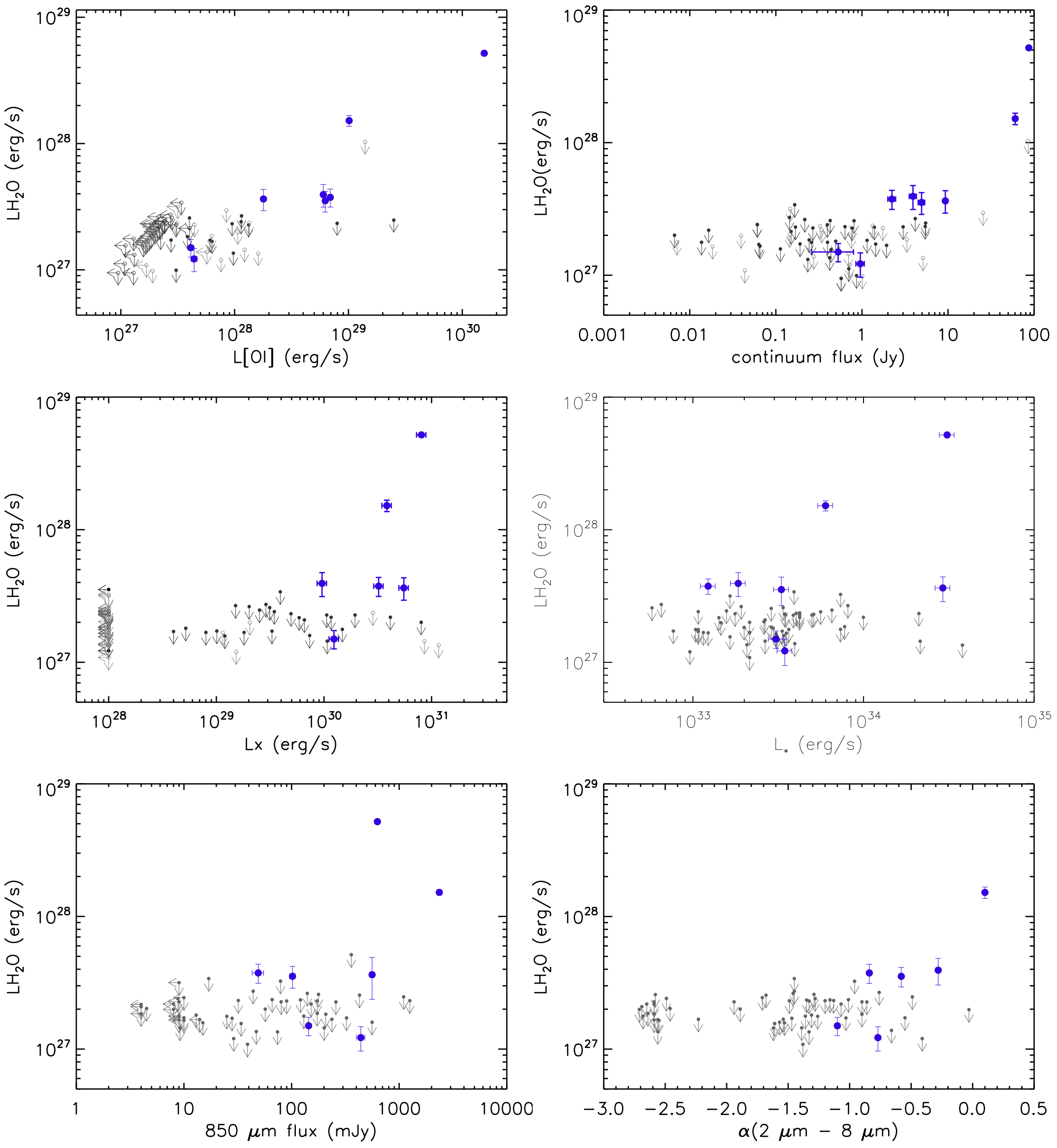

Figure 2.2: Plots of the 63.32 μm o-H_2O line luminosity versus different star and disc parameters. Blue filled dots are detections, while arrows are upper limits. Solid, dark grey arrows represent objects with non-detections spanning the same spectral range as the objects with detections. Light grey, empty arrows represent non-detections with other spectral types. Top left: versus [OI] line luminosity. Top right: versus continuum flux at 63 μm. Middle left: versus X-ray luminosity. Middle right: versus star luminosity. Bottom left: versus 850 μm continuum flux. Bottom right: versus 2–8 μm slope.

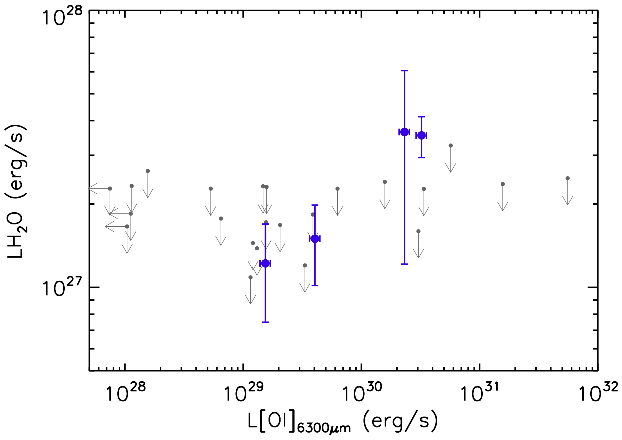

Figure 2.3: H_2O line luminosity versus OI line luminosity at 6300 Å.

one order of magnitude smaller than for the random sample, the Kendall probability is two orders of magnitude smaller. Inspection of Fig. 2.2, middle left, also shows that the o-H_2O line flux is detected only for sources with X-ray luminosities higher than 10^{30} erg s^{-1}, which is consistent with photochemical disc models that show that far-IR line fluxes increase significantly above this X-ray luminosity threshold (Aresu et al., 2011). We note that $\log L_x = 10^{30}$ erg s^{-1} is above the median (mean) X-ray luminosity in Taurus ($\log L_x = 29.8$ (29.75) erg s^{-1} respectively, Güdel et al. (2007)). Interestingly, more than half of the sources with $L_x > 10^{30}$ erg s^{-1} do not display the o-H_2O line. This behaviour may stem from either (1) the different shape of the X-ray spectrum (hardness ratio), (2) the duty cycle of the flares responsible for the high levels of X-ray fluxes, and/or (3) that X-rays are not the only driver of H_2O chemistry and excitation, let alone any inner disc geometry and radiative transfer considerations. We caution that the correlation with X-rays is significantly weaker when T Tau is removed from the analysis.

All the stars detected in o-H_2O are outflow/jet sources, although three of them AA Tau, DL Tau, and RY Tau do not show any excess in [OI], i.e. all the emission is consistent with coming from the disc (Howard et al. 2013, submitted). Two of these (AA Tau and DL Tau) are classified as outflow sources based on blue-shifted forbidden optical emission lines, although the emission is only slightly blue-shifted for AA Tau. However, in the sample there are also some prominent jet sources ($L_{[OI]6300Å} > 10^{-2}$ $L_\odot$) that show no hint of emission from this o-H_2O line, such as DG Tau, where other H_2O lines have been detected. However, these H_2O lines are believed to originate in the outflow. Furthermore, the [OI] at 63.18 μm line is sometimes extended (Podio et al., 2012; Herczeg et al., 2011), while we find the o-

H_2O to be unresolved, suggesting a more compact origin for the o-H_2O line.

We therefore assume that the o-H_2O emission at 63.32 μm originates from the disc and ask whether it comes from the same gas reservoir as the hot H_2O lines observed by Spitzer. Carr & Najita (2011) detected six out of eleven stars: AA Tau, BP Tau, DK Tau, GI Tau, RW Aur, and UY Aur. Our sample contains all of their detected sources. We detected the 63.32 μm H_2O emission only in AA Tau and UY Aur. Pontoppidan et al. (2010b) reported H_2O detections toward three out of eight stars in their sample: DR Tau, AA Tau, and IQ Tau. We did not detect o-H_2O in IQ Tau. Salyk et al. (2008), Pontoppidan et al. (2009) and Meijerink et al. (2009) argued that the *Spitzer* hot H_2O emission comes from the 0.1 to 1.0 AU annular region of the disc.

Assuming the same temperature, column density, and emitting areas as Carr & Najita (2011), i.e., 1AU, we computed the 63.32 μm local thermodynamic equilibrium (LTE) line flux in AA Tau and UY Aur. The model line emission is too optically thick to derive the H_2O mass reliably. The size of the emitting region is instead estimated. In both cases, the model flux is ten times lower than measured. To recover the measured fluxes, the radius of the emitting area has to be about three times larger than the value they quote, i. e., 3.0 AU for AA Tau and 3.5 AU for UY Aur, a result that is consistent with the lower excitation temperature of the line we observed.

A radiation thermo-chemical model of a typical T Tauri disc obtained with the ProDiMo code (Woitke et al., 2009a; Kamp et al., 2010; Thi et al., 2010; Aresu et al., 2011) predicts that the emission region of the 63.32 μm o-H_2O line is of the order of 3 AU, about five times larger than the Spitzer emission-line region (see Fig. 2.4). One particular o-H_2O line at 15.738 μm was selected as a representative Spitzer mid-IR H_2O emission line. This model does not intend to fit any particular object. A large non-LTE H_2O ro-vibrational model calculation was included to consistently calculate the Spitzer as well as the Herschel H_2O emission lines by applying escape probability theory (Faure et al., 2004, 2007; Faure & Josselin, 2008). At $\sim$ 3 AU, the gas densities are high enough to excite the 63.32 μm o-H_2O line and the dust temperature close to the mid-plane is low enough for H_2O to freeze onto grains.

The 63.32 μm line could provide the missing link between the mid-IR Spitzer detections of hot H_2O vapour in T Tauri discs and the cold far-IR H_2O lines observed with *Herschel*. Searches for the lower excitation H_2O lines have proven to be less successful. To date, the only clear detection of cold H_2O from a disc is TW Hya using *HIFI* (Hogerheijde et al., 2011) , and Kamp et al. (in prep.), using *PACS*. Possible reasons for the lower detection rate of cold H_2O might be the much lower

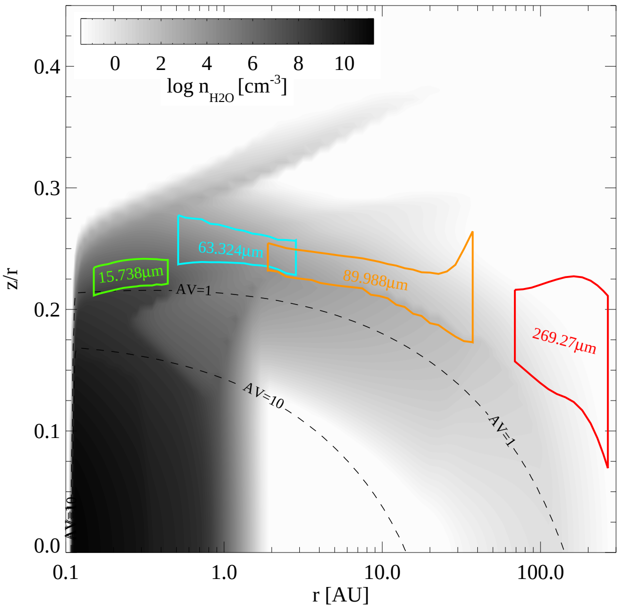

Figure 2.4: Location of the H_2O emission for a typical disc model (M_*=0.8$M_\odot$, L_*=0.7 $L_\odot$, $T_{\rm eff}$=4400K, UV excess $f_{\rm UV}$=0.01, X-ray luminosity L_X=10^{30} erg s^{-1}, $R_{\rm in}$=0.1AU, $R_{\rm out}$=300 AU, $M_{\rm disc}$=0.01 $M_\odot$, dust/gas=0.01, ϵ=-1, scale height H_0=1 AU at r_0=10 AU, flaring β = 1.1, astronomical silicate with uniform dust size distribution $a_{\rm min}$=0.05 μm, $a_{\rm max}$=1 mm, and index=3.5.). The 15.738 μm line is used as a typical H_2O line detected by *Spitzer*. We have marked the radii where the cumulative line flux reaches 15% and 85% with vertical lines, for the four selected H_2O lines. In addition, the horizontal lines mark the heights above the midplane where 15% and 85% of the line flux, from every vertical column, originate in. The encircled regions are hence responsible for 70% x 70% = 49% of the total line flux (for a pole-on disc).

H_2O abundances in the outer disc caused by the freeze-out of H_2O and/or significant (vertical) settling of icy grains (Bergin et al., 2010). Observing the same molecule in transitions with very different excitation temperatures may trace it through a broader range of different radial zones in protoplanetary discs.

According to the minimum mass solar nebula by Hayashi (1981), water condenses in ice when the temperature falls below 170 K, which occurs at 2.7 AU in his models for the Solar System. This distance is known as the snow line. Is is widely assumed that giant planets must form beyond the ice line, where the formation of an ice layer in the surface of grains dramatically increases the sticking coefficient. However, the ice line can be located inner in the disc, if the conditions are different from conditions in the solar nebula during the epoch of planetary formation. Sasselov & Lecar (2000) showed how the snow line can move to 0.7 AU for a passive T Tauri disc and 1.3 AU for a disc with an accretion rate of 10^{-8} $M_\oplus$/yr. Fig. 2.4, shows that water emission comes from the 0.5–3 AU region of the disc. Therefore, the emission comes a from a critical region that contains the snow line. A better understanding of the water behaviour in this region is of main interest to understand planet formation, and the present selection of Taurus stars with warm water emission make the sample an interesting probe for planet formation theories in T Tauri stars.

2.4 Conclusions

We have detected o-H_2O emission at 63.32 μm in 8 T Tauri stars in a sub-sample of 68 stars located in Taurus. The detection rate is ~24% in the sub-sample with gas-rich discs. The H_2O emission appears to be correlated with the continuum luminosities, the [OI] 63.18 μm line fluxes, and the X-ray luminosities. The gas temperature (500-600K) and density needed to excite the observed o-H_2O line suggest that the line is coming from the inner parts of the discs and from the upper layers of its atmosphere, where the disc is directly illuminated. The correlation with X-rays flux and the role of X-ray emission in heating the gas, in particular during flares, needs to be investigated further. The typical size of the emitting region is estimated to be $r \sim 3$ AU, which is consistent with the typical location of the snow line in these objects. More effort is needed to detect several H_2O lines simultaneously in more objects to understand the full radial distribution of H_2O vapour in planet-forming discs.

Chapter 3

Gas and dust in the TW Hydrae association

A version of this chapter has been accepted for publication in Astronomy and Astrophysics

3.1 The TW Hydrae Association: a general overview

The discovery of several nearby ($\lesssim$ 100 pc) young ($\lesssim$ 20 Myr) sparse stellar associations or moving groups (Torres et al., 2003, 2006) provides a valuable avenue to study evolution of gas and dust in circumstellar discs, because the ages of the stars in these moving groups are relatively well known (see Chapter 1). In the present chapter, we target the TW Hydrae Association (TWA, de la Reza et al., 1989). TWA is one of the closest (56 pc) and youngest moving groups (8 – 20 Myr, see Kastner et al., 1997; Stauffer et al., 1995; Soderblom et al., 1998; Hoff et al., 1998; Weintraub et al., 2000; Makarov & Fabricius, 2001; Makarov et al., 2005; Barrado y Navascués, 2006; de la Reza et al., 2006). The range in ages is due to different age determinations from different authors, although we assume the TWA members are coeval. It is a well known place for the study of star and planet formation, and properties of the TWA circumstellar discs have been extensively studied in other works (e.g. Low et al., 2005). The star that names the group, TW Hydrae (TWA 01), shows very strong and variable H_α emission, together with emission lines of HeI, OI and Ca, suggesting that it is a Classical T Tauri Star (Rucinski & Krautter, 1983) actively accreting far from any molecular cloud, which makes it a challenging object. Currently there are about 30 bona fide members of the TWA association (Schneider et al., 2012). There are two known transitional discs in the association, TWA 01 itself and TWA 03A; some authors also consider TWA 04B a transitional disc, while others consider it is a debris disc. There are also two debris discs: TWA 11A (HR 4796 A), with a prominent IR excess, and TWA 07, a cold debris disc. Finally, there are two brown dwarfs with a circumstellar disc, namely TWA 26 and TWA 28.

Fourteen TWA members were observed as a part of the *Herschel* Open Key Time Programme GASPS (see 1). In this chapter, we discuss our new *Herschel*-PACS photometric and spectroscopic observations. Images were obtained at 70 and/or 100, and 160 μm for all 14. Spectral line observations of [OI] at 63 μm and DCO$^+$ at 189 μm were obtained for 9 of them. We studied the properties of the dust and the geometry of the discs, by comparing the observed photometric fluxes with those predicted by simple, modified blackbody models. In Sec. 3.2 we briefly describe the characteristics of the sample, compute stellar properties and analyse the H_α emission as an estimator of accretion properties. In Sec. 3.3 we describe our PACS observations and the reduction of the data. In Sec. 3.4 we summarise the main results from spectroscopic and photometric observations. In Sec. 3.5 we produce simple modified blackbody models to characterise the dust emission in TWA members. In Sec. 3.6 we discuss the gas and sit content in TWA members individually, while in Sec. 3.7 we discuss the results in a more general framework.

3.2 The sample

The sample of 14 TWA members studied in this chapter, together with their spectral types (Sp Type), stellar luminosities, and effective temperatures, is shown in Table 4.1. The spectral types range from A0 to M3. Star distances are taken from Zuckerman & Song (2004a). In Fig. 3.1, we plot the stars on a Hertzsprung-Russell diagram. The stellar luminosities and effective temperatures used are discussed in section 4.2.1.

Among the sample, TWA 01 (Salyk et al., 2007), TWA 03A (Cieza et al., 2008), and TWA 04B (Furlan et al., 2007) are typically classified as transitional discs, while TWA 07 (Matthews et al., 2007) and TWA 11A (Telesco et al., 2000) are believed to be debris discs. TWA 13A was proposed to harbour a circumstellar disc by Low et al. (2005), but this was later rejected by Plavchan et al. (2009). The other eight systems are not known to harbour any circumstellar disc.

Archival data was collected for each TWA member in our target list, including Johnson, Tycho, Stromgren, 2MASS, IRAC, WISE, AKARI, MIPS, SMA and SCUBA photometry. *Spitzer*-MIPS values are taken from Low et al. (2005). TWA23 and TWA25 MIPS fluxes are not included in Low et al. (2005), but they were observed by the programme Disk Census of Nearby Young Stellar Groups (P.I. I.Song), with AORs 11264768 and 11265280, respectively. For these two stars, we computed our own photometry for the 24 μm MIPS band, using an aperture of 13 arcsec, a sky annulus between 20 arcsec and 32 arcsec, and applying the appropriate aperture corrections (as described in the *Spitzer* Data Analysis Cookbook[1]). Computed fluxes are 8.6 ± 0.5 mJy for TWA 23 and 10.5 ± 0.5 mJy for TWA 25.

3.2.1 Stellar parameters

In order to model the stars' SEDs, we need knowledge of their stellar properties (specifically, their temperature and luminosity), to choose the correct photosphere models. For each star in the sample, we selected the photometric data that do not show excess above the stellar photosphere, i.e. those data points in agreement with pure photospheric emission. Typically, this includes Johnson, Stromgren, and 2MASS data. Then we compared this photospheric emission with a grid of theoretical stellar photosphere models using the Virtual Observatory SED Analyzer (VOSA, Bayo et al., 2008), which provides the best-fitting model based on a χ^2 minimisation. We used the grid of Phoenix models from Hauschildt et al. (1999). The values for $T_{\rm eff}$ and L_* from each best-fitting model are summarised in Table 4.1.

3.2.2 Accretion in TWA

The relation between H_α emission, a tracer of disc material accreting onto the central star, and [OI] emission can help us to understand the gas properties of the TWA members. We took observed H_α emission equivalent widths from Barrado y Navascués (2006) and applied the criterion given in Barrado y Navascués & Martín (2003) to classify TWA members as accretors or non-accretors. The accretion criterion accounts for the effect of chromospheric activity, which also gives rise to H_α emission.

---

[1] http://ssc.spitzer.caltech.edu/dataanalysistools/cookbook/

Table 3.1: Stellar parameters

Name	Other name	Sp Type	Ref	d	$T_{\rm eff}$	L_*
				(pc)	(K)	(L_{sun})
TWA 01	TW Hya	M2.5	1	56	3400	0.23
TWA 02	CD-29 8887	M2	2	52	3700	0.30
TWA 03A	Hen 3-600	M3	2	42	3000	0.18
TWA 04B	HD 98800B	M5	3	47	4000	0.56
TWA 05A	CD-33 7795	M3	3	50	3100	0.28
TWA 07	CE Ant	M1	4	38	3300	0.15
TWA 10	V1252 Cen	M2.5	4	57	3400	0.10
TWA 11A	HR 4796A	A0	5	67	10000	21.3
TWA 12	V1217 Cen	M2	6	32	3400	0.03
TWA 13A	V547 Hya A	M2	6	38	3700	0.10
TWA 16	–	M1.5	7	66	3900	0.17
TWA 21	HD 298936	K3	8	69	4600	0.72
TWA 23	–	M1	9	37	3400	0.07
TWA 25	V1249 Cen	M0	9	44	3800	0.15

Notes. All distances are from Zuckerman & Song (2004a). $T_{\rm eff}$ and L_* for each target were computed using VOSA (Bayo et al., 2008). References for spectral type (Sp Type) are: (1) Vacca & Sandell (2011); (2) de la Reza et al. (1989); (3) Gregorio-Hetem et al. (1992); (4) Webb et al. (1999); (5) Houk & Fuentes-Williams (1982); (6) Sterzik et al. (1999); (7) Zuckerman et al. (2001); (8) Zuckerman & Song (2004a); (9): Weinberger et al. (2004)

In Fig. 3.2, we have plotted the H_α emission equivalent widths (EW) versus the spectral types of the stars in the sample, along with the line that separates accretors from non-accretors according to the criterion in Barrado y Navascués & Martín (2003). TWA 01 and TWA 03A show variable H_α levels in agreement with an accreting disc. On the other hand, for TWA 05A and TWA 10, only one epoch of data shows an H_α equivalent width larger than the expected chromospheric level. We note that these stars show MIPS 24 μm emission consistent with purely photospheric emission, indicating a lack of warm inner material that would be expected for an accreting disc. We therefore conclude that the two high H_α observations were due to extremely strong flaring events rather than episodic accretion.

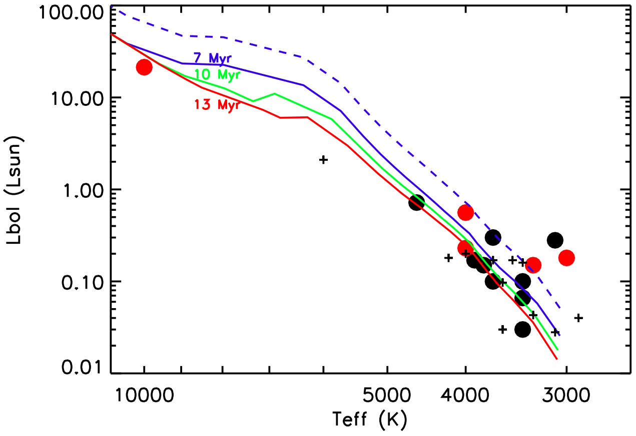

Figure 3.1: Hertzsprung-Russell diagram for TWA members in this programme. The red/green/blue solid lines represent the 13/10/7 Myr solar metallicity isochrones from Baraffe et al. (1998). The blue dashed line shows the 7 Myr Baraffe isochrone with 2 times larger luminosity to account for unresolved binary systems. Red dots are objects detected with PACS, while black dots are undetected objects. Plus symbols correspond to TWA members not observed in GASPS.

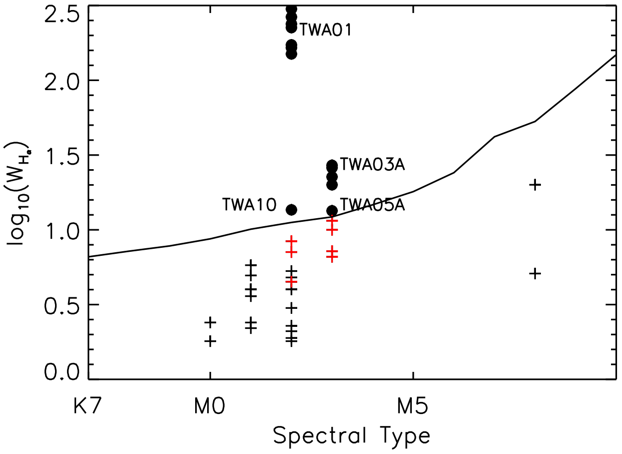

Figure 3.2: Accretion in TWA members. Plus symbols depict objects with H_α in agreement with pure chromospheric emission, while black dots are objects with H_α in agreement with ongoing accretion. Star showing variable H_α emission are depicted as red plus symbols when H_α is above the chromospheric level (namely, TWA 05A and TWA 10). The solid line shows the saturation criterion by Barrado y Navascués & Martín (2003).

3.3 Observations and data reduction

The TWA sample was observed with PACS as part of the GASPS Open Time Key programme. Fourteen TWA members were observed in photometric mode and a subset of nine TWA members were observed in spectral line mode.

3.3.1 Photometric data reduction

The PACS photometer simultaneously observes in either the 70 or 100 μm bands together with the 160 μm band, so we typically have, at least, two images to combine in the 160 μm band. PACS scan map observations at 70/160 μm were obtained for 12 objects. Seven of these objects were also observed at 100/160 μm. Two additional objects were observed only at 100/160 μm. Observation ID's are listed in Table 3.2. The exposure times range from 133 to 1122 s, based on the expected flux from the star. Each scan map was made with medium speed (20arcsec/s), with scan legs of 3 arcmin and cross scan length of 4-5 arcsec.

Table 3.2: TWA PACS photometry observation log

Name	Obs. ID	Band
TWA 01	1342187342	70/160
TWA 02	1342189163, 1342211995, 1342211996	70/160, 100/160, 100/160
TWA 03A	1342211991, 1342211992	100/160, 100/160
TWA 04B	1342188473, 1342212634, 1342212635	70/160, 100/160, 100/160
TWA 05AB	1342213111, 1342213112	70/160, 100/160
TWA 07	1342188515, 1342211993, 1342211994	70/160, 70/160, 100/160
TWA 10	1342188518, 1342213854, 1342213855	70/160, 70/160, 100/160
TWA 11	1342188519, 1342213852, 1342213853	70/160, 70/160, 100/160
TWA 13	1342213113, 1342213114	70/160, 100/160
TWA 16	1342188854, 1342213856, 1342213857, 1342213858, 1342213859	70/160, 70/160, 100/160, 70/160, 100/160
TWA 21	1342188514, 1342211983, 1342211984	70/160, 70/160, 100/160
TWA 23	1342188516, 1342188517	70/160, 70/160
TWA 25	1342213624,1342213625, 1342213626,1342213627	70/160, 100/160, 70/160, 100/160

The reduction of the photometric data was carried out using HIPE 8, with the latest version available for the calibration files. For bright IR sources (i. e., those with flux greater than 100 mJy) we used a version of the pipeline tuned for bright objects, while for faint objects and non-detected objects we used a different version optimised for noise dominated maps, as is the case for TWA 07. The difference between both versions of the pipeline comes from the way in which high-pass filtering is implemented. Before we apply high-pass filtering, we need to mask the sources that we want to study in order to preserve their absolute flux. For bright sources, we can detect and mask the sources in individual scans before performing the high-pass filtering; for faint sources that can not be detected in individual scans, a preliminary reduction is run without a high-pass filter, and the final image from this first reduction is then used to mask the source, and re-run the final reduction with high-pass filtering properly applied.

In both pipelines the reduction process includes the following main steps: bad and saturated pixel flagging and removal, flat field correction, deglitching, high pass filtering and map projection. Photometric maps were projected into the final image with pixel scale 2 arcsec/pixel in the 70 and 100 μm bands and with pixel scale 3 arcsec/pixel in the 160 μm. We also produced final maps with the native pixel scale of the detector that were used to perform the error calculation (3.2 arcsec/pixel for the 70/100 μm bands and 6.4 for the 160 μm band). When several images at the same wavelength were available for a single target, we combined all of them to improve the signal-to-noise ratio (SNR), averaging for each pixel and using the average sigma clipping algorithm to exclude bad pixels.

Aperture photometry was measured in final, combined images using an aperture of 6 arcsec for the 70 and 100 μm bands and 12 arcsec for the 160 μm band. The annulus for sky subtraction was placed at 25-35 arcsec from the star. We then applied the proper aperture correction for each band[2]. The photometric fluxes are listed in Table 4.5.

To compute photometric errors, we used native maps to minimise the impact of correlated noise, with pixel scale 3.2 arcsec/pixel in the 70 and 100 μm bands and 6.4 arcsec/pixel in the 160 μm band. Noise errors consist on the standard deviation of the photometry obtained at several sky positions surrounding the target. PACS calibration errors are 2.64/2.75/4.15 % for the 70/100/160 μm bands respectively[3]. Noise errors and calibration errors were added quadratically. The impact of

---

[2] http://herschel.esac.esa.int/twiki/pub/Public/PacsCalibrationWeb/

[3] PICC-ME-TN-037

correlated noise is negligible due to the fact that final photometric uncertainties are dominated by the calibration errors, with the only exception of TWA 07.

For non-detected sources, the derivation of upper limits is as follows: we compute the standard deviation in the sky background in several pointing surrounding the nominal position of the star on the detector; then, we compute the average value, and we use it as the sky background value. This value is multiplied by the square root of the number of pixels inside the aperture. Finally, we apply the proper aperture correction. The upper limits included in Table 4.5 are 3-σ.

3.3.2 Spectroscopic data reduction

Nine TWA stars were observed with PACS in LineScan spectroscopic chopped/nodded mode. The line targeted with the LineScan observations was [OI] at 63.18 μm. PACS spectra were reduced using HIPE 8 with the latest version of the pipeline and the proper calibration files.

In the following, we overview the main steps in the reduction of PACS chop/nod spectra. First, saturated data and bad pixels are flagged. Next, the observations are corrected for *Herschel* movement, and data affected by chopper and grating movements is flagged. The next is a major step that consist on flagging the data for glitches (i. e., cosmic rays) through a Q statistical test and create a mask to exclude cosmic rays from further analysis. Deglitching requires all previous masks to be de-activated before performing the test. The final mask is automatically applied to the data once created. Next, the instrumental response and dark current during the observations are calculated and data is corrected. After that, the difference between Chop On and Chop Off is computed and used to subtract the background plus the telescope contribution. Then, the data is divided by the relative spectral response function and the individual slices from each scan are then projected into a data cube that contains the spectra for the different spaxels. Next, the the data is rebined to a different wavelength grid. The reason to do that is that each of the 16 pixels that feed each spaxel have an slight offset in its wavelength grid with respect to the others, in a way that when put together, they cover the wavelength range with an slightly better definition. The upsample and oversample parameters control the sampling of the grid: oversample determines how many new wavelength are created for each old wavelength bin, while upsample determines how many bins forward the spectrum is moved in the original grid before new bins are defined. We used oversample = 2 and upsample = 3 to get a better wavelength sampling. Finally, the data is flat fielded

Table 3.3: TWA PACS photometry

name	Flux(70 μm) (mJy)	Flux(100 μm) (mJy)	Flux(160 μm) (mJy)
TWA 01[1]	3900 ± 100	–	7380 ± 300
TWA 03A	–	650 ± 19	459 ± 19
TWA 04B	6241 ± 165	4269 ± 117	2382 ± 100
TWA 07	77 ± 7	58 ± 4	42 ± 9
TWA 11	4980 ± 131	3553 ± 97	1653 ± 68
TWA 02	< 11.0	< 6.4	< 19
TWA 05	< 2.2	–	< 11.0
TWA 10	< 4.1	–	< 12.0
TWA 12	< 2.8	–	< 9.0
TWA 13A	–	< 6.4	< 19.0
TWA 16	< 4.4	< 4.6	< 8.6
TWA 21	< 4.0	–	< 14.0
TWA 23	< 5.1	< 6.0	< 13.0
TWA 25	< 5.7	< 6.3	< 12.0

Notes. Errors include a calibration error of 2.64, 2.75 and 4.15 % for the 70, 100 and 160 μm bands respectively (see text). Upper limits are 3-σ (1): from Thi et al. (2010).

and the average between Nods A and B is computed to give the final spectrum

Spectra were extracted from the central spaxel, because star were well centred in the slit. The extracted spectrum was then aperture corrected to account for flux loss in the surrounding spaxels. The line spectra from PACS typically show higher noise near the spectrum edges. To account for that effect, we exclude from the 63 μm spectra any wavelength shorter than 63.0 μm or longer than 63.4 μm, and from the 189 μm spectra any wavelength shorter than 189.0 μm or longer than 190.0 μm

We used a second degree polynomial to subtract the background. Then, a Gaussian function was used to fit the emission and derive the line fluxes, using the IDL task *mpfitpeak*, using estimators for the line centre, FWHM, and peak over continuum. Upper limits were computed by integrating a Gaussian with a width equal to the instrumental FWHM at the central wavelength, and maximum equal to three times the standard deviation of the continuum. Therefore, computed upper limits are 3-σ. Line fluxes are shown in Table 3.4

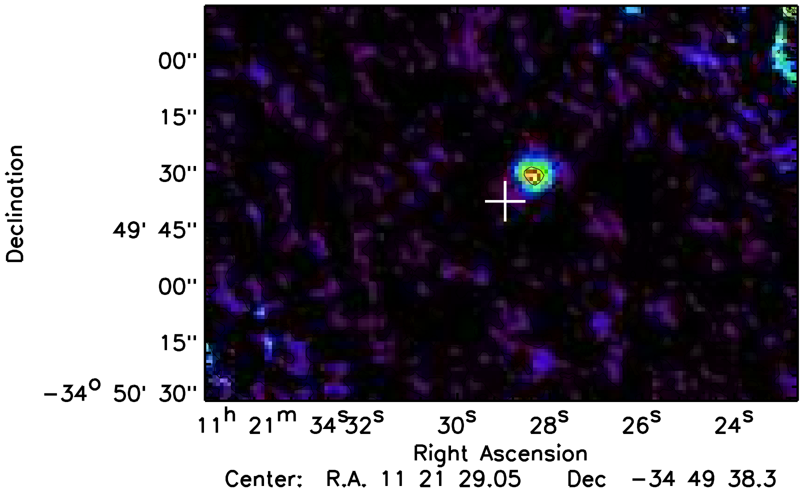

Figure 3.3: PACS observation of TWA 13A at 100 *μm*. The white plus symbol depicts the nominal position of TWA 13A.

3.4 Results

3.4.1 Herschel-PACS photometry

Within the 12 targets observed at 70 μm, we detected four sources. At 100 μm, we have detected four systems out of nine observed. All the targets detected in the 70/100 μm bands are also detected at 160 μm, and all of them show emission in excess above the photosphere, in agreement with the presence of circumstellar material. Excess fractions are 0.33/0.44/0.36 at 70/100/160 μm respectively. We have detected for the first time the 100/160 μm emission toward TWA 07, and 100 μm emission toward TWA 03A.

TWA 13A was considered a far-IR excess source by Low et al. (2005). They found a 27.6 mJy flux at 70 μm. But Plavchan et al. (2009) showed that the 70 μm emission is coincident with a background galaxy and not with TWA 13A. Our combined images for TWA 13A do not show any source at the nominal position of the star, therefore we agree with Plavchan et al. (2009) that there is no excess associated with TWA 13A. However there is a background galaxy that could have polluted the Low et al. (2005) observation at RA=11:21:16.6, DEC=-34:46:38.6, with a flux of 70 mJy at 100 μm and 93 mJy at 160 μm. We show the SED for TWA 13A in Fig. 3.4. The WISE and AKARI observations also seem to be polished by flux from this background galaxy.

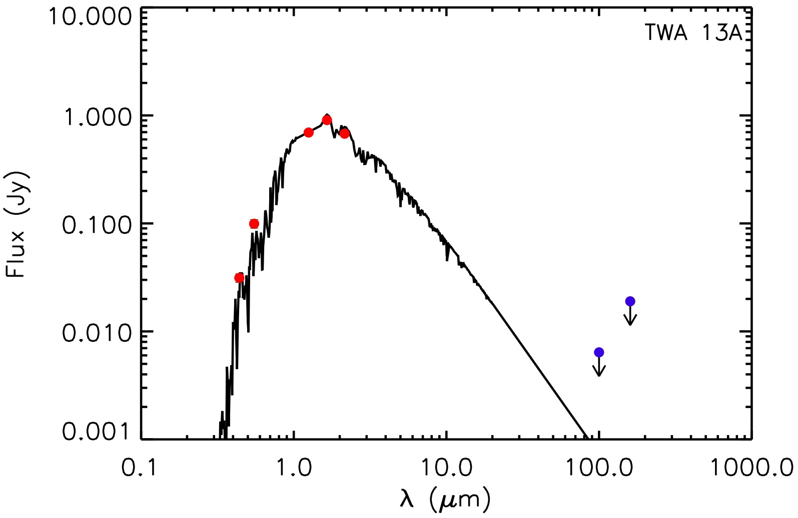

Figure 3.4: SED for TWA 13A. Blue dots are PACS detections from the present study.

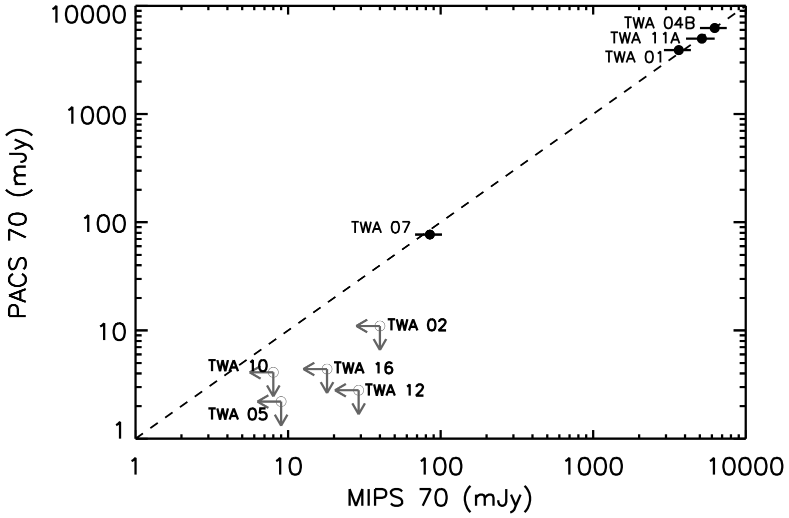

Figure 3.5: Comparison plot for PACS 70 μm flux vs MIPS 70 μm flux. The black dashed line represents the one to one relation. Displayed upper limits are 3-σ.

In Fig. 4.2, we show a comparison of the photometry at 70 μm from MIPS with that from PACS. We see that the agreement between MIPS and PACS for detected objects is good, although MIPS fluxes are typically slightly higher than PACS fluxes (the average difference is $\sim$ 2%). Any discrepancy can be due to problems in the calibration of the instruments, to the larger beam size in MIPS or to real variability. The most probable explanation lies on the larger beam size used by MIPS, which can include some contamination from the background. The upper limits from PACS are pushing further down to photospheric values, and are typically ~5 times smaller than previous upper limits from MIPS.

In Fig. 3.6, we plot the 70, 100 and 160 μm excess versus the effective temperature of the central star. The behaviour is the same for every PACS band; a system bright at 70 μm is also bright at 100 and 160 μm. A bimodal behaviour in the dust content among TWA members was first reported by Weinberger et al. (2004); stars in TWA can posses large amounts of dust or no dust at all. This behaviour was also resorted by Low et al. (2005), using 24 μm fluxes from MIPS. The bimodal distribution of excesses seen at 24 μm and lower mid-IR wavelengths is not as pronounced at 70 μm, but we note that the TWA 07 excess at 70 μm is more than order of magnitude smaller than any other detected flux in TWA, and that upper limits at 70 μm are near photospheric values, so probably no disc emission is present at this wavelength for those undetected sources. The bimodal nature of the distribution vanishes at 100 and 160 μm; excesses at 100 and 160 μm cover three orders of magnitude, with ratios on the order of 10–1000, depending on the star. Upper limits are far from the photospheric value at 100 μm, where typical values are 10 times larger than the photosphere. Finally upper limits at 160 μm are 10 to 100 times larger than the photospheric fluxes. Therefore, we can not exclude the presence of faint, cold discs in those targets.

In order to check for spatially resolved sources, we calculated azimuthally averaged radial profiles in all three PACS bands for every detected object and compared the results with the azimuthally averaged radial profile of a model PSF from the calibration star α Boo. We obtained the radial profiles making use of the IRAF task *pradprof*. Within the errors, none of the sources is extended in any of the PACS bands. The resulting radial profiles can be found in Appendix A.2.

We show in Fig. 3.7 the SED for objects not detected with PACS, while objects detected by PACS are studied in detail in Sec. 3.5.

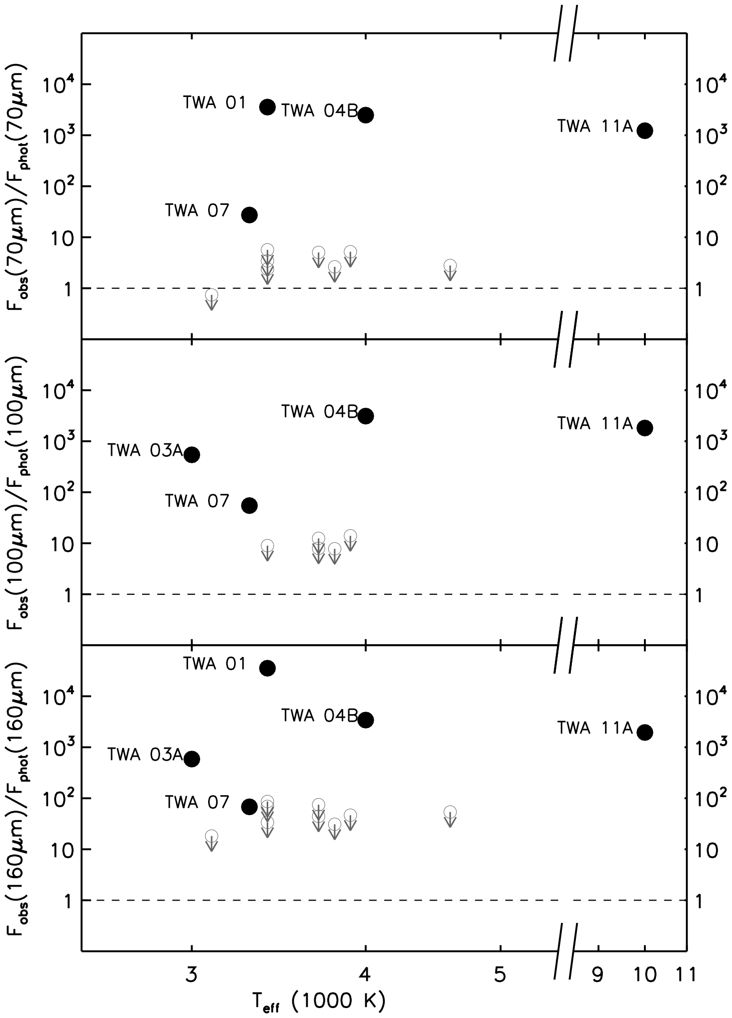

Figure 3.6: Excesses at 70 (top), 100 (middle) and 160 (bottom) μm band versus T_{eff}. Solid dots represent true detections, while empty circles with arrows represent upper limits. The black horizontal dashed line shows the limit for photospheric emission. Displayed upper limits are 3-σ.

3.4.2 Herschel-PACS spectroscopy

Among the nine TWA members observed with PACS in spectral line mode, we only detected the continuum level at 63 and 189 μm in four sources, namely TWA 01, TWA 03A, TWA 04B and TWA 11A, i. e. , those objects detected also with PACS photometry with the exception of TWA 07, whose spectroscopic continuum level is below the detection limit.

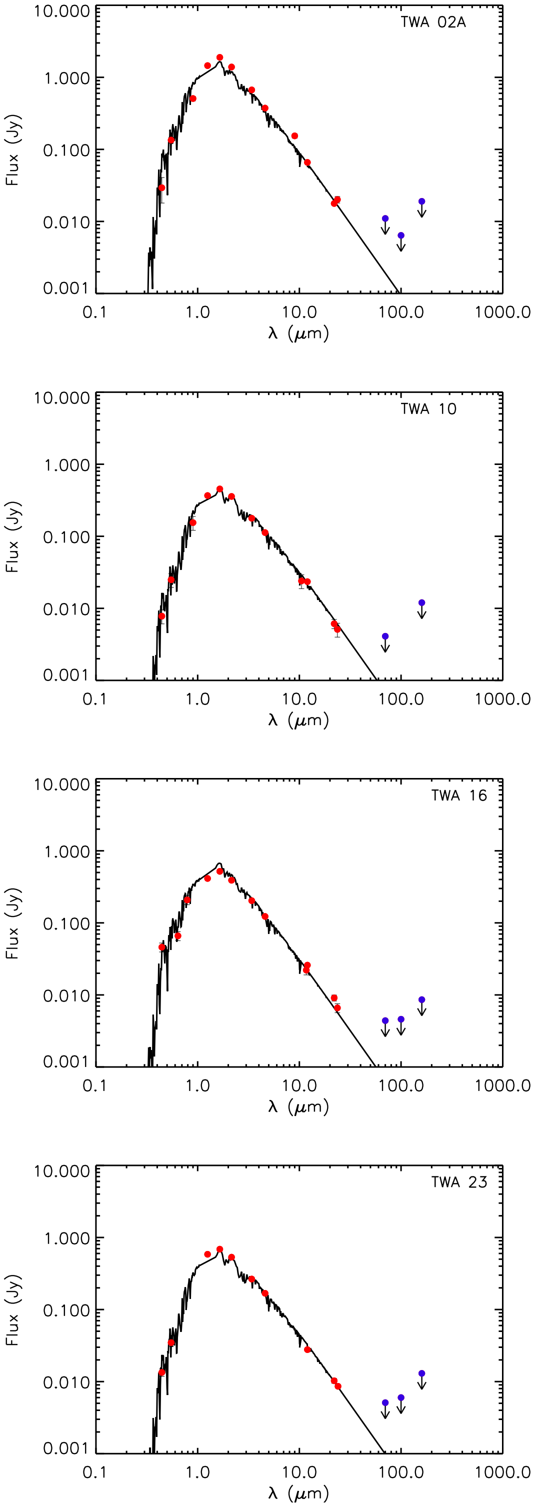

Figure 3.7: SEDs for TWA members not detected by PACS. The black solid line are the photosphere models from Sec. 4.2.1. Blue dots are PACS detections from the present study.

Table 3.4: TWA PACS line fluxes

name	$[OI]_{63.18\mu m}$ line flux	$o-H_2O_{63.32\mu m}$ line flux	Continuum $SNR_{63\mu m}$	DCO^+ line flux	Continuum $SNR_{189\mu m}$
–	$(10^{-18}W/m^2)$	$(10^{-18}W/m^2)$	–	$(10^{-18}W/m^2)$	–
TWA 01[1]	36.5 ± 12.1	< 7.26	13.3	< 4.8	29.4
TWA 01[2]	23.9 ± 5.5	< 7.44	13.7	< 5.2	27.4
TWA 02	< 8.3	< 8.3	0.19	< 3.6	0.04
TWA 03A	< 5.8	< 5.8	33.9	< 4.9	2.4
TWA 04B [3]	5.1 ± 1.4	< 4.3	50.3	< 2.5	13.8
TWA 04B [4]	2.8 ± 0.8	< 4.1	49.5	< 4.6	9.7
TWA 04B [5]	2.9 ± 0.8	< 3.7	60.8	< 2.6	17.0
TWA 04B [6]	3.7 ± 0.8	< 3.1	60.8	–	–
TWA 07	< 4.6	< 4.6	1.04	< 3.3	0.11
TWA 10	< 4.5	< 4.5	0.35	< 3.2	0.20
TWA 11A	< 4.7	< 4.7	39.67	< 3.7	6.8
TWA 13A	< 4.5	< 4.5	0.32	< 3.8	0.03
TWA 23	< 5.4	< 5.4	0.28	< 3.1	0.06

Notes. Listed values for SNR are continuum SNR. (1): TWA 01 flux from Thi et al. (2010). (2): TWA 01 new line flux after HIPE 9. (3): OBSID 1342199409. (4): OBSID 1342223821. (5): Averaged spectrum. (6): Averaged spectrum after re-centering.

Only two TWA members show [OI] emission at 63.18 μm: TWA 01 and TWA 04B. Line fluxes are given in Table 3.4. We note that [OI] line emission in TWA 01 was studied and modelled by Thi et al. (2010) in detail. Continuum subtracted spectra for TWA members showing IR excess μm are shown in Fig. 4.6, with the exception of TWA 04B, whose spectra are shown in a dedicated plot.

TWA 04B was observed at two different epochs. The resulting continuum subtracted spectra are shown in Fig. 3.9. The first one (OBSID 1342199409) shows a clear 3-σ detection, irrespective of the region used to compute the continuum. The second one is not as robust; it is a 3-σ detection if we exclude the noisy region that goes from 63.36 to 63.40 μm (shaded in green in Fig. 3.9) from the continuum computation. But if we include this region, it is at the limit of a 3-σ detection. In Fig. 3.10 we show the individual spectra together with the Gaussian models used to derive the line flux. The average spectrum shows also a clear 3-sigma detection of [OI] emission at 63.18 μm, irrespective of the region used to fit the continuum. Because there is a miss-alignment in the central wavelength of the [OI] line between

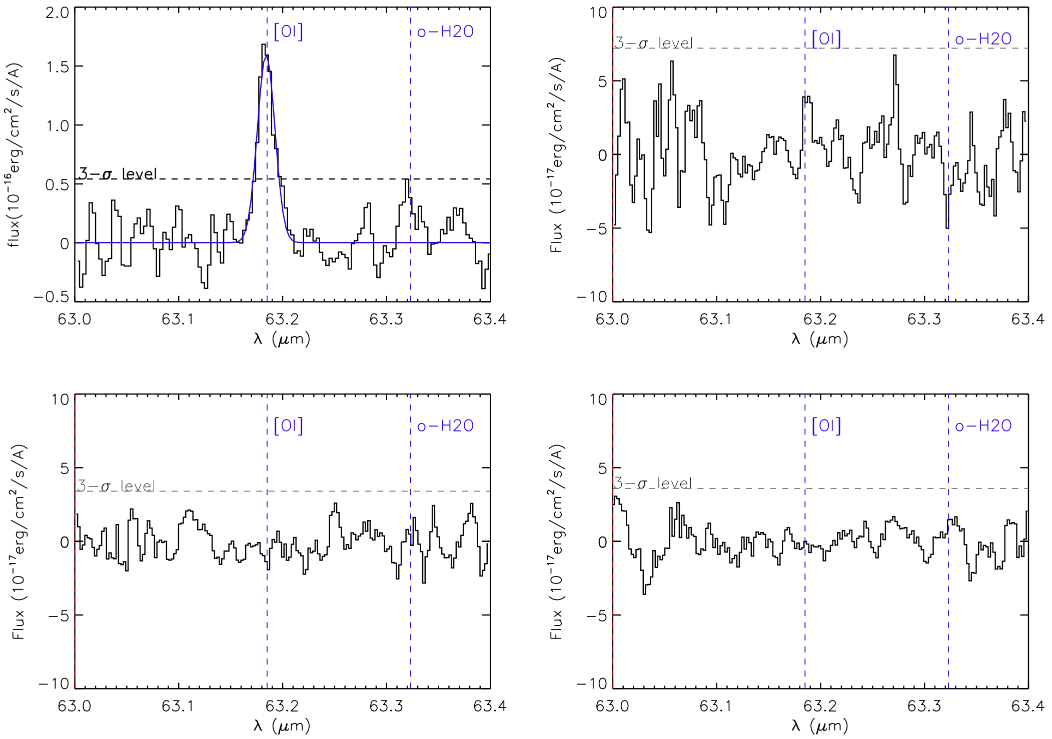

Figure 3.8: Continuum subtracted spectra of TWA members. The vertical blue dashed lines represent the position of the [OI] and o-H_2O. From left to right and from top to bottom, targets are: TWA 01, TWA 03A, TWA 07 and TWA 11A. We show 3-σ limits as horizontal, black dashed lines. For TWA 01, the solid blue line represent the Gaussian fit. TWA 04B spectra are shown in a dedicated plot.

individual observations, we decided to recenter them with respect to the rest frame wavelength (λ_0 = 63.185μm), and then average them again to get the final spectrum, resulting in a big improvement in the SNR of the line flux, and therefore in the quality of the fit. The [OI] detection in TWA 04B will be discussed further in Sec. 3.6.3. OBSID 1342199409 also shows a tentative detection of $o-H_2O$ at 63.32 μm: the peak of the emission in the region is over the pure 3-σ level. But the line is not seen in the second observation (OBSID 1342223821) nor in any of the averaged spectra. Also, the computed flux is only 2.2 times the flux noise. When using oversample = 2 and upsample = 1 (i. e., the native resolution of PACS, see Sec. 3.3.2) the feature is not even 3-σ in terms of line peak. Furthermore, the FWHM of the line is too large to be real (0.026 compared to the instrumental 0.018). Given all the caveats, we consider that this is not a real detection.

TWA 04B was also observed in range scan spectroscopic mode aiming to detect [CII] emission at 157.75 μm (OBSID 1342223820). The continuum subtracted

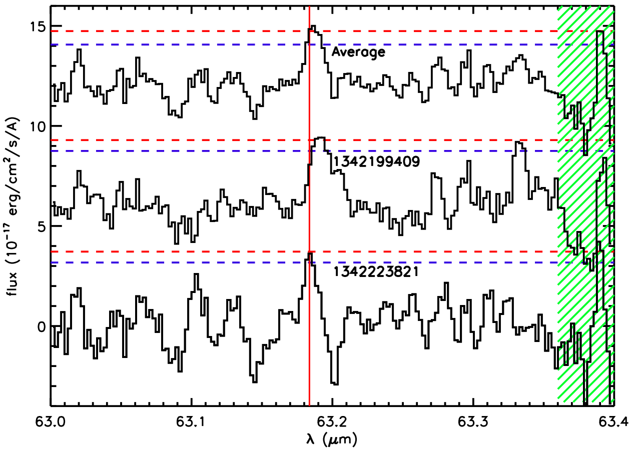

Figure 3.9: The three different continuum subtracted spectra in the region around 63 μm for TWA 04B. An arbitrary vertical shift was applied to the spectra for easy comparison. The vertical red line shows the rest wavelength of the [OI] 63.18 μm emission line. The green dashed area shows the position of a region where the SNR increases and dominates the emission. The red dashed horizontal lines show the the 3-σ limit for the three spectra. The blue dashed horizontal lines show the 3-σ limit when points inside the green dashed area are excluded.

spectra are shown in 3.11. No CO, CH or H_2O molecular emission is detected around 79 μm, and no [CII] or $\mathrm{H_2O}$ emission is detected around 158μm. Instead, we computed upper limits for the line fluxes of 1.8×10^{-18} W/m^2 for the 79 μm band and 6.5×10^{-19} W/m^2 for the 158 μm band.

3.5 Modified blackbody models for dusty discs

For every star in the sample, we have built the SED including the new *Herschel*-PACS data, aiming to compare the observed data with modified blackbody models to estimate basic dust properties in the TWA association. We are aware of the fact that this approach may be very simple for some of the targets studied, but it is a good starting point to estimate dust temperatures. In any case, each individual object will be discussed in the next sections. Fig. 4.9 includes SEDs for TWA members detected with *Herschel*. The disc models were built using the NextGen models from Sec. 4.2.1 plus a modified blackbody to describe the dust emission, defined as

$$F_{continuum} = B_\nu(T_{dust}) \times (\lambda_0/\lambda)^\beta \qquad (3.1)$$

Or more explicitly, the model flux is:

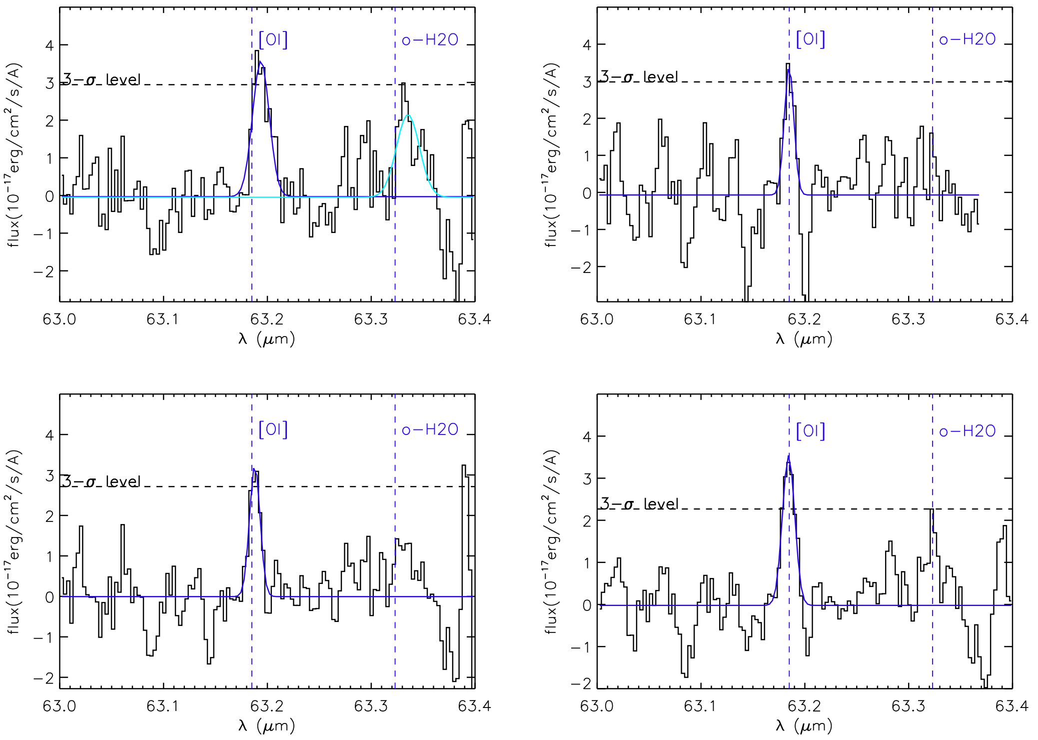

Figure 3.10: Continuum subtracted spectra of TWA 04B. The vertical blue dashed lines represent the position of the [OI] and o-H_2O lines. Top: individual spectra. Top left: OBSID 1342199409. Top right: OBSID 1342223821, without the noisy region from 63.36 to 63.4 μm. Bottom left: averaged spectrum. Bottom right: averaged spectrum after re-centering. We show 3-σ limits as horizontal, black dashed lines. The solid, dark blue lines represent the Gaussian fits to the [OI] line. The solid, light blue line in OBSID 1342199409 represents a fit to the tentative detection of o $-$ H_2O.

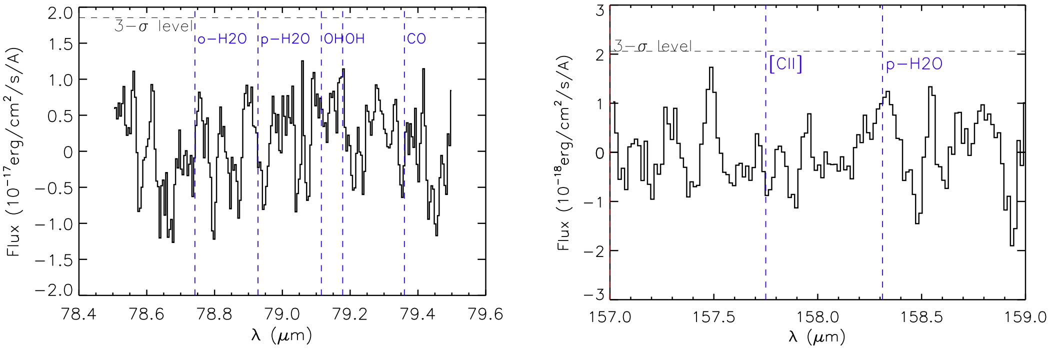

Figure 3.11: TWA 04B range spectra around the 79 and 158 μm wavelength range. The positions of lines present in each spectrum are shown as vertical, dashed blue lines. 3-σ detection limits are shown as horizontal black dashed lines. No line emission is detected in any of the range spectra.

$$F_{model} = F_* + B_\nu(T_{dust}) \times (\lambda_0/\lambda)^\beta \tag{3.2}$$

with λ_0= 2πa$_{\rm min}$ and β=0 for $\lambda < \lambda_0$, where B$_\nu$ is the Planck function, and F$_*$ the star flux model from Sec. 4.2.1. The choice for a$_{\rm min}$ depends on the target. TWA 11A is an A0 star, and therefore grains below the blow-out size (a$_{\rm blow}$) are expected to be blown out from the system in timescales much shorter than an orbital period. Therefore, for TWA 11A a$_{\rm min}$ = a$_{\rm blow}$, which can be computed using:

$$\frac{a_{blow}}{1\mu m} = 1.15\frac{L_*}{L_\odot}\frac{M_\odot}{M_*}\frac{1gcm^{-3}}{\rho} \tag{3.3}$$

(Backman & Paresce, 1993), with ρ= 2.5 g/cm^3, valid for astrosilicates. We get a$_{\rm blow}$ = 28μm. On there other hand, TWA 01, TWA 03A, TWA 04B and TWA 07 are M stars, where no grains are expected to be be blown out from the system as a result of radiation pressure. For these sources, we used a$_{\rm min}$ = 0.1 μm following the models from Augereau & Beust (2006) for AU Mic.

Both β and T$_{\rm dust}$ are free parameters. β can take any value from 0 to 2: a value of 2 was found for unprocessed interstellar grains Hildebrand (1983), while a value of 0 indicates dust grains radiating as pure blackbodies. Miyake & Nakagawa (1993) demonstrated that grain growth results in β values significantly smaller than the standard interstellar medium (ISM) value of 2; grain distributions with a$_{\rm max}$ $\gtrsim$ 1000 μm result in β< 1. Therefore, the β value from the modified blackbody fit gives us some information about the grain size distribution in TWA discs.

The best model was determined through χ^2 minimisation, with:

$$\chi^2 = \frac{1}{\nu}\sum_{i=1}^{N}\frac{(F_{obs,i} - F_{mod,i})^2}{\sigma_i^2} \tag{3.4}$$

where N is the total number of photometric points used in the fitting, $\nu = N - n$ the degrees of freedom, n the number of free parameters, $F_{obs,i}$ is the observed flux of the i-th photometric point, $F_{mod,i}$ the i-th model flux and σ_i is the error of the i-th photometric point. We used a genetic algorithm to search the models that minimizes χ^2. Basically a range (minimum and maximum) for each parameter must be supplied to the algorithm, which follows the these steps: 1) generate a random population of N individuals (i.e, sets of parameters, with N being user-defined and usually between 10 to 40) within the range limits for every parameter to fit; 2) generate the models corresponding to the random individuals; 3) select the best 10% of individuals based on a χ^2 minimization and 4) use these selection of best models to generate the next population of individuals with values in the range -20% to +20% of the model parameters from step 3. The process is iteratively repeated until a stable point is reached, i. e., when the best χ^2 does not change more than 1% with respect to the best value on the previous generation. At this point, a random population of $10 \times \mathrm{N}$ new individuals is added to destabilize the achieved minimum owing to avoid local minima. This process is then repeated 10 times. Hence, the final value must remain stable during more than 100 generations with 10 inclusions of $10 \times \mathrm{N}$ random points in the whole parameter space. Moreover, the random population of $10 \times \mathrm{N}$ created every time a stable point is reached, is used to compute the final errors in the parameters and to check for possible multi-valued solutions. In particular, we measure the 90% countours with respect to the best χ^2 value obtained by the genetic algorithm.

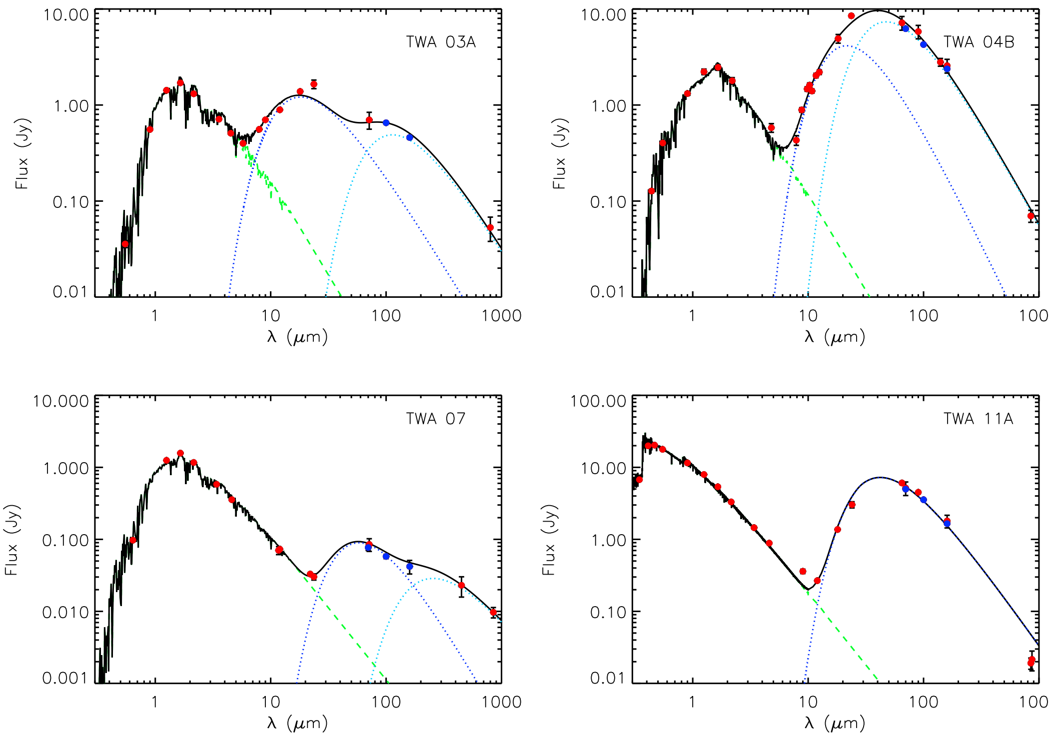

Figure 3.12: Blackbody models for TWA members. We show in different tones of blue the individual blackbody components of the model, while the stellar photosphere model is shown in green. The overall model is the black line. The blue dots are PACS observations at 70, 100 and 160 μm.

From these fits, we get estimates of the dust temperature and infrared excess. Such analysis is useful as it relies on few assumptions and allows easy comparison with other studies. For the sources with no IR excess detected we compute upper limits for the IR excesses by considering the flux upper limits as detections. For

TWA 01, TWA 03A, TWA 04B and TWA 07, the SED is better reproduced using a model consisting in the stellar photosphere model plus two blackbodies instead of only one, i. e., following:

$$F_{model} = F_* + B_\nu(T_{dust,1}) \times (\lambda_0/\lambda)^{\beta_1} + B_\nu(T_{dust,2}) \times (\lambda_0/\lambda)^{\beta_2} \tag{3.5}$$

The fact that we need two blackbodies to reproduce the emission points to the presence of two populations of grains at different radii or could be the signpost of a complex system. For TWA 11A, the inclusion of a second blackbody does not result in a significant improvement. Results of the fitting process are listed in Table 3.5, and model SEDs can be found in Fig. 3.12.

Using the dust temperature from the blackbody models, we can estimate the inner radius of the disc using

$$R_{\rm in} > \frac{1}{2} R_* \left(\frac{T_*}{T_{\rm dust}} \right)^{(4+\beta)/2} \tag{3.6}$$

(Beckwith et al., 1990). Furthermore, we can estimate the dust mass in the disc by using the following expression, which is valid for optically thin discs:

$$M_{dust} = \frac{F_\nu(\lambda_0) D^2}{\kappa_\nu B_\nu(T_{dust})} \tag{3.7}$$

where D is the distance to the star, $\mathrm{B}_\nu(\mathrm{T}_{\rm dust})$ can be approximated by the Rayleigh-Jeans regime, $\kappa_\nu = 2 \times (1.3\mathrm{mm}/\lambda)^\beta$ $\mathrm{cm}^2\mathrm{g}^{-1}$ (Beckwith et al., 1990) and $\mathrm{F}_\nu(\lambda_0)$ is the integrated flux density at a given wavelength emitting at the Rayleigh-Jeans regime. Considering that, for some targets, the far-IR and sub-millimeter fluxes seem to arise from different radii, we computed dust masses using the PACS flux at 160 μm and a sub-millimeter flux from the literature. Disc radii and dust masses are shown in Table 3.5.

Table 3.5: Photosphere plus modified blackbody fitting and disc parameters

Name	T_1	β_1	T_2	β_2	L_{IR}/L_*	$R_{in,1}$	$R_{in,2}$	$M_{dust,160\mu m}$	$M_{dust,submm}$
–	(K)	–	(K)	–	–	(AU)	(AU)	($\mathrm{M}_\oplus$)	
TWA 03A	280 ± 5	$0^{+0.06}$	45 ± 4	$0^{+0.09}$	9.8×10^{-2}	0.416 ± 0.015	16.1 ± 5.8	0.133 ± 0.042	0.384 ± 0.159
TWA 04B	190 ± 10	0.72 ± 0.55	102 ± 2	0.185 ± 0.023	2.4×10^{-1}	4.8 ± 1.0	7.9 ± 1.6	0.259 ± 0.029	0.256 ± 0.064
TWA 07	66 ± 5	0.86 ± 0.23	20 ± 2	$0^{+0.1}$	2.2×10^{-3}	38 ± 10	75 ± 15	0.022 ± 0.011	0.146 ± 0.045
TWA 11A	108 ± 5	$0.3^{+0.2}_{-0.1}$	–	–	4.6×10^{-3}	59 ± 19	–	0.271 ± 0.109	0.146 ± 0.042

3.6 Gas and dust content in TWA circumstellar discs

Next, we discuss the individual sources.

3.6.1 TWA 01

TWA 01 is a M2.5V star (Vacca & Sandell, 2011) at only 56 pc from the Sun and it is one of the most studied protoplanetary/transitional objects. As shown in section 3.2.2, TWA 01 is the strongest accretor among the sample. The blackbody model for TWA 01 produces a poor fit, especially when compared with other TWA members such as TWA 04B, TWA 07 and TWA 11A. This is due to the more complex spatial distribution of dust around TWA 01 and to its optical thickness.

Considering the importance of TWA 01 in the field of circumstellar systems, we decided to perform a more detailed analysis of the source. PACS observations of TWA 01 from the GASPS programme were studied and modelled in detail in Thi et al. (2010), where we modeled the circumstellar dust with a total dust mass of $\sim 63\ M_\oplus$. The dust disc was modeled using MCFOST (Pinte et al., 2006, 2009, see Chapter 4 for a detailed description of the code). The disc has an internal cavity up to 4 AU, with very small gas and dust densities. Imaging studies of the source constrain the inner (R_{in}) and outer (R_{out}) to ~4 and ~200 AU respectively (Qi et al., 2004; Roberge et al., 2005; Hughes et al., 2007). The disc radial density profile is described by a power law with index ϵ. The flaring of the disc is characterized by the opening angle H_0 at a reference radius R_0 and a flaring index γ. The scale height is then given by $H = H_0(R/R_0)^\gamma$. The low continuum flux in the range 30 to 100 μm suggest an outer disc with weak flaring. We used amorphous olivine grains (Dorschner et al., 1995) to describe the dust composition. The dust grains were described by a power-law size distribution going from a_{min} to a_{max}, with power law index p. We show the SED fit in Fig. 3.13, and the parameters for the best fit are shown in Table 3.6. We need grains as large as 10 cm to reproduce the observed flux at 7 mm and 3.6 cm (Wilner et al., 2000). The model fails to reproduce the flux around 25 μm, most probably due to the assumption that there is a unique temperature for grains of all sizes. The dust mass in grains smaller than 1mm is $M_{dust} = 63\ M_\oplus$, while the total solid mass (i. e., the mass in grains with sizes up to 10 cm) is $\sim 1000 M_\oplus$. We also estimated a mass of $\sim 100\ M_\oplus$ in small grains (i. e., up to ~1 mm) assuming optically thin emission in dust with a temperature of 20 K and opacity law $\kappa_\nu = 2(\lambda_0/\lambda)^\beta$ g/cm^2, with $\lambda_0 = 1.3$ mm and $\beta = 0.6$

Table 3.6: Disk parameters for TWA 01 detailed modeling

Fixed parameters			
		Inner cavity	Outer ring
Stellar mass	$M_*(\mathrm{M_\odot})$	0.6	
Stellar luminosity	$L_*(\mathrm{L_\odot})$	0.23	
Effective temperature	$T_{\mathrm{eff}}(\mathrm{K})$	4000	
Solid material mass density	$\rho_{\mathrm{dust}}(\mathrm{g\ cm^{-3}})$	3.5	
Inner radius	$R_{\mathrm{in}}(\mathrm{AU})$	0.25	4
Outer radius	$R_{\mathrm{out}}(\mathrm{AU})$	4	196
ISM UV field	χ	1.0	
α viscosity parameter	α	0.0	
Turbulent velocity	$v_{\mathrm{turb}}(\mathrm{km\ s^{-1}})$	0.05	
Disk inclination	i	7	
CO isotopologue ratio	$[^{12}\mathrm{CO}]/[^{13}\mathrm{CO}]$	69	
MCFOST best fit parameters			
Column density index	ϵ	1	
Reference scale height	$H_0(\mathrm{AU})$	2.0	10.0
Reference radius		100	100
Flaring index	γ	0.6	1.12
Minimum grain size	$a_{\mathrm{min}}(\mu\mathrm{m})$	3×10^{-2}	
Maximum grain size	$a_{\mathrm{max}}(\mathrm{cm})$	10	
Dust size distribution index	p	3.4	
Dust mass (a <1 mm)	$M_{\mathrm{dust}}(\mathrm{M_\odot})$	1.2×10^{-9}	1.9×10^{-4}
Solid mass	$M_{\mathrm{solid}}(\mathrm{M_\odot})$	2.0×10^{-8}	3.0×10^{-3}
ProDiMo parameter range			
Disk gas mass	$M_{gas}(M_\odot)$	3×10^{-4}–0.3	
UV excess	F_{UV}	0.018	
Fraction of PAHs w.r.t. ISM	f_{PAH}	0.01, 0.1	
Cosmic ray flux	$\zeta(\mathrm{s^{-1}})$	$(1.7–17) \times 10^{-17}$	

(Beckwith & Sargent, 1991). Both the mass from the MCFOST model and this second determination agree within a factor of 2 with each other.

As MCFOST lacks the ability to model the gas phase, we decided to model the gas emission using ProDiMo (Woitke et al., 2009a). Together with our PACS

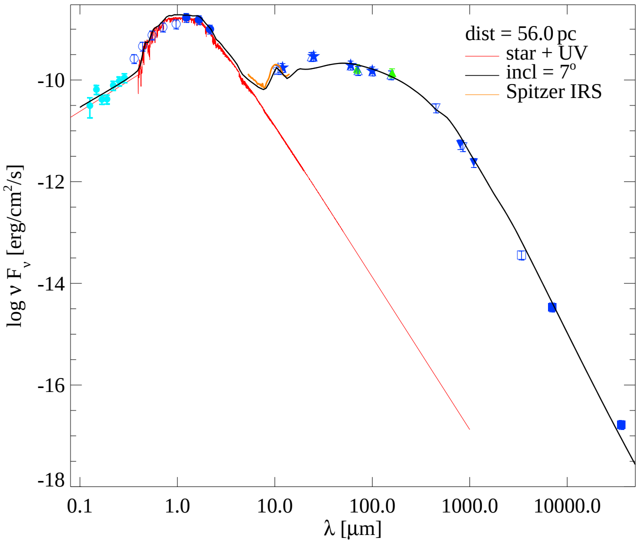

Figure 3.13: TWA 01 SED and MCFOST model for TWA 01 from Thi et al. (2010).

observations, we used the CO observations from SMA at CO 3–2 (Qi et al., 2004) and JCMT at ^{13}CO 3–2 (Thi et al., 2004). Following the dust model described in the previous paragraph, we ran three sets of models. ProDiMo computes species abundances at steady-state from the gas, and dust temperature as well as the local UV field to account for photodissociation reactions. The code computes the gas kinetic temperature by balancing heating and cooling processes. The line profiles are computed using non-LTE radiative transfer. We assumed a constant isotopologue ratio ([^{13}CO]/[^{12}CO]) of 69. The free parameters in the models are the total gas mass (M_{gas}), the fraction of polyciclic aromatic hydrocarbons (PAHs) with respect to the interstellar abundance (f_{PAH}), and the cosmic ray flux ζ (the ISM value is 1.7×10^{-17} s^{-1}). The main heating mechanism in the gas are photoelectrons ejected from PAHs, therefore the PAH abundance is the main parameter controlling the gas temperature. The range of values for free parameters in the gas models are shown in Table 3.6. The three series of models correspond to: a disc with very low PAH abundance (f_{PAH}=0.01), a disc with the typical PAH abundance (f_{PAH}=0.1) and a disc with very low PAH abundance (again f_{PAH}=0.01), but with a cosmic ray flux that is 10 times the standard ISM value to consider the influence of strong X-ray emission in the disc (Bruderer et al., 2009).

The model results for the gas model runs from ProDiMo are shown in Fig. 3.14. Results from series 3 are within 10% of values from series 2, suggesting that X-ray

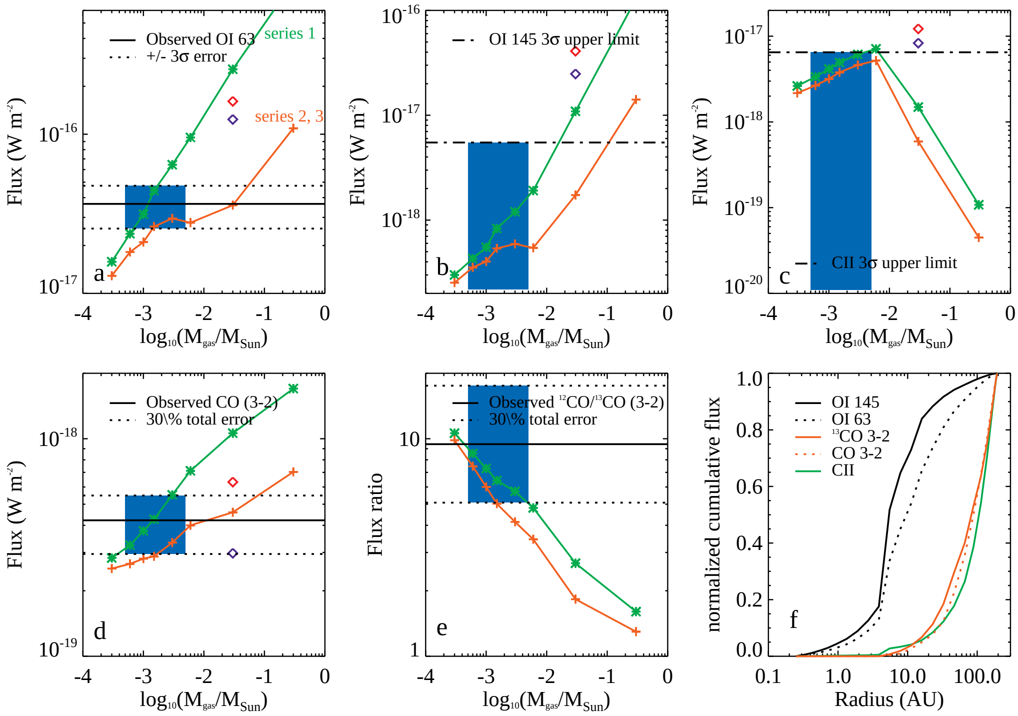

Figure 3.14: Three series of model results compared to observations from Thi et al. (2010). The blue boxes enclose the model outputs for disk gas mass between 5×10^{-4} $M_\odot$ and 5×10^{-3} $M_\odot$. Panel a shows the predictions and observation of the OI 63 μm line. The 3-σ uncertainty range is plotted as dashed lines. Panel b and c show the predicted fluxes and the 3-σ upper limits for the OI 145 μm and CII lines. The two lower panels (d and e) are the comparison between observations and model outputs for ^{12}CO 3-2 emission and the ^{12}CO/^{13}CO 3-2 ratio. Panel f shows the normalized cumulative fluxes for a 10^{-3} $M_\odot$ model (series 1). The diamonds (red for $R_{\rm out}$=174 AU model, blue for $R_{\rm out}$=120 AU model) show the predictions for TW Hya from Gorti & Hollenbach (2008).

does not influence the line fluxes at radii beyond a few AU. Panels a and b show that [OI] flux at 63 μm and 145 μm increase with the gas mass. Both lines mostly arise from a 4 to 10 AU, probing the gas mass up to 10-20 AU. The [CII] emission increases with the radius, and plummets for masses greater than $\sim$ 3300 M⊕: as the disc becomes more massive, more carbon is converted into CO, cooling the disc. CO 3–2 emission mostly comes from the outer disc (R > 50 AU). The CII and CO lines mainly probe the outer disc. The observed ^{12}CO/^{13}CO 3-2 ratio is consistent with a low-mass disk. The different line fluxes constrain the gas mass from ∼160 $M_\oplus$ to ∼1600 $M_{\rm oplus}$, suggesting a gas-to-dust ratio of 2.6–26 for dust grains smaller than 1 mm, almost a factor of ten lower than the standard ISM value. Bergin et al. (2013) reported the detection of hydrogen deuteride (HD), and derived a even larger gas mass $> 1.8 \times 10^5$ $M_\oplus$, high enough to form a planetary system at the age of TWA.

3.6.2 TWA 03A

TWA 03A is an M3 star (de la Reza et al., 1989) placed at 42 pc form the Sun. Andrews et al. (2010) performed high resolution observations of the thermal continuum emission towards TWA 03A at 880 μm with SMA. By modelling the 880 μm flux visibility and the SED, they deduced $R_{\rm out} \sim 15 - 25$ AU (the expected radius if the disc around TWA 03A is truncated by TWA 03B), $R_{\rm in} \sim 0.4$ AU, and a dust mass of 2.3 $M_{\oplus}$.

The best model for TWA 03A needs a population of hot grains (T = 280 K) at $\sim$ 0.4 AU to reproduce the mid-IR emission and a second population of cold grains (T = 40 K) at 16 AU. We note that the model fails to reproduce the MIPS observation at 24 μm. The flux at 160 μm is not at the Rayleigh-Jeans regime, and therefore the mass computed using this flux is a lower limit. A more accurate value for the dust mass is computed using the James Clerk Maxwell Telescope (JCMT) observations at 800 μmJensen et al. (1996). We get $\sim$ 0.38 $M_{\oplus}$, about six times smaller than the value by Andrews et al. (2010).

Muzerolle et al. (2000) studied H_{α} emission in TWA 03A and concluded that there is ongoing gas accretion in the system about one order of magnitude larger than the average value for discs in Taurus. Huenemoerder et al. (2007) studied the soft X-ray emission from the star and concluded that the shape of the spectrum was attributable to accretion shocks. The compilation of TWA 03A H_{α} equivalent widths by Barrado y Navascués (2006) shown in Fig. 3.2 are also in agreement with ongoing accretion as pointed out in section 3.2.2. This is in contrast with the non detection of [OI] emission at 63 μm and will be discussed in Sec. 3.7.2.

3.6.3 TWA 04B

TWA 04B is part of a peculiar quadruple system: it is two spectroscopic binaries A and B orbiting each other. The system shows a prominent infrared excess attributed to a circumbinary disc around the B pair (Koerner et al., 2000; Prato et al., 2001; Furlan et al., 2007), where both stars are separated by ~1 AU. Skinner et al. (1992) reported the detection of a silicate emission feature around 10 μm, indicating the presence of grains as small as 0.01 μm.

Different studies modelled the infrared emission toward TWA 04B in the past, showing inner radii ranging from 2 AU to 5 AU, and outer radii in the range from 10 to 18 AU. Some of these studies modelled the SED of TWA 04B using a complex geometry with two discs (Akeson et al., 2007; Furlan et al., 2007; Andrews et al., 2010). The most recent work by Andrews et al. (2010), suggested an outer radius of 10-15AU based in SMA observations at 880 μm and modeled the SED with an inner disc extending from 2 to 3.5 AU, and a second one extending from 3.5 to ~ 15 AU.

Our best model for TWA 04B consists on a population of dust grains at 180 K placed at 4.8 AU and second population of dust grains at 102 K placed at 7.9 AU from the star, with a total dust mass of ~ 0.26 $M_\oplus$. Our deduced radius for the inner disc is compatible within the errors with the value proposed by Andrews et al. (2010) while the radius of the outer disc is larger in our model. Our dust mass is two times larger than the value by Nilsson et al. (2010), but we note that they used a single blackbody at 155 K to model the whole SED. Also, their flux at 870 μm is smaller than fluxes at similar wavelengths from the literature.

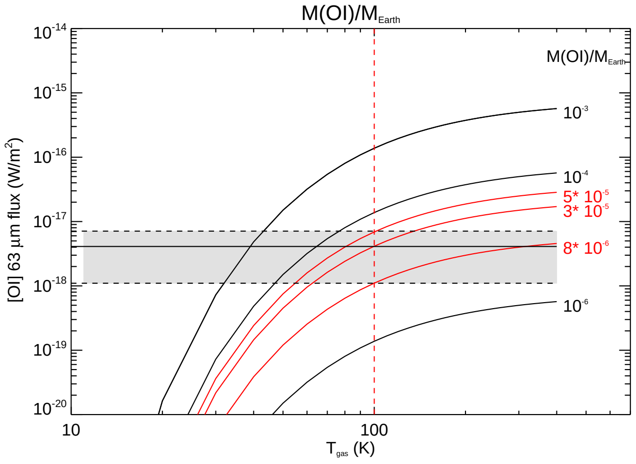

Figure 3.15: Line luminosity versus gas excitation temperature for TWA 04B. The black and red curves represent the behaviour for different gas masses. The red ones show masses compatible with the observed flux range in TWA 04B for T_{gas} = 100 K. The grey dashed region shows the flux density values consistent with our observations".

Since we detected the [OI] emission in this system, we can study the gas content of the disc. In Fig. 3.15, we show the line luminosity versus the excitation temperature for different gas masses. Assuming an excitation temperature of ~100 K for the [OI] line at 63.18 μm, we can constrain the atomic oxygen gas mass to be between $8.0 \times 10^{-6} M_\oplus$ and 5.0×10^{-5} $M_\oplus$. Assuming a primordial gas abundance for oxygen, i.e. 8.5×10^{-4} with respect to H nuclei, the total gas mass ranges from 9.5×10^{-3} $M_\oplus$ to 6.0×10^{-2} $M_\oplus$, implying a gas-to-dust ratio that ranges roughly from 3.6×10^{-2} to 0.23. We note that, depending on the origin of the gas, the oxygen abundance can be larger, resulting in even smaller gas masses and

Table 3.7: Gas detections in TWA members and comparison with the BPMG member HD 172555

Target	$\frac{F_{[OI]}}{\lambda_{70\mu m}\times F(\lambda_{70\mu m})}$	M_{dust}	M_{gas}
–	–	$M_\oplus$	$M_\oplus$
TWA 04B	1.5×10^{-5}	0.26	$(0.95-6)\times10^{-2}$
TWA 01	2.2×10^{-4}	63	160-1600
HD 172555	5.5×10^{-3}	4.8×10^{-4}	$4.8\times10^{-4(1)}$
TWA 03A	$< 2.0\times10^{-4}$	0.38	$< 0.042^{(2)}$
TWA 07	$< 1.3\times10^{-3}$	0.15	$< 0.027^{(2)}$
TWA 11A	$< 2.1\times10^{-5}$	0.15	$< 0.082^{(2)}$

Notes. (1): atomic oxygen mass only, see Riviere-Marichalar et al. (2012a). (2): computed assuming primordial gas abundance for oxygen, i.e. 8.5×10^{-4} with respect to H-nuclei.

gas to dust ratios. Thus, we are detecting gas in a very small ratio to dust, and therefore the system seems to be in a very advanced evolutionary stage. We can compare the OI gas detection in TWA 04B with those in TWA 01 (Thi et al., 2010) and HD172555 (Riviere-Marichalar et al., 2012a), as they share similar evolutionary stages (the general agreement is that the Beta Pictoris Moving Group is slightly older than TWA, with an absolute age in the range 12 to 20 Myr), although we must caution that HD 172555 has a very different spectral type (A0 versus M). The result of this comparison is shown in Table 3.7. TWA 04B shows the smallest ratio with respect to the 70 μm continuum emission. The gas in TWA 01 is probably primordial, while some authors (Lisse et al., 2009; Johnson et al., 2012) argue that the gas in HD 172555 comes from the sublimation of silicates (olivines, pyroxenes) in an hypervelocity collision. Considering the low line to continuum flux ratio in TWA 04B when compared with TWA 01, we suggest that the gas should have a second generation origin, possibly from cometary evaporation.

Soderblom et al. (1996) proposed a chromospheric origin for the H_α emission as we did in section 3.2.2. Dent et al. (2005) did not detect CO emission in TWA 04B. The fact that TWA 04B shows [OI] in emission at 63 μm while showing no accretion would be pointing to a disc with an inner gap empty of gas, but with measurable amounts of gas at larger radius. The origin of the gap may be related to the binary nature of the system, with separation of $\sim$ 1.0AU.

3.6.4 TWA 07

TWA 07 is an M1 star (Webb et al., 1999) placed at 38 pc from the Sun. Low et al. (2005) used MIPS observations to study dust emission in TWA 07 and modeled the SED with an 80 K blackbody at 6.8 AU from the star, with a minimum mass of $\sim 4 \times 10^{-5}$ $M_{\oplus}$. Later on, Matthews et al. (2007) observations at 450 and 850 μm demonstrated dust in a range of temperatures is needed to fit simultaneously the 24 μm and the sub-millimeter flux densities.

Fitting TWA 07 with a single blackbody model results in a poor fit, while the inclusion of a second blackbody highly increases the quality of the fit. The best model consists of an inner disc at 66 K, with β= 0.86 placed at ~ 38 AU from the star, and a second, very cold blackbody (20 K) at ~ 75 AU from the star; this is the coldest disc among the sample, and it is more than two times cooler than the Sun's Edgeworth-Kuiper Belt, at ~ 45 K. As pointed out by Matthews et al. (2007), no single temperature can fit both the near and mid-IR and the sub-millimetre fluxes. The inclusion of the 160 μm PACS photometric point pushes the outer blackbody to cooler temperatures, and clearly demonstrates the bimodal shape of the SED. We are aware that the combination of many different grain size distributions can result also in a bimodal shape (see Matthews et al., 2007), but we consider the presence of dust at different radii as the most plausible explanation, because two different bumps (with local maxima) are seen. Because the flux at 160 μm will underestimate the dust mass, we deduced a value of 0.15 $M_{\oplus}$ using the flux at 870 μm by Matthews et al. (2007).

According to section 3.2.2, the H_{α} equivalent width is in agreement with no ongoing accretion in TWA 07. The PACS line spectrum of this source does not show line emission. Both facts agree with an evolved, second generation debris disc.

3.6.5 TWA 11A

TWA 11A is an A0 star (Houk & Fuentes-Williams, 1982) at 67 pc from the Sun. Infrared excess around TWA 11A was reported for the first time by Jura (1991), who highlighted the prominence of this excess when compared with β Pictoris. Jura et al. (1993) studied the TWA 11A SED, and proposed a typical size of 10 μm for dust grains located at 40 AU from the star. Koerner et al. (1998) showed that the morphology of the emission at 20.8 μm agrees with a ring-like structure extending from 55 to 85 AU, while the excess at 12.5 μm arises predominantly from the region interior to this radius, from gravitationally confined grains. Resolved images of the disc have been studied by several authors (Koerner et al., 1998; Jayawardhana et al., 1998; Schneider et al., 1999; Telesco et al., 2000), who agree that the detected emission should arise from material at least at 55 AU. Augereau et al. (1999) modelled the SED with an outer disc at ~70 AU, and an inner disc at ~9 AU, with a total solid mass of $\sim 3.9 M_\oplus$ in a grain size distribution with $a_{max} = 100$ cm; as the dust mass goes like $M_{dust} \propto a_{max}^{0.5}$ in this model, the dust mass in grains < 1 mm is $\sim 0.11\ M_\oplus$.

For TWA 11A, the inclusion of a second blackbody in the model does not result in a big improvement, and therefore we kept a single blackbody model as the best option. The dust temperature is 108 K, corresponding to a disc at 59 AU, in good agreement with previous results, with β= 0.3. If we use the 160 μm flux to derive the dust mass we get $M_{dust} = 0.27\ M_\oplus$, only two times the mass deduced by Augereau et al. (1999), a difference that can be considered satisfactory given the uncertainties associated with the dust opacity law. We note that the model over estimates the observed flux at sub-millimeter wavelengths. The dust mass was then computed using the flux at 870 μm by Nilsson et al. (2010) is $\sim 0.146\ M_\oplus$, in even better agreement with previous results.

TWA 11A does not show [OI] emission at 63 μm. The lack of atomic emission in TWA 11A was already reported and discussed in the study of atomic and molecular emission in the GASPS sample of HAeBe stars by Meeus et al. (2012). The authors showed how other stars with similar spectral types emit in [OI] at 64.18 μm (e. g. AB Aur, HD 97048). Therefore the lack of [OI] emission towards TWA 11A cannot be attributed to its spectral type. But we caution that discs around AB Aur and HD 97048 are protoplanetary, gas-rich systems. Therefore, the lack of [OI] is not linked to the spectral type, but to the evolutionary stage of the system.

3.7 Discussion

The TWA members detected with PACS show a wide variety of dust and gas properties, from TWA 01, harbouring a protoplanetary-like disc, with strong gas emission and active gas accretion ongoing, to TWA 07, which seems to be devoid of gas but shows two debris discs at different radii. TWA 04B is considered a transitional disc, and shows no accretion according to its H_α emission, but shows [OI] in emission at 63.18 μm. Inner radii span a large range of values, from ~ 0.4 AU for TWA 03A to 59 AU for TWA 11A, independent of the spectral type. The wide variety of properties in the five TWA discs studied most likely indicates that there are several factors driving disc evolution, and not just the age, like the dust/gas initial mass, the mass of the central object, angular momentum, multiplicity, composition of the original cloud and possibly planet formation itself. Other authors have arrived at the same conclusion (Furlan et al., 2006; Bayo et al., 2012; Lada et al., 2006; Hernández et al., 2007; Currie & Sicilia-Aguilar, 2011).

3.7.1 Dust in TWA

TWA 01 shows the largest dust mass in the sample, ~ 63 $M_{\oplus}$ (Thi et al., 2010, including PACS observations from GASPS), while other TWA members studied in the present work show dust masses in the range 0.15 to 0.38 $M_{\oplus}$. According to our numbers, except for TWA 01, there is no mass left to form planets within the TWA members studied here. The same result for a different TWA sample was already reported by Weinberger et al. (2004), using mid-IR photometry only, so the present result extends the result to longer wavelengths, and therefore to the cold component of the discs. Furthermore, we find no correlation between the spectral type and the dust mass; TWA 11A and TWA 07, which are A0 and M1 stars respectively, have approximately the same dust mass. On the other hand, TWA 01, which is an M2.5 star, shows a mass that is ~ 400 times larger than TWA 07 mass.

Another interesting point is the fact that TWA 11A, which is an A0 star (Barrado y Navascués, 2006), does not show gas emission, while showing a very prominent IR excess. The disc is clearly a second generation debris disc, while TWA 01 and TWA 03A and TWA 04B show SEDs that resemble those of transitional discs. This result agrees with the hypothesis that discs around early type stars tend to evolve faster toward the debris phase than late type stars. We note that we only have one early spectral type object, and therefore this conclusion have to be taken with some caveats.

Grain sizes are very important to understand the dust behavior in circumstellar systems, because the distribution of sizes can help us to understand the origin of the circumstellar material. β values in the outer discs are typically around 0 (pure blackbody emission), with an average value of β_2= 0.12, which implies grains with sizes of the order of ~ 1000 μm, significantly larger than ISM grains. This may be indicating the second generation nature of the dust in the outer discs, with grains coming from the collisional grinding of planetesimals, but also may be a signpost of grain growth. On the other hand, β values for inner discs have an average value of β_1= 0.53, i. e., similar to those values found for T Tauri stars in Taurus-Auriga (Mannings & Emerson, 1994, with a typical value of 0.6). This illustrates the need for populations with different sizes at different radii.

There are some facts in our PACS observations in TWA that can help us to understand some evolutionary trends in the transition from a protoplanetary disc to a debris disc. The first is that all the detected objects in TWA show large IR excess, as already reported by Low et al. (2005) using *Spitzer* data. There are no detections of weak excesses in the sample. This may suggest that the dust (and gas) depletion rate is faster than the replenishment rate by collisions between planetesimals from an unseen population. If discs are formed with an initially low gas and dust content, it may be that large planetesimals never form. On the other hand, the high mass objects detected in this survey may be those with enough initial gas and dust such that a significant population of planetesimals exist.

Donaldson et al. (2012) recently modelled the SED of some Tuc Hor members that were also part of the GASPS sample, and concluded that all the detected discs were debris discs, with no [OI] emission. In the present study, we have detected five discs in TWA, but they span a wide range of disc parameters, including both debris discs and protoplanetary discs. Tuc Hor is a 30 Myr old association, while TWA is much younger (8 to 20 Myr, depending on different authors). The different range of ages can explain not only the presence of protoplanetary/transitional systems in TWA, but also the fact that we detect [OI] emission at 63 μm in two systems (namely TWA 01 and TWA 04 B) while no [OI] emission is observed in Tuc Hor.

3.7.2 Gas in TWA

There are some interesting questions regarding the gas content in TWA member discs. The [OI] detection in TWA 01 (TW Hya) was studied in detail in Thi et al. (2010), where they estimated a gas mass of 160 to 1600 $\times 10^{-3}$ $M_\oplus$. This mass is four to six orders of magnitude larger than the mass that we have estimated for TWA04 B. If we estimate the gas mass for TWA 01 in the same way that we did for TWA 04B, we get a mass in the range 0.3 to 0.6 $M_\oplus$, much smaller than the more realistic value by Thi et al. (2010), but again 5 to 61 times higher than the gas mass in TWA 04B. Both stars have similar spectral types: M2.5 for TWA 01 (Vacca & Sandell, 2011) and M5 for TWA 04B (Gregorio-Hetem et al., 1992). Given that the spectral types are so similar, what is driving the large difference in gas mass? One possibility is that the difference comes from the size of the disc, and therefore, the total initial mass available. The disc in TWA 04B is truncated by the primary, TWA 04A, at ~ 15AU, while TWA 01 is expected to be much more extended (196 AU, Qi et al., 2004). Also, TWA 04B is itself a close spectroscopic binary, which opens a large inner gap devoid of gas and dust; therefore the difference in dust and gas evolution can also be related to multiplicity.

In Fig. 3.16 we show [OI] luminosity at 63 μm versus the excitation temperature for objects not detected with PACS at 63.18 μm. As can be seen, upper limits on the [OI] gas mass are of the order of a few 10^{-5} $M_{\oplus}$, similar to the [OI] gas mass in TWA 04B. The gas mass in TWA 01 is therefore more than one order of magnitude larger than any other gas mass in the association.

It is also interesting to compare the detection of [OI] gas in TWA 04B with the non-detection in TWA 03. In Sec. 3.2.2 we classified TWA 03 as an accreting disc and TWA 04B as a non accreting disc. The [OI] gas detection combined with the absence of accretion in TWA 04B can be explained by the fact that TWA 04B is a close spectroscopic binary, therefore no gaseous material could survive inside 1 AU, and no accretion could be detected (see Prato et al., 2001). Our own determination of the inner radius in TWA 04B agrees with an inner hole > 1 AU.

The fact that we do not detect [OI] emission in TWA 03A while we see signs of accretion is intriguing. A possible explanation relies on the geometry of the disc. If the disc is very flat, then there is not enough material irradiated by the central star, small amounts of oxygen are excited, and the resultant [OI] emission should be too weak to be detected. We do not claim that this is the only possible explanation. A lower UV flux also could explain the difference between TWA 03A and TWA 04B, as the UV flux is the main source of energy for the gas heating via photoelectric effects on dust grains and polycyclic aromatic hydrocarbons. However, both targets are a similar spectral type and therefore we expect that the UV flux is very similar. Indeed, TWA 03A is actively accreting, and therefore we expect a higher UV flux from that source, so a difference in the flaring geometry is the most plausible explanation for the difference in [OI] emission. In Fig. 3.17 we represent the [OI] luminosity at 63.18 μm versus the flaring index (γ) for a model system taken from the DENT grid of models (Kamp et al., 2011) scaled to the distance of TWA 03A, 42 pc. As can be seen, the flux for the same star dramatically changes by more than one order of magnitude by changing the flaring index, in such a way that only the system with γ= 1.2 could be detected by our PACS observations, while all of them share the same gas and dust mass. Overall, Fig. 3.17 shows that in discs with low-mass gas, and hence low mass-accretion rate, OI is very difficult to detect with present

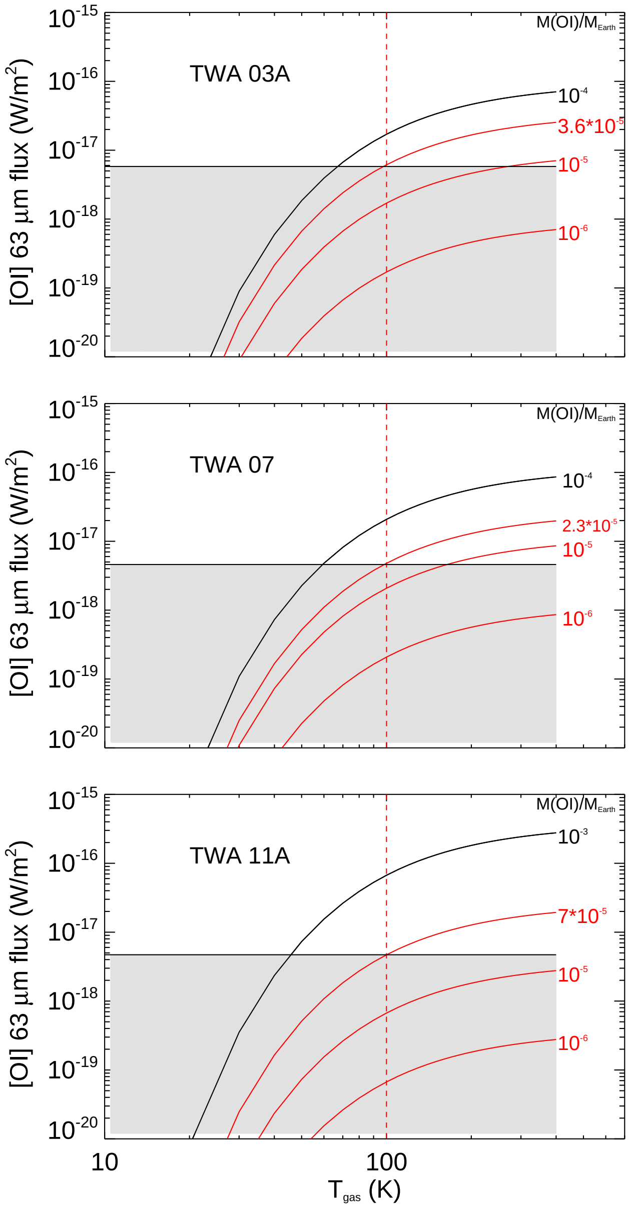

Figure 3.16: Line luminosity versus gas excitation temperature for TWA members with no [OI] emission detected. The black and red curves represent the behaviour for different gas masses. The red ones show masses compatible with the flux upper limits for T_{gas} = 100 K. The grey dashed region shows the parameter space compatible with observations.

instrumentation.

In Taurus, 46 stars with discs out of 76 observed show [OI] emission (Howard et al. 2013, submitted), while in TWA we detected line emission in two systems out of 9 observed, and in two out of 5 known to have discs. Although the number of

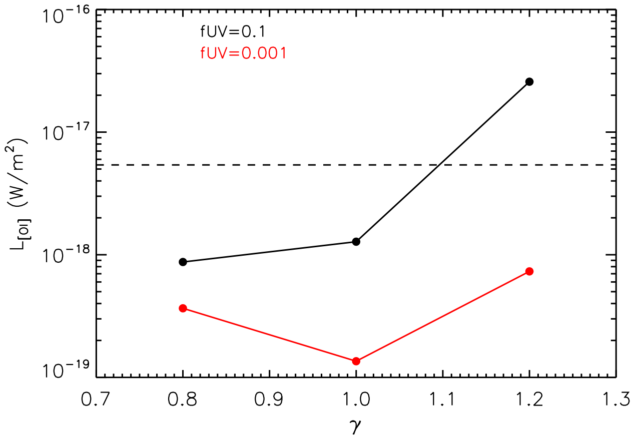

Figure 3.17: [OI] luminosity at 63.18 μm versus flaring index (γ) for a model star with $L_* = 0.13\ L_\odot$, $R_{in} = R_{sub}$, $R_{out} = 100$ AU, $a_{min} = 0.05\ \mu$m, $a_{min} = 1000\ \mu$m, $\epsilon = -1.0$ and $M_{dust} = M_{gas} = 10^{-6}\ M_\odot$ at the distance of TWA 03A. The model is for illustration, and is not intended to represent TWA 03A exactly, but a generic system with similar stellar parameters. The horizontal, dashed line represents the average upper limit for objects in TWA. The black solid line represents models UV fractional flux $f_{UV} = 0.1$, while the red one represents models with $f_{UV} = 0.001$

observations/detections in TWA is to low to make statistical arguments, we highlight the difference in gas rich discs fractions from Taurus (0.6) to TWA (0.4). Finally, Riviere-Marichalar et al. (2012b) showed that warm water emission is a commonly found among Taurus T Tauri stars, but we do not detect warm water emission toward TWA members; while ~ 24% of the gas-rich Taurus members (i. e., those showing [OI] emission at 63 μm) show water emission at 63.32 μm, no TWA member shows water emission at 63 μm. According to Riviere-Marichalar et al. (2012b), the water emission around T Tauri stars in Taurus comes from a region at ~ 1 AU and ~ 3 AU wide. TWA 04B, TWA 07 and TWA 11A show inner radii larger than 3 AU, and therefore no water could be detected in the regions. For TWA 01 and TWA 03A the lack of warm water emission must have a different explanation, most probably related to reprocessing of circumstellar gas or the geometry of the discs.

3.8 Summary and conclusions.

We have observed 14 TWA members with the PACS instrument on board the *Herschel Space Observatory*. All of them were observed with the PACS photometer (70, 100, and/or 160 μm). Nine were observed with PACS Line Spectrsocopy, targeting [OI] at 63 μm and DCO at 189 μm. The main conclusions are:

1. We detected excess photometric emission at 70/100/160 μm in 4/4/5 systems out of 12/9/14 observed at these wavelengths. We have detected for the first time 100/160 μm emission towards TWA 07, and also 100 μm emission towards TWA 03A. Objects not detected at 70 μm show upper limits near the photospheric level. Therefore, if present, any circumstellar material must be cold or be very low mass.

2. Among the five systems detected with IR excess, two of them (TWA 01 and TWA 04B) show [OI] emission at 63.18 μm, indicating the presence of gas in those systems. None of the systems show water emission at 63.32 μm. Future research is needed in order to understand the gas emission in TWA 01 and TWA 04B. TWA 04B itself requires detailed modeling.

3. We have modelled the dust IR emission with blackbody models, and used them to derive dust masses and inner radii, providing temperatures in the range 20 (TWA 07) to 280 K (TWA 04B). Dust masses are in the range 0.146 (TWA 07 and TWA 11A, from blackbody models) to 63 $M_\oplus$ (TWA 01, from detailed modelling). Disc radii are in the range 0.4 to 59 AU.

4. Detailed modeling of the TWA 01 disc showed a disc with a gas mass of 160-1600 M⊕, with a very low gas-to-dust ratio of 2.6–26. This is the first case where the disc gas mass around a transitional T Tauri star can be accurately computed from gas phase lines. Future, and more precise analysis of the source is needed to confirm the low gas-to-dust ratio. TWA 01 shows the largest mass for TWA members, several orders of magnitude larger than any other gas mass in the association.

TWA members show a wide variety of disc properties, implying different stages of disc evolution, from the protoplanetary/transitional, gas rich disc around TWA 01 to the very cold, gas free debris disc surrounding TWA 07. We propose that there must be several factors (others than the age) driving the evolution of the gas and dust contents in circumstellar environments, such as multiplicity, disc mass, stellar mass, angular momentum and composition, and, in general, initial conditions.

Appendix A

A.1 Photometry for TWA members detected with PACS.

Table A.1: Photometry for TWA members detected with PACS

Name	Filter	λ_0	Magnitude	Flux
–	–	μm	mag	Jy
TWA 01	Johnson I	0.90	9.18 ± 0.05	0.5171 ± 0.024
"	2MASS J	1.2518	8.217 ± 0.024	0.8456 ± 0.019
"	2MASS H	1.6504	7.558 ± 0.042	1.0576 ± 0.041
"	2MASS Ks	2.1539	7.297 ± 0.024	0.8095 ± 0.02
"	IRAC 1	3.5634	7.14 ± 0.02	0.3913 ± 0.007
"	IRAC 2	4.5110	7.04 ± 0.02	0.2745 ± 0.005
"	IRAC 3	5.7593	6.90 ± 0.04	0.1998 ± 0.007
"	IRAC 4	7.9594	5.98 ± 0.04	0.2600 ± 0.009
"	N	10.8	–	0.58 ± 0.058
"	MIPS 24	24	–	2.270 ± 0.23
"	PACS 70	70	–	3.895 ± 0.10
"	AKARI 90	90	–	3.5064 ± 0.23
"	AKARI 140	140	–	6.4692 ± 0.62
"	PACS 160	160	–	7.364 ± 0.3
"	UKT14 [1]	800	–	1.45 ± 0.31
"	UKT14 [1]	1100	–	0.874 ± 0.054
"	ATCA [2]	3400	–	0.041 ± 0.004
"	VLA 7 mm [3]	7000	–	0.008 ± 0.001
"	VLA 3.6 cm [3]	36,000	–	0.020 ± 0.003
TWA03A	JohnsonB	0.4443	14.04 ± 0.1	0.0107 ± 0.001
"	Johnson V	0.5483	12.57 ± 0.1	0.0357 ± 0.003

Table A.1: continued.

Name	Filter	λ_0	Magnitude	Flux
–	–	μm	mag	Jy
"	Johnson I	0.9000	9.10 ± 0.01	0.5566 ± 0.005
"	2MASS J	1.2518	7.651 ± 0.019	1.4242 ± 0.025
"	2MASS H	1.6504	7.041 ± 0.027	1.7027 ± 0.04
"	2MASS Ks	2.1539	6.774 ± 0.020	1.3105 ± 0.024
"	WISE 1	3.4	6.601 ± 0.038	0.708 ± 0.025
"	IRAC 1	3.5634	6.49 ± 0.02	0.7121 ± 0.013
"	IRAC 2	4.5110	6.37 ± 0.02	0.5088 ± 0.009
"	WISE 2	4.6	6.341 ± 0.021	0.4995 ± 0.0096
"	IRAC 3	5.7593	6.15 ± 0.03	0.3987 ± 0.011
"	IRAC 4	7.9594	5.15 ± 0.03	0.5585 ± 0.015
"	AKARI 9	9	–	0.7015 ± 0.018
"	IRAS 12	11.6893	–	0.988 ± 0.
"	WISE 3	12	3.876 ± 0.016	0.8918 ± 0.0131431
"	AKARI 18	18	–	1.384 ± 0.05
"	WISE 4	22	1.734 ± 0.014	1.6934 ± 0.0218356
"	MIPS 24	23.6750	–	1.650 ± 0.17
"	IRAS 25	24.3452	–	1.75 ± 0.
"	IRAS 60	62.2349	–	0.919 ± 0.
"	AKARI 65	65	–	0.960 ± 0.
"	MIPS 70	71.4200	–	0.700 ± 0.14
"	AKARI 90	90	–	0.5443 ± 0.039
"	IRAS 100	100	–	< 1.108
"	PACS 100	100	–	0.653 ± 0.019
"	AKARI 140	140	–	< 1.835
"	PACS 160	160	–	0.459 ± 0.019
"	MIPS 160	160	–	0.740 ± 0.
"	SCUBA 800	800	–	0.053 ± 0.015
TWA 04B	Johnson B	0.44	11.358 ± 0.05	0.1271 ± 0.006
"	Johnson V	0.55	9.941 ± 0.05	0.4022 ± 0.018
"	Johnson I	0.9	8.165 ± 0.05	1.3170 ± 0.06
"	J	1.251	–	2.22 ± 0.15
"	H	1.658	–	2.47 ± 0.17
"	K	2.20	–	1.79 ± 0.14
"	M	4.80	–	0.58 ± 0.06

Table A.1: continued.

Name	Filter	λ_0	Magnitude	Flux
–	–	μm	mag	Jy
"	L 7.9	7.90	–	0.43 ± 0.05
"	L 8.8	8.8	–	0.89 ± 0.05
"	L 9.8	9.8	–	1.47 ± 0.08
"	L 10.3	10.3	–	1.61 ± 0.09
"	N 10.8	10.8	–	1.4 ± 0.07
"	L 11.7	11.7	–	2.03 ± 0.11
"	L 12.5	12.5	–	2.20 ± 0.12
"	IHW 18	18.2	–	4.92 ± 0.51
"	MIPS 24	23.6750	–	8.5 ± 0.35
"	AKARI 65	65	–	7.1849 ± 1.17
"	PACS 70	70	–	6.241 ± 0.165
"	AKARI 90	90	–	5.8209 ± 0.93
"	PACS 100	100	–	4.269 ± 0.117
"	AKARI 140	140	–	2.7954 ± 0.26
"	PACS 160	160	–	2.382 ± 0.099
"	AKARI 160	160	–	2.5711 ± 0.42
"	SCUBA 450	450	–	< 3.6
"	SCUBA 850	850	–	0.07 ± 0.01
"	CSO 1300	1300	–	0.0307 ± 0.0082
"	SCUBA 1350	1350	–	0.0368 ± 0.0042
TWA 07	Johnson I	0.64	9.10 ± 0.01	0.0974 ± 0.005
"	2MASS J	1.2518	7.792 ± 0.021	1.251 ± 0.024
"	2MASS H	1.6504	7.125 ± 0.029	1.576 ± 0.043
"	2MASSKs	2.1539	6.899 ± 0.027	1.168 ± 0.029
"	WISE 1	3.4	6.816 ± 0.030	0.581 ± 0.016
"	WISE 2	4.6	6.708 ± 0.019	0.356 ± 0.006
"	12 μm [4]	11.7	–	0.0704 ± 0.009
"	WISE3	12.0	6.595 ± 0.015	0.073 ± 0.001
"	WISE4	22.0	6.005 ± 0.039	0.033 ± 0.001
"	MIPS24	23.6750	–	0.0302 ± 0.003
"	IRAS60	62.2349	–	< 0.1719
"	PACS70	70	–	0.077 ± 0.007
"	MIPS70	71.4200	–	0.085 ± 0.017
"	PACS100	100	–	0.058 ± 0.004

Table A.1: continued.

Name	Filter	λ_0	Magnitude	Flux
–	–	μm	mag	Jy
"	IRAS100	100	–	< 0.9420
"	PACS160	160	–	0.042 ± 0.009
"	JCMT450	450	–	0.023 ± 0.0072
"	JCMT850	850	–	0.0097 ± 0.0016
TWA 11A	stromgren u	0.345056	7.122 ± 0.05	6.7484 ± 0.31
"	stromgren v	0.410939	5.972 ± 0.03	19.943 ± 0.55
"	stromgren b	0.466901	5.805 ± 0.03	20.344 ± 0.56
"	stromgren y	0.547803	5.796 ± 0.01	17.792 ± 0.16
"	Johnson I	0.9	5.81 ± 0.06	11.524 ± 0.6
"	2MASS J	1.2518	5.784 ± 0.019	7.9504 ± 0.14
"	2MASS H	1.6504	5.794 ± 0.036	5.3697 ± 0.18
"	2MASS Ks	2.1539	5.769 ± 0.023	3.3072 ± 0.07
"	WISE 1	3.4	5.82 ± 0.049	1.454 ± 0.07
"	WISE 2	4.6	5.719 ± 0.024	0.886 ± 0.02
"	AKARI 9	9	–	0.3598 ± 0.025
"	WISE 3	12	5.186 ± 0.015	0.267 ± 0.004
"	AKARI 18	18	–	1.3710 ± 0.022
"	MIPS 24	24	–	3.030 ± 0.3
"	AKARI 65	65	–	6.0706 ± 0.31
"	MIPS 70	70	–	5.160 ± 1.1
"	PACS 70	70	–	4.980 ± 0.131
"	AKARI 90	90	–	4.5012 ± 0.19
"	PACS 100	100	–	3.553 ± 0.097
"	AKARI 140	140	–	< 3.2582
"	PACS 160	160	–	1.653 ± 0.068
"	MIPS 160	160	–	1.800 ± 0.36
"	SUBMM 850	850	–	0.0191 ± 0.0034
"	SUBMM 870	870	–	0.0215 ± 0.0066

Notes. UBVRI average photometry for TWA 01 comes from Rucinski & Krautter (1983). (1): from Weintraub et al. (1989). (2): from Wilner et al. (2003). (3): from Wilner et al. (2000). (4): from Weinberger et al. (2004)

A.2 TWA PACS radial profiles.

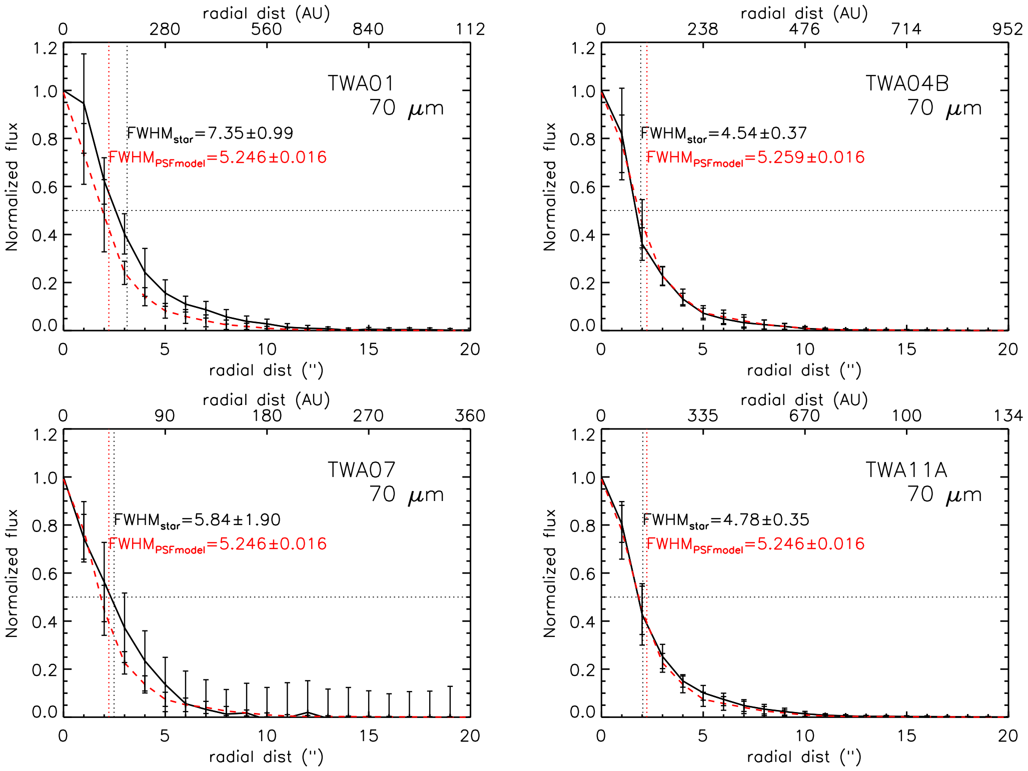

Figure A.1: Azimuthally averaged radial profiles at 70 μm for TWA members detected with PACS

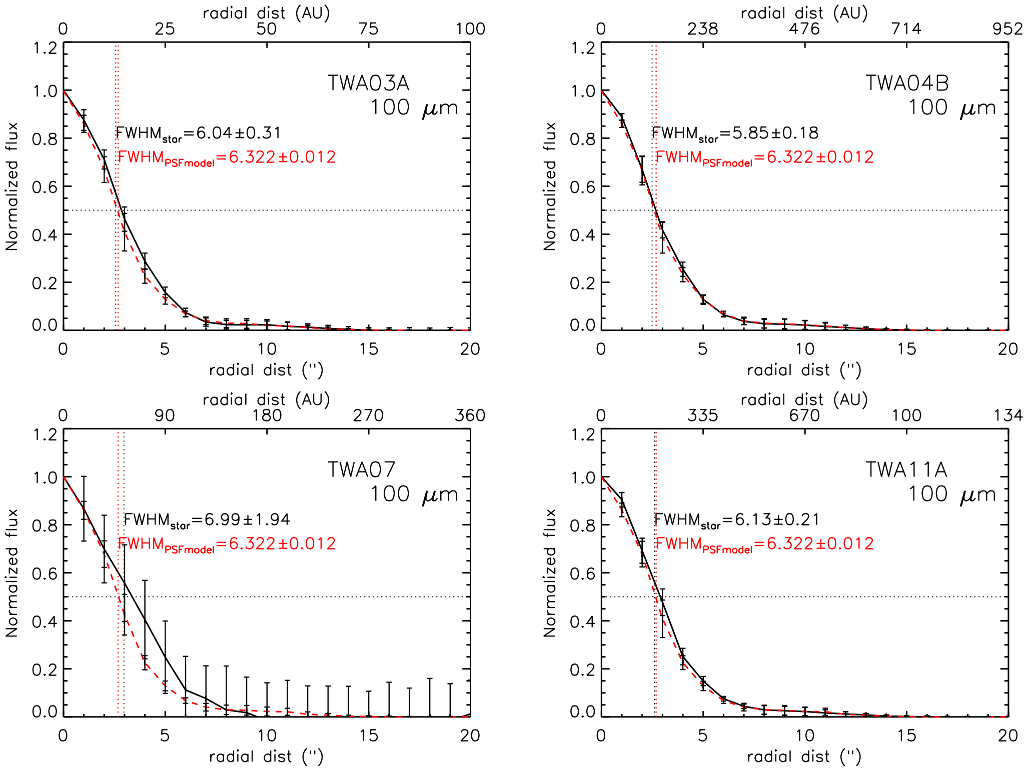

Figure A.2: Azimuthally averaged radial profiles at 100 μm for TWA members detected with PACS

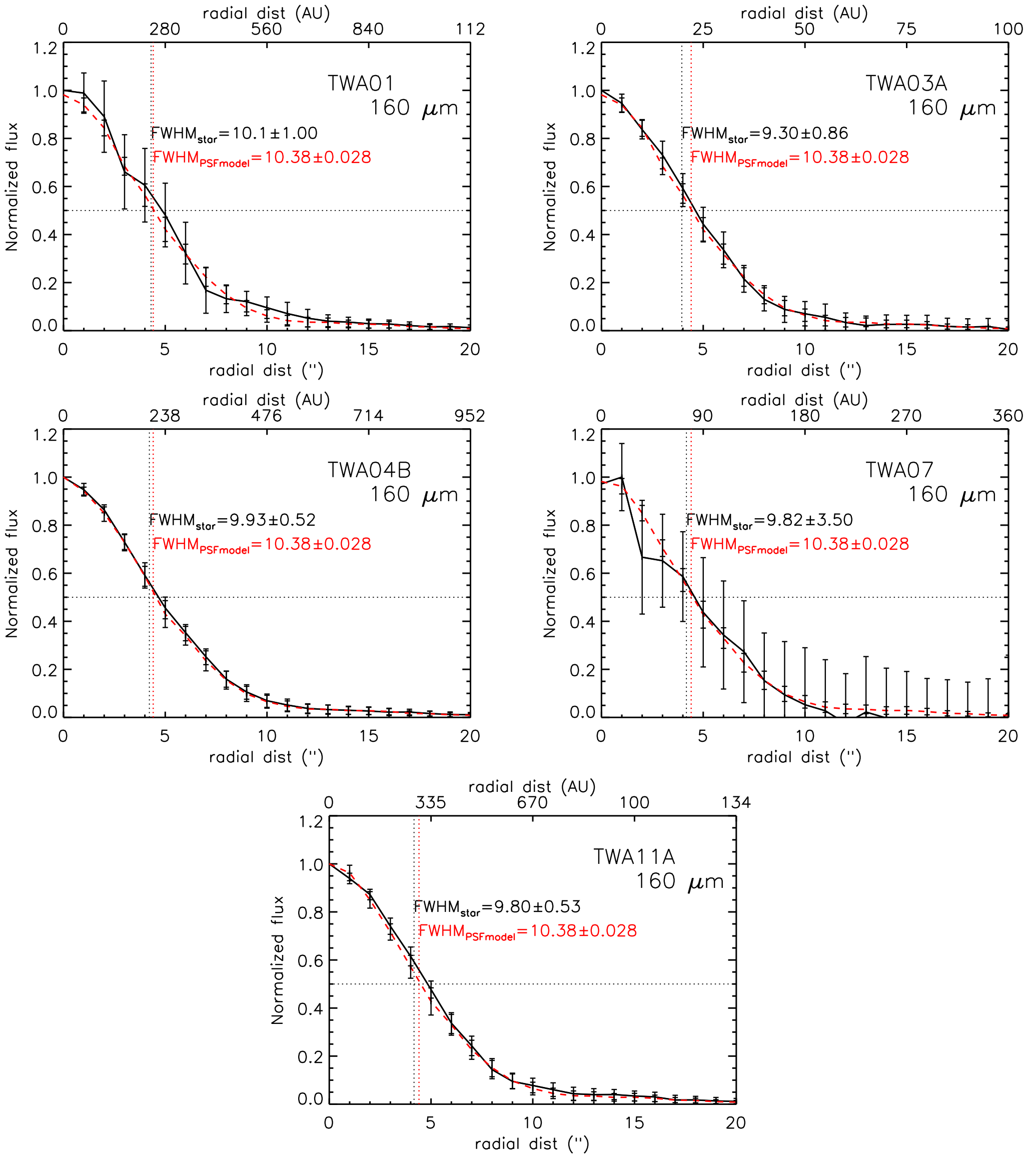

Figure A.3: Azimuthally averaged radial profiles at 160 μm for TWA members detected with PACS

Chapter 4

Gas and dust in the Beta Pictoris Moving Group

4.1 The Beta Pictoris Moving Group: a general overview

In this chapter we present *Herschel*-PACS observations of the Beta Pictoris Moving Group (BPMG), a ~12 Myr (Barrado y Navascués et al., 1999) association with a typical distance of ~ 30 pc that makes it one of the best locations for the study of debris discs. The star that names the group, β Pictoris, is an A5V star that harbours one of the most studied debris discs and shares its space motion with more than 30 coeval stars that constitute the BPMG (Torres et al., 2006, proposed a list of 43 candidates). 19 BPMG members were observed with PACS as part of the *Herschel* Open Time Key Programme GASPS (see Chapter 1). Photometry at 70/100 and 160 μm was obtained for the 19 stars, and 4 of them were also observed in Specral Line mode. We compared their SEDs with modified blackbody models and a grid of MCFOST (Pinte et al., 2006, 2009) SED models to derive their disc properties.

In Sec. 4.2 we describe the sample of BPMG members observed with PACS. In Sec. 4.3 we describe the observations and the data reduction technics, both for photometry and spectroscopy. In Sec. 4.4 we present our main photometric and spectroscopic results. Blackbody models and MCFOST models and results are shown in 4.5. In 4.6 we discuss the main results from the paper in the frame of the BPMG and debris discs in general.

4.2 The sample

BPMG members studied in the present work, together with their distances, spectral types, effective temperatures and luminosities, are shown in Table 4.1. Star distances are taken from Zuckerman & Song (2004b), and are in the range from 10.7 to 50.6 pc, while spectral types, in the range A0 to M5, come from Torres et al. (2006). Effective temperatures and stellar luminosities are those computed in section 4.2.1.

Table 4.1: Stellar parameters

name	d	Sp. Type	T_{eff}	L_*
	(pc)		(K)	L_{sun}
AT Mic	10.7	M4V	3100	0.066
CD64-1208	29.2	K5V	4200	0.25
GJ 3305	29.8	M1V	3600	0.166
HD 203	39.1	F3V	6600	3.7
HD 29391	29.8	F0V	8200	6.3
HD 35850	26.8	F7V	6000	1.26
HD 45081	38.5	K4V	4200	0.329
HD 139084	39.8	M5V	5000	1.23
HD 146624	43.1	A0V[1]	9750	22
HD 164249	46.9	F6V	6600	2.7
HD 172555	29.2	A7V	7800	7.8
HD 174429	49.7	G9IV	5200	0.85
HD 181296	47.7	A0V	10000	23.1
HD 181327	50.6	F6V	6600	3.2
HD 199143	47.7	F7V	6000	1.93
HIP 10679	34.0	G2V	5800	0.87
HIP 10680	39.4	F5V	6200	2.4
HIP 11437	42.3	K6V	4200	0.242
HIP 12545	40.5	K6V	4000	0.238

Notes. All spectral types are taken from Torres et al. (2006) except for HD 146624 (from Rebull et al., 2008) and HD 172555 (from Gray et al., 2006). $T_{\rm eff}$ and L_* from VOSA analysis.

Archival photometry data was collected for each BPMG member in the sample, including Johnson, Stromgren, 2MASS, IRAC, WISE, AKARI, MIPS (from Rebull et al., 2008), and sub-millimeter observations from Simba, LABOCA (from Nilsson et al., 2009, 2010) and the Sub-Millimeter Array (SMA).

We also included *Spitzer*-IRS data in the analysis, by collapsing the spectra taken from the archive to photometric points 1 μm wide, including a 5% calibration uncertainty in the errors (see Chen et al., 2006). The different orders were scaled to be consistent with the photospheric fluxes at short wavelengths when possible. The inclusion of IRS spectra is of main interest, given that the rise of the excess is seen at mid-IR wavelengths in BPMG members. Given the lack of agreement between IRS data and WISE fluxes, we decided to exclude WISE data from the model analysis in Sec. 4.5.

PACS photometry was acquired for 19 BPMG stars in 17 pointings (CD-64 1208/HD 172555 and HIP 10679/HIP 10680 are contained in a single observations each). PACS line spectroscopy was acquired for four of them.

Table 4.2: IRS AORs and program IDs for BPMG members

name	IRS AOR	Program ID
GJ 3305	14982144	20691
HD 203	14983424	20691
HD 35850	5252096	148
HD 45081	5222400	148
HD 139084	5223168	148
HD 146624	21809408	40651
HD 164249	21810432	40651
HD 172555	3563264	2
HD 174429	14983680	20691
HD 181296	3563776	2
HD 181327	3564032	2
HD 199143	5254400	148
HIP 11437	14983168	20691

Notes. Program names per ID are: ID 20691, Coeval Cluster (P. I.: J. Bowman); ID 148, Rubble (P. I.: M. R. Meyer); ID 40651, Debris II (P. I.: J. R. Houck); ID 2, IRS discs (P. I.: J. R. Houck)

4.2.1 Stellar parameters

A first step before modeling the entire SED is to know what photospheric models are able to describe the stellar emission. For each BPMG member in the sample we selected photometric points with a pure photospheric origin (typically Johnson, Stromgren and 2MASS photometry) and used them to compare the non-excess SED with theoretical models using the Virtual Observatory SED Analyzer (VOSA, Bayo et al., 2008). We used the grid of Phoenix models by Hauschildt et al. (1999), as we did for TWA members in Chapter 3. The values for T_{eff} and L_* coming from the best fit are summarised in Table 4.1. In Fig. 4.1, we plot the Hertzsprung-Russell diagram for the stars in the sample.

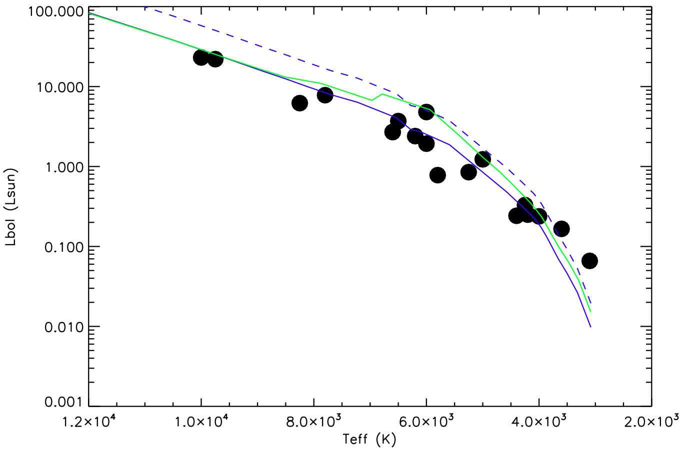

Figure 4.1: Hertzsprung-Russell diagram for BPMG members in the sample. The blue solid line represents the 12 Myr isochrone, the green solid one represents the 20 Myr isochrone, the blue dashed one represents 12 Myr isocrhone with 2 times larger luminosity to include not resolved binary systems. Red dots are objects detected by PACS while black dots are objects not detected by PACS. Plus symbols are BPMG members not observed by Herschel.

4.3 Observations and data reduction

The BPMG sample was observed with PACS as part of the GASPS Open Time Key programme. 19 BPMG members were observed in photometric mode with 16 pointings and a subset of four BPMG members were observed in spectral line mode also.

4.3.1 Photometric data reduction

We observed 16 objects at 70 μm, and another 15 at 100 μm, making a total of 19 observations in the 160 μm band. Observation ID's are listed in Table 4.3. The exposure times range from 133 to 1122 s, based on the expected flux from the star. Each scan map was made with medium speed (20arcsecs^{-1}), with scan legs of 3 arcmin and cross scan length of 4-5 arcsec. We note that the 70/160 μm observation of HD 181327 is not an scan map, but a pointed/chopped observation.

Table 4.3: BPMG PACS photometry observation log

Name	Obs. ID	Band
AT Mic	1342196104, 1342209488, 1342209489	70/160, 70/160, 70/160
CD-64 1208	1342209059, 1342209060, 1342209061, 1342209062	70/160, 70/160, 100/160, 100/160
HD 203	1342188366	70/160, 100/160, 100/160
HD 29391	1342190967, 1342216153, 1342216154	70/160, 100/160, 100/160
HD 45081	1342188506, 1342212832, 1342212833	70/160, 70/160, 70/160
HD 146624	1342215617, 1342215618, 1342215619, 1342215620	70/160, 70/160, 100/160, 100/160
HD 164249	1342215574, 1342215575	100/160, 100/160
HD 174429	1342215576, 1342215577, 1342215578, 1342215579	70/160, 70/160, 100/160, 100/160
HD 181296	1342209055, 1342209056	70/160, 100/160
HD 181327	1342209057, 1342183658	70/160, 100/160
HD 199143	1342193550, 1342208861, 1342208862	70/160, 70/160, 70/160
HIP 10679	1342189193, 1342223862, 1342223862	70/160, 100/160, 100/160
HIP 11437	1342189210, 1342223864, 1342223865	70/160, 100/160, 100/160
HIP 12545	1342189150, 1342223574, 1342223575	70/160, 70/160, 70/160

We reduced the scan map photometric observations using HIPE 8 and the most recent version of the calibration files. For bright IR-excess targets (i. e., those with flux greater than ~ 100 mJy) we used a version of the pipeline tuned for bright objects, while for faint objects and non-detected objects we used a different version optimised for noise dominated maps (see Chapter 3 for a detailed discussion of the differences and similarities between both versions). Photometric maps were projected into the final image with pixel scale 2 arcsec/pixel in the 70 and 100 μm bands and with pixel scale 3 arcsec/pixel in the 160 μm. We also produced final maps with the native pixel scale of the detector that were used to perform the error calculation (3.2 arcsec/pixel for the 70/100 μm bands and 6.4 for the 160 μm band). We combined images at the same wavelength to improve the SNR, averaging for each pixel and excluding bad pixels with an average sigma clipping algorithm. The pointed/chopped observation of HD 181327 was reduced using a different pipeline tuned for this kind of observing strategy.

Aperture photometry was measured using an aperture of 6 arcsec for the 70 and 100 μm bands and 12 arcsec for the 160 μm band. The annulus for sky subtraction was placed at 25-35 arcsec from the star. We then applied the proper aperture correction for each band[1]. Final fluxes are listed in Table 4.5. Noise errors consist of the standard deviation of the photometry obtained at several sky positions surrounding the target. PACS calibration errors are 2.64/2.75/4.15 % for the 70/100/160 μm bands respectively[2]. Noise errors and calibration errors were added quadratically.

For non-detected sources, we derived upper limits in the same way as we did for TWA members (see Chapter 3). The upper limits included in Table 4.5 are 3-σ.

Table 4.4: BPMG Spectroscopy Observation log

Name	Obs. ID
HD 164249	1342215648
HD 172555	1342215649
HD 172555	1342228417
HD 181296	1342209730
HD 181327	1342186311

---

[1] http://herschel.esac.esa.int/twiki/pub/Public/PacsCalibrationWeb/

[2] PICC-ME-TN-037

4.3.2 Spectroscopic data reduction

Four BPMG members were observed with PACS in LineScan spectroscopic mode. The line of interest in the LineScan observations was [OI] at 63.18 μm. Riviere-Marichalar et al. (2012b) reported the detection of o-H_2O emission at 63.32 μm in the PACS spectra of 8 T Tauri stars in Taurus, therefore we also searched for line emission at this wavelength. DCO^+ can be observed at 189.57 μm in the red band, but our focus was on the blue band, as we did not expected DCO^+ emission from debris discs. PACS spectra were reduced using HIPE 9 with the latest version of the pipeline and the proper calibration files (see Chapter 3 for an overview of the main reduction steps). Spectra were extracted from the central spaxel and aperture corrected to account for flux spread in the surrounding spaxels. The line spectra from PACS typically show higher SNR near the spectrum edges, that are excluded from the spectra in order to calculate accurate line fluxes.

Line fluxes were computed by applying a Gaussian fit to the line profile and calculating the integrated flux from that fit. Upper limits were computed by integrating a Gaussian with a width equal to the instrumental FWHM at the central wavelength, and maximum equal to three times the standard deviation of the continuum. Therefore, computed upper limits are 3-σ. Line fluxes are shown in Table 4.6

4.4 Results

4.4.1 Heschel-PACS photometry

Photometry results are shown in Tab. 4.5. Following Bryden et al. (2006), we used the parameters χ_{70}, χ_{100} and χ_{160} to identify excess sources, defined as:

$$\chi_{\rm band} = \frac{{\rm F}_{\rm obs,band} - {\rm F}_{*,\rm band}}{\sigma_{\rm band}} \tag{4.1}$$

where $\mathrm{F}_{\rm obs,band}$ is the observed flux at any of the 70, 100 or 160 μm bands, $\mathrm{F}_{*,\rm band}$ is the expected photospheric flux at the corresponding wavelength and $\sigma_{\rm band}$ is the corresponding error. We consider excess sources at each band those sources with $\chi_{\rm band} > 3$.

We detected 8 objects at 70 μm out of 15 observed, but two of them, namely AT Mic and HD 146624, showed fluxes in agreement with photospheric emission

Table 4.5: HSO photometry

name	Flux(70 μm)	Flux(100 μm)	Flux(160 μm)
	(mJy)	(mJy)	(mJy)
HD 203	68 ± 3	26 ± 2	< 14
HD 164249	–	493 ± 20	249 ± 10
HD 172555	191 ± 7	79 ± 4	31 ± 2
HD 181296	–	250 ± 8	111 ± 6
HD 181327	1453 ± 6	1400 ± 40	850 ± 40
HD 29391	22 ± 2	< 10	< 16
HD 35850	–	42 ± 2	18 ± 4
HIP 10679	53 ± 3	46 ± 2	39
HIP 11437	70 ± 4	69 ± 3	50 ± 4
AT Mic	13 ± 2	–	< 14
HD 146624	13 ± 2	< 7	< 13
CD64-1208	< 8	< 9	< 8
GJ 3305	< 4	< 4	< 8
HD 139084	< 7	< 10	< 29
HD 174429	< 7	< 7	< 13
HD 199143	< 5	–	< 11
HD 45081	< 3	–	< 8.2
HIP 10680	no det. corregir	–	< 21
HIP 12545	< 4	–	< 19

Notes. The first horizontal line separates objects with an observed IR-excess from objects without an observed IR excess. The second horizontal line separates objects with/without a photospheric PACS detection.

($\chi_{70} \simeq -1.3$ and 0.1 respectively). HD 29391 shows a flux of 22 ± 2 mJy at 70 μm, while the expected, photospheric flux is $\sim$ 13 mJy. The difference between the expected and the observed flux is more than 3-σ ($\chi_{70} \simeq 4.5$), and therefore, we consider HD 29391 as an excess source, although it is not detected in any other band. No photospheric flux was detected at 100/160 μm. The excess detection fraction at 70 μm is therefore 0.53. We detected 8 out of 14 systems observed at 100 μm (0.57 excess detection fraction) and 7 out of 18 observed at 160 μm (excess 0.39 detection fraction).

In Fig. 4.2 we show a comparison of *Herschel*-PACS photometry at 70 and 160 μm versus *Spitzer*-MIPS photometry from Rebull et al. (2008).The agreement is generally good. In Rebull et al. (2008) HD 146624 was not detected; instead they

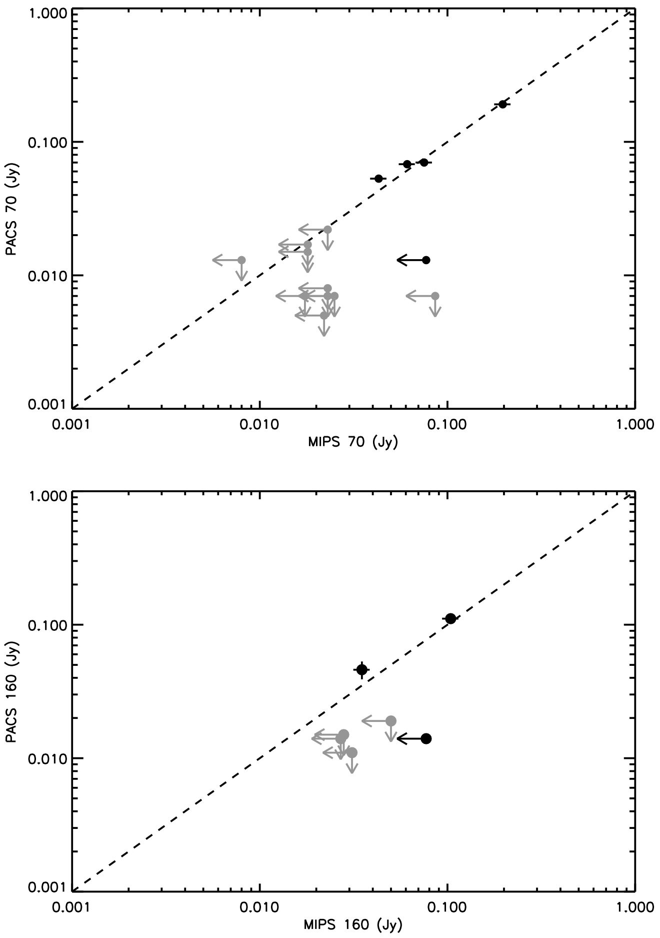

Figure 4.2: Top: Comparison plot for PACS 70 μm fluxes vs MIPS 70 μm fluxes and upper limits. The black dashed line represents the one to one relation. Bottom: comparison for PACS 160 μm versus MIPS 160 μm.

computed an upper limit of 77 mJy; we have detected HD 146624 with a flux of 13 mJy, only 1.02 times the photospheric value. We show in Fig. 4.3 SEDs for BPMG members with no far-IR excess. Rebull et al. (2008) considered HD 174429 as an excess source at 70 μm with a flux of 17.4 mJy, compared to the photospheric flux of 2.5 mJy. We did not detected it in our PACS observations, and instead computed an upper limit of 7 mJy, less than three times the photospheric value. We visually inspected MIPS images of HD 174429 at 70 μm and we did not saw any source emission at the nominal position of the star, therefore we conclude that the MIPS IR excess is not real.

In Fig. 4.4 we show the ratio of the observed fluxes to the photospheric fluxes at 70/100/160 μm versus the effective temperature of the central star. Objects not

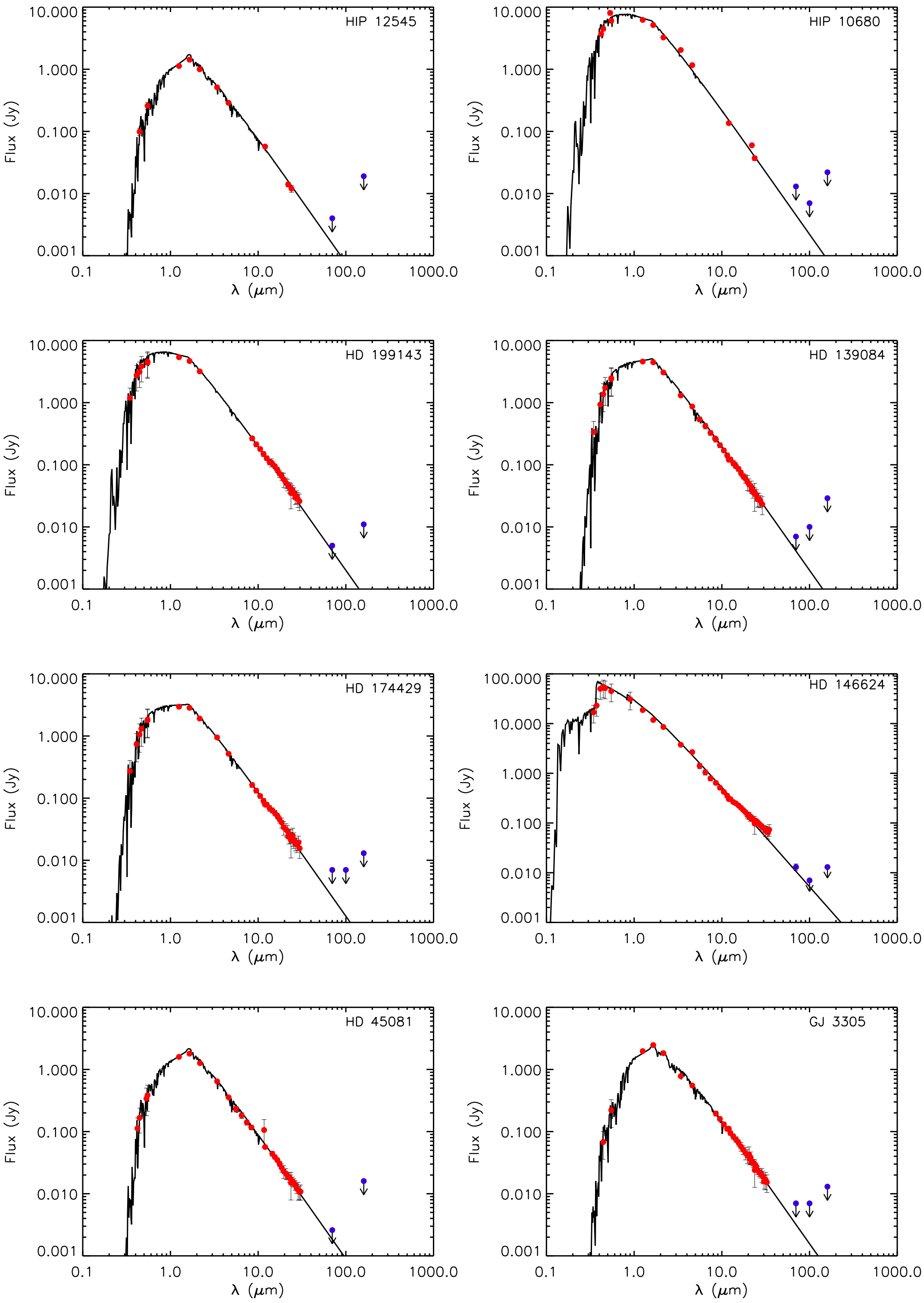

Figure 4.3: SEDs for BPMG members not detected by PACS. The black solid lines are the photosphere models from Sec. 4.2.1. Blue dots are PACS detections from the present study.

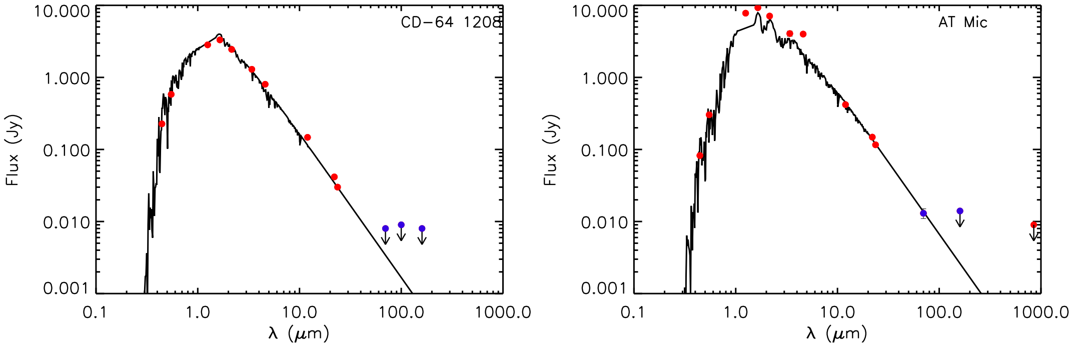

Figure 4.3: SEDs for BPMG members not detected by PACS. The black solid lines are the photosphere models from Sec. 4.2.1. Blue dots are PACS detections from the present study.

detected at 70 μm show upper limits that are 1.0 to 10 times larger than the expected photospheric value. Upper limits at 100 μm also range from 1.0 to 10 times the photospheric value. Therefore, it seems that those objects do not emit in excess at 70 and 100 μm at all. Upper limits at 160 μm are 10 to 100 times larger than the photospheric value. We can not exclude the presence of very cold, faint discs for some of these objects that are not detected at 160 μm. We find no correlation between the strength of the IR excess at any of the PACS bands and the temperature of the central object.

In order to study whether we have spatially resolved the sources, we performed azimuthally averaged radial profiles in all the three PACS bands for every detected object and compared the results with the azimuthally averaged radial profile of the model PSF star αBoo. The resulting radial profiles are shown in Appendix B.2. Only HD 181327 seems to be extended in the 100 μm band. The resultant profile for HD 181327 is shown in Fig. 4.5. Because we did not have a model PSF for pointed/chopped observations, we did not performed the radial profile at 70 μm for HD 181327.

4.4.2 Herschel-PACS spectroscopy

Among the four BPMG members observed with PACS in LineScan mode, we detected the continuum level at 63 μm for three of them (namely, HD 172555, HD 181296 and HD 181327). We did not detect the continuum level for none of them at 189 μm. Continuum subtracted spectra at 63 μm for objects with no line detections are shown in Fig. 4.6

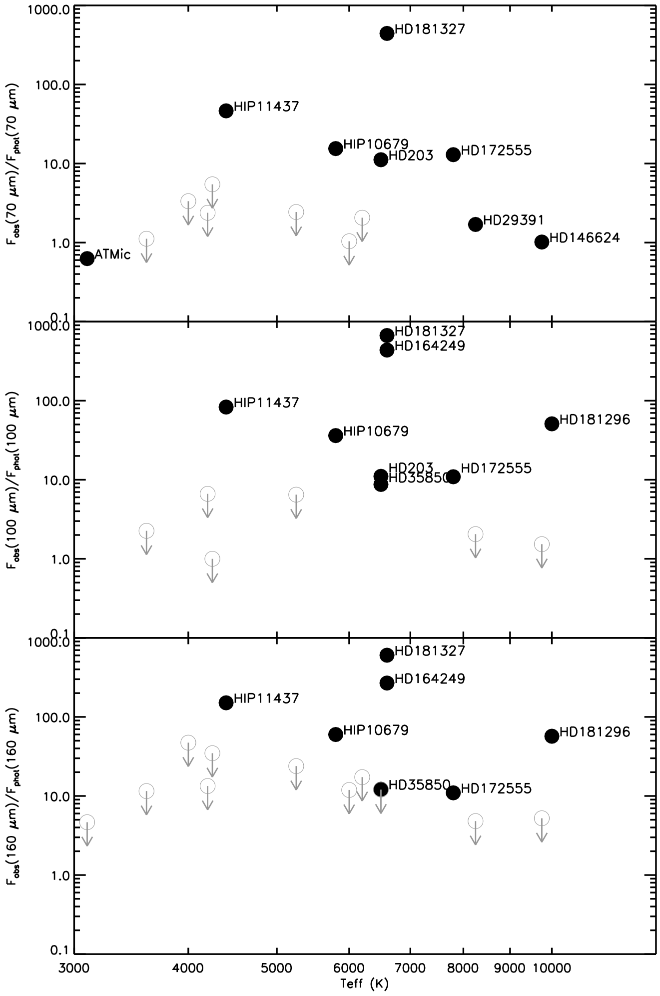

Figure 4.4: Excess for the 70/100/160 μm band versus T_{eff}. Filled dots represent true detections, while empty circles with arrows represent upper limits

We detected [OI] emission towards HD 172555 (SNR $\sim$ 3.0) in the first observation (OBSID 1342215649), and therefore we requested a second LineScan observation (OBSID 1342228417, SNR = 3.7) that confirmed the detection of atomic oxygen in HD 172555. The presence of atomic oxygen will be discussed in Chapter 5 (see also Riviere-Marichalar et al., 2012b), although we will review the main results in Section 4.5.3. Because the combination of individual spectra did not resulted in the expected increase in the SNR, and instead produced an artificial broadening of the line profile, we decided to re-center both individual spectra with respect to the rest frame wavelength of the [OI] line, as we did in Chapter 4 for TWA 04B. Both individual and averaged spectra are shown in Fig. 4.8. None of the systems do show water emission at 63.32 μm nor DCO$^+$ emission in the red band.

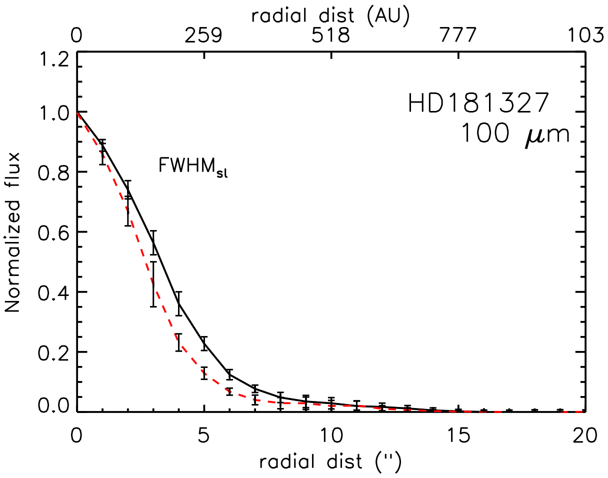

Figure 4.5: Azimuthally averaged radial profile for HD 181327 at 100 μm. The red dashed line represents the azimuthally averaged radial profile for the model PSF star τ Boo

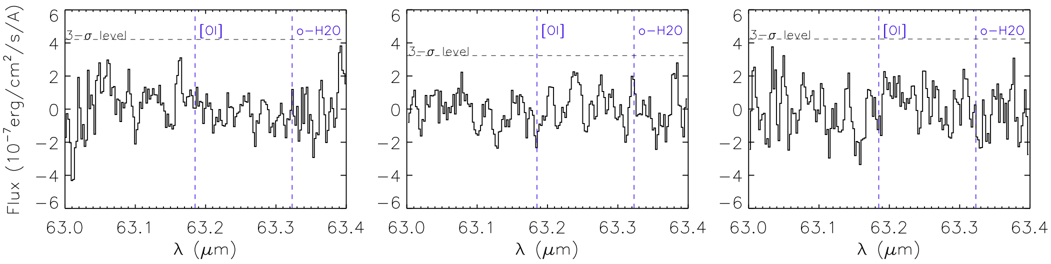

Figure 4.6: Continuum subtracted spectra of BPMG members showing IR excess but no line emission at 63 μm. The vertical blue dashed lines represent the position of the [OI] and o-H_2O emission lines central wavelengths (λ_0). From left to right, targets are: HD 164249, HD 181296 and HD 181327. We show 3-σ limits as horizontal, black dashed lines.

After the detection of atomic oxygen toward HD 172555, we requested a PACS range scan observation at 158 μm (OBSID 1342228416), where [CII] at 157.75 μm and p-H_2O at 158.312 μm transitions are present, aiming to detect [CII] emission from the disc (see Chapter 1.3). None of them was detected in HD 172555, and instead we derived an upper limit of 5.3×10^{-18} W/m^2 for both lines. Together with the 158 μm we observed the source at 79 μm, where $o - H_2O$, $p - H_2O$, OH and CO transition lines are present at 78.742, 78.928m 79.115/79.178 and 79.36 μm respectively. No molecular emission was detected toward the source, and instead we compute an upper limit of 1.9×10^{-18} W/m^2 for the line fluxes.

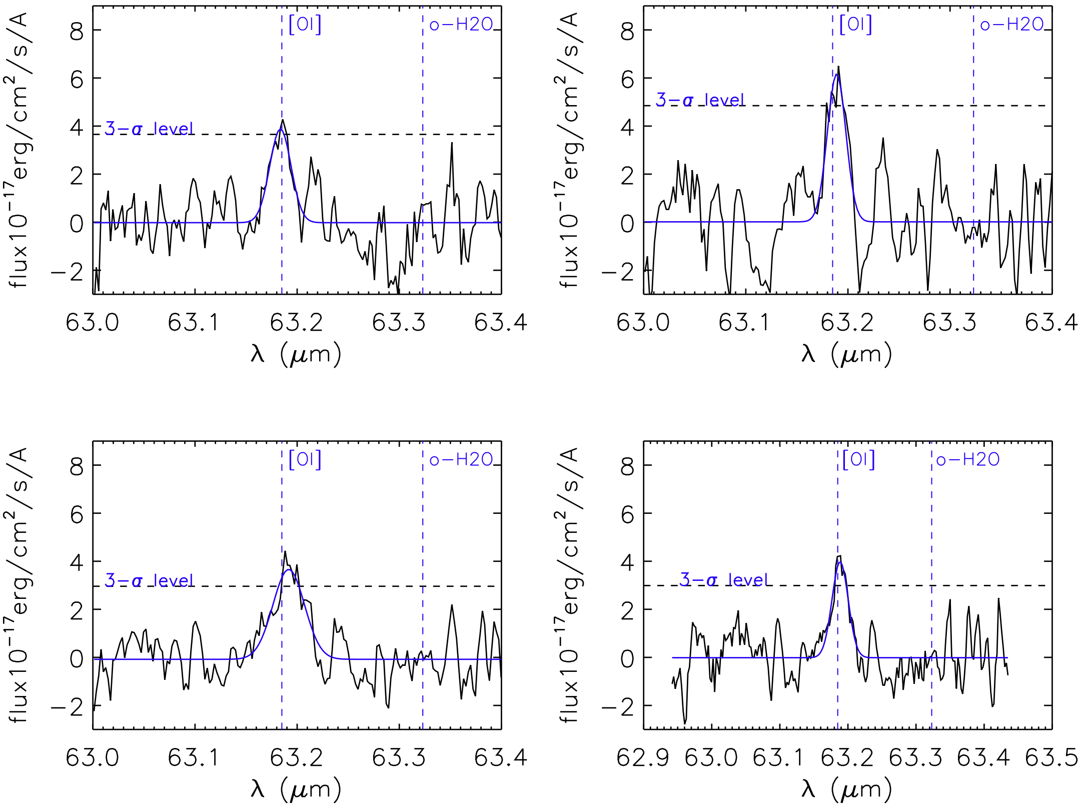

Figure 4.7: Continuum subtracted spectra of HD 172555. Top: individual observations, left side AOR is 1342215649, and right side AOR is: 1342228417. The vertical blue dashed lines represent the position of the [OI] and o-H_2O emission lines central wavelengths (λ_0). We show 3-σ limits as horizontal, black dashed lines. Bottom left: averaged spectrum. Bottom right: averaged spectrum after re-centering the individual spectra with respect to the [OI] rest frame wavelength (63.185 μm). The blue curves represent the Gaussian fit.

4.5 Models of dust discs

For every BPMG member in the sample, we have built the SED including the new PACS photometric data (see examples with IR excess in Fig. 4.9), with the aim of comparing the observed photometry with synthetic models to get insight in the BPMG disc properties. We have proceed with two types of modeling: simple blackbody models and more sophisticated MCFOST models. Details follow.

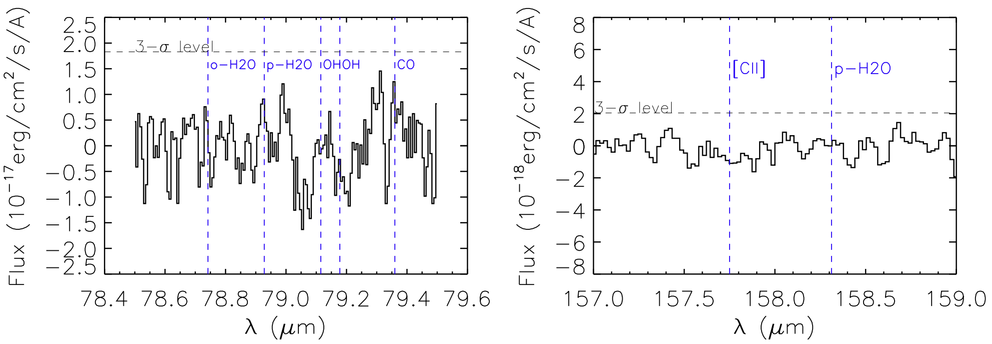

Figure 4.8: Continuum subtracted spectra of HD 172555 around 79 μm (left side) and 158 μm (right side). The blue, dashed lines mark the position of the different transition lines present in the spectra. The black dashed line represent the 3-σ detection limits.

Table 4.6: HSO spectroscopy

name	$[OI]_{63.18\mu m}$ line flux	$o-H_2O_{63.32\mu m}$ line flux	Continuum $SNR_{63\mu m}$	DCO$^+$ line flux	Continuum $SNR_{189\mu m}$
–	(10^{-18}W/m^2)	(10^{-18}W/m^2)	–	(10^{-18}W/m^2)	–
HD 164249	< 5.8	< 5.8	2.4	< 3.1	0.11
HD 172555[1]	7.2 ± 2.2	< 5.0	41.8	< 11.0	0.006
HD 172555[2]	9.9 ± 2.6	< 6.7	46.3	< 6.2	0.5
HD 172555[3]	10.2 ± 2.7	< 4.1	56.9	< 4.9	0.3
HD 172555[4]	8.4 ± 2.1	< 4.1	56.9	–	–
HD 181296	< 4.4	< 4.4	3.5	< 7.0	0.29
HD 181327	< 5.8	< 5.8	10.7	< 13.0	1.2

Notes. (1): OBSID 1342215649. (2): OBSID 1342228417. (3): Averaged spectrum. (4): average spectrum after re-centering. The line fluxes for HD 172555 differ from those shown in Chapter 5 because we recomputed them after reducing the spectra with HIPE version 9, instead of version 7.

4.5.1 Blackbody models

A first approach to disc properties in BPMG members consists on fitting blackbody models to the dust emission. In a more general way, we have compared the whole observed SED with photosphere plus blackbody models. The photosphere models are described by the stellar parameters listed in Table 4.1, while the modified blackbody is described following Equation 3.1. We remind that $\lambda_0 = 2\pi a_{blow}$ and $\beta = 0$ if $\lambda < \lambda_0$, where a_{blow} is the size of the minimum dust grain that can survive in a debris disc due to radiation pressure and is defined by Equation 3.3, with

$\rho = 2.5$ g/cm^3, valid for astrosillicates. Computed blow out sizes for the BPMG members with an IR excess are given in Table 4.7.

Table 4.7: Blow out sizes for BPMG members with PACS IR excesses, as derived from Equation 3.3.

Name	$a_{\rm blow}$
–	(μm)
HD 164249	0.9
HD 181296	4.8
HD 203	1.2
HD 35850	0.7
HIP 10679	0.3
HIP 11437	0.1
HD 172555	2.1
HD 181327	1.0

Such simple models are a good starting point for the modelling effort that provide estimates about the dust temperature and IR excess. The value of β for the modified blackbody model is a free parameter, as well as the dust temperature. The best model was determined through χ^2 minimisation (see Equation 3.4). Following Donaldson et al. (2012), we evaluated the goodness of the fit using the parameter Q, that measures the probability that a given value of χ^2 occurs by chance. Q is described as:

$$Q(a,x) = \frac{\int_x^\infty e^{-t} t^{a-1}\,\mathrm{d}t}{\int_0^\infty e^{-t} t^{a-1}\,\mathrm{d}t} = 1 - \frac{\int_0^x e^{-t} t^{a-1}\,\mathrm{d}t}{\int_0^\infty e^{-t} t^{a-1}\,\mathrm{d}t} = 1 - P(a,x) \tag{4.2}$$

where P(a,x) is the incomplete gamma function, with a $= \frac{\nu}{2}$ and x $= \frac{\chi^2}{2}$. Higher Q values indicate better quality fits. According to Press et al. (1992), acceptable Q values are those > 0.001.

Blackbody temperatures range from 71 to 278 K, and we highlight the presence of two warm debris discs in the sample, namely, HD 172555 and HD 181296. The average dust temperatures is $\sim$ 109 K. For some targets (HD 181296, HIP 10679) a single blackbody fit clearly fails to reproduce the SED, probably due to the presence of a second disc or a more complex geometry.

For the sources not detected in excess we computed upper limits on the infrared excess luminosity by considering them as true detections and comparing their fluxes with blackbody models. Results of the fitting process are listed in Table 4.8, and model SEDs can be found in Fig. 4.9.

Table 4.8: Black body models

Name	T	β	L_{IR}/L_*	Q
–	K	–	–	
HD 164249	68 ± 9	$0.2^{+0.6}_{-0.2}$	8.8×10^{-4}	0.041
HD 181296	160 ± 12	0.0	2.5×10^{-4}	0.0
HD 203	87 ± 20	1.5 ± 0.5	1.4×10^{-4}	0.68
HD 35850	71 ± 19	$0.2^{+0.8}_{-0.2}$	3.8×10^{-5}	0.99
HIP 10679	95 ± 15	0.0	2.5×10^{-4}	~ 0
HIP 11437	68 ± 11	0.0	1.3×10^{-3}	0.99
HD 172555	278 ± 21	0.2	7.5×10^{-4}	0.16
HD 181327	78 ± 2	0.0	2.8×10^{-3}	1.9×10^{-7}
HD 29391	101 ± 16	1.2 ± 0.5	$< 4.6 \times 10^{-6}$	–
AT Mic	19	–	$< 2.7 \times 10^{-5}$	–
CD 64-1208	40	–	$< 3.9 \times 10^{-5}$	–
GJ 3305	45	–	$< 4.5 \times 10^{-5}$	–
HD 45081	20	–	$< 4.8 \times 10^{-5}$	–
HD 139084	28	–	$< 1.6 \times 10^{-5}$	–
HD 146624	18	–	$< 9.8 \times 10^{-7}$	–
HD 174429	48	–	$< 1.8 \times 10^{-5}$	–
HD 199143	26	–	$< 8.5 \times 10^{-6}$	–
HIP 10680	66	–	$< 6.9 \times 10^{-6}$	–
HIP 125450	31	–	$< 1.4 \times 10^{-4}$	–

Notes. The number in brackets is the fitted value for β. The first horizontal line separates objects with IR excess detections in many wavelengths from HD 29391, with only one IR excess detection at 70μm with PACS. The second line separates HD 29391 from objects with no detections.

4.5.2 MCFOST models

Aiming to better understand the properties of the circumstellar systems in the BPMG, we moved to a more sophisticated analysis and used MCFOST (Pinte et al., 2006, 2009) to produce a grid of models to compare with our observations through χ^2 minimisation. MCFOST is a 3D Monte Carlo based radiative transfer code that includes multiple scattering with a complete treatment of polarization. The code assumes passive dust heating in radiative equilibrium with continuum thermal re-emission.

The vertical structure is parametrized with an axisymmetric Gaussian density

Table 4.9: MCFOST input model parameters

Fixed parameters				
Parameter	Value			
R_{out} (AU)	250			
h_0 (AU)	10			
β	1.1			
a_{min} (μm)	0.1/a_{blow}			
a_{max} (μm)	1000			
p	-3.5			
Free parameters				
Parameter	Min.	Max.	# bins	sampling
α	-1.5	-0.5	3	linear
R_{in}(AU)	0.1	30	32	linear
$M_{dust}(M_{sun})$	1.0×10^{-9}	1.0×10^{-5}	38	logarithmic

profile, in the form

$$\rho(r, z) = \rho(r)e^{-z^2/2h(r)^2}, \tag{4.3}$$

with a scale height described as

$$h(r) = h_0(r/r_0)^{\gamma}. \tag{4.4}$$

Because we can not constraint γ and h_0 for optically thin discs by pure SED fitting, we fixed both values to standard values, $h_0 = 10$AU and $\gamma = 1.1$. The surface density is described by a power law,

$$\Sigma(r) = \Sigma_0(r/r_0)^{\alpha}, \tag{4.5}$$

with $r_0 = 100AU$. The exponent of the power law, α, can take the values -0.5, -1.0 and -1.5. The disc extends from the inner radius R_{in} to the outer radius R_{out}. We let R_{in} vary from 0.1 to 30 AU, in 32 bins with steps of 1 AU, except for the first two bins (0.1 and 0.5 AU respectively). R_{out} is fixed to take the value of 250 AU.

The grain composition is a mixture of astro-silicates, with optical properties taken from Draine & Lee (1984). Dust grains are treated as homogeneous spherical particles (Mie theory). The dust grain size distribution follows a power-law $dn(a) \propto a^p da$, with minimum and maximum sizes a_{min} and a_{max}. For each system, a_{min} can be 0.1 μm or equal to the blowout size. We fix a_{max} to 1000 μm, as circumstellar discs in BPMG are expected to be in the debris phase, where grains larger than 1 mm are expected to be present from the collisional grinding of planetesimals. For the exponent of the size distribution, p, we use p $= -3.5$, the expected value for a steady-state collisional cascade (Dohnanyi, 1969).

We ignored viscous heating, as we did not expected active accretion at the age of BPMG ($\sim 12 - 20$Myr). In Table 4.9, we give an overview of all parameters. The stellar parameters are those from Table 4.1 and the central stars are represented by the corresponding Phoenix model (Hauschildt et al., 1999).

4.5.3 Targets with Far-IR excess

For the targets with detected IR excesses, we made a χ^2 comparison between observed and synthetic SEDs from the grid of models. We used χ^2 minimization to detect the best model that can fit the SED and to perform a Bayesian Analysis of the parameter space that allowed us to estimate the probability distribution for the parameters modeled within the grid. The Bayesian inference method is described in Press et al. (1992) and explained in detail in the Appendix in Lebreton et al. (2012). Examples about how it can be applied in astrophysics can be found in Lay et al. (1997) and Pinte et al. (2007, 2008). To compute the likelihood distribution for the parameters of the grid we did the following. First, a probability p_i was assigned to every model:

$$p_i = e^{-\chi_i^2/2} \tag{4.6}$$

With the probability $P(y_0)$ associated with a single parameter value:

$$P(y_0) = \sum_{i=1}^{N} p_i(y_0) \tag{4.7}$$

where the sum is performed over models with the same value y_0 for the parameter y. Finally we normalised the probability distribution to unity by dividing the obtained $P(y_0)$ by the total probability:

$$P^{'}(y_0) = \frac{P(y_0)}{\sum_{j=1}^{N} P(y_j)} \tag{4.8}$$

The results for the the best models from χ^2 minimisation are shown in Table 4.10, together with the expectance and variance values from the Bayesian Analysis. Inclination angles can not be constrained by means of SED fitting alone for optically thin discs. Therefore, we decided not to include them in the analysis. Considering that we only have one far-IR photometric detection for HD 29391, we decided not to model HD 29391 in detail with MCFOST, and instead rely on the more simple blackbody models. The results from MCFOST modeling are shown in Table 4.10. In the following we briefly discuss the model results for each object.

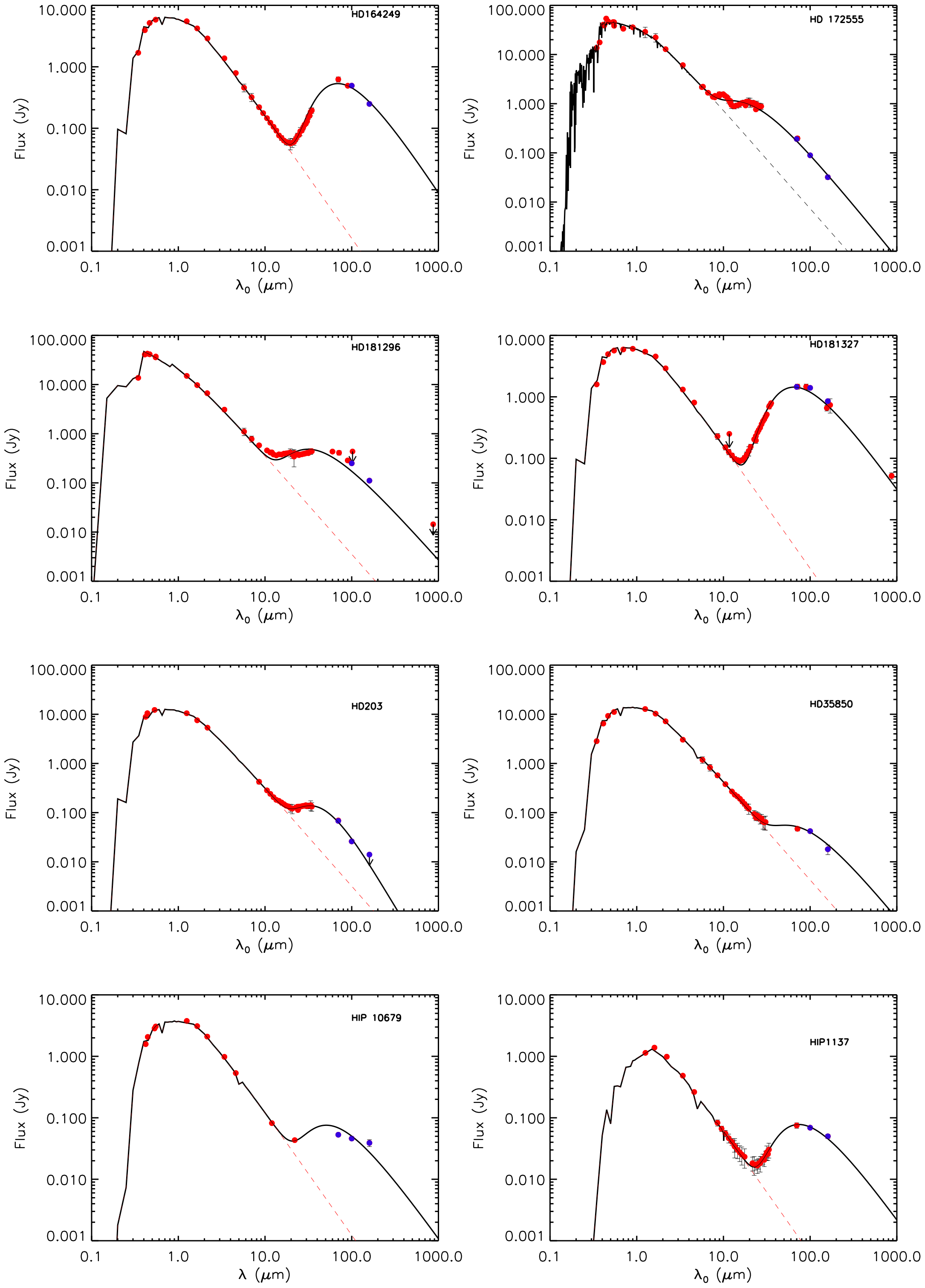

Figure 4.9: Blackbody models for BPMG members with IR excesses as derived with *Herschel*/PACS photometry. For HD 181296 and HIP 10679 we show the best two blackbodies model in black solid line, the best one blackbody model in dot-dashed violet line and the isolated blackbodies for the two blackbodies model in dashed blue.

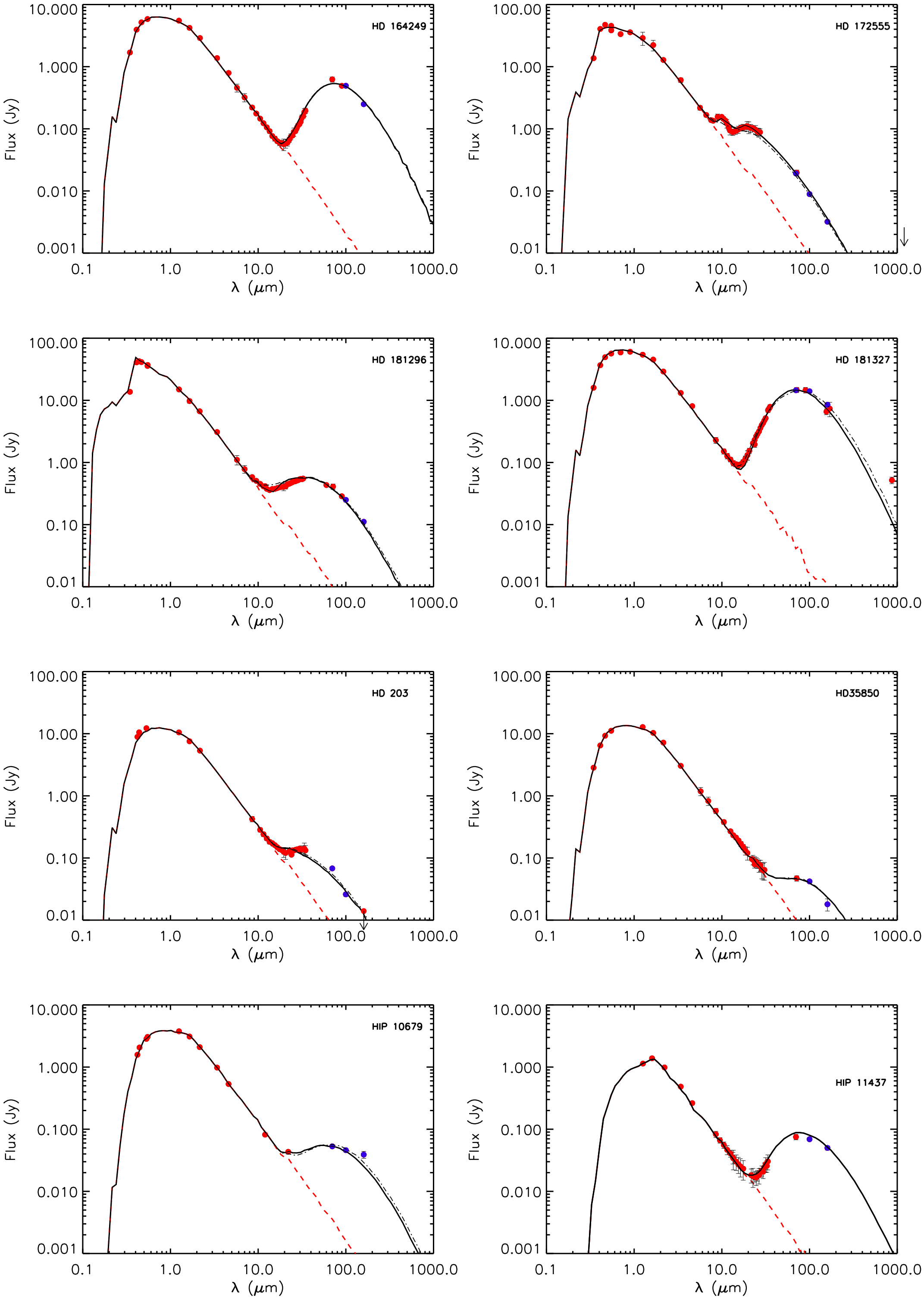

Figure 4.10: Blackbody models for BPMG members with IR excesses as derived with *Herschel*/PACS photometry. The red dashed line shows the pure photosphere model. The black continuum line depict the models with $a_{\rm min} = 0.1\ \mu$m. The dotted-dashed line depict the models with $a_{\rm min} = a_{\rm blow}$.

Table 4.10: Model results from coarse grid.

name	$M_{dust,0}$	$M_{dust,BA}$	$R_{in,0}$	$R_{in,BA}$	p_0	p_{BA}	Q
–	($M_\oplus$)	($M_\oplus$)	(AU)	(AU)	–	–	–
HD 164249[1]	2.9×10^{-2}	$(2.8 \pm 0.3) \times 10^{-2}$	34	34 ± 1	-1.0	-1.13 ± 0.22	0.29
HD 164249[2]	2.9×10^{-2}	$(3.0 \pm 0.2) \times 10^{-2}$	27	26.8 ± 0.7	-1.5	-1.47 ± 0.12	0.68
HD 181296[1]	4.0×10^{-3}	$(4.0 \pm 7 \times 10^{-4}) \times 10^{-3}$	9	8.7 ± 0.5	-0.5	$-0.50 \pm 6.0 \times 10^{-7}$	4.4×10^{-13}
HD 181296[2]	5.1×10^{-3}	$(5.1 \pm 7 \times 10^{-4}) \times 10^{-3}$	4	4.00 ± 0.01	-1.0	$-1.00 \pm 2 \times 10^{-8}$	2.0×10^{-8}
HD 203[1]	3.3×10^{-4}	$(4.3 \pm 0.1) \times 10^{-4}$	7	7.0 ± 0.2	-1.5	-1.50 ± 0.01	1.2×10^{-4}
HD 203[2]	4.3×10^{-4}	$(5.4 \pm 0.3) \times 10^{-4}$	4	4.9 ± 0.2	-1.5	-1.49 ± 0.01	0.003
HD 35850[1]	9.0×10^{-4}	$(9.5 \pm 1.7) \times 10^{-3}$	31	33.0 ± 4	-1.0	-0.98 ± 0.40	0.25
HD 35850[2]	9.0×10^{-4}	$(1.1 \pm 0.2) \times 10^{-4}$	28	29 ± 8	-1.5	-1.19 ± 0.35	0.21
HIP 10679[1]	1.9×10^{-3}	$(2.6 \pm 0.6) \times 10^{-3}$	9	7.6 ± 1.7	-1.0	-0.73 ± 0.28	3.7×10^{-10}
HIP 10679[2]	2.4×10^{-3}	$(2.2 \pm 0.6) \times 10^{-3}$	10	9.9 ± 1.5	-1.0	-1.10 ± 0.28	6.7×10^{-11}
HIP 11437[1,2]	8.5×10^{-3}	$(1.0 \pm 0.3) \times 10^{-2}$	11	10.7 ± 1.0	-1.5	-1.34 ± 0.23	0.99
HD 172555[1,3]	3.3×10^{-4}	$(3.33 \pm 0.4) \times 10^{-4}$	2	2.00 ± 0.2	-1.5	-1.5 ± 0.2	0.41
HD 172555[2]	3.3×10^{-4}	$(3.3 \pm 0.1) \times 10^{-4}$	1	1.00 ± 0.005	-1.5	-1.50 ± 0.005	1.5×10^{-8}
HD 181327[1]	8.0×10^{-2}	$(8.3 \pm 0.9) \times 10^{-2}$	31	30.3 ± 1.6	-1.0	-0.91 ± 0.19	1.0×10^{-8}
HD 181327[2]	0.131	0.131 ± 0.001	15	15.00 ± 0.06	-0.5	-0.50 ± 0.01	9.8×10^{-5}

Notes. Sub-index 0 refers to the value for the best model, while subindex BA refers to the expectance (with variance included) from Bayesian analysis. (1): models with $a_{min} = 0.1\ \mu$m. (2): models with $a_{min} = a_{blow}$. (3): the distribution of χ^2 values resulted in a bayesian distribution with a very narrow peak, resulting in non-realistic errors. We therefore give errors based on the size of the bins for each parameter. We separate with horizontal lines sets of models for the different BPMG members with IR excess detected with PACS.

HD 164249

HD 164249 is an F6V star 46.9 pc away. Rhee et al. (2007) modeled the disc emission with a blackbody model at 70 K, and derived an inner radius of 27 AU and a dust mass of $\sim 8.2 \times 10^{-2}$ $M_{\oplus}$. Rebull et al. (2008) and Nilsson et al. (2010) modeled the IR excess emission with a pure blackbody at 78 K. In our analysis, the SED is better reproduced with a modified black body with a small $\beta \sim 0.2$ and $T = 68 \pm 9$ K, in good agreement with previous results, given the uncertainties associated with dust opacity.

For HD 164249 we get fits of better quality using $a_{\rm min} = a_{\rm blow}$. The expected dust mass is $(3.0 \pm 0.2) \times 10^{-2}$ $M_{\oplus}$, $\sim$ 2.7 times smaller than the value proposed in Rhee et al. (2007), but we highlight that their study is based on IRAS data, that typically show larger values than PACS data due to the larger beam size that translates to contamination from background sources. The expected value for the inner radius is (26.8 ± 0.7) AU, in perfect agreement with the value of 27 AU by Rhee et al. (2007).

HD 181296

HD 181296 is a binary system that harbors a debris disc, composed of an A0 star (HD 181296A) plus an M7 brown dwarf (HD 181296B, Lowrance et al., 2000), with a separation of 4.6 arcsec (~ 216 AU at a distance of 47.7 pc). Therefore, the debris disc is circumstellar and not circumbinary, and is associated to the primary. IRAS IR excess emission in HD 181296 was studied by Rhee et al. (2007), who proposed an inner radius of 15 AU in a disc with a total dust mass of 5.2×10^{-3} $M_{\oplus}$. Through observations with T-Recs, Smith et al. (2009) resolved the mid-IR emission toward HD 181296, concluding that there are two populations of grains and that the disc extends to ~ 45 AU.

In Fig. 4.9 we can see that a single blackbody model can not reproduce the IR emission in HD 181296. The best BB model, with T = (153 ± 16) K and $\beta = 0.0$, produces a poor fit that underestimates the flux at far-IR wavelengths. The blowout size in HD 181296 is $\sim 4.8 \mu$m. The best MCFOST model with $a_{\rm min} = 0.1$ μm produces a very poor fit ($Q \sim 5.2 \times 10^{-9}$) that underestimates the IRS data in the near-IR, as can be seen in Fig. 4.10. It seems clear that no sub-micron sized grains have survived radiation pressure in the system. The total dust mass in models with $a_{\rm min} = 4.8$ μm is $(8.5. \pm 0.1) \times 10^{-2}$ $M_{\oplus}$, with an inner radius of $\sim$ 1 AU. But we must note here that the outer radius of 250 AU used in the coarse grid does not agree with the outer radius found by Smith et al. (2009). Models with R_{out} = 45 AU and the same range of values for the inner radius and dust mass also fail to reproduce the SED. Therefore we agree with Smith et al. (2009) that we need two different grain populations to reproduce the whole SED, or at least a more complex grain composition, different from astro-silicates.

HD 203

HD 203 is an F3V star 39.1 pc away. Rebull et al. (2008) modeled the SED with a disc with a dust mass of 3×10^{-3} $M_\oplus$

HD 203 is not detected at 160 μm. Therefore, when fitting both the modified blackbody model and the MCFOST models, we rejected models where the emission at 160 μm is larger than the 14 mJy upper limit. The best modified blackbody model shows T_{dust} = (87 ± 20) K and β = (1.5 ± 0.5) , with infrared excess $L_{IR}/L_* = 1.4 \times 10^{-4}$. Rebull et al. (2008) computed T_{dust} = 120 K for pure blackbody models with the same value for the infrared fractional luminosity that we get.

The upper limit at 160 μm help us to reject many parameter combinations. Models with $a_{min} = a_{blow}$ produce better quality fits, with an expected dust mass of $(5.4 \pm 0.3) \times 10^{-4}$ $M_\oplus$, and an expected inner radius of (7.0 ± 0.2)AU. Our dust mass is 5.7 times smaller than the value by Rebull et al. (2008), but we note that the PACS upper limit that we used is much more restrictive than the MIPS upper limit used by them (14 mJy compared to 27 mJy). We note that the way the far-IR emission plummets around 160 μm, and the large β in the modified blackbody model, suggest an overabundance of small grains when compared with other BPMG members.

HD 35850

HD 35850 is an F8V star at 26.8 pc. It was observed as part of the *Spitzer* Legacy Science Program FEPS (Hillenbrand et al., 2008), but the disc was not detected at 160 μm, therefore our measurement will help to better constrain the properties of this object.

For HD 35850, both the grid of models with $a_{min} = 0.1$ μm and with $a_{min} = a_{blow}$ produced similar quality results, but models with $a_{min} = 0.1$ μm showed an slightly better Q value (0.35). The expected inner radius is (33.1 ± 3.8) AU, ~ 5 times smaller than the derived radius ~ 100 AU in Rebull et al. (2008), and the expected dust mass is (7.6 ± 4.3) × 10^{-4} $M_{\oplus}$, also ~ 5 times smaller than the dust mass predicted by Rebull et al. (2008) , but they only detected HD 35850 at 70 mum, and they did not include the IRS spectra in the SED. As a result, they derived a dust temperature of 41 K by directly computing the temperature of a blackbody peaking at 70 μm, while our analysis shows that we need grains almost two times warmer (T ~ 86 K, in good agreement with Hillenbrand et al., 2008) to reproduce the SED, which explains the difference in radius.

HIP 10679

HIP 10679 is a G2V star placed 34 pc away. It belongs to a binary system together with HIP10680, with an angular separation of ~13.9 arcsec (~ 470AU at 34 pc). Rebull et al. (2008) modeled the circumstellar dust in this system with a blackbody at 100 K and with a more complex disc model with total mass 4.9 × 10^{-4} $M_{\oplus}$ and R_{in} = 35 AU. The IRS spectrum was too noisy, and therefore we decided not to include it in the analysis of the SED.

In Fig. 4.9 we can see that a single blackbody model can not reproduce the IR emission in HIP 10679. The best model, with T = 97 K and $\beta = 0.0$, produces a poor fit that clearly underestimates the flux at 160 μm, while overestimates the flux at 70 μm. Differences between the best MCFOST models with $a_{min} = 0.1$ μm and $a_{min} = a_{blow}$ are very small, given that a_{blow} is only 0.3 μm. Both models show very small inner radii (3 and 4 AU, respectively) with an small mass of 3.3 × 10^{-3} $M_{\oplus}$. Our inner radius is much smaller than the value proposed by Rebull et al. (2008). The difference is probably due to their choice of a minimum grain size of 0.001 μm, more than 100 times smaller than our more realistic value.

HIP 11437

HIP 11437 is a K7V star, with a companion at ~ 22 arcsec. At the distance of 42.3 pc, the separation translates into ~ 930 AU, therefore, we expect little influence from the binary on the dynamics of the dust disc. Rebull et al. (2008) modeled the dust emission with a blackbody at 65 K, in good agreement with our blackbody temperature of (71 ± 7) K, and derived a minimum inner radius of 10 AU. The blow out size for HIP 11437 is 0.14 μm, hence we only developed one grid of models, with $a_{min} = 0.1$ μm. The expected dust mass for HIP 11437 is (9.5 ± 7.0) × 10^{-3}, and the expected inner radius is (17 ± 6) AU, larger than the radius proposed by Rebull et al. (2008), but we have detected HIP 11437 at 160 μm, making the SED analysis more restrictive.

HD172555

HD 172555 is an A7 star at 29.2 pc that harbors a warm debris disc with solid silicate feature emission in its IRS spectrum (Chen et al., 2006). Wyatt et al. (2007) showed that its infrared emission is $\sim$ 86 times higher than the maximum value expected from steady-state collisional evolution at an age of 12 Myr. Lisse et al. (2009) analyzed its IRS spectrum and proposed that both an SiO gas tentative detection and a strong silicate feature around 10 μm could be explained as the outcome of an hypervelocity collision between two planetary mass objects.

The detection of atomic oxygen emission at 63.18 μm shown in Sec. 4.4.2 will be discussed in detail in Chapter 5 (see also Riviere-Marichalar et al., 2012a). We propossed a possible origin for the emission in agreement with an hypervelocity collision, as previously proposed by Lisse et al. (2009). More recently, Johnson et al. (2012) reviewed the work by Lisse et al. (2009) and concluded that the amount of oxygen gas proposed by Riviere-Marichalar et al. (2012a) at 6 AU is enough to keep SiO vapour from being destroyed by photo-dissociating photons, and that an hypervelocity collision can explain both the IRS spectra, the high IR fractional luminosity and the gas detections.

Smith et al. (2012), after re-analyzing TReCs data by Moerchen et al. (2010), showed that the disc emission is resolved in the Q band (18.3 μm), arising from $r > 8$ AU, but not in the N band (11.66 μm), with the emission coming from 1.0 to 7.9 AU from the central star. These results may suggest that there are two dust populations in the system, but the authors also consider the possibility that there is a single, extended disc producing both emissions.

The best modified blackbody model for HD 172555 has $T_{\rm dust} = 274$ K ($\beta = 0.2$), the warmest in the sample. Although it is a poor fit for the IRS data, it demonstrates the presence of warm dust in the disc. The MCFOST model with $a_{\rm min} = a_{\rm blow}$ fails to reproduce the SED, specially in the near and mid-IR range (IRS spectra), therefore we discuss results with $a_{\rm min} = 0.1$ μm and highlight the fact that we need a population of sub-micron sized grains, as proposed by Johnson et al. (2012). The expected dust mass is $(3.33 \pm 0.05) \times 10^{-4}$ $M_\oplus$, with an inner radius of 2.0 AU, consistent with the results by Smith et al. (2012) that the disc is devoid of dust inside 1 AU. The dust mass is slightly smaller than the value computed using simple assumptions in Riviere-Marichalar et al. (2012a). If the atomic oxygen emission is produced at 2 AU, in the same region where the dust seems to be located, then the oxygen gas mass is ~ $0.1 M_\oplus$.

HD 181327

HD 181327 is an F5.5 V star located 51.8 pc away (Holmberg et al., 2009). Schneider et al. (2006) , by means of NICMOS coronagraphic observations in scattered light, discovered a ring of circumstellar dust peaking at ∼ 89 AU from the central star, with FWHM ∼ 12AU.

For HD 181327, the blowout size is $a_{blow} = 1.0\ \mu$m. Models with $a_{min} = a_{blow}$ produce a better fit, although both sets of models clearly fail to reproduce the submilimetric flux at 870 μm, resulting in a poor quality ($Q = 9.8 \times 10^{-5}$ in the best case). The dust mass is 0.13 $M_\oplus$, the highest among the sample, with $R_{in} = 15$AU. We note here that the location of the disc is inconsistent with previous observations (Schneider et al., 2006). Overall, problems with the model, most probably with the grain composition, result in a poor fit. Therefore, we need a more detailed analysis of the source, accounting for different grain compositions to reproduce the shape of the SED.

Aiming to better understand the mineralogy of the disc, and to better reproduce the shape of the SED, the system, including the new PACS data, and taking into account the constraints by Schneider et al. (2006) ,was recently modeled by the GASPS team in Lebreton et al. (2012), with a dust mass of 0.05 $M_\oplus$ in grains from 1 to 1000 μm. We refer the reader to our detailed study of the source (Lebreton et al., 2012). The main results are: 1) the 100 μm image is partially resolved; and 2) by using the HST/NICMOS coronographic observations, we can break the degeneracy between gran properties and spatial structure of the disc. The image reveals a narrow belt of dust that peaks at 89.5 AU from the star.

The SED was modeled using GRaTeR (Augereau et al., 1999). GRaTeR is an SED data fitter specially designed to efficiently model optically thin discs with parametric grain size and radial distributions.The SED of the disc is well reproduced using a mixture of silicates, carbonaceous material and amorphous ice with high levels of porosity, in grains larger than 1 μm that follow the typical power-law distribution for collisional grinding up to 1 mm, with a total mass of 0.05 $M_\oplus$. Extending the size distribution to the parent bodies of the observed dust grains leads to a mass of $\sim$ 50 $M_\oplus$ for planetesimals up to 1 km with similar composition. The inferred composition could be a good representation of a reservoir of hidden material in unseen planetesimals.

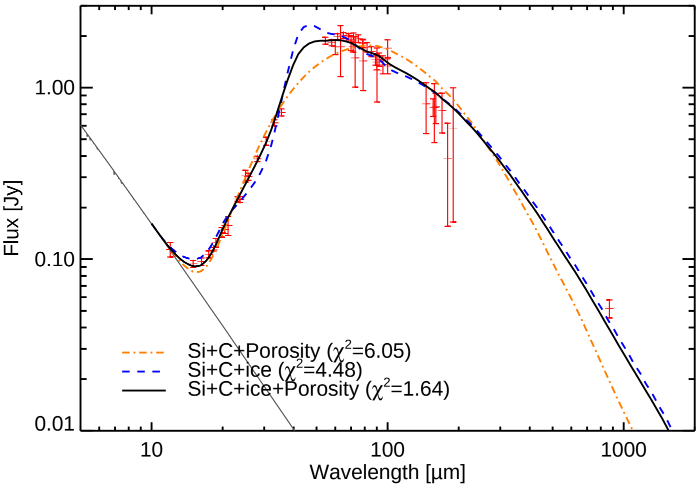

Figure 4.11: GRaTeR SED model for HD 181327 taken from Lebreton et al. (2012).

The upper limits for the [OI] and [CII] line emission were used to estimate the maximum amount of gas present through ProDiMo runs. The gas followed the density profile of the dust, with the dust mass from previous paragraph and gas-to-solid radios in the range $10^{-2} - 10^{3}$. The main parameter controlling the energy balance in the disc was the PAH abundance. Two extreme options were adopted for the PAH abundance: low abundance ($f_{PAH} = 10^{-5}$) and high abundance ($f_{PAH} = 0.1$). Line fluxes for low PAH abundance models are consistent with PACS upper limits for every gas mass in the grid, while for the high abundance models the disc gas mass is constrained to be $< 17\ M_\oplus$.

HD 29391

HD 29391 is an F0 star (Zuckerman & Song, 2004b) 29.8 pc away. We only detected HD 29391 at 70 μm, but the observed flux is in excess over the photosphere ($\chi_{70} \simeq 4.5$). We did not try to produce any MCFOST model for this source, given the lack of photometric points.

The lack of an excess at 24 μm (Rebull et al., 2008) implies a limit on the maximum temperature of 120 K. We compute a temperature of 101 ± 16 K, with $\beta = 1.2 \pm 0.5$, by using the detection at 70 μm and forcing the model to fall below

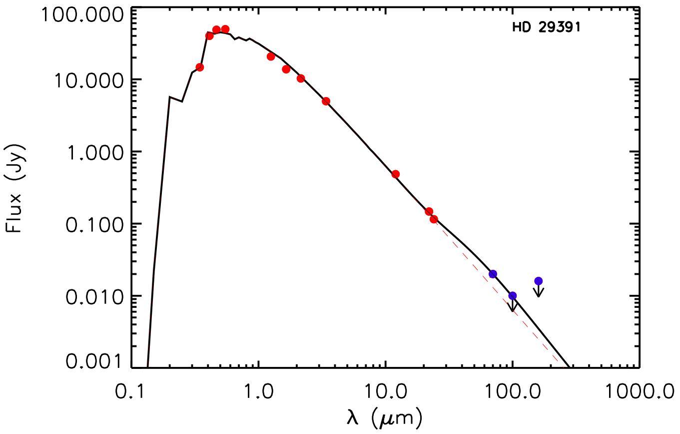

Figure 4.12: Modified blackbody model for HD 29391.

upper limits at 100 and 160 μm. The large β value suggests the presence of small grains. The SED plus the resulting model are shown in Fig. 4.12. Using

$$R_{\rm in} > \frac{1}{2} R_* \left(\frac{T_*}{T_{\rm dust}}\right)^{(4+\beta)/2} \tag{4.9}$$

(Beckwith et al., 1990), we derive an inner radius of $\sim$ 370 AU, with large uncertainties. Because the upper limit for the flux at 160 μm is less restrictive than the one at 100 μm, we used the last to estimate the maximum dust mass of the dust disc using

$$M_{\rm dust} = \frac{F_\nu(\lambda_0) D^2}{\kappa_\nu B_\nu(T_{dust})} \tag{4.10}$$

valid for optically thin discs, where D is the distance to the star (29.8 pc), B_ν can be approximated with the Rayleigh-Jeans regime and $\kappa_\nu = 2 \times (1.3{\rm mm}/\lambda)$ cm^{2}g^{-1}. The maximum mass is $\sim 1.2 \times 10^{-5}$ $M_\oplus$. We note that $L_{\rm IR}/L_* < 4.6 \times 10^{-6}$ is a very small value, similar to the fractional infrared excess of the Sun's Kuiper Belt (10^{-7} to 10^{-6}, Stern, 1996), but the best temperature found is 101 K, much warmer than material in the Kuiper Belt, which is at 45 K.

4.6 Discussion: grain sizes and gas in BPMG members

As shown in the previous section, the IR excess in BPMG members is due to the presence of a debris disc, with dust temperatures in the range 71 to 278 K. Derived dust masses range from 3.3^{-4} $M_\oplus$ to 0.13 $M_\oplus$, with an average value of 2.2×10^{-3} $M_\oplus$, and radii in the range 0.5 to > 35 AU. Some of the large radii present among the sample could be due to giant planet formation within the disc, but there are also other mechanisms that can result in large inner radii.

4.6.1 Grain sizes

In debris discs, dust grains smaller than the blowout size are expected to be ejected from the system in timescales much smaller than the production rate, resulting in a population devoid of small grains. The blowout size depends on the assumed grain composition and on the properties of the star; we assumed that grains are astro-silicates and computed blow out sizes accordingly. Most of the SEDs in BPMG are better reproduced by discs with minimum grain sizes equal to the blowout size, as expected. However, our analysis shows that we need sub-micron sized grains to reproduce the observed SED of HD 172555, contradicting the fact that grains below the blow out size ($\sim 2.1\ \mu$m) must have been expelled out from the system. Other systems, like HD 203, may also need small grains to explain their properties. An option is a different chemical composition that allows small grains to survive, like the one proposed by Johnson et al. (2012), where the disc is devoid of grains in the range 0.2 to 1.5 μm, but grains smaller than 0.2 μm can survive. Another option is that the phenomenon originating the gas (e. g., an hypervelocity collision) is recent enough, in a way that grains have not had time to be blown out from the system.

4.6.2 Gas in BPMG

There are two circumstellar systems in the BPMG that show gas emission: β Pic and HD 172555. β Pict has long been known to posses a large amount of gas in its disc (Hobbs et al., 1985; Lagrange et al., 1986; Roberge et al., 2000; Olofsson et al., 2001; Thi et al., 2001). Lagrange et al. (1987) showed that the profiles of UV absorption lines in β Pic are asymmetric with a redshifted wing showing variations on time scales of months, a signature of infalling gas (Lagrange-Henri et al., 1989). Olofsson et al. (2001) showed Na I in Keplerian rotation and spread over a large area (30 to 140 AU form the star). A braking mechanism was proposed to keep Na stable against radiation pressure; Fernández et al. (2006) showed that an overabundance of C by a factor of 10 with respect to solar abundance is enough to brake the gas and make it remain in orbit. Later on, observations with the Far-UV Space Explorer (FUSE) showed that C is indeed overabundant by a factor of 20 with respect to other species (Roberge et al., 2006).

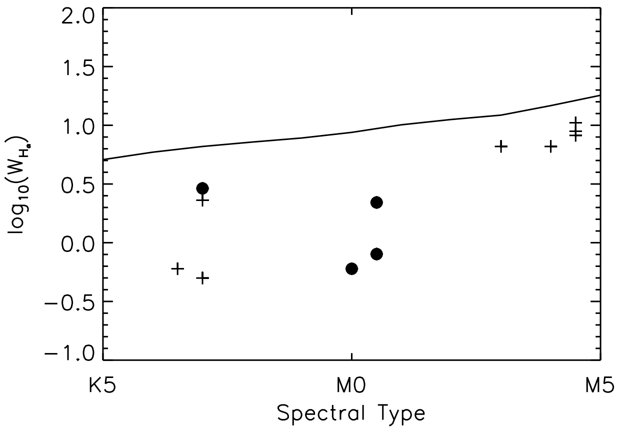

Figure 4.13: H_α equivalent width (EW) versus spectral type for BPMG members. Plus symbols indicate BPMG members not observed with Herschel, while filled circles represent BPMG members observed with Herschel. The solid line shows the saturation criterion by Barrado y Navascués & Martín (2003). H_α equivalent width (EW) taken from Jayawardhana et al. (2006).

In Fig. 4.13 we represent H_α equivalent width (EW) for BPMG members against their spectral type, together with the accretion criterion by Barrado y Navascués & Martín (2003) described in Chapter 3. As can be seen, no BPMG member show signs of active accretion, as expected for debris discs with large inner holes.

The detection of atomic oxygen emission around HD 172555 was recently reported by Riviere-Marichalar et al. (2012a) and will be discussed in detail in Chapter 5. In the following we make a brief discussion in the framework of BPMG members. Lisse et al. (2009) proposed a tentative detection of SiO gas toward HGD 172555, later on confirmed by Johnson et al. (2012). Fernández et al. (2006) suggested that the gas around β Pic must be second generation. The gas around HD 172555 must be also second generation, considering the age of the system and the time scales proposed for gas clearing. Overall, HD 172555 is a peculiar system in many ways: the disc is warm, with a dust population with considerable amounts of very small grains, producing silicate features, with a very large fractional luminosity and atomic gas present. Therefore, the presence of gas seems to be linked to the warm disc phenomenon. The gas in β Pic could have originated through local evaporation of dust grains (Fernández et al., 2006) or as the result of falling evaporating bodies (Beust et al., 1990). In contrast, the origin of the gas in HD 172555 has been attributed to an hypervelocity collision like the one that created the Moon (Lisse et al., 2009; Riviere-Marichalar et al., 2012a;

Johnson et al., 2012). Therefore, different mechanisms seem to operate at the same age; and stochastic events may play a role by producing huge amounts of gas in a short period of time, while a more quiescent gas production results from dust grain collisions and evaporation. Future research is needed in order to understand the gas production mechanisms in debris discs, and the identification of observables useful to distinguish among the various mechanisms is a main goal for future work. The detection of other gaseous species towards HD 172555 will help us to better understand the origin of the gas.

We did not detected water in any of the observed BPMG members, while in Taurus ~ 24% of the gas rich discs (those with detectable emission of [OI] at 63.18 μm) show water emission. Therefore, the lack of water emission in BPMG members observed is the expected result: only HD 172555 shows [OI] emission, but the origin of the gas is far from being the same as for gas rich Taurus members.

4.7 Summary and conclusions

We have observed 19 BPMG members with the *Herschel Space Observatory* instrument PACS. All of them were observed in photometric mode at 160 μm, 16 were observed at 70 μm and another 15 were observed at 100 μm. Spectroscopic observations were obtained for a subsample of 4 objects, namely HD 164249, HD172555, HD181327 and HD 181296. Our main conclusions are:

1. We have detected infrared emission in excess at 70/100/160 μm in 6/8/7 out of the 16/15/19 objects observed at each band. We have detected for the first time emission at 70 μm towards AT Mic, HD 146624 and HD 29391. The 70 μm flux in HD 29391 is in excess over the photosphere, resulting in a very small infrared fractional luminosity of $L_{IR}/L_* < 4.6 \times 10^{-6}$. We have detected the 100 emission toward seven BPMG members for the first time, namely HD 203, HD 164249, HD 172555, HD 181296, HD 35850, HIP10679 and HIP 11437. We also have detected the 160 μm flux toward HD 172555, HD 35850, HIP 10679 and HIP 11437 for the first time.

2. One of the systems studied, namely HD 172555 shows [OI] emission at 63 μm. Together with β Pic itself, is the only disc in BPMG showing gas emission.

3. We have modeled the dust emission with modified blackbody models and MCFOST models. Blackbody temperatures range from 68 K (HD 164249) to 278

K (HD 172555). Dust masses range from $\sim 3 \times 10^{-4}$ $M_{\oplus}$ to 0.13 $M_{\oplus}$ and inner radii range from 2 to ∼ 34 AU.

4. According to blackbody models, HD 172555 is a warm debris disc and we note that the presence of gas in this system could be linked with the presence of hot dust, in a way that the same phenomenon producing the gas is also producing a population of small grains near the star. None of the systems show o-H_2O emission in their spectra. None of the sources showed $o - H_2O$ emission at 63.32 μm.

Discs in the BPMG are all in the debris stage, all of them showing inner holes. The presence of gas in the system HD 172555 needs future work to correctly understand the origin of the gas. The lack of [CII] emission will help us to better constrain the total mass of dust present.

Appendix B

B.1 Photometry for BPMG members detected with PACS.

Table B.1: Photometry for BPMG members detected with PACS

Name	Filter	λ_0	Magnitude	Flux
–	–	μm	mag	Jy
HD 164249	stromgren u	0.34505600	8.625 ± 0.01	1.6900 ± 0.015
"	stromgren v	0.41093900	7.732 ± 0.01	3.943 ± 0.036
"	stromgren b	0.46690100	7.293 ± 0.01	5.167 ± 0.048
"	stromgren y	0.54780300	7.005 ± 0.01	5.843 ± 0.054
"	2MASS J	1.2500000	6.159 ± 0.019	5.502 ± 0.098
"	2MASS H	1.6500000	6.022 ± 0.031	4.213 ± 0.124
"	2MASS Ks	2.1700000	5.913 ± 0.020	2.889 ± 0.053
"	WISE 1	3.4	5.882 ± 0.046	1.3738 ± 0.064
"	WISE 2	4.6	5.841 ± 0.021	0.7917 ± 0.016
"	IRS 03	5.73	–	0.4568 ± 0.066
"	IRS 120	7.00	–	0.3200 ± 0.048
"	IRS 10165	8.54	–	0.2202 ± 0.022
"	IRS 12199	10.54	–	0.1458 ± 0.012
"	IRS 13216	11.51	–	0.1230 ± 0.011
"	IRS 14233	12.54	–	0.1057 ± 0.008
"	IRS 15250	13.50	–	0.0916 ± 0.009
"	IRS 07	14.49	–	0.0862 ± 0.006
"	IRS 160	15.51	–	0.0784 ± 0.008
"	IRS 2113	16.52	–	0.0711 ± 0.006
"	IRS 3166	17.54	–	0.0671 ± 0.008
"	IRS 4219	18.56	–	0.0664 ± 0.008

Table B.1: Continued.

Name	Filter	λ_0	Magnitude	Flux
–	–	μm	mag	Jy
"	IRS 5272	19.57	–	0.0636 ± 0.014
"	IRS 12657	20.59	–	0.0656 ± 0.019
"	IRS 14763	22.62	–	0.0751 ± 0.008
"	IRS 15816	23.64	–	0.0843 ± 0.012
"	IRS 16869	24.65	–	0.0880 ± 0.008
"	IRS 17922	25.50	–	0.1005 ± 0.019
"	IRS 18975	26.52	–	0.1032 ± 0.008
"	IRS 191028	27.53	–	0.1155 ± 0.012
"	IRS 201081	28.55	–	0.1282 ± 0.010
"	IRS 211134	29.57	–	0.1340 ± 0.009
"	IRS 221187	30.58	–	0.1469 ± 0.012
"	IRS 231240	31.60	–	0.1722 ± 0.019
"	IRS 251346	33.63	–	0.2086 ± 0.034
"	IRS 261399	34.65	–	0.2197 ± 0.027
"	MIPS 70	70.	–	0.6240 ± 0.060
"	AKARI 90	90.	–	0.4915 ± 0.0
"	PACS 100	100.00000	–	0.4930 ± 0.013
"	PACS 160	160.00000	–	0.2490 ± 0.011
HD 172555	stromgren u	0.345056	6.354 ± 0.010	13.69 ± 0.13
"	stromgren v	0.410939	5.203 ± 0.009	40.49 ± 0.34
"	stromgren b	0.466901	4.891 ± 0.005	47.21 ± 0.22
"	stromgren y	0.547803	4.779 ± 0.003	45.40 ± 0.13
"	Johnson V	0.5483	4.990 ± 0.015	38.45 ± 0.53
"	Johnson R	0.7000	4.887 ± 0.023	33.40 ± 0.71
"	Johnson I	0.9000	4.581 ± 0.025	35.74 ± 0.82
"	2MASS J	1.2518	4.382 ± 0.26	28.92 ± 6.93
"	2MASS H	1.6504	4.251 ± 0.212	22.24 ± 4.34
"	2MASS Ks	2.1539	4.298 ± 0.031	12.82 ± 0.37
"	WISE 1	3.4	4.269 ± 0.094	6.069 ± 0.52
"	IRS 102	5.64	–	2.17 ± 0.18
"	IRS 101	6.64	–	1.67 ± 0.12
"	IRS 100	7.55	–	1.379 ± 0.047
"	IRS 114	7.97	–	1.349 ± 0.018
"	IRS 113	8.97	–	1.56 ± 0.17

Table B.1: Continued.

Name	Filter	λ_0	Magnitude	Flux
–	–	μm	mag	Jy
"	IRS 112	9.97	–	1.556 ± 0.082
"	IRS 1181	10.42	–	1.45 ± 0.11
"	IRS 111	10.96	–	1.362 ± 0.052
"	IRS 1180	11.39	–	1.22 ± 0.19
"	IRS 110	11.96	–	1.054 ± 0.095
"	IRS 1179	12.39	–	0.94 ± 0.14
"	IRS 1178	13.36	–	0.89 ± 0.10
"	IRS 1177	14.34	–	0.92 ± 0.11
"	IRS 1176	15.35	–	0.97 ± 0.13
"	IRS 1175	16.40	–	1.03 ± 0.11
"	IRS 1174	17.42	–	1.05 ± 0.13
"	IRS 1173	18.36	–	1.064 ± 0.089
"	IRS 1129	19.35	–	1.10 ± 0.20
"	IRS 1128	20.29	–	1.06 ± 0.23
"	IRS 1127	21.33	–	1.03 ± 0.15
"	IRS 1126	22.39	–	1.036 ± 0.092
"	IRS 1125	23.37	–	0.986 ± 0.086
"	IRS 1124	24.23	–	0.97 ± 0.16
"	IRS 1123	25.36	–	0.90 ± 0.12
"	IRS 1122	26.35	–	0.88 ± 0.14
"	IRS 1121	27.25	–	0.88 ± 0.12
"	PACS 70	70	–	0.191 ± 0.005
"	MIPS 70	70	–	0.197 ± 0.020
"	PACS 100	100	–	0.089 ± 0.003
"	PACS 160	160	–	0.032 ± 0.002
"	SIMBA	1200	–	<0.026
HD 181296	stromgren u	0.34	6.354 ± 0.028	13.690 ± 0.35
"	stromgren v	0.41	5.195 ± 0.014	40.793 ± 0.53
"	Johnson B	0.44	5.048 ± 0.001	42.480 ± 0.039
"	stromgren b	0.47	5.038 ± 0.004	41.232 ± 0.15
"	stromgren y	0.55	5.038 ± 0.001	35.763 ± 0.03
"	Johnson V	0.55	5.030 ± 0.001	37.062 ± 0.034
"	2MASS J	1.25	5.096 ± 0.037	14.983 ± 0.51
"	2MASS H	1.65	5.148 ± 0.082	9.735 ± 0.73

Table B.1: Continued.

Name	Filter	λ_0	Magnitude	Flux
–	–	μm	mag	Jy
"	2MASS Ks	2.15	5.008 ± 0.033	6.666 ± 0.20
"	WISE 1	3.4	5.003 ± 0.052	3.0868 ± 0.15
"	IRS 031	5.73	–	1.10 ± 0.19
"	IRS 140	7.00	–	0.78 ± 0.11
"	IRS 10	8.54	–	0.581 ± 0.030
"	IRS 11	9.51	–	0.506 ± 0.021
"	IRS 12	10.54	–	0.452 ± 0.014
"	IRS 13	11.51	–	0.413 ± 0.014
"	WISE 3	12	4.704 ± 0.018	0.4160 ± 0.0069
"	IRS 14	12.54	–	0.376 ± 0.012
"	IRS 15	13.50	–	0.359 ± 0.010
"	IRS 230	14.49	–	0.374 ± 0.021
"	IRS 231	15.51	–	0.376 ± 0.010
"	IRS 232	16.52	–	0.387 ± 0.015
"	IRS 233	17.54	–	0.398 ± 0.016
"	IRS 234	18.56	–	0.404 ± 0.012
"	IRS 235	19.57	–	0.406 ± 0.055
"	IRS 10	20.59	–	0.412 ± 0.039
"	IRS 1 1	21.61	–	0.446 ± 0.021
"	IRS 12	22.62	–	0.454 ± 0.024
"	IRS 13	23.64	–	0.468 ± 0.014
"	IRS 14	24.65	–	0.482 ± 0.018
"	IRS 15	25.50	–	0.495 ± 0.014
"	IRS 16	26.52	–	0.498 ± 0.013
"	IRS 17	27.53	–	0.510 ± 0.011
"	IRS 18	28.55	–	0.518 ± 0.014
"	IRS 19	29.57	–	0.534 ± 0.032
"	IRS 110	30.58	–	0.544 ± 0.014
"	IRS 111	31.60	–	0.537 ± 0.023
"	IRS 112	32.61	–	0.550 ± 0.027
"	ISOPHOT 60	60	–	0.433 ± 0.022
"	MIPS 70	70	–	0.409 ± 0.0409
"	ISOPHOT 90	90	–	0.286 ± 0.021
"	PACS100	100	–	0.250 ± 0.008

Table B.1: Continued.

Name	Filter	λ_0	Magnitude	Flux
–	–	μm	mag	Jy
"	IRAS 100	100	–	<0.435
"	PACS 160	160	–	0.111 ± 0.006
"	LABOCA 870	870	–	<0.0144
HD 181327	stromgren u	0.345056	8.688 ± 0.01	1.5951 ± 0.015
"	stromgren v	0.410939	7.808 ± 0.013	3.6761 ± 0.044
"	stromgren b	0.466901	7.341 ± 0.02	4.9435 ± 0.091
"	stromgren y	0.547803	7.040 ± 0.02	5.6576 ± 0.104
"	Johnson R	0.7	6.77 ± 0.01	5.8961 ± 0.054
"	Johnson I	0.9	6.51 ± 0.01	6.0479 ± 0.055
"	2MASS J	1.2518	6.200 ± 0.024	5.4198 ± 0.120
"	2MASS H	1.6504	5.980 ± 0.044	4.5242 ± 0.183
"	2MASS Ks	2.1539	5.910 ± 0.029	2.9044 ± 0.077
"	WISE 1	3.4	5.930 ± 0.042	1.3144 ± 0.051
"	WISE2	4.6	5.821 ± 0.023	0.8065 ± 0.017
"	IRS 10165	8.54	–	0.2279 ± 0.025
"	IRS 12199	10.54	–	0.1507 ± 0.014
"	IRS 13216	11.51	–	0.1271 ± 0.013
"	IRAS 12	11.69	–	<0.2499
"	IRS 14233	12.54	–	0.1115 ± 0.009567
"	IRS 15250	13.50	–	0.0974 ± 0.0097
"	IRS 07	14.49	–	0.0936 ± 0.0075
"	IRS 140	15.51	–	0.0901 ± 0.0057
"	IRS 273	16.52	–	0.0936 ± 0.0074
"	IRS 3106	17.54	–	0.1018 ± 0.0086
"	IRS 4139	18.56	–	0.114 ± 0.012
"	IRS 5172	19.57	–	0.131 ± 0.022
"	IRS 6193	14.49	–	0.0936 ± 0.0075
"	IRS 7226	15.51	–	0.0901 ± 0.0057
"	IRS 8259	16.52	–	0.0936 ± 0.0074
"	IRS 9292	17.54	–	0.1018 ± 0.0086
"	IRS 10325	18.56	–	0.113 ± 0.012
"	IRS 11358	19.57	–	0.131 ± 0.023
"	IRS 12427	20.59	–	0.153 ± 0.015
"	IRS 14493	22.62	–	0.203 ± 0.014

Table B.1: Continued.

Name	Filter	λ_0	Magnitude	Flux
–	–	μm	mag	Jy
"	IRS 15526	23.64	–	0.230 ± 0.01
"	MIPS 24	23.67	–	0.195 ± 0.02
"	IRS 16559	24.65	–	0.264 ± 0.014
"	IRS 17592	25.50	–	0.288 ± 0.015
"	IRS 18625	26.52	–	0.316 ± 0.018
"	IRS 19658	27.53	–	0.359 ± 0.018
"	IRS 20691	28.55	–	0.400 ± 0.012
"	IRS 21724	29.57	–	0.431 ± 0.023
"	IRS 22757	30.58	–	0.475 ± 0.026
"	IRS 23790	31.60	–	0.516 ± 0.033
"	IRS 25856	33.63	–	0.693 ± 0.058
"	IRS 26889	34.65	–	0.741 ± 0.044
"	IRS 27922	35.49	–	0.788 ± 0.060
"	PACS 70	70	–	1.4526 ± 0.0061
"	MIPS 70	71.4200	–	1.468 ± 0.14
"	AKARI 90	90	–	1.4594 ± 0.15
"	PACS 100	100	–	1.40 ± 0.04
"	MIPS 160	155.9000	–	0.658 ± 0.07
"	PACS 160	160	–	0.85 ± 0.04
"	ISOPHOT 170	170	–	0.736 ± 0.192
"	SMA 870	870	–	0.0517 ± 0.0062
HD 203	Tycho B	0.42044	6.618 ± 0.	8.8841 ± 0.
"	Johnson B	0.44	6.538 ± 0.	10.526 ± 0.
"	Tycho V	0.532185	6.218 ± 0.	12.249 ± 0.
"	2MASS J	1.25	5.451 ± 0.	10.5 ± 0.
"	2MASS H	1.65	5.331 ± 0.	7.55 ± 0.
"	2MASS Ks	2.17	5.240 ± 0.	5.34 ± 0.
"	IRS 07	8.54	–	0.424 ± 0.042
"	IRS 233	10.54	–	0.283 ± 0.022
"	IRS 346	11.51	–	0.241 ± 0.020
"	IRS 459	12.54	–	0.206 ± 0.015
"	IRS 572	13.50	–	0.182 ± 0.014
"	IRS 07	14.49	–	0.1731 ± 0.0083
"	IRS 160	15.51	–	0.1609 ± 0.0096

Table B.1: Continued.

Name	Filter	λ_0	Magnitude	Flux
–	–	μm	mag	Jy
"	IRS 2113	16.52	–	0.1486 ± 0.0075
"	IRS 3166	17.54	–	0.1386 ± 0.0087
"	IRS 4219	18.56	–	0.1342 ± 0.0088
"	IRS 5272	19.57	–	0.125 ± 0.023
"	IRS 12657	20.59	–	0.121 ± 0.026
"	IRS 14763	22.62	–	0.1269 ± 0.0092
"	IRS 15816	23.64	–	0.1320 ± 0.0073
"	MIPS 24	24	–	0.113 ± 0.
"	IRS 16869	24.65	–	0.1325 ± 0.0081
"	IRS 17922	25.50	–	0.1321 ± 0.0075
"	IRS 18975	26.52	–	0.1350 ± 0.0095
"	IRS 191028	27.53	–	0.1370 ± 0.0071
"	IRS 201081	28.55	–	0.138 ± 0.012
"	IRS 211134	29.56	–	0.141 ± 0.011
"	IRS 221187	30.58	–	0.135 ± 0.014
"	IRS 231240	31.60	–	0.138 ± 0.018
"	IRS 251346	33.63	–	0.141 ± 0.032
"	IRS 261399	34.65	–	0.133 ± 0.026
"	MIPS70	70	–	0.0692 ± 0.
"	PACS70	70	–	0.068 ± 0.003
"	PACS100	100	–	0.026 ± 0.002
"	PACS160	160	–	<0.014
HD 35850	stromgren u	0.345056	8.062 ± 0.028	2.8392 ± 0.073
"	stromgren v	0.410939	7.194 ± 0.017	6.4713 ± 0.10
"	stromgren b	0.466901	6.658 ± 0.01	9.2734 ± 0.085
"	stromgren y	0.547803	6.304 ± 0.01	11.143 ± 0.10
"	2MASS J	1.2518	5.268 ± 0.027	12.787 ± 0.32
"	2MASS H	1.6504	5.087 ± 0.026	10.297 ± 0.25
"	2MASS Ks	2.1539	4.926 ± 0.021	7.1889 ± 0.14
"	WISE 1	3.4	5.020 ± 0.052	3.0389 ± 0.14
"	IRS 03	5.73	–	1.18 ± 0.18
"	IRS 120	7.00	–	0.83 ± 0.13
"	IRS 10165	8.54	–	0.573 ± 0.056
"	IRS 12199	10.54	–	0.379 ± 0.030

Table B.1: Continued.

Name	Filter	λ_0	Magnitude	Flux
–	–	μm	mag	Jy
"	IRS 14233	12.54	–	0.269 ± 0.019
"	IRS 15250	13.50	–	0.232 ± 0.016
"	IRS 07	14.49	–	0.213 ± 0.015
"	IRS 160	15.51	–	0.191 ± 0.013
"	IRS 2113	16.52	–	0.168 ± 0.016
"	IRS 3166	17.54	–	0.150 ± 0.015
"	IRS 4219	18.56	–	0.131 ± 0.020
"	IRS 5272	19.57	–	0.120 ± 0.028
"	WISE 4	22	4.847 ± 0.027	0.0963 ± 0.0024
"	IRS 14763	22.62	–	0.094 ± 0.016
"	IRS 15816	23.64	–	0.087 ± 0.018
"	MIPS 24	24	–	0.0790 ± 0.
"	IRS 16869	24.65	–	0.086 ± 0.015
"	IRS 17922	25.50	–	0.082 ± 0.015
"	IRS 18975	26.52	–	0.075 ± 0.017
"	IRS 191028	27.53	–	0.076 ± 0.015
"	IRS 201081	28.55	–	0.065 ± 0.019
"	IRS 211134	29.57	–	0.063 ± 0.019
"	IRS 221187	30.58	–	0.064 ± 0.020
"	MIPS 70	70	–	0.0470 ± 0.0047
"	PACS100	100	–	0.042 ± 0.002
"	PACS160	160	–	0.018 ± 0.004
HIP 10679	Johnson V	0.5483	7.74 ± 0.01	3.054 ± 0.028
"	Johnson B	0.4443	8.33 ± 0.01	2.067 ± 0.019
"	Tycho B	0.42044	8.493 ± 0.01	1.580 ± 0.014
"	Tycho V	0.532185	7.805 ± 0.01	2.840 ± 0.026
"	2MASS J	1.2518	6.570 ± 0.021	3.768 ± 0.074
"	2MASS H	1.6504	6.355 ± 0.026	3.100 ± 0.077
"	2MASS K	2.1539	6.262 ± 0.017	2.095 ± 0.020
"	WISE 1	3.4	6.221 ± 0.039	0.9812 ± 0.035
"	WISE 2	4.6	6.251 ± 0.021	0.5339 ± 0.010
"	WISE 3	12	6.235 ± 0.013	0.0818 ± 0.001
"	WISE 4	22	5.667 ± 0.032	0.0433 ± 0.001
"	PACS 70	70	–	0.053 ± 0.003

Table B.1: Continued.

Name	Filter	λ_0	Magnitude	Flux
–	–	μm	mag	Jy
"	PACS 100	100	–	0.046 ± 0.002
"	PACS 160	160	–	0.039 ± 0.005
HIP 11437	2MASS J	1.26	7.870 ± 0.034	1.1379 ± 0.0364
"	2MASS H	1.60	7.235 ± 0.018	1.3849 ± 0.0236
"	2MASS Ks	2.22	7.080 ± 0.026	0.9864 ± 0.0237
"	WISE 1	3.4	7.014 ± 0.030	0.4843 ± 0.013
"	WISE 2	4.6	7.038 ± 0.021	0.2629 ± 0.005
"	IRS 00	8.54	–	0.0828 ± 0.0094
"	IRS 01	9.51	–	0.0664 ± 0.0067
"	IRS 02	10.54	–	0.0556 ± 0.0066
"	IRS 03	11.51	–	0.0466 ± 0.0077
"	IRS 04	12.54	–	0.0406 ± 0.0053
"	IRS 05	13.38	–	0.0350 ± 0.0074
"	IRS 572	13.50	–	0.034 ± 0.012
"	IRS 230	14.58	–	0.0300 ± 0.0084
"	IRS 231	15.42	–	0.0272 ± 0.0079
"	IRS 232	16.27	–	0.0252 ± 0.0082
"	IRS 233	17.54	–	0.0231 ± 0.0081
"	IRS 01	21.61	–	0.0182 ± 0.0047
"	IRS 14763	22.62	–	0.0174 ± 0.0059
"	IRS 03	23.64	–	0.0172 ± 0.0032
"	MIPS 24	24	–	0.017 ± 0.0017
"	IRS 04	24.65	–	0.0166 ± 0.0042
"	IRS 05	25.50	–	0.0181 ± 0.0035
"	IRS 06	26.52	–	0.0181 ± 0.0051
"	IRS 07	27.53	–	0.0202 ± 0.0034
"	IRS 08	28.55	–	0.0216 ± 0.0040
"	IRS 09	29.57	–	0.0206 ± 0.0046
"	IRS 010	30.58	–	0.0245 ± 0.0041
"	IRS 011	31.60	–	0.0274 ± 0.0074
"	IRS 012	32.61	–	0.0257 ± 0.0055
"	IRS 013	33.46	–	0.0303 ± 0.0082
"	MIPS 70	70	–	0.0751 ± 0.0075
"	PACS 100	100	–	0.069 ± 0.003

Table B.1: Continued.

Name	Filter	λ_0	Magnitude	Flux
–	–	μm	mag	Jy
"	PACS 160	160	–	0.050 ± 0.004
HD 29391	stromgren u	0.345056	6.277 ± 0.	14.696 ± 0.
"	stromgren v	0.41	5.215 ± 0.	40.048 ± 0.
"	stromgren b	0.47	4.859 ± 0.	48.622 ± 0.
"	stromgren y	0.55	4.684 ± 0.	49.549 ± 0.
"	2MASS J	1.25	4.744 ± 0.	20.719 ± 0.
"	2MASS H	1.65	4.770 ± 0.	13.789 ± 0.
"	2MASS Ks	2.15	4.537 ± 0.	10.286 ± 0.
"	WISE 1	3.4	4.486 ± 0.081	4.9695 ± 0.37
"	WISE 3	12	4.538 ± 0.014	0.4847 ± 0.0062
"	WISE 4	22	4.387 ± 0.021	0.1470 ± 0.0028
"	MIPS 24	24	− − ±0.	0.115 ± 0.
"	PACS 70	70	− − ±0.	0.020 ± 0.002
"	PACS 100	100	–	<0.010
"	PACS 160	160	–	<0.016

B.2 BPMG PACS radial profiles.

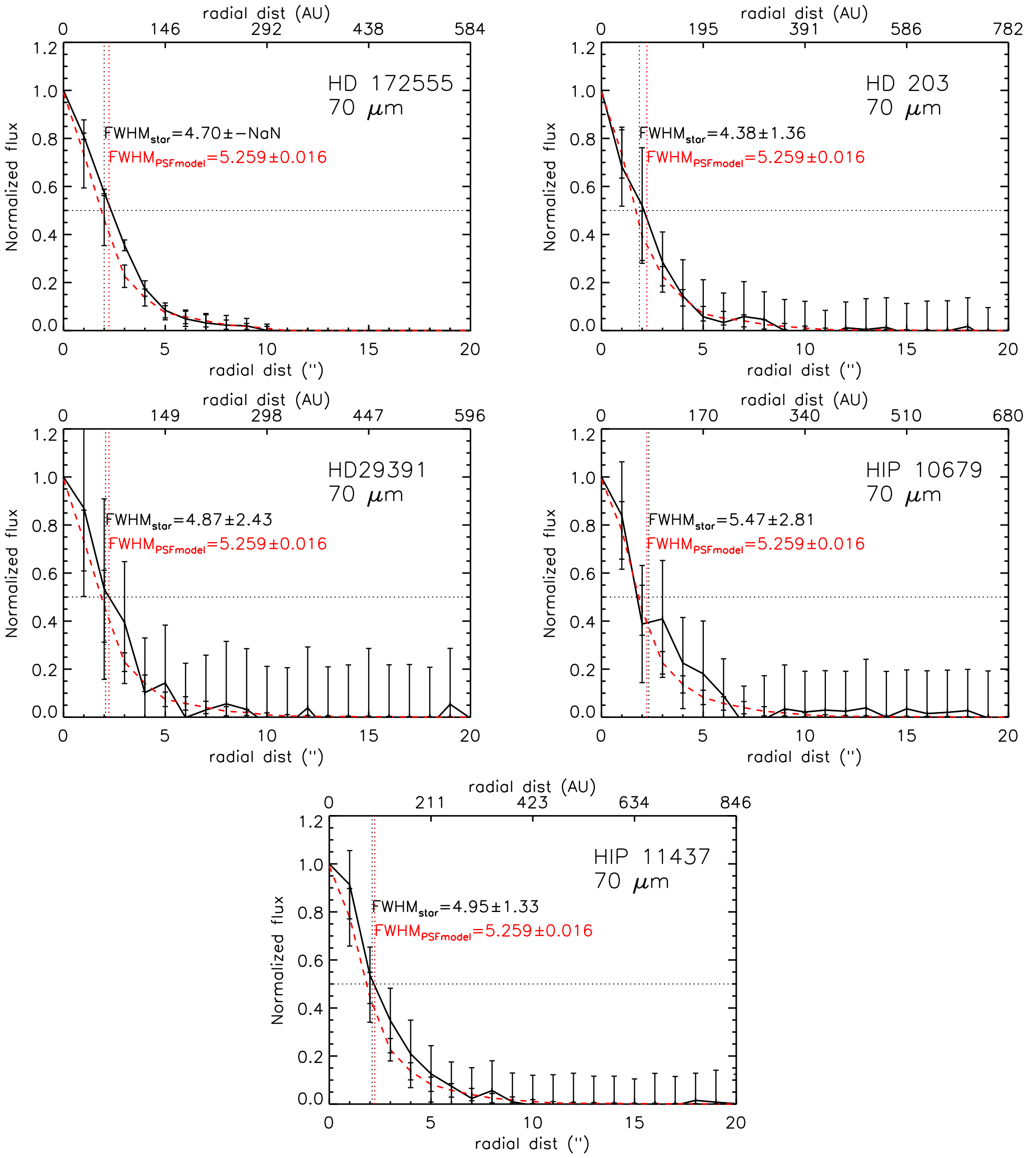

Figure B.1: Azimuthally averaged radial profiles at 70 μm for BPMG members detected with PACS

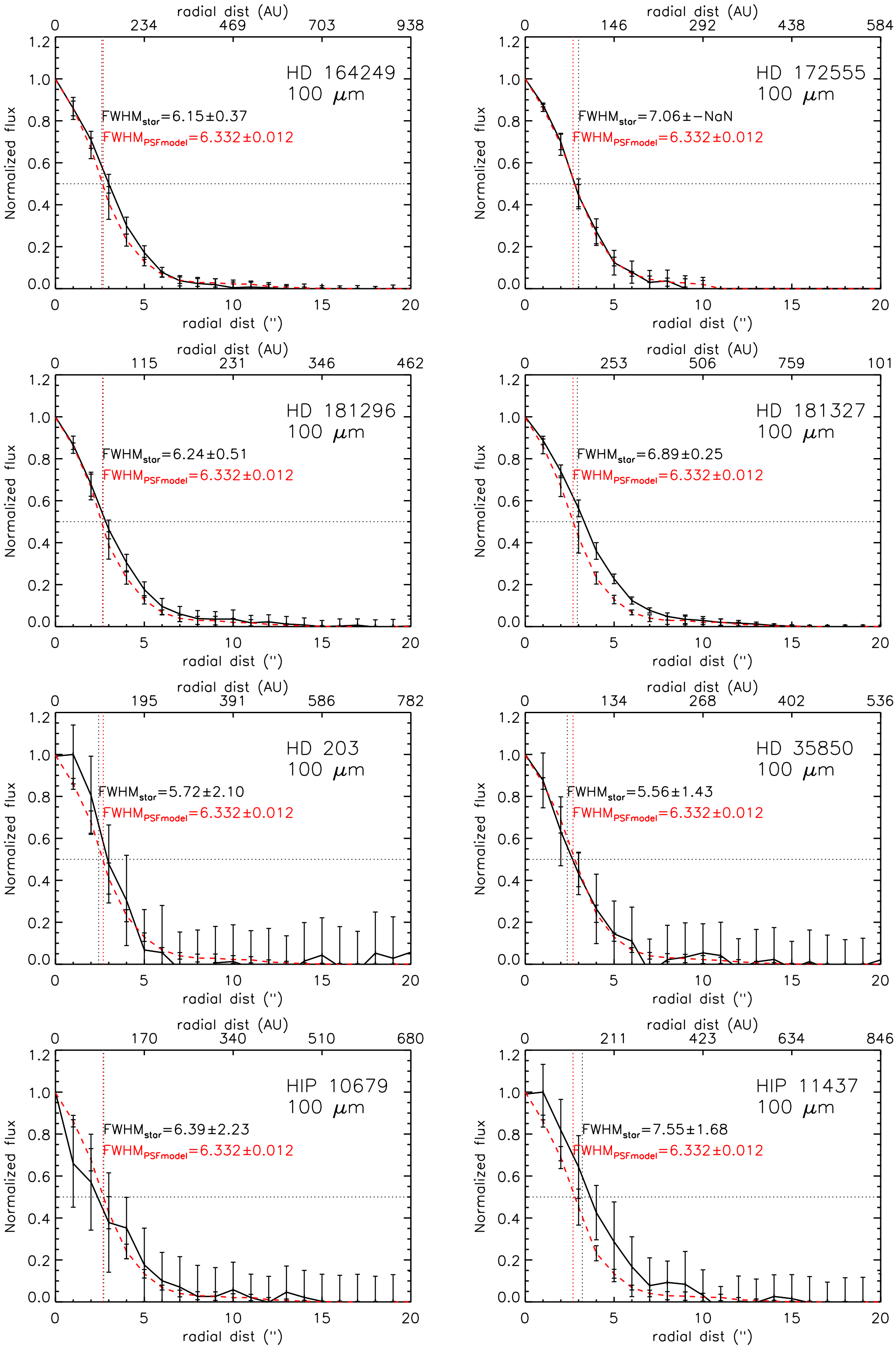

Figure B.2: Azimuthally averaged radial profiles at 100 μm for BPMG members detected with PACS

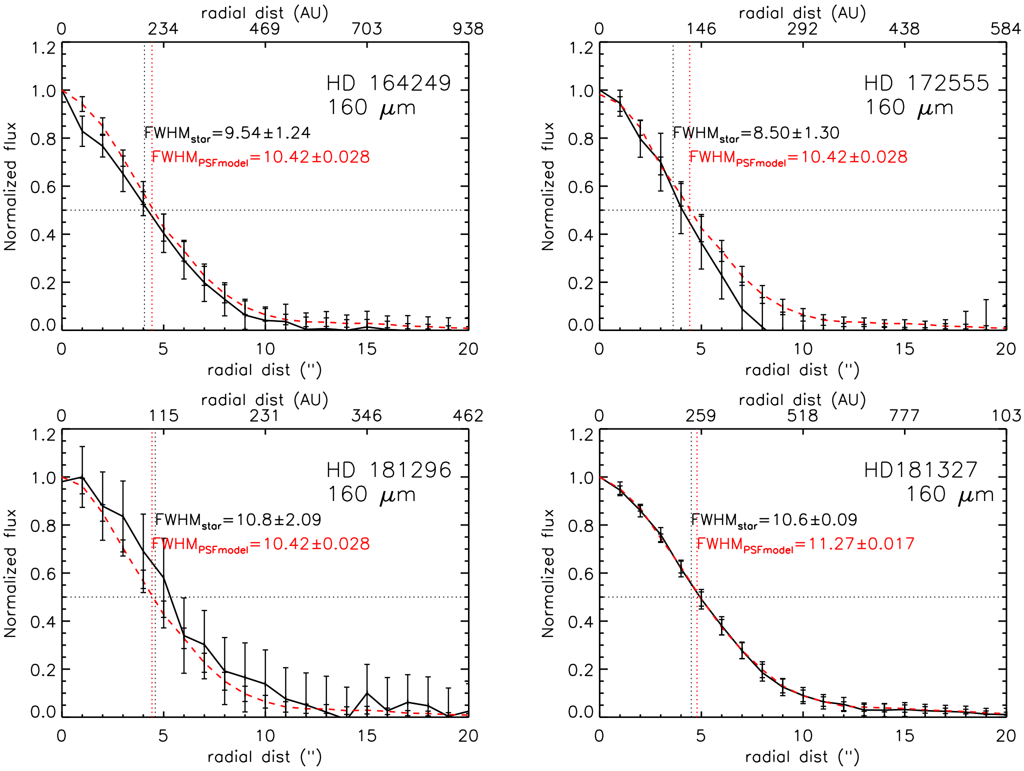

Figure B.3: Azimuthally averaged radial profiles at 160 μm for BPMG members detected with PACS. The 160 μm for HD 35850, HIP 10679 and HIP 11437 are too noisy, and therefore we did not performed radial profiles for these sources.

Chapter 5

Atomic oxygen gas detection in HD 172555

A version of this chapter has been published as a letter to the editor in Astronomy and Astrophysics, Riviere-Marichalar et al. (2012a)

5.1 Introduction and overview of HD172555: a key debris disk with 12-20 Myr

CIRCUMSTELLAR discs play a key role in understanding how planets form and evolve, since it is thought that they originate in gas-rich circumstellar discs around young stars, the so-called protoplanetary discs. Around older stars, with ages greater than about 5 to 10 Myr, another type of disc is seen: dusty, optically thin debris discs that are produced by destructive collisions between planetesimals formed in the protoplanetary disc phase. The younger debris discs (~ 5 – 100 Myr) are the likely sites of ongoing terrestrial planet formation, while the older ones (0.1 – 1 Gyr) correspond to the "clearing out" phase, when most planetesimals left over from planet formation are removed from the system.

While debris dust has been extensively observed, previous studies have provided little unambiguous information on the chemical composition of the dust. Most debris discs have featureless IR spectra, since the grains are large and cold. However, there are a few debris discs that show strong solid-state mid-IR spectral features, indicating the presence of small, warm grains. These debris discs are probably highly transient and are produced during periods of intense collisional grinding between large bodies (Lisse et al., 2008, 2009). Gas can provide additional compositional information, but it is rarely detected in debris discs. Only two – 49 Ceti and HD 21997 – show any trace of sub-mm CO emission, indicating that typical debris gas abundances are low relative to those in younger protoplanetary discs (Dent et al., 2005; Moór et al., 2011). The only debris disc with a fairly complete inventory of its gaseous species is β Pictoris, primarily obtained through UV/optical absorption spectroscopy (Roberge et al., 2006). In general, the debris gas studied so far appears to be primarily low density and ionized, because these low-density discs are optically thin to dissociating UV photons.

HD 172555 (Gray et al., 2006) is one of these rare stars with an observed warm debris disc. This A7V-type star located at 29.2 pc (Gray et al., 2006) belongs to the β Pictoris Moving Group (BPMG), and as such, its age is in the range 12 Myr (Zuckerman & Song, 2004b) to 20 Myr (Barrado y Navascués et al., 1999). HD 172555 was originally found to harbour a bright debris disc through IRAS measurements of excess thermal emission attributed to circumstellar dust grains (Cote, 1987). The *Spitzer*/IRS spectrum revealed strong solid-state emission features in the mid-IR, indicating that it contains a relatively large amount of warm dust in a fine μm-sized population at $T \sim 300$ K (Lisse et al., 2009). It has been proposed that this disc is the aftermath of a catastrophic collision between planetary mass bodies.

In this Chapter, we present *Herschel* (Pilbratt et al., 2010) far-IR photometry and spectroscopy of HD 172555, obtained as part of the "Gas in Protopolanetary Systems" (GASPS) *Herschel* Open Time Key Programme with the instrument PACS (Poglitsch et al., 2010). In Sec. 2 we describe the PACS spectroscopic and photometric observations. In Sec. 3 we describe the main observational and modelling results for the dust and gas discs. In Sec. 4, we discuss possible origins for the detected OI gas.

5.2 Observations and data reduction

5.2.1 *Herschel* photometry

HD 172555 falls into the field of view of our scan maps (obsids: 1342209059, 1342209060, 1342209061, 1342209062) centred on CD-64 1208, an M0-type star with which it forms a wide binary system on a ~ 2000 AU orbit (Feigelson et al.,

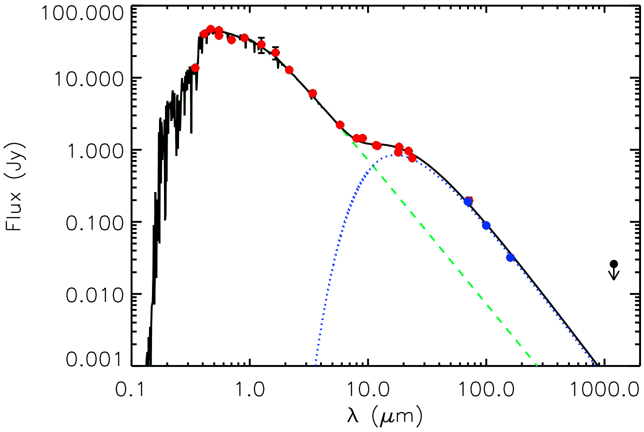

Figure 5.1: HD 172555 SED. The dashed line represents the photospheric contribution fitted using VOSA (Bayo et al., 2008) with $T_{\mathrm{eff}} = 7800$ K, $logg = 4.5$, $L_{\mathrm{star}} = 7.8\ L_{\oplus}$, while the solid one represents a photosphere plus modified blackbody model with $T = 280$ K and $\beta = 0.2$. Blue dots represent *Heschel*-PACS photometric points.

2006). Photometry was acquired with standard minimap configuration, with a scan length of 3 arcmin and scan angles 70 deg and 110 deg for the 70 and 100 μm bands. The *Herschel*-PACS photometer observes simultaneously in 70/100 μm and 160μm, so this gave us four maps at 160 μm. Photometric observations were reduced using HIPE 8. We combined the final images at the same wavelength using IRAF [1] IMCOMBINE, weighting the images with the exposure time. We performed aperture photometry with an aperture radius of 6 arcsec for the 70 and 100 μm bands and 12 arcsec for the 160 μm band. Photometric errors were computed by averaging the standard deviation in nine positions surrounding the source scaled with the square root of the number of pixels inside the aperture. Finally, we applied the aperture corrections supplied by the PACS team. Photometric fluxes are listed in Table 5.1. The source is point-like in the three PACS bands. The PACS photometric points are shown in blue in Fig. 5.1.

5.2.2 *Herschel* spectroscopy

The star was observed in chop/nod line spectroscopic mode with PACS on March 8, 2011 and September 10, 2011. PACS allows imaging of a 47 $arcsec \times 47\ arcsec$ field of view, resolved into 5×5 pixels known as spaxels. The observations were centred on the 63.18 μm [OI] $^3P_1 \rightarrow ^3P_2$ transition, within the wavelength range 62.94 to

---

[1] http://iraf.noao.edu/

Table 5.1: HD 172555 *Herschel* Space Observatory photometry

Wavelength (μm)	Flux density (mJy)	Statistical error (mJy)	Calibration error (mJy)	Total error (mJy)
70	191	1.6	5.1	5.3
100	89	1.8	2.4	3.0
160	32	3.2	1.3	3.5

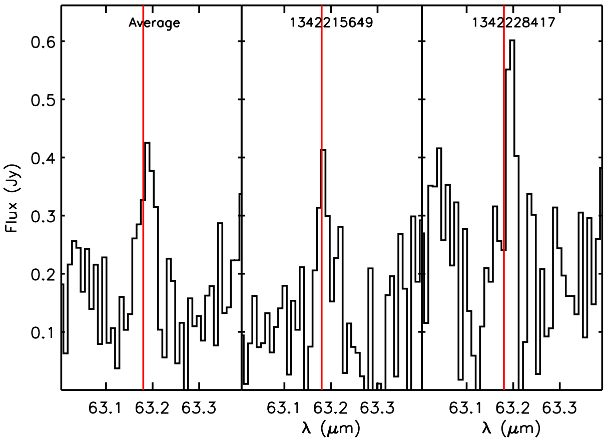

Figure 5.2: [OI] $^3P_1 \rightarrow^3 P_2$ spectral feature. The vertical red lines show the positions in the rest frame wavelength for the [OI] $^3P_1 \rightarrow ^3P_2$ transition at 63.18 μm.

64.44 μm, with a spectral resolution $\lambda/\Delta\lambda$ of 3570. We also observed the star with PACS in pointed chopped range spectroscopic mode on September 10, 2011, with the red channel centred around 158 μm, with a spectral resolution of 1265, aiming at the detection of [CII] emission at 157.74 μm. All spectra were reduced using HIPE 7 and a modified version of the reduction pipeline, including saturated and bad pixel removal, chop subtraction, relative spectral response correction, and flat-fielding. The spectra were extracted from the central spaxel and aperture corrected to account for dispersion in the surrounding spaxels. The final, reduced line spectra are shown in Fig. 5.2.

5.3 Results

5.3.1 Star properties and evolutionary status

A compilation of data from the literature was made to model the Spectral Energy Distribution (SED, see Table 5.2). The WISE magnitude limits in the Explanatory Suplement indicate that the 3.4, 4.6 and 12 μm photometry of HD 172555 is saturated. However, the WISE pipeline performs PSF fitting when dealing with saturated sources and produces accurate results for bands 1, 3, and 4. Unfortunately, for band 2 at 4.6 μm the pipeline does not produce good results for saturated sources (K. Stapelfeldt, private communication). We also retrieved IRAC observations from the *Spitzer* Space Telescope archive (AOR 3923456 for 3.4, 4.5 and 5.0 μm bands and 25202432 for the 8.0 μm) and extracted aperture photometry using MOPEX. The IRAC 3.6 and 4.5 μm photometry is saturated. The stellar parameters were computed by fitting Johnson, Strömgren, and 2MASS photometry with Kurucz photospheric models making use of the Virtual Observatory SED Analyzer (VOSA, Bayo et al., 2008). We find a value of 7.8 ± 0.7 $L_\oplus$ for the stellar luminosity (while Wyatt et al., 2007, finds 9.5 $L_\oplus$) and 7800±200 K for the effective temperature, while Chen et al. (2006) finds $T_{\rm eff} = 8550$ K, and Wyatt et al. (2007); Lisse et al. (2009) used $T_{\rm eff} = 8000$ K.

Table 5.2: Available photometry for HD 172555

Filter –	λ_0 (μm)	mag (mag)	$\sigma_{\rm mag}$ (mag)	flux (Jy)	$\sigma_{\rm flux}$ (Jy)	Ref –
Stromgren u	0.35	6.354	0.010	13.69	0.13	6
Johnson U	0.37	5.070	0.025	17.63	0.40	1
Stromgren v	0.41	5.203	0.009	40.49	0.34	6
Tycho B	0.42	5.015	0.014	38.89	0.50	3
Johnson B	0.44	4.790	0.019	53.87	0.94	1
Stromgren b	0.47	4.891	0.005	47.21	0.22	6
Tycho V	0.53	4.793	0.009	45.51	0.38	3
Johnson V	0.55	4.990	0.015	38.45	0.53	1
Stromgren y	0.55	4.779	0.003	45.40	0.13	6
Johnson R	0.70	4.887	0.023	33.40	0.71	1
Johnson I	0.90	4.581	0.025	35.74	0.82	1
2MASS J	1.25	4.382	0.26	28.92	6.93	2

Table 5.2: Continued.

Filter –	λ_0 (μm)	mag (mag)	σ_{mag} (mag)	flux (Jy)	σ_{flux} (Jy)	Ref –
2MASS H	1.65	4.251	0.212	22.24	4.34	2
2MASS Ks	2.15	4.298	0.031	12.82	0.37	2
WISE1	3.35	4.269	0.094	6.069	0.52	11
IRAC1	3.56	–	–	4.949	0.035	13
IRAC2	4.51	–	–	3.238	0.038	13
WISE2	4.60	3.775	0.059	5.309	0.29	11
IRAC3	5.76	–	–	2.214	0.007	13
IRAC4	7.96	–	–	1.458	0.004	13
AKARI9	9	–	–	1.451	0.017	10
WISE3	11.56	3.615	0.015	1.134	0.016	11
Si-5	11.7	–	–	1.155	0.002	8
WISE4	22.09	2.348	0.020	0.962	0.018	11
AKARI18	18	–	–	0.921	0.020	10
Qa	18.3	–	–	1.094	0.011	8
MIPS24	23.84	–	–	0.766	0.030	5
MIPS70	71.42	–	–	0.197	0.020	5
PACS70	70	–	–	0.191	0.005	7
PACS100	100	–	–	0.089	0.003	7
PACS160	160	–	–	0.036	0.002	7
LABOCA	870	–	–	0.040	0.01	9
SIMBA	1200	–	–	< 0.026	0.	12

(1): Johnson et al. (1966); (2): 2MASS catalogue (Skrutskie et al., 2006);
(3): Tycho-2 catalogue (Høg et al., 2000); (4) IRAS faint source catalogue;
(5): Rebull et al. (2008); (6) Hauck & Mermilliod (1998); (7): present work;
(8): Moerchen et al. (2010); (9): Nilsson et al. (2009), see text;
(10): Ishihara et al. (2010); (11): WISE Preliminary Release Source Catalog
(12): Schütz et al. (2005); (13): present work.

Fig. 5.3 shows the position of the star in the Hertzsprung-Russell (HR) diagram. An error of ±200 K was adopted for T_{eff} and the error bar in the luminosity corresponds to the uncertainty of 0.2 pc. The evolutionary tracks and isochrones from the Yonsei-Yale group (Yi et al., 2001) were used. Since the metallicity of

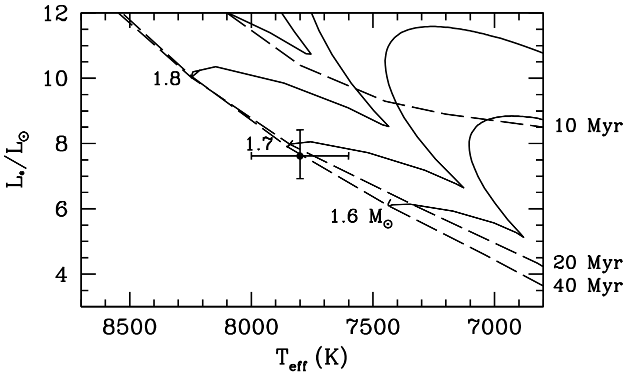

Figure 5.3: HR diagram for HD 172555. Dashed lines depict the position of the theoretical isochrones for different ages (Yi et al., 2001) while solid lines depict evolutionary tracks for different stellar masses.

this object is almost solar ([M/H]=0.09, Gray et al. (2006)) the set with $Z = 0.02$ (solar) was chosen. According to this comparison, we find $M_\star \simeq 1.68\ M_\odot$, and $\log g_\star = 4.28$, which implies $R_\star = 1.56\ R_\odot$. Given the position of the star and the uncertainties, we can only set a lower limit to the age of ∼ 17 Myr (Fig. 5.3). The different ages quoted for BPMG members range from 12 to 50 Myr, although the latter is an upper limit.

5.3.2 The dust disc

As can be seen in Fig. 5.1, little or no excess is detected at wavelengths shorter than 7 μm, while significant excess is seen at longer wavelengths.

We used a modified blackbody model to fit the IR excess in HD 172555: $F_{\rm cont} = B_\nu \times (\lambda_0/\lambda)^\beta$ where B$_\nu$ is the Planck function, $\lambda_0 = 13\,\mu$m and $\beta = 0$ for $\lambda < \lambda_0$. We do not use the 870 μm LABOCA point reported by Nilsson et al. (2009) because the association of the detected 2-σ signal with HD 172555 is ambiguous.

The modified blackbody model gives a temperature of 280 ± 9 K, with an opacity index (for $\lambda > \lambda_0$) $\beta = 0.2 \pm 0.2$, while a simple blackbody fit gives a higher temperature of 329 ± 6 K, but produces a poor fit to the SED. Rebull et al. (2008) fitted the HD 172555 IR excess with a blackbody at 310 K, in good agreement with our determination. We note that we can fit the whole SED with a single modified blackbody, implying that we do not see evidence from this data set for a reservoir of colder dust producing the far-IR emission. This means that the same dust population that produces the mid-IR excess can also produce the entire *Herschel*/PACS excess.

Table 5.3: HD 172555 PACS line observations.

Obs ID –	Center (μm)	Width (μm)	[OI] flux (10^{-18}W/m^2)
1342215649	63.183 ± 0.005	0.025 ± 0.014	8.2 ± 3.0
1342228417	63.195 ± 0.005	0.018 ± 0.005	9.1 ± 3.8
Average spectrum	63.188 ± 0.004	0.032 ± 0.008	9.2 ± 2.4

Notes. See Table 4.6 for updated fluxes using HIPE 9.

Using $R_{\rm in} > \frac{1}{2} R_* \left(\frac{T_*}{T_{\rm dust}}\right)^{(4+\beta)/2}$ (Beckwith et al., 1990), we computed the minimum radius for the dust distribution. We get $R_{\rm in,min} = 4.0 \pm 0.3$ AU. The infrared excess computed by integrating the model is $L_{\rm IR}/L_* \simeq 7.3{\times}10^{-4}$, slightly higher than the value shown in Wyatt et al. (2007) of 5×10^{-4}. We used the flux at 160 μm to estimate the dust mass of the dust disc using $M_{\rm dust} = F_\nu(160\mu{\rm m})D^2/(\kappa_\nu B_\nu(T_{\rm dust}))$, valid for optically thin discs, where $F_\nu(160\mu{\rm m})$ is the integrated flux density at 160 μm, D is the distance to the star (29.2 pc), B_ν can be approximated with the Rayleigh-Jeans regime and $\kappa_\nu = 2 \times (1.3{\rm mm}/\lambda)^\beta$ cm^{2}g^{-1}. The final dust mass is $(4.8 \pm 0.6) \times 10^{-4}\, M_\oplus$.

5.3.3 The gas disc

The [OI] $^3P_1 \rightarrow {}^3P_2$ transition at 63.18 μm was detected in both observations, with a signal-to-noise ratio of ~4 in the average spectrum. The emission is only detected on the central spaxel, indicating that it is centred on the star. Line fluxes ($F_{\rm line}$) were obtained by fitting a Gaussian plus continuum fit to the line and are shown in Table 5.3. In both spectral line observations, the line is spectrally unresolved within the uncertainties. The [CII] $^2P_{3/2} \rightarrow {}^2P_{1/2}$ emission line at 157.74 μm was not detected; instead, we determine a 3-σ upper limit of 5.3×10^{-18} W/m^2 for its flux. No molecular emission was observed in the blue channel in range scan observations, as reported in Chapter 4.

5.4 How to derive the oxygen gas mass

In the following we explain how to derive the atomic oxygen gas mass from prompt emission level population. To estimate the mass of oxygen gas we consider the excitation of atomic oxygen to its first fine structure level in the absence of a collisional partner. This situation happens in very low density environments such as debris discs. The main mechanism involved is the so-called prompt emission and fluorescence. The prompt emission involves the absorption of a photon from the star or from the dust at the precise wavelength of the atomic emission, and subsequent re-emission. To model the emission, we assume that the ground state is the most populated. The population at steady-state for level $^3P_2$ is given by:

$$0 = -n_1(A_{10} + B_{10}J_{10}) + n_0B_{01}J_{10} \tag{5.1}$$

Assuming that only the first two levels are populated ($n = n_0 + n_1$) then:

$$x = \frac{n_1}{n} = \frac{1}{1 + B_{10}/B_{01} + A_{10}/B_{01}J_{10}} \tag{5.2}$$

since $g_0B_{01} = g_1B_{10}$ and $B_{10} = (c^2/2h\nu^3)A_{10}$, the fractional population is:

$$x = \frac{n_1}{n} = \frac{1}{1 + g_0/g_1 + (g_0/g_1)(2h\nu^3/c^2J_{10})} \tag{5.3}$$

For OI we have $g_0 = 5$, $g_1 = 3$. J_{10} is computed using the distance-dilluted stellar flux in the Rayleigh-Jeans regime at 63 μm:

$$J_{10} = \frac{1}{4\pi}\left(\frac{R_*}{R}\right)^2 \frac{2kT_*}{\lambda^2}, \tag{5.4}$$

where R is the distance to the star and R_* the stellar radius. We obtain $J_{10} = 2.273 \times 10^{-13} \times (1\mathrm{AU}/\mathrm{R(AU)})^2$ erg s^{-1} cm^{-2} Hz^{-1} sr^{-1}, and the fractional population is thus: $x = 8.67 \times 10^{-5}$

The number of oxygen atoms given the flux in cgs is then

$$\mathrm{N_{[OI]}} = 9.5216 \times 10^{36} \frac{F_{\mathrm{line}}(erg\ s^{-1}\ cm^{-2}) \times D^2(pc^2)}{\frac{h\nu}{4\pi}A_{ul}\ x} R(AU)^2 \tag{5.5}$$

where 9.5216×10^{36} combines the conversion from arcsec^2 to steradian and from AU to parsec.

The effect of including additional excitation paths is negligible. We make here the comparison when the emission is produced at 1 AU from the star. For example, if we include all the main fluorescence pumping paths ($^2P_2 \rightarrow {}^1S_0 \rightarrow {}^3P_1$, $^3P_2 \rightarrow {}^1D_2 \rightarrow {}^3P_1$, and $^3P_2 \rightarrow {}^1S_0 \rightarrow {}^1D_2 \rightarrow {}^3P_1$) the final mass of oxygen is M([OI]) = 0.0247 $\mathrm{M_\oplus}$, compared to M([OI]) = 0.025 $\mathrm{M_\oplus}$ obtained when we only include the main excitation path.

If the emission is originated at the minimal possible position of the dust ring at ∼ 4.0 AU, then the [OI] mass is ∼ 0.39 $\mathrm{M_\oplus}$. If the emission comes from the inner ring location computed in Chapter 4.5.3, then the gas mass is$\sim$ 0.1 $M_\oplus$. The computed mass is huge, so the reservoir for the [OI] gas must have been very large. Nevertheless, the total atomic oxygen mass strongly depends on the location where the emission comes from (as R^2). For instance, the [OI] gas mass decreases to between a few $10^{-4}\,M_\oplus$ and a few $10^{-3}\,M_\oplus$ if it is located near the size-, and composition-dependent dust sublimation radius (~0.1–0.5 AU). But we note that, even in this case, the [OI] gas mass remains large compared to the dust mass.

5.5 Origin of the gas

Our *Herschel*/PACS observations reveal a copious amount of atomic oxygen, although the exact mass depends somewhat on its unconstrained radial location (Sec. 5.3.3). This raises the question of its origin. HD 172555 is a rare debris disc. The dust is located in the inner system at only a few AU from the star (Sec. 5.3.2), in contrast to typical debris discs composed mainly of cold Kuiper belt-like dust at much larger distances from the star (e.g. the co-eval BPMG member HD 181327, Lebreton et al., 2012). Here, we speculate about two different origins for the observed [OI] gas.

5.5.1 Recent release during a catastrophic event

The models of Wyatt et al. (2007) argue that HD 172555 infrared fractional luminosity is $\sim$ 86 times higher than the maximum value expected from steady-state collisional evolution under their modelling assumptions at an age of 12 Myr. Although a different parameter selection could perhaps explain the departure from the maximum value, the authors pointed out that a major stochastic event may be playing a role.

Emission features in the *Spitzer*/IRS spectrum of HD 172555 were modelled by Lisse et al. (2009), who suggested the presence of glassy silica. They also tentatively attributed faint features to rovibrational transitions of SiO gas. They concluded that the dust composition, and the presence of SiO gas (if confirmed), point to a violent production process, such as an hypervelocity collision between massive planetary bodies. This suggestion was additionally supported by the hypervelocity collision experiments conducted by Takasawa et al. (2011). These authors found that the ejecta typically had a steeper grain size distribution than expected for an equilibrium distribution in a standard collisional cascade, as proposed by Lisse et al. (2009) to describe the warm dust in HD 172555 ($dn/da \sim a^{-4}$). This would argue for a source of fresh material, which would have had to be produced within the last 0.1 Myr to be consistent with SiO recondensation. Recently, Pahlevan et al. (2011) showed that silicate constituents (Si, Fe, Mg and O) can be produced in the form of gas during hypervelocity collisions. Therefore, one can speculate that the origin of atomic oxygen detected with *Herschel* could be the violent event proposed by Lisse et al. (2009) to explain the shape of the *Spitzer*-IRS spectrum. The lack of [CII] emission further supports this physical origin for the [OI] gas: the sublimation of pyroxenes and olivines will produce copious amounts of O and Si, Fe and Mg, but as C is not a constituent of silicate materials, no C emission would be expected.

5.5.2 Gas accumulation over time

The extremely low sensivity of OI to the radiation pressure from this A-type star (Fernández et al., 2006) opens the door to alternative, perhaps less catastrophic scenarios as for the origin of the detected OI gas. Atomic oxygen could indeed accumulate over time at the place where it is produced. For instance, the considerable collisional activity in the dust ring presumably releases a population of poorly bound, or unbound grains due to radiation pressure, which can collisionaly vaporize larger grains due to high relative velocities (β-meteoroids). This has been proposed by Czechowski & Mann (2007) to explain the stable gas in the co-eval β Pictoris system. Assuming that oxygen is originally locked into olivine grains, a dust mass of $\sim 0.9\,M_{\oplus}$ would need to have been vaporized in less than 12 Myr, corresponding to a mass rate higher than $7 \times 10^{-8}\,M_{\oplus}$/yr ($10^{13}$ g/s). Interestingly, this value compares to the mass rate derived by Czechowski & Mann (2007) at the peak position of the β Pictoris dust disc (50–100 AU).

The sublimation of grains close to the star, at ~0.1–0.5 AU, could also contribute to the production of OI. Although the 4 AU-radius dust ring is collision-dominated, models by Wyatt (2005c) and Löhne et al. (2012) show that, even in this case, a fraction of the dust grains can escape the collisional cascade and migrate toward the star by Poynting-Robertson (P-R) drag. Silicates extracted from the ring will eventually reach sufficiently high temperatures as they approach the star and produce O, SiO and MgO, and ultimately Si, Mg and O. Assuming again that O is locked in olivine grains, a reference dust mass of $\sim 10^{-3}\,\mathrm{M}_{\oplus}$ would need to have been extracted from the dust belt by P-R drag to explain the PACS data over an unknown time span. A strict minimum supplying mass rate of about $10^{-10}\,\mathrm{M}_{\oplus}$/yr is obtained assuming a unit efficiency in atomic O production by sublimation over the longest possible time span (12 Myr), and assuming that the gas has not viscously flown inward or outward. On the other hand, the P-R drag timescale for bound grains in the 4-AU radius dust ring, $t_{\mathrm{PR}} > 7500$ yr (e.g. Wyatt, 2005c), yields an upper limit on the present-day P-R drag mass loss rate of a few $10^{-8}\ M_{\oplus}$/yr. This implies that this process had to last for longer than a few 10^4yr.

5.5.3 Discussion

Different scenarios can qualitatively explain the OI enrichment of the HD 172555 disc. We note that these are not necessarily mutually exclusive since gas accumulation could follow the giant collision proposed by Lisse et al. (2009), if it did not occur too recently. For instance, it takes about 1 Myr for the debris created in a giant impact to form an axisymmetric disc (Jackson & Wyatt, 2012), and be consistent with observational constraints (Smith et al., 2012). This may leave sufficient time to accumulate OI gas at some place in the disc. Additional processes, such as comet evaporation or grain photodesorption (Chen et al., 2007), also deserve to be mentioned as possible OI providers. In summary, the origin of the detected OI gas remains open, and detailed modelling of the processes discussed here, as well as the detection of atomic or ionized Fe, Mg, and Si will help to identify the source of OI gas.

5.6 Summary and conclusion

Our main results can be summarized as follows:

1. We report the detection of the [OI] line in the debris disc of HD 172555 with a flux of $(9.2 \pm 2.4) \times 10^{-18}$W/m^2. This is the first unambiguous detection of gas in this system.
2. We modelled the SED of the object with a Kurucz photospheric model ($T_{\mathrm{eff}} = 7800$ K, $\log g = 4.5$, $L_{\mathrm{star}} = 7.8\ L_{\oplus}$) plus a modified blackbody to fit the infrared excess at $\lambda > 7\ \mu$m. We obtain $T_{\mathrm{dust}} = 280$ K and $\beta = 0.2$. We derive a dust mass of $\sim 4.8 \times 10^{-4} M_{\oplus}$.
3. Using purely analytical relations and simple assumptions, we derive an [OI] mass of $2.5 \times 10^{-2} R^2\ M_{\oplus}$ where R is the unconstrained radial location of the gas.

4. Although the spatial origin of the line is uncertain, we speculate about a possible origin in an hypervelocity collision, or in gas accumulation over time due to the low radiation pressure on atomic oxygen. The lack of [CII] emission further supports this statement.
5. HD 172555 provides a valuable window on the processes that occur during the early stages of terrestrial planet formation, including massive collisions like the one that produced Earth's moon (Canup & Esposito, 1996).

Chapter 6

General discussion

In the following chapter, the main results in the individual associations will be discussed in an evolutionary framework, with special emphasis on the gas contents.

The most important conclusion on the overall properties of circumstellar discs is that there must be several factors, and not only age, driving disc evolution. These factors could be related to the mass and composition of the original cloud, the mass of the central object, binarity, angular momentum, the history of planet formation and others. This fact is illustrated by the great diversity of disc properties in TWA: at 7 Myr, both transitional/debris, and gas-rich/gas-poor discs coexist in the same association.

6.1 Dust evolution

In the following we discuss dust properties in the BPMG and TWA associations and in a more general framework, in the GASPS sample, with special emphasis on the time scale for dust clearing.

As we showed in Chapter 1, the evolution of the fraction of stars with discs with age has been extensively studied in the past. In Fig. 6.1 we show the fraction of stars with discs for associations in the GASPS sample (left panel), and including more associations from the study by Mamajek (2009) (right panel). We also plot the exponential law for the decay of the disc fraction by Mamajek (2009) and our own fit to GASPS associations according to disc fractions in Dent et al. 2013 (submitted).

The exponential model used to fit the data is define by the expression:

$$f = e^{-t/\tau_{disc}} \tag{6.1}$$

where f is the fraction of discs an $\tau_{\rm disc}$ is the e-folding timescale for the decay of the disc fraction. In Mamajek (2009), $\tau_{\rm disc} = 2.5$ Myr, while our fit to GASPS data shows a much larger value of $\tau_{\rm disc} = 5.2$ Myr. As we include more associations in the analysis (Fig. 6.1, right panel, with data for other associations from the literature) we approach the value obtained by Mamajek (2009). The big difference therefore reflex the fact that there is not a unique timescale for the decay of protoplanetary discs, i. e., there is not a single disc lifetime; instead, there is a range of possible lifetimes. We conclude that they depend on several factors, including environmental influences. We can estimate protoplanetary disc lifetimes for individual associations using:

$$\tau_{disc} = -\tau/ln(f) \tag{6.2}$$

(Mamajek, 2009), where τ is the age of the association and f is the fraction of protoplanetary discs in the association. The mean protoplanetary disc lifetime for associations in the GASPS sample is $\tau = 5.5 \pm 2.1$ Myr. This result for the disc lifetimes further strengthen the statement made in Chapter 3 that there are several factors driving disc evolution and not only the age. Hence, the timescale for protoplanetary disc clearing have to be considered in a statistical way, because it changes not only from one association to another, but from one disc to another in the same association depending on the conditions.

Once in the debris stage, the evolution is much more quiescent: Wyatt et al. (2007) showed that the evolution of the infrared fractional luminosity can be explained by pure steady state evolution. The decay timescale for the 70 μm excesses is much longer than that of the 24 μm excess (Su et al., 2006), hence the evolution of the cold dust (debris like dust) takes much more time. According to Wyatt et al. (2007) the wide range of disc properties observed can be explained in terms of steady evolution, due to the spread in initial disc masses and radii. But stochastic events can dramatically increase the infrared excess, resulting in outliers departing from pure steady state evolution. The main problem is to know the frequency of such stochastic events to weight their influence in circumstellar dust and gas evolution in debris discs. Objects like HD 172555 can help us to better understand the impact of such events. It is a warm debris disc, with a fractional infrared luminosity that is about 86 times larger than the maximum value expected from pure collisional

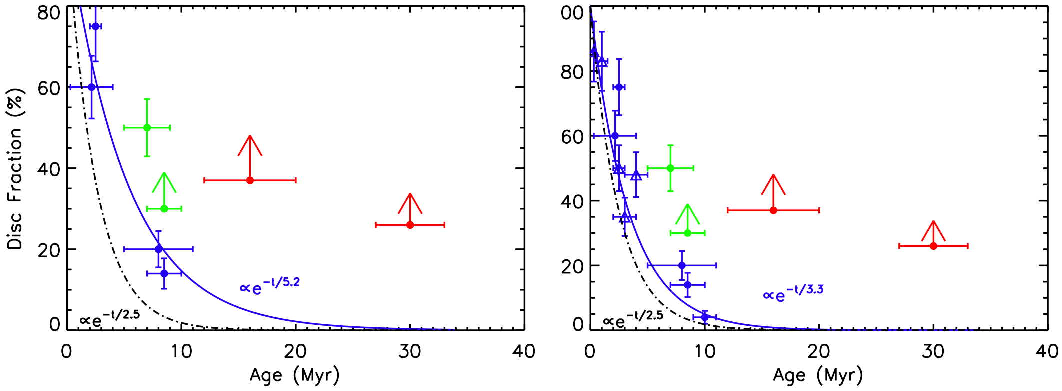

Figure 6.1: Fraction of discs as a function of the age age for the different associations in the GASPS sample. Error bars in the age axe represent the range of ages proposed by different authors. The error in the fraction of discs is the counting error ($f^{1/2}$, where f is the fraction of discs). Left panel shows the disc fraction for associations in the GASPS sample, with the last disc fractions from the GASPS overview paper (Dent et al. 2013, submitted). Right panel includes extra information for some associations studied by Mamajek (2009). Blue points depicts protoplanetary disc fractions only; green points include both debris discs and T Tauri stars in the disc fraction; red points include only debris discs in the disc fraction. The blue solid line shows an exponential fit to the protoplanetary fractions, while the dashed-doted black line depicts the fit by Mamajek (2009). For TWA two fractions are shown: the overall fraction of discs and the fraction of protoplanetary/transitional discs.

evolution. Most important, we have detected atomic oxygen emission from its disc. Warm debris disc and debris discs with a large infrared fractional luminosity are then important targets for the study of the influence of stochasticity; nevertheless, they are also very interesting targets for future surveys of gas in debris discs. If the gas in HD 172555 comes from an stochastic event, and considering that it is the only member of the BPMG experiencing such event, then the frequency of stochastic events should smaller than 1 every few hundred Myr ($< 5 \times 10^{-3}$ Myr^{-1}).

The TWA association is very interesting, not only because it is the nearest association with actively accreting discs (TWA01, TWA 03A), but because the variety of disc properties. TWA members detected with PACS do not show tiny infrared excesses, while in BPMG we detect fractional infrared excesses in a wide dynamical range (10^{-6} – 10^{-3}), including the detection of one of the smallest to date: that in HD 29391, $L_{IR}/L_* < 4.6 \times 10^{-6}$, slightly higher than that of our own Kuiper Belt. Discs in TWA include both transitional and debris systems, while in BPMG we only see optically thin, dusty debris discs. Therefore, it seems that the TWA association age is critical for the transition from primordial dust to second generation dust formed through collisional grinding. Also, the gas and dust masses in TWA 01 are large enough to form a planetary system, therefore the timescale for planet formation could be slightly larger for some peculiar systems like TWA 01. In a general way, we can say that the timescale for planet formation is slightly different for each association/system.

6.2 Gas evolution

6.2.1 Gas clearing timescales

While the timescales for dust clearing in protoplanetary systems have been extensively studied in the past, the timescale for gas clearing is less known due to the limitations to detect gas with old instrumentation. Thanks to the great *Herschel* sensitivity in the far-IR, the problem can now be tackled.

In Fig. 6.2 we plot the fraction of discs versus the age for the associations studied by the GASPS team. A clear decline of the fraction of discs with gas is seen toward older systems, in agreement with previous results. We note that the gas in the different associations must have different origins. The gas in Taurus is primordial, therefore reflects the composition of the original molecular cloud after some reprocessing in the viscosity dominated disc. The gas toward TWA 01 seems to have also a primordial origin, considering the line flux-to-continuum flux ratios shown in Chapter 3, but the gas in TWA 04B must have a different origin, most probably cometary, again according to the flux ratios. The gas in β Pictoris has a cometary origin, as shown by different authors (Lagrange et al., 1987; Lagrange-Henri et al., 1989) although NaI in keplerian rotation has been found (Olofsson et al., 2001). The gas in HD 172555 seems to have its origin in an hypervelocity collision or in cometary activity: if the gas comes from the sublimation of pyroxenes and olivines, then we would have expected emission of Fe, MG and Si, but not from C. We observed HD 172555 around 158 μm aiming at the detection of [CII], but did not succeed. The lack of [CII] emission in HD 172555 (also in TWA 04B) favors the hypervelocity/cometary activity origin.

Because we are now interested in the timescale for gas clearing in protoplanetary systems, we restrict the analysis to the young associations with protoplanetary/transition discs in the GASPS sample, i. e., Taurus, Chamaeleon II, Upper Scorpius and protoplanetary systems in TWA (blue dots). For the purposes of the following analysis, we consider TWA 04B as a debris disc, and include TWA 03A

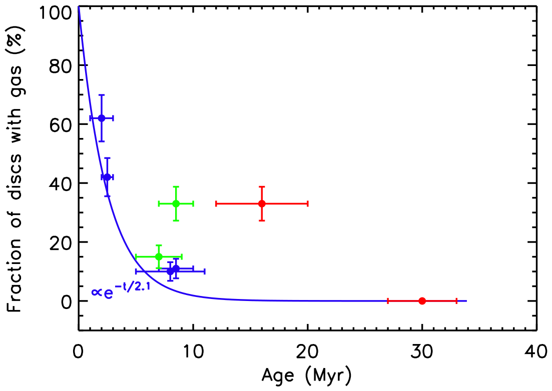

Figure 6.2: Fraction of discs with gas versus age for the different associations studied based in [OI] emission at 63.18 μm. Legend as in fig 6.1.

as a gas rich transitional system because the system is actively accreting. We fitted the data using an exponential function, following 6.1. The resulting exponential law is shown in blue in Fig. 6.2, with an e-folding time $\tau = 2.1$ Myr. By comparing the timescale for gas clearing and the timescale for dust clearing from the previous section, we see that the timescale for gas clearing seems to be smaller. To further study this difference, we show in Table 6.1 the dust and gas clearing timescales for individual associations with protoplanetary/transitional discs in the GASPS sample. Gas clearing timescales are always smaller than dust clearing timescales, with the only exception of Taurus, illustrating how the clearing of gas is most probably a preliminary step before the clearing of the dust.

Table 6.1: Gas and dust clearing timescales

Association	$\tau_{\rm dust}$	$\tau_{\rm gas}$
–	(Myr)	(Myr)
Taurus	4.2	4.2
Cha II	8.7	2.9
TWA	4.3	3.5
Upper Scorpius	5.0	3.5

6.2.2 Statistics and characteristics of [OI] gas detections

In the following, we rely on the more general results of the GASPS programme. The first results from the GASPS sample demonstrate that [OI] at 63 μm is the brightest and most abundant line emission in the far-IR for circumstellar systems. It is present in ~ 49% of the targets observed, while [OI] at 145 μm is present in ~ 38% of the observed targets, and [CII] in the ~ 25%. These detection fractions demonstrate that [OI] at 63 μm is the best far-IR probe of gas in discs. The [OI] line emission is not resolved in most of the GASPS observations: the flux ratio between the central and the surrounding spaxels agrees with non-extended emission. Therefore, emitting regions are typically ≤ 500 AU.

Regarding the mass of the central object, the [OI] line is detected in all HAeBe stars in the sample, while it is detected in ~ 45% of the sample of T Tauri stars. Therefore, the mass of the central object seems to play a role in [OI] emission at 63 μm. The total mass of the disc itself also plays an important role: in Dent et al. 2013 (submitted) we showed that emission from discs 140 pc away is detected in ~ 85% of objects with a total disc mass > 10^{-3} $M_\odot$, and in ~ 95% of objects with > 10^{-2} $M_\odot$. But these numbers are computed assuming a gas-to-dust ratio of 100, while we have shown that the ratio can be much smaller in certain systems like TWA 01. Considering this limitations, we can say that [OI] observations can detect discs with $M \geq 10^{-4}$ $M_\odot$. But there are important exceptions to this law, like HD 172555. Therefore, for objects with atypical gas origins and abundances, we can detect oxygen emission implying disc masses as low as a few 10^{-7} $M_\oplus$. The opposite situation also happens: very massive discs with huge masses but without [OI] emission, like the young Taurus star GO Tau. Woitke et al. (2010) pointed that the [OI] emission can be hard to detect for massive discs when the flaring index γ is below 1.0. We get a similar result for TWA 03A (see Chapter 3.7.2).

Multiplicity seems also to influence the detection of [OI]: lower detection rates were found in multiple systems with separations ≤ 300 AU, whereas objects with separations > 300 AU show detection fractions (47%) similar to those of single stars. This result suggest that the emitting region of [OI] is < 300 AU.

A conclusion from the previous paragraphs is that there is not a single parameter driving gas detectability, but an interplay between many factors like star/disc masses, binary, geometry of the disc, etc...

6.2.3 Statistics and characteristics for other gas lines

In Chapter 2 it was shown that 49 % of T Tauri stars in Taurus (1–3 Myr) show [OI] emission and therefore are gas rich systems. In 8 of these gas rich systems (24 %) we also observed an emission of warm water; nevertheless, we found 10 tentative detections in the 2–3 σ level, so the real fraction of water rich systems could be even

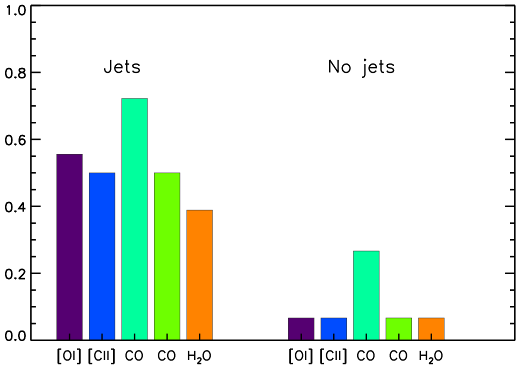

Figure 6.3: Histogram representing the fraction of Taurus stars showing the different species according to the analysis of PACS range spectra. Two different emitting lines of CO are shown, with wavelengths 144.78 μm and 153.27 μm.

higher. When extended to the whole sample, the detection rate of water at 63 μm is smaller than 7 %. By a certain age, the whole sample of warm water vapour has disappeared.

In Fig. 6.3 we show an histogram representing the fraction of discs showing each line emission, from a sample of 35 T Tauri stars in Taurus observed with PACS in range scan spectroscopic mode as part of the GASPS program. The 35 stars showed [OI] emission at 63 μm. Results are preliminary. We plot two different groups: objects with jets and objects without jets. As can be seen, gas emission is most widely detected in system with outflows. The most detected specie is CO, present in more than 70 % objects with jets and in ~ 25% of objects without disc. The most important result from this plot is that a rich chemistry seems to be associated with the presence of an outflow. But we note that this histogram does not imply that the emission arises from the jet: for most cases, emission is detected only in the central spaxel (at the distance of Taurus this translates into a distance a size of ~1300 AU), and therefore it seems to be confined to a small region, in better agreement with a disc origin, as stated for the water emission at 63.32 μm in Chapter 2. However, to distinguish whether the lines originate in a disc or in an outflow requires spectroscopy with high angular resolution.

6.2.4 Comparison of Taurus, TWA and BPMG detections of [OI] and H_2O

Finally, we compare the gas detections in the three associations studied in detail in the present Thesis.

TWA is an old association (8-20), but three of their members show different signatures of gas. The first is TWA 01, a gas rich system that has been considered a transitional/protoplanetary disc depending on the author. We have detected atomic oxygen emission toward TWA 01, and estimated a gas mass of 160–1600 $M_{\oplus}$. Furthermore, recent work by Bergin et al. (2013) demonstrates that the gas mass could be even higher. TWA 03A has been classified as an accretor by different authors (Muzerolle et al., 2000; Huenemoerder et al., 2007), a result that we have confirmed by comparing its H_{α} equivalent width with the accretion criterions by Barrado y Navascués & Martín (2003). But TWA 03A does not show [OI] emission, a result that we tentatively explain in terms of a flat disc. TWA 04B, in the other hand, shows [OI] emission, but no signatures of accretion. We consider that the lack of accretion is linked to the binary nature of the system, that opens a gap in the disc in the region < 1 AU. Although the result is preliminary and requires dedicated work, the trends in the previous sections in [OI] gas detections for the GASPS sample point to a second generation origin for the gas detected in TWA 04B. According to previous work, and our own results, there are seven systems with discs in TWA: TWA 01, TWA 03A, TWA 04B, TWA 07, TWA 11A, TWA 26 and TWA 28 (two brown dwarfs with discs detected in excess at 24 μm using Spitzer Riaz et al., 2006). We do not have information about the gas content in the last two systems. None of these systems with gas show water emission at 63.32 μm.

There are 10 stars with discs in the BPMG, including β Pictoris itself and our new discovery of an excess toward HD 29391. Gas emission has been found only in two discs in the association: the well known reservoir of gas species in β Pictoris and our new discovery of atomic gas emission in HD 172555. The percentage of discs with gas is therefore in the range 20–70 %. We have claimed that atomic oxygen gas in HD 172555 has a stochastic origin, but stochastic events seem to be rare, according to the law detection rate of warm debris discs (which we consider a signpost of stochasticity). Therefore, the range is most probably not real, and the real fraction, considering all BPMG members, is much smaller than 20 %. Again, no water have been observed toward any disc in BPMG.

As we showed in Chapter 2, the water emission comes from a region 3 AU wide at ~ 1 AU from the central star. Discs in BPMG are mostly devoid of material 2 AU inward, and are second generation debris discs, where little or no gas is expected to be detected. Discs in TWA are less evolved that BPMG discs: TWA 01, TWA 03 A are typically considered transitional discs, while TWA 04B is sometimes considered a debris and sometimes a transitional disc. Finally, TWA 07 and TWA 11A are both debris discs. Therefore, although [OI] gas can be detected in evolved, debris and transitional systems, with different origins, but water emission is harder to detect, if possible. The warm water reservoir have disappeared in those evolved systems, due to the different mechanisms of gas dispersal explained in Chapter 1. We speculate that, considering the emitting region, the dispersal mechanism could be directly related with telluric planet formation. Following the ages of these systems, by the age of 7 Myr, the reservoir of warm water has most probably disappeared. Furthermore, no water emission was found in any protoplanetary disc in Upper Scorpius (Mathews et al., in prep.), so the the timescale for clearing the warm water vapour could be even smaller (< 5 Myr). This kind of information will help us to understand the process and timescales involved in planet formation.

Again, results on [OI] detection rates in the three associations studied in detail indicate that:

1) There is not a unique timescale for gas clearing.
2) There are several factors driving gas detectability and evolution.

Chapter 7

Conclusions

The use of *Herschel* observations of circumstellar systems is helping the astronomical community to deep in our knowledge of the gas and dust contents in those systems, allowing for the first time the detection of atomic and molecular emission in the far-IR range. Also, photometry with PACS takes advantage of this instrument great sensitivity to detect cold, faint emission from debris discs with SEDs peaking around 100 μm. We have used the GASPS program observations of circumstellar systems in Taurus, TWA and BPMG to deep in our knowledge of evolutionary trends in both the gas and dust components.

In Chapter 2 we studied PACS line spectra observations of T Tauri stars in Taurus, highlighting the presence of warm water emission in some of them. Of the 68 T Tauri stars observed, 33 ($\sim$ 49%) show [OI] emission above the 3-σ level, and therefore can be considered gas rich systems. Eight of these systems also show water vapor emission around 63.32 μm ($\sim$ 24% of the gas rich sample, 12% of the whole sample). All the systems showing water emission are also jet sources, but the emitting region seems to be small when compared to [OI] and continuum emission, and therefore we concluded that, most likely, the emission comes from the disc alone. Aiming to better understand the physical origin of the line, we made a survival analysis of the correlations with some star and disc parameters. Possible correlations between the intensity of the line emission and the continuum flux at 63 and 850 μm, [OI] line luminosity, X-ray flux and the slope of the SED in the 2–8 μm range were found. They correlation with [OI] emission may suggest a similar origin for both lines, but may also be just related with gas abundances: the more gas is present, the more prominent is the [OI] emission, and more H_2O can be detected. The correlation with the X-ray flux is more interesting: only objects with X-ray luminosities higher than 10^{30}erg/s were detected. Therefore, it seems that the X-ray flux acts as threshold mechanism: when the X-ray luminosity is over this threshold (10^{30}erg/s), warm water emission is triggered. Aiming to understand the origin of the water emission, we developed a ProDiMo model which predicted an emitting region of the order of 3 AU wide at $\sim$ 1 AU from the star, consistent with the typical location of the snow line.

In Chapter 3 we analyzed PACS spectroscopic and photometric observations of stars in the TWA association. We reported the first detection of 100 μm emission toward TWA 03A and of 100/160 μm emission toward TWA 07. We also reported the first detections of atomic oxygen emission toward TWA 01 and TWA 04B with very different levels of emission. We note the lack of [CII] emission toward TWA 04B. We modeled dust emission using simple modified blackbody models, and derived dust mass and radii. We noted the great diversity of discs in the association, from the protoplanetary/transitional disc around TWA 01 to the gas poor/empty disc with two different rings for TWA 07, the outer at only 20 K. MCFOST models were also used to model the dust around TWA 01, and ProDiMo to model the gas component, resulting in a mass of 160-1600 $M_{\oplus}$. Given the lack of other gas species detections toward TWA 04B, we modeled the gas emission using simple assumptions for gas at 100 K, and derived a gas mass of $(0.8–5.0)\times10^{-3}$ $M_{\oplus}$, thus several orders of magnitude smaller than the gas mass in TWA 01. Considering the low ratio of gas to dust emission, we favour gas production through cometary activity rather than a primordial origin. We also computed upper limits for the gas mass assuming an excitation temperature of 100 K. The main conclusion from this chapter is that disc evolution is not only driven by the age of the system, but by several factors together, such as disc and stellar masses, chemical composition or planetary formation itself.

In Chapter 4 we analyzed PACS photometric and spectroscopic observations of BPMG members. We reported the detection of several objects for the first time at 70/100/160 μm. Flux in excess at 70 μm was detected for the first time in HD 29391, with a very small infrared fractional luminosity, similar to that of the Sun's Kuiper Belt. Atomic oxygen emission was detected for the first time toward HD 172555, but no [CII] emission was observed, like for TWA 04B. We modeled dust emission with modified blackbody models, resulting in temperatures in the range 68 to 278 K. We also modelled the dust emission with more sophisticated MCFOST models, resulting in dust masses in the range 3.3×10^{-4} $M_{\oplus}$ to 0.13 $M_{\oplus}$, and inner radii in the range 4–34 AU. We also show results of a more sophisticated GRaTeR model for HD 181327, with big details about the mineralogy of the dust. All discs in BPMG are debris discs, compared with the great diversity of objects in TWA. Therefore, it seems that the TWA Association is in a critical stage for the transition from primordial to debris discs, while the slightly older BPMG members have already cleaned all the primordial material.

In Chapter 5 we discussed with more detail the detection of atomic oxygen emission toward HD 172555. This is the first clear detection of gas in the system, and one of the first detections of atomic oxygen in a debris disc. Using blackbody models we derived a dust temperature of 280 K, slightly larger than that shown in Chapter 4, but we note that in the HD 172555 deep analysis we did not included IRS observations. Using analytical relations and simple assumptions, we computed a gas mass of $2.5 \times 10^{-2} R^2$ $M_\oplus$. Using the more accurate estimation of the disc inner radii from Chapter 4 (2 AU) we get $M_{gas} = 0.1$ $M_\oplus$. This atomic oxygen gas mass is huge. We propose a possible origin for the gas in HD 172555 in an hypervelocity collision. IRS data analyzed by Lisse et al. (2009) supports the idea of an hypervelocity collision producing huge amounts of gas and warm dust. Given the peculiarities in the system, we consider that the presence of warm dust and atomic oxygen gas must be linked phenomenons.

Finally, in Chapter 6 we have shown that the timescales for gas and dust clearing must be different, and also that there are several factors driving gas and dust evolution, therefore any consideration about a timescale must be considered carefully. The presence of [OI] gas seems to be influenced by the mass of the disc, the mass of the central object, multiplicity and most probably by many other parameters.

7.1 Future work

Future work will help us to better understand the evolutionary trends in gas and dust by comparing PACS data in different associations at different ages. The GASPS program has observed not only Taurus, TWA and BPMG, but also Upper Scorpius, η Chamaleontis and Tucana Horologium discs. The photometric and spectroscopic data is now ready for scientific exploitation. The next step in the GASPS project is to produce a final, open catalogue that can be used by the whole astronomical community. We plan to use the last version available of HIPE, together with the most recent calibration files. The final catalogue will contain not only reduced images and spectra, but also photometric and spectroscopic fluxes, resulting in the most extensive library of observed far-IR line fluxes in circumstellar systems to date.

Although the GASPS program has already produced a large amount of scientific papers, most of them have focused on the analysis of individual objects or associations. Another task to be tackled in the future is to statistically analyze the whole dataset in a coherent way. Also, the analysis of the different lines in Taurus members range spectra will result in the widest catalogue of far-IR gas detections toward protoplanetary discs to date. We will get useful insight on the gas properties and evolution for Class II objects. A preliminary reduction and analysis of the data is being performed, as we showed in Chapter 6.

The origin of the water line at 63.32 μm needs to be understood. As we showed in 6.2, high spatial and spectral resolution will help us to study the mechanism that originates the line and the location of the emitting region. Observing water emission in the near-IR with high angular resolution in Taurus members with a water detection at 63.32 with the VLT Cryogenic high-Resolution Infrared Echelle Spectrograph (CRIRES) will help us to better understand the origin of the water emission, assuming that both sets of lines originate from the same reservoir. If the line comes from the disc, we expect the line center to be at the rest frame wavelength, with blue shifted and red shifted peaks due to Keplerian rotation. Otherwise, if the emission has a velocity shift we would see evidence that the lines are emitted in a wind or in a jet. A proposal with this objectives is in the process of being submitted.

The detection of [OI] gas emission toward TWA 04B and HD 172555 requires dedicated work, in order to understand the mechanism producing the gas. Also, the lack of [CII] emission needs to be understood, although it is an expected result if the gas is originated in an hypervelocity collision, as we showed in Chapter 5. The detection of other gas species is of main interest, because different compositions of the gas indicate different origins.

The research of circumstellar environments will highly benefit form the use of the *Atacama Large MIlimeter/submilimeter Array* (ALMA). Thanks to its unprecedented spatial resolution we will get insight in the detailed distribution of dust in discs, allowing the systematic detection of structures that may result of the interaction of the disc with a planet. Also, its high sensitivity will allow the detection of gas in gas-poor systems where the emission have escaped past instrumentation. In that sense, the participation in ALMA observing runs is the perfect complement to *Herscel*-PACS data. To that aim, acquiring the abilities to reduce and analyze ALMA data is of main interest.

Finally, modeling gas in debris discs requires a code able to treat separately the gas and dust phases, as they are not any more coupled in low density discs. Nevertheless, the code must be adapted to work with non solar abundances and with time-dependent gas chemistry. We plan to adapt the PRoDiMo code to the described needs.

References

AKESON, R. L., RICE, W. K. M., BODEN, A. F., SARGENT, A. I., CARPENTER, J. M. ET AL. (2007). The Circumbinary Disk of HD 98800B: Evidence for Disk Warping. *ApJ*, 670, 1240–1246.

ANDRE, P., WARD-THOMPSON, D. & BARSONY, M. (1993). Submillimeter continuum observations of Rho Ophiuchi A - The candidate protostar VLA 1623 and prestellar clumps. *ApJ*, 406, 122–141.

ANDREWS, S. M., CZEKALA, I., WILNER, D. J., ESPAILLAT, C., DULLEMOND, C. P. ET AL. (2010). Truncated Disks in TW Hya Association Multiple Star Systems. *ApJ*, 710, 462–469.

ANDREWS, S. M. & WILLIAMS, J. P. (2005). Circumstellar Dust Disks in Taurus-Auriga: The Submillimeter Perspective. *ApJ*, 631, 1134–1160.

ARESU, G., KAMP, I., MEIJERINK, R., WOITKE, P., THI, W.-F. ET AL. (2011). X-ray impact on the protoplanetary disks around T Tauri stars. *A&A*, 526, A163+.

AUGEREAU, J.-C. & BEUST, H. (2006). On the AU Microscopii debris disk. Density profiles, grain properties, and dust dynamics. *A&A*, 455, 987–999.

AUGEREAU, J. C., LAGRANGE, A. M., MOUILLET, D., PAPALOIZOU, J. C. B. & GROROD, P. A. (1999). On the HR 4796 A circumstellar disk. *A&A*, 348, 557–569.

AUMANN, H. H., BEICHMAN, C. A., GILLETT, F. C., DE JONG, T., HOUCK, J. R. ET AL. (1984). Discovery of a shell around Alpha Lyrae. *ApJ*, 278, L23–L27.

BACKMAN, D. E. & PARESCE, F. (1993). Main-sequence stars with circumstellar solid material - The VEGA phenomenon. In LEVY, E. H. & LUNINE, J. I., eds., Protostars and Planets III. 1253–1304.

Baraffe, I., Chabrier, G., Allard, F. & Hauschildt, P. H. (1998). Evolutionary models for solar metallicity low-mass stars: mass-magnitude relationships and color-magnitude diagrams. *A&A*, 337, 403–412.

Barrado y Navascués, D. (2006). On the age of the TW Hydrae association and 2M1207334-393254. *A&A*, 459, 511–518.

Barrado y Navascués, D. & Martín, E. L. (2003). An Empirical Criterion to Classify T Tauri Stars and Substellar Analogs Using Low-Resolution Optical Spectroscopy. *AJ*, 126, 2997–3006.

Barrado y Navascués, D., Stauffer, J. R., Song, I. & Caillault, J.-P. (1999). The Age of beta Pictoris. *ApJ*, 520, L123–L126.

Bayo, A., Barrado, D., Huélamo, N., Morales-Calderón, M., Melo, C. et al. (2012). Spectroscopy of very low-mass stars and brown dwarfs in the Lambda Orionis star-forming region. II. Rotation, activity and other properties of spectroscopically confirmed members of Collinder 69. *A&A*, 547, A80.

Bayo, A., Rodrigo, C., Barrado Y Navascués, D., Solano, E., Gutiérrez, R. et al. (2008). VOSA: virtual observatory SED analyzer. An application to the Collinder 69 open cluster. *A&A*, 492, 277–287.

Beckwith, S. V. W. & Sargent, A. I. (1991). Particle emissivity in circumstellar disks. *ApJ*, 381, 250–258.

Beckwith, S. V. W., Sargent, A. I., Chini, R. S. & Guesten, R. (1990). A survey for circumstellar disks around young stellar objects. *AJ*, 99, 924–945.

Bergin, E. A., Cleeves, L. I., Gorti, U., Zhang, K., Blake, G. A. et al. (2013). An old disk still capable of forming a planetary system. *Nature*, 493, 644–646.

Bergin, E. A., Hogerheijde, M. R., Brinch, C., Fogel, J., Yildiz, U. A. et al. (2010). Sensitive limits on the abundance of cold water vapor in the DM Tauri protoplanetary disk. *A&A*, 521, L33+.

Bertout, C., Robichon, N. & Arenou, F. (1999). Revisiting Hipparcos data for pre-main sequence stars. *A&A*, 352, 574–586.

Beust, H., Vidal-Madjar, A., Ferlet, R. & Lagrange-Henri, A. M. (1990). The Beta Pictoris circumstellar disk. X - Numerical simulations of infalling evaporating bodies. *A&A*, 236, 202–216.

Birnstiel, T., Ricci, L., Trotta, F., Dullemond, C. P., Natta, A. et al. (2010). Testing the theory of grain growth and fragmentation by millimeter observations of protoplanetary disks. *A&A*, 516, L14.

Blum, J., Wurm, G. & Kempf, S. (2000). The Onset of Planetesimal Formation - Results from the Cosmic Dust Aggregation Experiment (CODAG). In AAS/Division for Planetary Sciences Meeting Abstracts #32, vol. 32 of *Bulletin of the American Astronomical Society*. 1101.

Bouwman, J., Meeus, G., de Koter, A., Hony, S., Dominik, C. et al. (2001). Processing of silicate dust grains in Herbig Ae/Be systems. *A&A*, 375, 950–962.

Bruderer, S., Doty, S. D. & Benz, A. O. (2009). Chemical Modeling of Young Stellar Objects. I. Method and Benchmarks. *ApJS*, 183, 179–196.

Bryden, G., Beichman, C. A., Trilling, D. E., Rieke, G. H., Holmes, E. K. et al. (2006). Frequency of Debris Disks around Solar-Type Stars: First Results from a Spitzer MIPS Survey. *ApJ*, 636, 1098–1113.

Canup, R. M. & Esposito, L. W. (1996). Accretion of the Moon from an Impact-Generated Disk. *Icarus*, 119, 427–446.

Carr, J. S. & Najita, J. R. (2008). Organic Molecules and Water in the Planet Formation Region of Young Circumstellar Disks. *Science*, 319, 1504–.

Carr, J. S. & Najita, J. R. (2011). Organic Molecules and Water in the Inner Disks of T Tauri Stars. *ApJ*, 733, 102–+.

Cernicharo, J., Ceccarelli, C., Ménard, F., Pinte, C. & Fuente, A. (2009). The Foggy Disks Surrounding Herbig Ae Stars: A Theoretical Study of the H_2O Line Spectra. *ApJ*, 703, L123–L126.

Chen, C. H., Li, A., Bohac, C., Kim, K. H., Watson, D. M. et al. (2007). The Dust and Gas Around β Pictoris. *ApJ*, 666, 466–474.

Chen, C. H., Sargent, B. A., Bohac, C., Kim, K. H., Leibensperger, E. et al. (2006). Spitzer IRS Spectroscopy of IRAS-discovered Debris Disks. *ApJS*, 166, 351–377.

Cieza, L. A., Swift, J. J., Mathews, G. S. & Williams, J. P. (2008). The Masses of Transition Circumstellar Disks: Observational Support for Photoevaporation Models. *ApJ*, 686, L115–L118.

Cote, J. (1987). B and A type stars with unexpectedly large colour excesses at IRAS wavelengths. *A&A*, 181, 77–84.

Currie, T., Lada, C. J., Plavchan, P., Robitaille, T. P., Irwin, J. et al. (2009). The Last Gasp of Gas Giant Planet Formation: A Spitzer Study of the 5 Myr Old Cluster NGC 2362. *ApJ*, 698, 1–27.

Currie, T. & Sicilia-Aguilar, A. (2011). The Transitional Protoplanetary Disk Frequency as a Function of Age: Disk Evolution In the Coronet Cluster, Taurus, and Other 1-8 Myr Old Regions. *ApJ*, 732, 24.

Czechowski, A. & Mann, I. (2007). Collisional Vaporization of Dust and Production of Gas in the β Pictoris Dust Disk. *ApJ*, 660, 1541–1555.

Dahm, S. E. & Carpenter, J. M. (2009). Spitzer Spectroscopy of Circumstellar Disks in the 5 Myr Old Upper Scorpius OB Association. *AJ*, 137, 4024–4045.

de Graauw, T., Helmich, F. P., Phillips, T. G., Stutzki, J., Caux, E. et al. (2010). The Herschel-Heterodyne Instrument for the Far-Infrared (HIFI). *A&A*, 518, L6.

de la Reza, R., Jilinski, E. & Ortega, V. G. (2006). Dynamical Evolution of the TW Hydrae Association. *AJ*, 131, 2609–2614.

de la Reza, R., Torres, C. A. O., Quast, G., Castilho, B. V. & Vieira, G. L. (1989). Discovery of new isolated T Tauri stars. *ApJ*, 343, L61–L64.

Dent, W. R. F., Greaves, J. S. & Coulson, I. M. (2005). CO emission from discs around isolated HAeBe and Vega-excess stars. *MNRAS*, 359, 663–676.

Dohnanyi, J. S. (1969). Collisional Model of Asteroids and Their Debris. *J. Geophys. Res.*, 74, 2531.

Donaldson, J. K., Roberge, A., Chen, C. H., Augereau, J.-C., Dent, W. R. F. et al. (2012). Herschel PACS Observations and Modeling of Debris Disks in the Tucana-Horologium Association. *ApJ*, 753, 147.

Dorschner, J., Begemann, B., Henning, T., Jaeger, C. & Mutschke, H. (1995). Steps toward interstellar silicate mineralogy. II. Study of Mg-Fe-silicate glasses of variable composition. *A&A*, 300, 503.

Draine, B. T. & Lee, H. M. (1984). Optical properties of interstellar graphite and silicate grains. *ApJ*, 285, 89–108.

Evans, N. J. & c2d Team (2005). From Cores to Planets: the Spitzer c2d Legacy program. In American Astronomical Society Meeting Abstracts, vol. 37 of *Bulletin of the American Astronomical Society*. 1323.

Faure, A., Crimier, N., Ceccarelli, C., Valiron, P., Wiesenfeld, L. et al. (2007). Quasi-classical rate coefficient calculations for the rotational (de)excitation of H{2}O by H{2}. *A&A*, 472, 1029–1035.

Faure, A., Gorfinkiel, J. D. & Tennyson, J. (2004). Electron-impact rotational excitation of water. *MNRAS*, 347, 323–333.

Faure, A. & Josselin, E. (2008). Collisional excitation of water in warm astrophysical media. I. Rate coefficients for rovibrationally excited states. *A&A*, 492, 257–264.

Feigelson, E. D., Lawson, W. A., Stark, M., Townsley, L. & Garmire, G. P. (2006). 51 Eridani and GJ 3305: A 10-15 Myr old Binary Star System at 30 Parsecs. *AJ*, 131, 1730–1739.

Feigelson, E. D. & Nelson, P. I. (1985). Statistical methods for astronomical data with upper limits. I - Univariate distributions. *ApJ*, 293, 192–206.

Fernández, R., Brandeker, A. & Wu, Y. (2006). Braking the Gas in the β Pictoris Disk. *ApJ*, 643, 509–522.

Furlan, E., Hartmann, L., Calvet, N., D'Alessio, P., Franco-Hernández, R. et al. (2006). A Survey and Analysis of Spitzer Infrared Spectrograph Spectra of T Tauri Stars in Taurus. *ApJS*, 165, 568–605.

Furlan, E., Sargent, B., Calvet, N., Forrest, W. J., D'Alessio, P. et al. (2007). HD 98800: A 10 Myr Old Transition Disk. *ApJ*, 664, 1176–1184.

Gorti, U. & Hollenbach, D. (2008). Line Emission from Gas in Optically Thick Dust Disks around Young Stars. *ApJ*, 683, 287–303.

Gray, R. O., Corbally, C. J., Garrison, R. F., McFadden, M. T., Bubar, E. J. et al. (2006). Contributions to the Nearby Stars (NStars) Project: Spectroscopy of Stars Earlier than M0 within 40 pc-The Southern Sample. *AJ*, 132, 161–170.

Gregorio-Hetem, J., Lepine, J. R. D., Quast, G. R., Torres, C. A. O. & de La Reza, R. (1992). A search for T Tauri stars based on the IRAS point source catalog. *AJ*, 103, 549–563.

Griffin, M. J., Abergel, A., Abreu, A., Ade, P. A. R., André, P. et al. (2010). The Herschel-SPIRE instrument and its in-flight performance. *A&A*, 518, L3.

Güdel, M., Briggs, K. R., Arzner, K., Audard, M., Bouvier, J. et al. (2007). The XMM-Newton extended survey of the Taurus molecular cloud (XEST). *A&A*, 468, 353–377.

Gutermuth, R. A., Myers, P. C., Megeath, S. T., Allen, L. E., Pipher, J. L. et al. (2008). Spitzer Observations of NGC 1333: A Study of Structure and Evolution in a Nearby Embedded Cluster. *ApJ*, 674, 336–356.

Haisch, K. E., Jr., Lada, E. A. & Lada, C. J. (2001). Disk Frequencies and Lifetimes in Young Clusters. *ApJ*, 553, L153–L156.

Hartigan, P., Edwards, S. & Ghandour, L. (1995). Disk Accretion and Mass Loss from Young Stars. *ApJ*, 452, 736.

Hartmann, L., Calvet, N., Gullbring, E. & D'Alessio, P. (1998). Accretion and the Evolution of T Tauri Disks. *ApJ*, 495, 385.

Hauck, B. & Mermilliod, M. (1998). Uvbybeta photoelectric photometric catalogue. *A&AS*, 129, 431–433.

Hauschildt, P. H., Allard, F. & Baron, E. (1999). The NextGen Model Atmosphere Grid for 3000< T_eff < 10,000 K. *ApJ*, 512, 377–385.

Hayashi, C. (1981). Structure of the Solar Nebula, Growth and Decay of Magnetic Fields and Effects of Magnetic and Turbulent Viscosities on the Nebula. *Progress of Theoretical Physics Supplement*, 70, 35–53.

Herczeg, G. J., Karska, A., Bruderer, S., Kristensen, L. E., van Dishoeck, E. F. et al. (2011). Water in star-forming regions with Herschel: highly excited molecular emission from the NGC 1333 IRAS 4B outflow. *ArXiv e-prints*.

Hernández, J., Hartmann, L., Megeath, T., Gutermuth, R., Muzerolle, J. et al. (2007). A Spitzer Space Telescope Study of Disks in the Young σ Orionis Cluster. *ApJ*, 662, 1067–1081.

Hildebrand, R. H. (1983). The Determination of Cloud Masses and Dust Characteristics from Submillimetre Thermal Emission. *QJRAS*, 24, 267.

Hillenbrand, L. A., Carpenter, J. M., Kim, J. S., Meyer, M. R., Backman, D. E. et al. (2008). The Complete Census of 70 μm-bright Debris Disks within "the Formation and Evolution of Planetary Systems" Spitzer Legacy Survey of Sun-like Stars. *ApJ*, 677, 630–656.

Hobbs, L. M., Vidal-Madjar, A., Ferlet, R., Albert, C. E. & Gry, C. (1985). The gaseous component of the disk around Beta Pictoris. *ApJ*, 293, L29–L33.

Hoff, W., Henning, T. & Pfau, W. (1998). The nature of isolated T Tauri stars. *A&A*, 336, 242–250.

Høg, E., Fabricius, C., Makarov, V. V., Urban, S., Corbin, T. et al. (2000). The Tycho-2 catalogue of the 2.5 million brightest stars. *A&A*, 355, L27–L30.

Hogerheijde, M. R., Bergin, E. A., Brinch, C., Ilsedore Cleeves, L., Fogel, J. K. J. et al. (2011). Detection of the Water Reservoir in a Forming Planetary System. *ArXiv e-prints*.

Holmberg, J., Nordström, B. & Andersen, J. (2009). The Geneva-Copenhagen survey of the solar neighbourhood. III. Improved distances, ages, and kinematics. *A&A*, 501, 941–947.

Houk, N. & Fuentes-Williams, T. H. (1982). Vol. 3 of the Michigan Catalogue of Two-Dimensional Spectral Types (-40 deg to -26 deg) and Future Plans. In Bulletin of the American Astronomical Society, vol. 14 of *Bulletin of the American Astronomical Society*. 615.

Huenemoerder, D. P., Kastner, J. H., Testa, P., Schulz, N. S. & Weintraub, D. A. (2007). Evidence for Accretion in the High-Resolution X-Ray Spectrum of the T Tauri Star System Hen 3-600. *ApJ*, 671, 592–604.

Hughes, A. M., Wilner, D. J., Calvet, N., D'Alessio, P., Claussen, M. J. et al. (2007). An Inner Hole in the Disk around TW Hydrae Resolved in 7 mm Dust Emission. *ApJ*, 664, 536–542.

Ishihara, D., Onaka, T., Kataza, H., Salama, A., Alfageme, C. et al. (2010). The AKARI/IRC mid-infrared all-sky survey. *A&A*, 514, A1+.

Isobe, T., Feigelson, E. D. & Nelson, P. I. (1986). Statistical methods for astronomical data with upper limits. II - Correlation and regression. *ApJ*, 306, 490–507.

Jackson, A. P. & Wyatt, M. C. (2012). Debris from terrestrial planet formation: the Moon-forming collision. *MNRAS*, 425, 657–679.

Jayawardhana, R., Coffey, J., Scholz, A., Brandeker, A. & van Kerkwijk, M. H. (2006). Accretion Disks around Young Stars: Lifetimes, Disk Locking, and Variability. *ApJ*, 648, 1206–1218.

Jayawardhana, R., Fisher, R. S., Hartmann, L., Telesco, C., Pina, R. et al. (1998). A Dust Disk Surrounding the Young A Star HR 4796A. *ApJ*, 503, L79.

Jensen, E. L. N., Mathieu, R. D. & Fuller, G. A. (1996). The Connection between Submillimeter Continuum Flux and Binary Separation in Young Binaries: Evidence of Interaction between Stars and Disks. *ApJ*, 458, 312.

JOHNSON, B. C., LISSE, C. M., CHEN, C. H., MELOSH, H. J., WYATT, M. C. ET AL. (2012). A Self-Consistent Model of the Circumstellar Debris Created by a Giant Hypervelocity Impact in the HD172555 System. *ArXiv e-prints*.

JOHNSON, H. L., MITCHELL, R. I., IRIARTE, B. & WISNIEWSKI, W. Z. (1966). Ubvrijkl Photometry of the Bright Stars. *Communications of the Lunar and Planetary Laboratory*, 4, 99.

JURA, M. (1991). The dust debris around HR 4796. *ApJ*, 383, L79.

JURA, M., ZUCKERMAN, B., BECKLIN, E. E. & SMITH, R. C. (1993). Constraints on the Evolution of Remnant Protostellar Dust Debris around HR 4796. *ApJ*, 418, L37.

KAMP, I., TILLING, I., WOITKE, P., THI, W.-F. & HOGERHEIJDE, M. (2010). Radiation thermo-chemical models of protoplanetary disks. II. Line diagnostics. *A&A*, 510, A18.

KAMP, I., WOITKE, P., PINTE, C., TILLING, I., THI, W.-F. ET AL. (2011). Continuum and line modelling of discs around young stars. II. Line diagnostics for GASPS from the DENT grid. *A&A*, 532, A85.

KASTNER, J. H., ZUCKERMAN, B., WEINTRAUB, D. A. & FORVEILLE, T. (1997). X-ray and molecular emission from the nearest region of recent star formation. *Science*, 277, 67–71.

KENYON, S. J. & BROMLEY, B. C. (2004). Collisional Cascades in Planetesimal Disks. II. Embedded Planets. *AJ*, 127, 513–530.

KENYON, S. J., GÓMEZ, M. & WHITNEY, B. A. (2008). Low Mass Star Formation in the Taurus-Auriga Clouds. 405.

KOERNER, D. W., JENSEN, E. L. N., CRUZ, K. L., GUILD, T. B. & GULTEKIN, K. (2000). A Single Circumbinary Disk in the HD 98800 Quadruple System. *ApJ*, 533, L37–L40.

KOERNER, D. W., RESSLER, M. E., WERNER, M. W. & BACKMAN, D. E. (1998). Mid-Infrared Imaging of a Circumstellar Disk around HR 4796: Mapping the Debris of Planetary Formation. *ApJ*, 503, L83.

KRIVOV, A. V. (2010). Debris disks: seeing dust, thinking of planetesimals and planets. *Research in Astronomy and Astrophysics*, 10, 383–414.

LADA, C. J. (1987). Star formation - From OB associations to protostars. In PEIMBERT, M. & JUGAKU, J., eds., Star Forming Regions, vol. 115 of *IAU Symposium*. 1–17.

LADA, C. J., MUENCH, A. A., LUHMAN, K. L., ALLEN, L., HARTMANN, L. ET AL. (2006). Spitzer Observations of IC 348: The Disk Population at 2-3 Million Years. *AJ*, 131, 1574–1607.

LADA, C. J. & WILKING, B. A. (1984). The nature of the embedded population in the Rho Ophiuchi dark cloud - Mid-infrared observations. *ApJ*, 287, 610–621.

LAGRANGE, A. M., FERLET, R. & VIDAL-MADJAR, A. (1986). The circumstellar gas around Beta Pictoris. In ROLFE, E. J., ed., New Insights in Astrophysics. Eight Years of UV Astronomy with IUE, vol. 263 of *ESA Special Publication*. 569–571.

LAGRANGE, A. M., FERLET, R. & VIDAL-MADJAR, A. (1987). The Beta Pictoris circumstellar disk. IV - Redshifted UV lines. *A&A*, 173, 289–292.

LAGRANGE-HENRI, A. M., BEUST, H., FERLET, R. & VIDAL-MADJAR, A. (1989). The circumstellar gas around Beta Pictoris. VIII - Evidence for a clumpy structure of the infalling gas. *A&A*, 215, L5–L8.

LAY, O. P., CARLSTROM, J. E. & HILLS, R. E. (1997). Constraints on the HL Tauri Protostellar Disk from Millimeter- and Submillimeter-Wave Interferometry. *ApJ*, 489, 917.

LEBRETON, J., AUGEREAU, J.-C., THI, W.-F., ROBERGE, A., DONALDSON, J. ET AL. (2012). An icy Kuiper belt around the young solar-type star HD 181327. *A&A*, 539, A17.

LIN, D. N. C. & PAPALOIZOU, J. C. B. (1993). On the tidal interaction between protostellar disks and companions. In LEVY, E. H. & LUNINE, J. I., eds., Protostars and Planets III. 749–835.

LISSE, C. M., CHEN, C. H., WYATT, M. C. & MORLOK, A. (2008). Star System HD172555 - Spectral Evidence of Abundant Silica Created by a Massive In-System Collision? In Lunar and Planetary Institute Science Conference Abstracts, vol. 39 of *Lunar and Planetary Inst. Technical Report*. 2119.

LISSE, C. M., CHEN, C. H., WYATT, M. C., MORLOK, A., SONG, I. ET AL. (2009). Abundant Circumstellar Silica Dust and SiO Gas Created by a Giant Hypervelocity Collision in the ˜12 Myr HD172555 System. *ApJ*, 701, 2019–2032.

LÖHNE, T., AUGEREAU, J.-C., ERTEL, S., MARSHALL, J. P., EIROA, C. ET AL. (2012). Modelling the huge, Herschel-resolved debris ring around HD 207129. *A&A*, 537, A110.

LORENZETTI, D. (2005). Pre-Main Sequence Stars Seen by ISO. *Space Sci. Rev.*, 119, 181–199.

LOW, F. J., SMITH, P. S., WERNER, M., CHEN, C., KRAUSE, V. ET AL. (2005). Exploring Terrestrial Planet Formation in the TW Hydrae Association. *ApJ*, 631, 1170–1179.

LOWRANCE, P. J., SCHNEIDER, G., KIRKPATRICK, J. D., BECKLIN, E. E., WEINBERGER, A. J. ET AL. (2000). A Candidate Substellar Companion to HR 7329. *ApJ*, 541, 390–395.

LUHMAN, K. L., ALLEN, P. R., ESPAILLAT, C., HARTMANN, L. & CALVET, N. (2010). The Disk Population of the Taurus Star-Forming Region. *ApJS*, 186, 111–174.

MAKAROV, V. V. & FABRICIUS, C. (2001). Internal kinematics of the TW Hya association of young stars. *A&A*, 368, 866–872.

MAKAROV, V. V., GAUME, R. A. & ANDRIEVSKY, S. M. (2005). Expansion of the TW Hydrae association and the encounter with Vega. *MNRAS*, 362, 1109–1113.

MAMAJEK, E. E. (2009). Initial Conditions of Planet Formation: Lifetimes of Primordial Disks. In USUDA, T., TAMURA, M. & ISHII, M., eds., American Institute of Physics Conference Series, vol. 1158 of *American Institute of Physics Conference Series*. 3–10.

MANNINGS, V. & EMERSON, J. P. (1994). Dust in discs around T Tauri stars: Grain growth? *MNRAS*, 267, 361–378.

MATHEWS, G. S., DENT, W. R. F., WILLIAMS, J. P., HOWARD, C. D., MEEUS, G. ET AL. (2010). GAS in Protoplanetary Systems (GASPS). I. First results. *A&A*, 518, L127.

MATTHEWS, B. C., KALAS, P. G. & WYATT, M. C. (2007). Mass and Temperature of the TWA 7 Debris Disk. *ApJ*, 663, 1103–1109.

MEEUS, G., MONTESINOS, B., MENDIGUTÍA, I., KAMP, I., THI, W. F. ET AL. (2012). Observations of Herbig Ae/Be stars with Herschel/PACS. The atomic and molecular contents of their protoplanetary discs. *A&A*, 544, A78.

MEIJERINK, R., PONTOPPIDAN, K. M., BLAKE, G. A., POELMAN, D. R. & DULLEMOND, C. P. (2009). Radiative Transfer Models of Mid-Infrared H_2O Lines in the Planet-Forming Region of Circumstellar Disks. *ApJ*, 704, 1471–1481.

MEYER, M. R., SPITZER LEGACY SCIENCE PROGRAM “FORMATION & EVOLUTION OF PLANETARY SYSTEMS COLLABORATION (2004). The Formation and Evolution of Planetary Systems: First Results from a Spitzer Legacy Science Program. In American Astronomical Society Meeting Abstracts #204, vol. 36 of *Bulletin of the American Astronomical Society*. 702.

MIYAKE, K. & NAKAGAWA, Y. (1993). Effects of particle size distribution on opacity curves of protoplanetary disks around T Tauri stars. *Icarus*, 106, 20.

MOERCHEN, M. M., TELESCO, C. M. & PACKHAM, C. (2010). High Spatial Resolution Imaging of Thermal Emission from Debris Disks. *ApJ*, 723, 1418–1435.

MOÓR, A., ÁBRAHÁM, P., JUHÁSZ, A., KISS, C., PASCUCCI, I. ET AL. (2011). Molecular Gas in Young Debris Disks. *ApJ*, 740, L7.

MORALES, F. Y., WERNER, M. W., BRYDEN, G., PLAVCHAN, P., STAPELFELDT, K. R. ET AL. (2009). Spitzer Mid-IR Spectra of Dust Debris Around A and Late B Type Stars: Asteroid Belt Analogs and Power-Law Dust Distributions. *ApJ*, 699, 1067–1086.

MUSTILL, A. J. & WYATT, M. C. (2009). Debris disc stirring by secular perturbations from giant planets. *MNRAS*, 399, 1403–1414.

MUZEROLLE, J., CALVET, N., BRICEÑO, C., HARTMANN, L. & HILLENBRAND, L. (2000). Disk Accretion in the 10 MYR Old T Tauri Stars TW Hydrae and Hen 3-600A. *ApJ*, 535, L47–L50.

NAJITA, J. R., STROM, S. E. & MUZEROLLE, J. (2007). Demographics of transition objects. *MNRAS*, 378, 369–378.

NAKAGAWA, Y., SEKIYA, M. & HAYASHI, C. (1986). Settling and growth of dust particles in a laminar phase of a low-mass solar nebula. *Icarus*, 67, 375–390.

NILSSON, R., LISEAU, R., BRANDEKER, A., OLOFSSON, G., PILBRATT, G. L. ET AL. (2010). Kuiper belts around nearby stars. *A&A*, 518, A40.

NILSSON, R., LISEAU, R., BRANDEKER, A., OLOFSSON, G., RISACHER, C. ET AL. (2009). A submillimetre search for cold extended debris disks in the β Pictoris moving group. *A&A*, 508, 1057–1065.

OLIVEIRA, I., OLOFSSON, J., PONTOPPIDAN, K. M., VAN DISHOECK, E. F., AUGEREAU, J.-C. ET AL. (2011). On the Evolution of Dust Mineralogy, from Protoplanetary Disks to Planetary Systems. *ApJ*, 734, 51.

OLOFSSON, G., LISEAU, R. & BRANDEKER, A. (2001). Widespread Atomic Gas Emission Reveals the Rotation of the β Pictoris Disk. *ApJ*, 563, L77–L80.

PAHLEVAN, K., STEVENSON, D. J. & EILER, J. M. (2011). Chemical fractionation in the silicate vapor atmosphere of the Earth. *Earth and Planetary Science Letters*, 301, 433–443.

PILBRATT, G. L., RIEDINGER, J. R., PASSVOGEL, T., CRONE, G., DOYLE, D. ET AL. (2010). Herschel Space Observatory. An ESA facility for far-infrared and submillimetre astronomy. *A&A*, 518, L1+.

PINTE, C., FOUCHET, L., MÉNARD, F., GONZALEZ, J.-F. & DUCHÊNE, G. (2007). On the stratified dust distribution of the GG Tauri circumbinary ring. *A&A*, 469, 963–971.

PINTE, C., HARRIES, T. J., MIN, M., WATSON, A. M., DULLEMOND, C. P. ET AL. (2009). Benchmark problems for continuum radiative transfer. High optical depths, anisotropic scattering, and polarisation. *A&A*, 498, 967–980.

PINTE, C., MÉNARD, F., DUCHÊNE, G. & BASTIEN, P. (2006). Monte Carlo radiative transfer in protoplanetary disks. *A&A*, 459, 797–804.

PINTE, C., PADGETT, D. L., MÉNARD, F., STAPELFELDT, K. R., SCHNEIDER, G. ET AL. (2008). Probing dust grain evolution in IM Lupi's circumstellar disc. Multi-wavelength observations and modelling of the dust disc. *A&A*, 489, 633–650.

PLAVCHAN, P., WERNER, M. W., CHEN, C. H., STAPELFELDT, K. R., SU, K. Y. L. ET AL. (2009). New Debris Disks Around Young, Low-Mass Stars Discovered with the Spitzer Space Telescope. *ApJ*, 698, 1068–1094.

PODIO, L., KAMP, I., FLOWER, D., HOWARD, C., SANDELL, G. ET AL. (2012). Herschel/PACS observations of young sources in Taurus: the far-infrared counterpart of optical jets. *A&A*, 545, A44.

POGLITSCH, A., WAELKENS, C., GEIS, N., FEUCHTGRUBER, H., VANDENBUSSCHE, B. ET AL. (2010). The Photodetector Array Camera and Spectrometer (PACS) on the Herschel Space Observatory. *A&A*, 518, L2+.

PONTOPPIDAN, K. M., MEIJERINK, R., DULLEMOND, C. P. & BLAKE, G. A. (2009). A New Raytracer for Modeling AU-Scale Imaging of Lines from Protoplanetary Disks. *ApJ*, 704, 1482–1494.

PONTOPPIDAN, K. M., SALYK, C., BLAKE, G. A. & KÄUFL, H. U. (2010a). Spectrally Resolved Pure Rotational Lines of Water in Protoplanetary Disks. *ApJ*, 722, L173–L177.

PONTOPPIDAN, K. M., SALYK, C., BLAKE, G. A., MEIJERINK, R., CARR, J. S. ET AL. (2010b). A Spitzer Survey of Mid-infrared Molecular Emission from Protoplanetary Disks. I. Detection Rates. *ApJ*, 720, 887–903.

PRATO, L., GHEZ, A. M., PIÑA, R. K., TELESCO, C. M., FISHER, R. S. ET AL. (2001). Keck Diffraction-limited Imaging of the Young Quadruple Star System HD 98800. *ApJ*, 549, 590–598.

PRESS, W. H., TEUKOLSKY, S. A., VETTERLING, W. T. & FLANNERY, B. P. (1992). Numerical recipes in FORTRAN. The art of scientific computing.

QI, C., HO, P. T. P., WILNER, D. J., TAKAKUWA, S., HIRANO, N. ET AL. (2004). Imaging the Disk around TW Hydrae with the Submillimeter Array. *ApJ*, 616, L11–L14.

REBULL, L. M., PADGETT, D. L., MCCABE, C.-E., HILLENBRAND, L. A., STAPELFELDT, K. R. ET AL. (2010). The Taurus Spitzer Survey: New Candidate Taurus Members Selected Using Sensitive Mid-Infrared Photometry. *ApJS*, 186, 259–307.

REBULL, L. M., STAPELFELDT, K. R., WERNER, M. W., MANNINGS, V. G., CHEN, C. ET AL. (2008). Spitzer MIPS Observations of Stars in the β Pictoris Moving Group. *ApJ*, 681, 1484–1504.

RHEE, J. H., SONG, I., ZUCKERMAN, B. & MCELWAIN, M. (2007). Characterization of Dusty Debris Disks: The IRAS and Hipparcos Catalogs. *ApJ*, 660, 1556–1571.

RIAZ, B., GIZIS, J. E. & HMIEL, A. (2006). Spitzer Observations of Two TW Hydrae Association Brown Dwarfs. *ApJ*, 639, L79–L82.

RIVIERE-MARICHALAR, P., BARRADO, D., AUGEREAU, J.-C., THI, W. F., ROBERGE, A. ET AL. (2012a). HD 172555: detection of 63 microns [OI] emission in a debris disc. *ArXiv e-prints*.

RIVIERE-MARICHALAR, P., MÉNARD, F., THI, W. F., KAMP, I., MONTESINOS, B. ET AL. (2012b). Detection of warm water vapour in Taurus protoplanetary discs by Herschel. *A&A*, 538, L3.

ROBERGE, A., FELDMAN, P. D., LAGRANGE, A. M., VIDAL-MADJAR, A., FERLET, R. ET AL. (2000). High-Resolution Hubble Space Telescope STIS Spectra of C I and CO in theβ Pictoris Circumstellar Disk. *ApJ*, 538, 904–910.

ROBERGE, A., FELDMAN, P. D., WEINBERGER, A. J., DELEUIL, M. & BOURET, J.-C. (2006). Stabilization of the disk around β Pictoris by extremely carbon-rich gas. *Nature*, 441, 724–726.

ROBERGE, A., WEINBERGER, A. J. & MALUMUTH, E. M. (2005). Spatially Resolved Spectroscopy and Coronagraphic Imaging of the TW Hydrae Circumstellar Disk. *ApJ*, 622, 1171–1181.

RUCINSKI, S. M. & KRAUTTER, J. (1983). TW Hya - A T Tauri star far from any dark cloud. *A&A*, 121, 217–225.

SALYK, C., BLAKE, G. A., BOOGERT, A. C. A. & BROWN, J. M. (2007). Molecular Gas in the Inner 1 AU of the TW Hya and GM Aur Transitional Disks. *ApJ*, 655, L105–L108.

SALYK, C., PONTOPPIDAN, K. M., BLAKE, G. A., LAHUIS, F., VAN DISHOECK, E. F. ET AL. (2008). H_2O and OH Gas in the Terrestrial Planet-forming Zones of Protoplanetary Disks. *ApJ*, 676, L49–L52.

SASSELOV, D. D. & LECAR, M. (2000). On the Snow Line in Dusty Protoplanetary Disks. *ApJ*, 528, 995–998.

SCHNEIDER, A., MELIS, C. & SONG, I. (2012). TW HYA Association Membership and New WISE-detected Circumstellar Disks. *ApJ*, 754, 39.

SCHNEIDER, G., SILVERSTONE, M. D., HINES, D. C., AUGEREAU, J.-C., PINTE, C. ET AL. (2006). Discovery of an 86 AU Radius Debris Ring around HD 181327. *ApJ*, 650, 414–431.

SCHNEIDER, G., SMITH, B. A., BECKLIN, E. E., KOERNER, D. W., MEIER, R. ET AL. (1999). NICMOS Imaging of the HR 4796A Circumstellar Disk. *ApJ*, 513, L127–L130.

SCHÜTZ, O., MEEUS, G. & STERZIK, M. F. (2005). Mid-IR observations of circumstellar disks. II. Vega-type stars and a post-main sequence object. *A&A*, 431, 175–182.

SHU, F. H., ADAMS, F. C. & LIZANO, S. (1987). Star formation in molecular clouds - Observation and theory. *ARA&A*, 25, 23–81.

SICILIA-AGUILAR, A., HARTMANN, L., CALVET, N., MEGEATH, S. T., MUZEROLLE, J. ET AL. (2006). Disk Evolution in Cep OB2: Results from the Spitzer Space Telescope. *ApJ*, 638, 897–919.

SIEGLER, N., MUZEROLLE, J., YOUNG, E. T., RIEKE, G. H., MAMAJEK, E. E. ET AL. (2007). Spitzer 24 μm Observations of Open Cluster IC 2391 and Debris Disk Evolution of FGK Stars. *ApJ*, 654, 580–594.

SKINNER, C. J., BARLOW, M. J. & JUSTTANONT, K. (1992). Silicate dust in a Vega-excess system. *MNRAS*, 255, 31P–36P.

SKRUTSKIE, M. F., CUTRI, R. M., STIENING, R., WEINBERG, M. D., SCHNEIDER, S. ET AL. (2006). The Two Micron All Sky Survey (2MASS). *AJ*, 131, 1163–1183.

Smith, B. A. & Terrile, R. J. (1984). A circumstellar disk around Beta Pictoris. *Science*, 226, 1421–1424.

Smith, R., Churcher, L. J., Wyatt, M. C., Moerchen, M. M. & Telesco, C. M. (2009). Resolved debris disc emission around η Telescopii: a young solar system or ongoing planet formation? *A&A*, 493, 299–308.

Smith, R., Wyatt, M. C. & Haniff, C. A. (2012). Resolving the terrestrial planet forming regions of HD 113766 and HD 172555 with MIDI. *MNRAS*, 422, 2560–2580.

Soderblom, D. R., Henry, T. J., Shetrone, M. D., Jones, B. F. & Saar, S. H. (1996). The Age-related Properties of the HD 98800 System. *ApJ*, 460, 984.

Soderblom, D. R., King, J. R., Siess, L., Noll, K. S., Gilmore, D. M. et al. (1998). HD 98800: A Unique Stellar System of Post-T Tauri Stars. *ApJ*, 498, 385.

Stauffer, J. R., Hartmann, L. W. & Barrado y Navascues, D. (1995). An Age Estimate for the beta Pictoris Analog HR 4796A. *ApJ*, 454, 910.

Stern, S. A. (1996). On the Collisional Environment, Accretion Time Scales, and Architecture of the Massive, Primordial Kuiper Belt. *AJ*, 112, 1203.

Sterzik, M. F., Alcalá, J. M., Covino, E. & Petr, M. G. (1999). New T Tauri stars in the vicinity of TW Hydrae. *A&A*, 346, L41–L44.

Strom, K. M., Strom, S. E., Edwards, S., Cabrit, S. & Skrutskie, M. F. (1989). Circumstellar material associated with solar-type pre-main-sequence stars - A possible constraint on the timescale for planet building. *AJ*, 97, 1451–1470.

Su, K. Y. L., Rieke, G. H., Stansberry, J. A., Bryden, G., Stapelfeldt, K. R. et al. (2006). Debris Disk Evolution around A Stars. *ApJ*, 653, 675–689.

Takasawa, S., Nakamura, A. M., Kadono, T., Arakawa, M., Dohi, K. et al. (2011). Silicate Dust Size Distribution from Hypervelocity Collisions: Implications for Dust Production in Debris Disks. *ApJ*, 733, L39.

Telesco, C. M., Fisher, R. S., Piña, R. K., Knacke, R. F., Dermott, S. F. et al. (2000). Deep 10 and 18 Micron Imaging of the HR 4796A Circumstellar Disk: Transient Dust Particles and Tentative Evidence for a Brightness Asymmetry. *ApJ*, 530, 329–341.

Terebey, S., Shu, F. H. & Cassen, P. (1984). The collapse of the cores of slowly rotating isothermal clouds. *ApJ*, 286, 529–551.

Thi, W.-F., Mathews, G., Ménard, F., Woitke, P., Meeus, G. et al. (2010). Herschel-PACS observation of the 10 Myr old T Tauri disk TW Hya. Constraining the disk gas mass. *A&A*, 518, L125.

Thi, W. F., van Dishoeck, E. F., Blake, G. A., van Zadelhoff, G. J., Horn, J. et al. (2001). H_2 and CO Emission from Disks around T Tauri and Herbig Ae Pre-Main-Sequence Stars and from Debris Disks around Young Stars: Warm and Cold Circumstellar Gas. *ApJ*, 561, 1074–1094.

Thi, W.-F., van Zadelhoff, G.-J. & van Dishoeck, E. F. (2004). Organic molecules in protoplanetary disks around T Tauri and Herbig Ae stars. *A&A*, 425, 955–972.

Torres, C. A. O., Quast, G. R., da Silva, L., de La Reza, R., Melo, C. H. F. et al. (2006). Search for associations containing young stars (SACY). I. Sample and searching method. *A&A*, 460, 695–708.

Torres, C. A. O., Quast, G. R., de La Reza, R., da Silva, L., Melo, C. H. F. et al. (2003). SACY - a Search for Associations Containing Young stars. In Lépine, J. & Gregorio-Hetem, J., eds., Astrophysics and Space Science Library, vol. 299 of *Astrophysics and Space Science Library*. 83.

Torres, R. M., Loinard, L., Mioduszewski, A. J. & Rodríguez, L. F. (2009). VLBA Determination of the Distance to Nearby Star-Forming Regions. III. HP TAU/G2 and the Three-Dimensional Structure of Taurus. *ApJ*, 698, 242–249.

Trilling, D. E., Stansberry, J. A., Stapelfeldt, K. R., Rieke, G. H., Su, K. Y. L. et al. (2007). Debris disks in main-sequence binary systems. *ApJ*, 658, 1289.

Vacca, W. D. & Sandell, G. (2011). Near-infrared Spectroscopy of TW Hya: A Revised Spectral Type and Comparison with Magnetospheric Accretion Models. *ApJ*, 732, 8.

Webb, R. A., Zuckerman, B., Platais, I., Patience, J., White, R. J. et al. (1999). Discovery of Seven T Tauri Stars and a Brown Dwarf Candidatein the Nearby TW Hydrae Association. *ApJ*, 512, L63–L67.

Weidenschilling, S. J. (1977). Aerodynamics of solid bodies in the solar nebula. *MNRAS*, 180, 57–70.

Weinberger, A. J., Becklin, E. E., Zuckerman, B. & Song, I. (2004). A Search for Warm Circumstellar Disks in the TW Hydrae Association. *AJ*, 127, 2246–2251.

Weintraub, D. A., Sandell, G. & Duncan, W. D. (1989). Submillimeter measurements of T Tauri and FU Orionis stars. *ApJ*, 340, L69–L72.

WEINTRAUB, D. A., SAUMON, D., KASTNER, J. H. & FORVEILLE, T. (2000). NICMOS Narrowband Infrared Photometry of TW Hydrae Association Stars. *ApJ*, 530, 867–874.

WILLIAMS, J. P. & CIEZA, L. A. (2011). Protoplanetary Disks and Their Evolution. *ARA&A*, 49, 67–117.

WILNER, D. J., BOURKE, T. L., WRIGHT, C. M., JØRGENSEN, J. K., VAN DISHOECK, E. F. ET AL. (2003). Disks around the Young Stars TW Hydrae and HD 100546 Imaged at 3.4 Millimeters with the Australia Telescope Compact Array. *ApJ*, 596, 597–602.

WILNER, D. J., HO, P. T. P., KASTNER, J. H. & RODRÍGUEZ, L. F. (2000). VLA Imaging of the Disk Surrounding the Nearby Young Star TW Hydrae. *ApJ*, 534, L101–L104.

WINSTON, E., MEGEATH, S. T., WOLK, S. J., MUZEROLLE, J., GUTERMUTH, R. ET AL. (2007). A Combined Spitzer and Chandra Survey of Young Stellar Objects in the Serpens Cloud Core. *ApJ*, 669, 493–518.

WOITKE, P., KAMP, I. & THI, W.-F. (2009a). Radiation thermo-chemical models of protoplanetary disks. I. Hydrostatic disk structure and inner rim. *A&A*, 501, 383–406.

WOITKE, P., PINTE, C., TILLING, I., MÉNARD, F., KAMP, I. ET AL. (2010). Continuum and line modelling of discs around young stars - I. 300000 disc models for HERSCHEL/GASPS. *MNRAS*, 405, L26–L30.

WOITKE, P., THI, W.-F., KAMP, I. & HOGERHEIJDE, M. R. (2009b). Hot and cool water in Herbig Ae protoplanetary disks. A challenge for Herschel. *A&A*, 501, L5–L8.

WYATT, M. C. (2005a). Spiral structure when setting up pericentre glow: possible giant planets at hundreds of AU in the HD 141569 disk. *A&A*, 440, 937–948.

WYATT, M. C. (2005b). The insignificance of P-R drag in detectable extrasolar planetesimal belts. *A&A*, 433, 1007–1012.

WYATT, M. C. (2005c). The insignificance of P-R drag in detectable extrasolar planetesimal belts. *A&A*, 433, 1007–1012.

WYATT, M. C., SMITH, R., SU, K. Y. L., RIEKE, G. H., GREAVES, J. S. ET AL. (2007). Steady State Evolution of Debris Disks around A Stars. *ApJ*, 663, 365–382.

Yi, S., Demarque, P., Kim, Y.-C., Lee, Y.-W., Ree, C. H. et al. (2001). Toward Better Age Estimates for Stellar Populations: The Y^2 Isochrones for Solar Mixture. *ApJS*, 136, 417–437.

Yorke, H. W., Bodenheimer, P. & Laughlin, G. (1993). The formation of protostellar disks. I - 1 M(solar). *ApJ*, 411, 274–284.

Zuckerman, B. & Song, I. (2004a). Young Stars Near the Sun. *ARA&A*, 42, 685–721.

Zuckerman, B. & Song, I. (2004b). Young Stars Near the Sun. *ARA&A*, 42, 685–721.

Zuckerman, B., Song, I., Bessell, M. S. & Webb, R. A. (2001). The β Pictoris Moving Group. *ApJ*, 562, L87–L90.

Acknowledgements

La elaboración de una tesis doctoral es a la vez la culminación de un trabajo científico y de un desafío personal que implica un recorrido de años. Es imposible, así las cosas, que no tenga un cierto impacto a nivel personal en quien se encarga de escribirla. En mi caso, me ha permitido mejorar como individuo, aprender a ser paciente y observador, a prestar a los detalles la atención que merecen. Pero el aprendizaje no se restringe a mejorar las capacidades del investigador como tal, sino que también tiene impacto en su forma de ver la vida, ya que en muchos casos es su primer contacto con un entorno laboral serio. Así, también aprendemos a relacionarnos a distintos niveles y mejoramos nuestra capacidad de valoración de las personas, aunque solo sea de su nivel de compromiso y capacidad de trabajo. Por tanto, al agradecer a continuación a tanta gente que hayan estado a mi lado durante la tesis y me hayan apoyado, también les agradezco que me hayan permitido hacer ese otro aprendizaje que me será útil durante el resto de mi vida.

En primer lugar, tengo mucho que agradecer a mis padres. Les tengo que agradecer, que no es poco, mi existencia, claro está, pero también haberme dado una educación que me hizo inquieto, con preguntas en la boca siempre por formular, inquisitivo, escéptico... Tengo que agradecerles que siempre me apoyasen, que me enseñasen a ser trabajador, que la mejor recompensa (quizá la única válida) es el sentirse orgulloso del trabajo realizado. Les agradezco así mismo que me diesen las oportunidades que necesarias para realizar estudios superiores, algo que por desgracia no está al alcance de todos. Y como no, les agradezco su cariño todos estos años. Si bien no soy una persona religiosa, me gustaría pensar que mi padre sabe de algún modo que he conseguido dedicarme a la ciencia y unirme a la academia, en el sentido más bello de la palabra, y que se siente orgulloso. De mi madre lo sé bien.

Tengo que agradecerles también a mis hermanos todos estos años aguantándome y queriéndome. Fueron ellos los primeros que, de pequeño, me enseñaron el valor de la humildad. También fueron ellos los primeros, con mi madre, en aguantar mis delirios científicos, con el resultado que con esta tesis culmina. Tengo que agradecerles, claro, su paciencia conmigo, reconozco que hace falta mucha.

Quiero agradecerle a Laura todos estos años juntos: su apoyo, su esfuerzo por hacerme ver la luz cuando solo veía oscuridad. Su cariño y sus palabras de aliento. Su pasión por mi trabajo, sus consejos. Su oído eternamente dispuesto a escucharme, tanto frustrado como motivado. Quiero agradecerle el contrapeso que su presencia ha supuesto para el esfuerzo tan grande que supone la elaboración de una tesis y el agobio que muchas veces conlleva.

Le agradezco, como no, a David que me diese la oportunidad de cumplir mi sueño. Solo por eso, siempre tendrá un un bello hueco en mi memoria. Le agradezco la confianza depositada en mí. Pero es que también me ha enseñado a ser mejor científico, más autoexigente, inquisitivo e independiente. Y en los momentos duros en que yo despreciaba mi trabajo y su calidad, era él quien me hacía cambiar de idea. Por no mencionar que a observar aprendí por él y gracias a él. Y cuando uno observa, lo hace desde lugares privilegiados de nuestra querida Tierra, y esos también se lo agradezco.

Hay una persona del LAEFF/CAB-Villafranca que estos años ha dejado una impronta imborrable en mí. Esa persona es Benjamín. Le quiero agradecer ya no lo que ha hecho por mí, que ha sido mucho, sino lo maravillosa persona que es. Le agradezco su sabiduría reposada, su honestidad, su humildad, en general, su bondad. Espero algún día reunir tan sólo un diez por ciento de su calidad humana. Además, le agradezco su apoyo en momentos duros (y algunos muy duros), tanto a nivel personal como académico, y como no, le agradezco todos estos años de debate matinal que por desgracia ya concluyen.

Le tengo que agradecer a Carlos Eiroa que me introdujese en el mundo de la astrofísica y que, ya como profesor, me hiciese partícipe de esta gran pasión que es la ciencia, y más en concreto, la astronomía. Que me ayudase a encontrar un lugar, que me valorase y confiase en mí. Le agradezco también esos momentos de relajación y humor en mis primeros congresos, donde la vergüenza se apoderaba de mí. Sospecho que son más las cosas que le debo agradecer que las que he listado.

Le quiero agradecer a todo el mundo en el LAEFF/Cab-Villafranca todos estos años compartidos. El buen ambiente que he respirado durante estos cuatro años temo que sea muy difícil encontrarlo en otro lugar. Las risas en las comidas, las catas, las interminables conversaciones sobre los temas más absurdos jamás discutidos: todo.

Pero hay y ha habido gente en el LAEFF/CAB-Villafranca que quiero mencionar por separado, por la amistad que nos ha unido. A Ignacio, por las risas, la simpatía, por ayudarme a tomarme menos en serio aquello que me pudiese agobiar. A Héctor, le agradezco la sintonía en tantos temas, el compartir alguna de mis más importantes aficiones, como la literatura y el humor negro. A Amelia, por ser mi "hermana mayor", por ayudarme, enseñarme, aguantarme y apoyarme en momentos duros. A Nuria, por su eterna sonrisa, que siempre me aleja de los pensamientos oscuros. A su lado me resulta imposible seguir enfadado. A María, porque desde el primer momento, como Amelia y Nuria, me adoptó como hermano y no solo me ayudó, sino que me transmitió algo de su alegría. A Jorge, por tantos años compartiendo despacho y tiempo, por haberse convertido en un gran amigo. Y porque espero que en el futuro hagamos grandes cosas juntos. A Paco, amigo ya en la época de la facultad, por ayudarme a tomarme a mí mismo menos en serio. Mucho menos. A Juan Ángel, David y Santi, por tantos buenos momentos de risas rotas. A Hervé por su ayuda y buen humor. A Pili, por el buen royo y los tiempos de Guantánamo, y por su plantilla. A Mauro, por ser uno de los grandes responsables del funcionamiento humano del LAEFF, y por ser tan buena persona. A Sergio y Antonio, por ayudarme tantas veces con mis problemas téncnicos, más allá de la paciencia, y por los momentos de relajación. Y como no, a Natalia, que me ha dado no solo cariño y amistad, sino coscorrones cuando me pasaba de listo, que es algo realmente importante para la vida. En serio, gracias. Y gracias a Margie, porque seamos sinceros, con lo despistado que soy, vete a saber donde estaría yo hoy si no fuese por ella.

Gracias a mis amigos (Samer, Roy, Cristina, Demer, Teresa, Iria, todos, que si enumero no termino) por haberme aportado remansos de paz en los momentos más difíciles del proceso.

Espero no haberme dejado a nadie en el tintero, pero temo que sea demasiado esperar. Por eso, y como soy muy despistado, gracias a tí si me he olvidado, sabes que no ha sido aposta.

Pablo Rivière Marichalar,

Abril, 2012